UNIVERSITÀ
DEGLI STUDI
DI PADOVA

Università degli Studi di Padova
Dipartimento di Ingegneria Civile, Edile e Ambientale

SCUOLA DI DOTTORATO DI RICERCA IN:
Scienze dell'Ingegneria Civile e Ambientale

CICLO XXV

SYSTEM IDENTIFICATION AND STRUCTURAL HEALTH MONOTORING OF BRIDGE STRUCTURES

Direttore della Scuola: Ch.mo Prof. Stefano Lanzoni
Supervisore: Ch.mo Prof. Claudio Modena
Co-Supervisore: Ch.mo Prof. Andrew W. Smyth

Dottorando: Kleidi Islami

Gennaio 2013

SYSTEM IDENTIFICATION AND SHM OF BRIDGE STRUCTURES

Kleidi Islami

Advisor: Claudio Modena

Co-advisor: Andrew W. Smyth

Submitted in Partial Fulfillment of the
Requirements for the Degree of
Doctor of Philosophy in
Civil and Environmental Engineering Sciences

Università
degli Studi
di Padova

UNIVERSITY OF PADUA

January 2013

ACKNOWLEDGEMENTS

First of all, I would like to express my very great appreciation to Prof. Claudio Modena for his valuable and constructive suggestions during the planning and development of this research work. I have to address my thanks to him as my supervisor for the main sources in this study. The opportunity given by the collaborative projects led to new innovative ideas that are included in this thesis.

Acknowledgements are also due to Prof. Andrew W. Smyth for his precious help, the scientific knowledge and the nice welcome during the exchange 2011-2012 period at Columbia University. All the interesting discussions and guidance made me learn a lot from him.

I would like to gratefully thank also Prof. Raimondo Betti in New York for his valuable advices, his kindness and his patience without which this work would not be completed. Many of his ideas contributed to further develop and accurately estimate the structural parameters of numerous case studies.

Furthermore, I am really grateful to Dr. Francesca da Porto for the help, the suggestions, the composition of the thesis and the encouragement during my research.

Special thanks go also to Dr. Filippo Casarin and Dr. Carlo Pellegrino for the support, the interest in my work and the helpful discussions. A warm gratitude must be extended to all my colleagues at the University of Padua for the stimulating work environment and for the nice times spent besides the daily work.

Last but not least, I wish to thank my family and my fiancé for supporting and encouraging me throughout my study. Thanks for the warm love.

ABSTRACT

This research study addresses two issues for the identification of structural characteristics of civil infrastructure systems. The first one is related to the problem of dynamic system identification, by means of experimental and operational modal analysis, applied to a large variety of bridge structures. Based on time and frequency domain techniques and mainly with output-only acceleration, velocity or strain data, modal parameters have been estimated for suspension bridges, masonry arch bridges, concrete arch and continuous bridges, reticular and box girder steel bridges. After giving an in-depth overview of standard and advanced stochastic methods, differences of the existing approaches in their performances are highlighted during system identification on the different kinds of civil infrastructures. The evaluation of their performance is accompanied by easy and hard determinable cases, which gave good results only after performing advanced clustering analysis. Eventually, real-time vibration-based structural health monitoring algorithms are presented during their performance in structural damage detection by statistical models.

The second issue is the noise-free estimation of high order displacements taking place on suspension bridges. Once provided a comprehensive treatment of displacement and acceleration data fusion for dynamic systems by defining the Kalman filter algorithm, the combination of these two kinds of measurements is achieved, improving the deformations observed. Thus, an exhaustive analysis of smoothed displacement data on a suspension bridge is presented. The successful tests were subsequently used to define the non-collocated sensor monitoring problem with the application on simplified models.

RIASSUNTO

Questo lavoro di ricerca mira a due obiettivi per l'identificazione delle caratteristiche strutturali dei sistemi infrastrutturali civili. Il primo è legato al problema della identificazione del sistema dinamico, mediante analisi modale sperimentale e operativa, applicata ad una grande varietà di strutture da ponte. Basandosi su tecniche nel dominio del tempo e delle frequenze e, soprattutto, su dati di output di accelerazione, velocità o strain, i parametri modali sono stati stimati per ponti sospesi, ponti ad arco in muratura, ponti a travi in calcestruzzo e ad arco, ponti reticolari e ponti in acciaio a cassone. Dopo aver dato una panoramica approfondita dei metodi stocastici standard ed avanzati, sono state evidenziate le differenze degli approcci esistenti nelle loro performance per l'identificazione del sistema sui diversi tipi di infrastrutture civili. La valutazione della loro performance viene accompagnata da casi facilmente e difficilmente determinabili, che hanno dato buoni risultati solo dopo l'esecuzione di analisi avanzate di Clustering. Inoltre, sono stati sviluppati algoritmi di identificazione dinamica automatica in tempo reale basandosi sulle vibrazioni strutturali dei ponti monitorati, a sua volta utilizzati nel rilevamento dei danni strutturali tramite modelli statistici.

Il secondo problema studiato riguarda la stima di spostamenti di ordine superiore che si svolgono sui ponti sospesi, eliminando il rumore di misura e di processo. Una volta fornito un trattamento completo della fusione dei dati di spostamento e accelerazione per i sistemi dinamici tramite il filtro di Kalman, la combinazione di questi due tipi di misurazioni ha mostrato un miglioramento nelle deformazioni osservate. Pertanto, è stata presentata un'analisi esauriente di un ponte sospeso e dei sui dati dinamici e di spostamento filtrati. I test positivi sono stati successivamente utilizzati per definire il problema dei sensori non collocati alla stessa locazione ed applicazione su modelli semplificati.

Contents

INTRODUCTION

The purpose of Dynamic Identification of structural systems is to define, from testing and experimental recordings, the values of modal parameters, in terms of natural frequencies and respective vibration modes, with the scope of characterizing the dynamic behavior. After determining the characteristics of the system, it is possible to calibrate a numerical model, in order to obtain results as similar as possible to the real behavior of the structure. A calibrated Finite Element Model with experimental data reveals to be a very effective tool for evaluating capacity or structural changes, giving a reliable estimation of the system.
Extending the dynamic tests to long-term periods it is most likely to monitor the global behavior of the structure and detect any possible damage due to abnormal dynamic behavior. Although the process of recording time-histories through Structural Health Monitoring is quite feasible, extracting the exact modal parameters (natural frequencies, damping ratios and mode shapes) is a delicate process. This is because these parameters represent the real physical system and their variation may imply changes in the structural properties.

The mechanical behavior of a structure depends on its inertial characteristics and stiffness, which govern the response to an external excitation. While in general these characteristics are known, in system identification we want to determine this functional relation i.e. the relation between excitation and response. If measurements of input and output are available, the process is called *deterministic system identification*. In civil structures it is very difficult and costly to excite the system. Thus, output-only identification technique, which is performed by just measuring the structural response under ambient excitation (wind traffic, etc.), is the most commonly used procedure to get information from a structure

without exciting it on purpose. So, if only the response is measurable and the excitation is ambient vibration, the SI is named *stochastic system identification*. The main assumption made in stochastic system identification is that the exciting force is white noise.

Numerous papers have been published over the last 40 years on system identification. But, only after the publications of Astorm and Bohlin [1] [2], in which the *maximum likelihood* method was extended to a serially correlated time series to estimate ARMAX models, and of Ho and Kalman [3], in which the deterministic *state space realization* problem was solved using a certain Hankel matrix formed in terms of impulse response, the system identification theory started.

Experimental tests for the determination of the modal parameters are based on the possibility to describe the dynamic behavior of the structure either by means of a set of differential equations in the time domain, or by a set of algebraic equations in the frequency domain. The techniques of dynamic identification can, therefore, be grouped in *frequency domain* techniques and *time domain* techniques.

Methods defined in the frequency domain operate by obtaining the Frequency Response Function (FRF) from which it is possible to identify natural frequencies, damping ratios and mode shapes. The FRF is typically obtained by means of analysis based on Fast Fourier Transform (FFT). The simplest form of Frequency Domain is the *Basic Frequency Domain* or *Peak Picking* [4], where the identification of modes is obtained by evaluating the frequency corresponding to the peaks of the Power Spectral Density (PSD) plot. The method named *Complex Mode Indication Function* (CMIF) [5] is considered an extension of the PP method, in which a singular value decomposition (SVD) of the matrix of cross-spectra is introduced in order to separate the contribution of individual modes. This method was subsequently improved in the non-parametric method of *Frequency Domain Decomposition* (FDD) [6], and it is a method capable of taking into account the multiplicity of modes (more modes at close frequencies).

A key step in stochastic realization (time domain) is either to apply the deterministic realization theory (*Eigensystem realization Algorithm* [24]) to a certain Hankel matrix constructed with sample estimates of the process covariances (later called *covariance-driven stochastic system identification*), or to apply the canonical correlation analysis (CCA) [7] to the future and past of the observed process. A well-known form of stochastic system identification is also the *data-driven stochastic system identification* where the estimate of the modal

parameters is represented by the error minimization (*prediction error*) between the *Auto-Regressive Moving Average* (ARMA) model estimate and the observations.

These algorithms have shown to be implemented very efficiently and in a numerically stable way by using the tools of modern numerical algebra such as the SVD. In the mid-1980s QR decomposition and SVD emerged, and realization theory-based techniques have led to a development of *subspace system identification* (SSI) methods [8] [9] where we do not need optimization techniques or imposition of a canonical form system, so that they do not suffer from inconveniences encountered in applying *prediction error* methods. The method requires the model's order selection and the distinction between structural and non-structural modes. This operation is usually carried out by means of stabilization diagrams. Subspace methods define the equation of motion in state form, given input signals and output responses using simple algebraic techniques such as QR decomposition, SVD and least-squares procedures. The name *subspace* is due to the property for which the matrices containing the measured signal can be interpreted as a vector space where the columns of this matrix represent a base of vectors, while the rows allow to obtain a sequence of estimates evaluated by Kalman filters [10]. A stochastic model in state space is then directly identified by the data output or measured by the correlation functions between the outputs. Accordingly to what has been described above, the subspace methods can be distinguished in *data-driven SSI* and *covariance-driven SSI* [11].

An extensive comparison of *time and frequency domain* techniques has been carried out in this work, applied to several case studies of bridge structures.

During the last years of technology development, sensors for SHM (especially the wireless one) are becoming very sophisticated for the particular use in civil infrastructures. Not only acceleration sensors but also displacement ones have become very accurate and provide high sampling frequencies compared to some years ago. The presence of both acceleration and displacement sensors during measurement campaigns provide a beneficial redundancy that can be utilized to better assess the structural behavior. As the sampling frequencies of the different measurements are different, a multi-rate Kalman filter can be applied to process the data fusion [12]. Exploiting the smoothed results, a clear scene of the structural displacements taking place under heavy traffic loads can be achieved.

Outline of the thesis

The primary goal of this work is to provide an in-depth overview of procedures of commonly used methods for system identification and to reveal their performance in real applications of bridge structures. Different kinds of structures will be analyzed, beginning from suspension bridges, slender concrete arch bridges, masonry arch bridges, concrete beam bridges, railway steel bridges, ending with highway steel box bridges. A new technique will be shown in the case of redundant acceleration and displacement measurements, in particular for suspension bridges, where an algorithm of data fusion will be analyzed in order to get noise-free and accurate deformation results. As a future research, the problem of non-collocated sensors will be defined: displacement estimation in nodes where only acceleration measurements are present.

The first part of the thesis is devoted to some concepts frequently used throughout this study. More precisely, Chapter 1 introduces basic facts in stochastic processes and random signals, including probability and physical-variable state representation for stochastic estimation. After describing the observer design problem, the implementation of the Kalman filter for stochastic estimation is presented. The rest of Chapter 1 deals with the theory of dynamic systems and in particular with the state-space representation of the equation of motion, Impulse and Frequency Response Functions and discrete state-space representation.

Chapter 2 considers the system identification problem going from the definition of controllability and observability matrices, identification of the DT Markov parameters and the modal parameter identification through the Eigensystem Realization Algorithm. Finally, an introduction to Stochastic Realization is given in the case of un-known input.

Chapter 3 enters with more details in the stochastic system identification methods, giving a wide view of time and frequency domain system identification techniques. In particular, the Frequency Domain Decomposition and the Stochastic Subspace Identification (data-driven with principal component analysis and Canonical Correlation Analysis) will be also described, in relation to the applications that will be presented in Chapter 4. The last part of the chapter is dedicated to the description of three different procedures implemented for automated system identification used on SHM. Great effort has been focused on the cluster analysis implemented in an automatic system identification that accurately estimates modal parameters even in difficult case studies.

In Chapter 4, the application of stochastic identification methods is carried out by analyzing the field data of ten bridges. It deals with the

modal analysis through different stochastic system identification for different kinds of structures as suspension bridges, slender concrete arch bridges, masonry arch bridges, concrete beam bridges, railway steel bridges and highway steel box bridges. The structural identification will be applied in cases of demolition process, validation of a seismic retrofit intervention, damage assessment, strain measurements utilization in modal analysis and long term monitoring. Damage detection analysis is performed through implementation of regression models in the cases of bridge monitoring. Finally, for most structures, the comparison between newly developed techniques (SSI-ECCA [13]) and the conventional ones will be presented.

Chapter 5 provides a comprehensive treatment of displacement and acceleration data fusion for dynamic systems. By defining the Kalman filter algorithm, the combination of these two kinds of measurements is achieved, improving the deformations observed. The efficiency of this technique is then demonstrated through the application on the measurements of the Manhattan Bridge in New York City. In fact, several accurate displacement plots will be presented for different load conditions of the studied structure. A future research topic is introduced at the end of the chapter concerning the problem of displacement estimation in nodes where only acceleration measurements are present. So, a simple 3-dof example for the 'non-collocated sensor problem' is presented.

Finally, the principal deductions are summarized in the Conclusion section.

1

STOCHASTIC PROCESSES AND DYNAMIC SYSTEMS

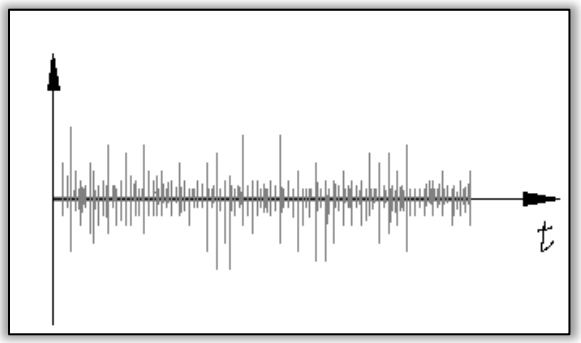

This chapter follows a basic introduction to probability and random variables, with which all of us have some acquaintance. It deals with the concepts of random processes and the mathematical description of noise-like signals with their spectral explanation. The concept of state model is described and how this contributes in analyzing stochastic data. Then a short explanation of the Kalman Filter process is reported as an accurate tool playing an important role in every sensing in systems of the real world. The second part of the chapter describes dynamic systems and in particular the state-space representation of the equation of motion.

1.1 Probability and random variables

1.1.1 Why stochastic models are useful?

In a physical system, such as a vehicle performance, a navigation system or a monitored bridge, the first step in understanding the behavior of the system is to formulate an adequate represented model. Through physical insights, fundamental "laws," and empirical testing, the engineer tries to establish the relationships among certain variables of interest, inputs to the system, and outputs from the system. With such a mathematical model and the tools provided by system and control theories, he is able to investigate the system structure and its response.

In order to observe the actual system behavior, measurement devices are constructed to quantify data signals proportional to certain variables of interest. These output signals and the known inputs to the system are the only information that is directly visible from the system behavior. There are several reasons why stochastic data processing helps to improve the performance of these systems. As we know, no mathematical system model is perfect because it is approximated by mathematical and physical laws, leaving some sources of uncertainty.

A second deficiency of deterministic models is that dynamic systems are driven not only by our own control inputs, but also by disturbances which we can neither control nor model deterministically. At the other hand the sensors that we use to collect data from our system do not provide perfect responses because are affected by noise. Another situation is when we have different devices that measure the same signal and one must ask how to generate the best estimate based on these redundant data. So, to assume an adequate form of our model and reality, the techniques developed in stochastic science are very useful.

1.1.2 Random signals and probability.

If we look at the chart in the first page of this chapter, we see a signal that cannot be described with explicit mathematical functions such as sine waves or step functions. It was discovered in the early nineteen century that random signals could be described by probabilistic approaches and in particular in terms of their spectral content. Noise is usually present in every signal but we have to know how much does it condition our signals

and suppress it by means of filtering techniques. That is why one needs to understand noise and accordingly probability that plays a key role because it characterizes random signals.

The probability that the outcome of a discrete event will favor a particular event is defined as

$$P(A) = \frac{Possible\ outcomes\ favoring\ event\ A}{Total\ number\ of\ possible\ outcomes}$$

where we read P(A) as "probability of event A". This concept is then expanded to include the relative-frequency-of-occurrence or statistical viewpoint of probability.
The probability of an outcome favoring either A or B is given by

$$P(A \cup B) = p(A) + p(B) \tag{1.1}$$

If the probability of two outcomes is independent (one does not affect the other) then the probability of both occurring is the product of their individual probabilities:

$$P(A \cap B) = p(A) \cdot p(B) \tag{1.2}$$

that is called the joint probability.
Meanwhile the probability of outcome A, given an occurrence of outcome B, is called the conditional probability of A given B, and is defined as

$$P(A \mid B) = \frac{P(A \cap B)}{P(B)} \tag{1.3}$$

This is also called the conditional probability and similarly the conditional probability of B given A:

$$P(B \mid A) = \frac{P(B \cap A)}{P(A)} \tag{1.4}$$

It is assumed here that P(B) and P(A) are not zero. If we combine (1.3) and (1.4) each equation can be solved for the probability A intersection B and the results equated. This leads to Bayes rule:

$$P(B \mid A) = \frac{P(B \mid \mathrm{A})P(A)}{P(B)} \tag{1.5}$$

The joint probability array $P(A \cap B)$ contains all the necessary information for computing all marginal and conditional probabilities.

A common function representing the probability of random variables is defined by the cumulative distribution function that describes the probability assignment as it reflects onto equivalent events in the random variable (A) space.

$$F_A(x) = P(A \leq \delta) \tag{1.6}$$

where δ is a parameter representing a realization of A.

Even more commonly used is its derivative, known as the probability density function:

$$f_A(x) = \frac{d}{dx} F_A(x) \tag{1.7}$$

which has the following properties:

1. $f_A(x)$ is a non-negative function
2. $\int_{-\infty}^{\infty} f_A(x)dx = 1$
3. $P_A[a, b] = \int_a^b f_A(x)dx$

From the definition of average or sample mean μ we can derive the Expected Value (or first statistical moment) for the continuous random variable as

$$E(A) = \int_{-\infty}^{\infty} x f_A(x)dx. \tag{1.8}$$

It can be also used to define the expectation of a function of A:

$$E(g(A)) = \int_{-\infty}^{\infty} g(x) f_A(x)dx. \tag{1.9}$$

If we express $g(A) = A^k$ we can obtain the second moment of the random variable:

$$E(A^2) = \int_{-\infty}^{\infty} x^2 f_A(x)dx. \tag{1.10}$$

If we let $g(A) = A - E(A)$, we get the variance of the signal about the mean:

$$Variance\ A = E\left[\left(A - E(A)\right)^2\right] = E(A^2) - \left(E(A)\right)^2 \tag{1.11}$$

The square root of the variance, known as the *standard deviation*:

$$\sigma_A = \sqrt{Variance\ of\ A}. \tag{1.12}$$

1.1.3 Description of random signals.

A special probability distribution known as the *Normal or Gaussian distribution* [14] has historically been popular in modeling random systems for a variety of reasons.

$$f_A(x) = \frac{1}{\sqrt{2\pi\sigma^2}} e^{\frac{1}{2\sigma^2}(x-\mu)^2} \tag{1.13}$$

Many random processes occurring in nature actually appear to be normally distributed, or very close, such is the case of the signals that are being recorded to study the behavior of a structure. It is defined a Normal signal, one in which all the density functions describing the process are normal in form. In the case of Gaussian process the variates are random variables $A(t_1)$, $A(t_2)$, … , $A(t_k)$,where the points in time may be chosen arbitrarily.

A way to describe the process is to correlate it with itself at two different times. It is known that this is called *the Autocorrelation function* for a random process X(t):

$$R_x(t_1, t_2) = E[X(t_1)X(t_2)] \tag{1.14}$$

Or in stationary case: $R_x(t_1, t_2) = E[X(t)X(t + dt)]$ where dt is the sampling interval.

The autocorrelation function contains information about the frequency content of the process. For a stationary process, there is an important relation known as the *Wiener-Khinchine relation*:

$$S_X(j\omega) = \Im[R_X(\tau)] = \int_{-\infty}^{+\infty} R_X(\tau) e^{-j\omega\tau} d\tau \tag{1.15}$$

where $\Im[R_X(\tau)]$ indicates the Fourier transform and ω is the frequency. This function is also called the *power spectral density* of the random signal. This important relationship ties together the time *and frequency spectrum* representations of the same signal.

Cross spectral density functions for stationary processes X(t) and Y(t) are defined as

$$S_{YX}(j\omega) = \Im[R_{XY}(\tau)] = \int_{-\infty}^{+\infty} R_{XY}(\tau) e^{-j\omega\tau} d\tau \tag{1.16}$$

Another function that is closely related to the cross density is the coherence function. It is defined as

$$\gamma_{XY}^2 = \frac{|S_{XY}(j\omega)|^2}{S_x(j\omega)S_Y(j\omega)} \tag{1.17}$$

Both the cross spectral density and coherence function are useful in analysis of experimental data, because computer technology has made it possible to easily transform time data to frequency.

White noise is defined to be a stationary random process having a constant spectral density function, i.e. the autocorrelation function is a dirac delta function $\delta(\tau)$. Denoting the white noise spectral as A, we then have $S_{WN}(j\omega) = A$ and the correspondent autocorrelation function $R_{WN}(j\omega) = A\delta(\tau)$.

1.2 Physical-variable states for stochastic estimation

In many applications the noisy nature of the measurements is not taken into consideration. The noise is typically statistical in nature, which leads us to stochastic methods for addressing these problems.

1.2.1 Deriving the state-variable model.

State-space models are essentially a notational convenience for estimation and control problems, developed to make tractable what would otherwise be intractable analysis.

If it is assumed that the various internal parameters (M,K,C) are determined, the problem can be considered as solved, but from an input-output point of view it is really not necessary to know what these specific values are. From an external viewpoint, one only needs to determine, experimentally if you will, a relationship between the output function of time for a given input function of time, and a set of initial conditions, or the State.

There are two distinct methods for deriving a state-variable model of a given linear time-invariant system: first deriving the state model from a given output-input transfer function; the second, deriving the state model directly from the original physical relationships. In the second case, the states are selected to correspond directly to physical variables in the system. These variables can be measured. The state model is not unique, indeed there are actually an infinite number of state model forms all describing the same system. The state-variable model is termed an internal model of the system, because the model can include dynamics that do not appear in the input-output, external transfer function model of the system.

A linear first order, time invariant state variable set of differential equations has the general form [15]:

$$\begin{aligned} \dot{x}(t) &= Ax(t) + Bu(t), \\ y(t) &= Cx(t) + Du(t) \end{aligned} \tag{1.18}$$

where $x(t)$ is the *n-th* order state vector and $u(t)$ is a single input signal; $y(t)$ is the single output signal; A is termed $n \times n$ plant matrix; B is the $n \times 1$ input matrix; C is the $1\times$ n output matrix and D is a scalar.

Taking the Laplace transform solved for *X(s)* and *X(0)* as initial state:

$$X(s) = (s-a)^{-1}X(0) + (s-a)^{-1}bU(s) \tag{1.19}$$

Taking the inverse Laplace transform of the first term (zero input portion of the state):

$$X_{zi} = e^{at}(0) \tag{1.20}$$

The second term in Eq. (1.19) is the zero-state portion of the state, and its inverse Laplace transform is

$$X_{zi} = \int_0^t e^{a(t-\tau)} bu\,(\tau)d\tau \tag{1.21}$$

So the complete state solution will be:

$$X_{zi} = e^{a\tau}x(0) + e^{a\tau}\int_0^t e^{-a\tau} bu\,(\tau)d\tau \tag{1.22}$$

In general for a resolvent matrix e^{At}

$$\begin{aligned} A_d &= e^{At} = I + AT + \frac{A^2T^2}{2!} + \cdots \\ B_d &= \int_0^T e^{AT}dT = \left\{ I + AT + \frac{A^2T^2}{2!} + \cdots \right\} B \end{aligned} \tag{1.23}$$

One of the main reasons for going to a state-space description of the linear dynamic system is to be able to readily apply the tool of digital computing.

If we set $x_d(k)$, $A_d = e^{AT}$, $B_d = \left(\int_0^T e^{AT}dT\right)B$, $u(kT-\xi) + u_d(k)$, than the discrete time-state representation of the continuous-state differential equation (1.12) is:

$$x_d(k) = A_d x_d(K-1) + B_d u_d(k-1)$$
$$y_d(k) = C_d x_d(k) + D_d u_d(k-1) \tag{1.24}$$

To propagate the state forward in time, one only has to propagate the discrete state propagation. Only the current stage $x_d(k)$ is stored in the computer memory and the discrete parameters A_d and B_d.

$$A_d = e^{AT} \approx I + AT \qquad B_d = \left(\int_0^T e^{A\xi} d\xi\right) B \approx BT + \frac{ABT^2}{2} \qquad C_d = C \qquad D_d = D$$

1.2.2 The Observer Design Problem.

There is a related general problem in the area of linear systems theory generally called the observer design problem. The basic problem is to determine (estimate) the internal states of a linear system, given access only to the system's outputs. (Access to the system's control inputs is also presumed, but we omit that aspect here. See for example [16] for more information.) This is akin to what people often think of as the 'black box' problem where you have access to some signals coming from the box (the outputs) but you cannot directly observe what's inside. The many approaches to this basic problem are typically based on the state-space model presented in the previous section. There is typically a process model that models the transformation of the process state. This can usually be represented as a linear stochastic difference equation.

$$x_d(k) = A_d x_d(K-1) + d u_d(k-1) + w(k-1) \tag{1.25}$$

In addition there is some form of measurement model that describes the relationship between the process state and the measurements.

$$y_d(k) = C_d x_d(k) + D_d u_d(k-1) + v(k) \tag{1.26}$$

The terms w and v are random variables representing the process and measurement noise respectively.

We consider here the common case of noisy sensor measurements. There are many sources of noise in such measurements. For example, each type of sensor has fundamental limitations related to the associated physical medium, and when pushing the envelope of these limitations the signals are typically degraded. In addition, some amount of random electrical noise is added to the signal via the sensor and the electrical circuits. The time-varying ratio of "pure" signal to the electrical noise continuously affects the quantity and quality of the information. The result is that information obtained from each sensor must be qualified as part of an overall sequence

of estimates, and analytical measurement models typically incorporate some notion of random measurement noise or uncertainty as shown above.

There is the additional problem that the actual state transform model is completely unknown. While we can make predictions over relatively short intervals using models based on recent state transforms, such predictions assume that the transforms are predictable, which is not always the case. The result is that like sensor information, ongoing estimates of the state must be qualified as they are combined with measurements in an overall sequence of estimates. In addition, process models typically incorporate some notion of random motion or uncertainty as shown above.

1.3 The discrete Kalman filter

The Kalman filter is essentially a set of mathematical equations that implement a predictor-corrector type estimator that is optimal in the sense that it minimizes the estimated error covariance - when some presumed conditions are met. Since the time of its introduction, the Kalman filter has been the subject of extensive research and application, particularly in the area of autonomous or assisted navigation. This is largely due not only to the advances in digital computing that made the use of the filter practical, but also to the relative simplicity and robust nature of the filter itself. Rarely do the conditions necessary for optimality actually exist, and yet the filter apparently works well for many applications in spite of this situation.

An introduction to the general idea of the Kalman filter is offered in Chapter 1 of [14]. More extensive references include [10], [17] [18].

1.3.1 The principals

In the previous paragraph the terms w and v were random variables; they are assumed to be independent and with normal probability distributions:

$$\begin{aligned} p(w) &\sim N(0, Q), \\ pv &\sim N(0, R) \end{aligned} \tag{1.27}$$

In practice, the process noise covariance and measurement noise covariance matrices might change with each time step or measurement.

The A matrix in the difference equation (1.25) relates the state at the previous time step $k-1$ to the state at the current step k, in the absence of either a driving function or process noise.

We define $\hat{x}^-(k)$ to be our a priori state estimate at step k given knowledge of the process prior to step k, and $\hat{x}(k)$ to be our a posteriori state estimate at step k given measurement $y(k)$. We can then define the estimate error as

$$e^-(k) = x(k) - \hat{x}^-(k) \tag{1.28}$$

and associated error covariance matrix is

$$P^-(k) = E[e^-e^{-T}] + E[\big(x(k) - \hat{x}^-(k)\big)\big(x(k) - \hat{x}^-(k)\big)^T] \tag{1.29}$$

With the assumption of a priori estimate $\hat{x}^-(k)$, we now seek to use the measurement $y(k)$ to improve the prior estimate. We choose a linear connection of the noisy measurement and the prior estimate as expressed in the equation:

$$\hat{x}(k) = \hat{x}^-(k) + K[y(k) - C\hat{x}^-(k)] \tag{1.30}$$

where the $\hat{x}(k)$ is the updated estimate and K is called the Kalman gain, that is obtained minimizing the covariance matrix of the error:

$$K(k) = P^-(k)C^T[CP^-(k)C^T + R]^{-1} \tag{1.31}$$

The weighting by K is explained by thinking that as the measurement error covariance R approaches zero, the actual measurement $y(k)$ is "trusted" more and more, while the predicted measurement $C\hat{x}^-(k)$ is trusted less and less. On the other hand, as the a priori estimate error covariance $P^-(k)$ approaches zero the actual measurement is trusted less and less, while the predicted measurement $C\hat{x}^-(k)$ is trusted more and more.

The covariance matrix associated with the optimal estimate may now be computed. Referring to equation (1.25), substituting $\hat{x}^-(k)$ and $K(k)$ we have

$$P(k) = P^-(k) - K(k)[CP^{-1}(k)C^T + R]K^T(k) \tag{1.32}$$

or

$$P(k) = P^-(k)[I - K(k)C] \tag{1.33}$$

The Kalman filter estimates a process by using a form of feedback control: the filter estimates the process state at some time and then obtains feedback in the form of (noisy) measurements. As such, the equations for the Kalman filter fall into two groups: time update equations and

measurement update equations. The time update equations are responsible for projecting forward (in time) the current state and error covariance estimates to obtain the a priori estimates for the next time step. The measurement update equations are responsible for the feedback - i.e. for incorporating a new measurement into the a priori estimate to obtain an improved a posteriori estimate. The final estimation algorithm resembles that of a predictor-corrector algorithm for solving numerical problems.

So let's recall this algorithm omitting the subscripts:

Time Update:

$$\begin{aligned} x(k) &= Ax(k-1) + Bu(k) \\ P(k) &= AP(k-1)A^T + Q \end{aligned} \tag{1.34}$$

Measurement Update:

$$\begin{aligned} K(k) &= P(k)C^T[CP(k)C^T + R]^{-1} \\ x(k+1) &= x(k) + K(k)[y(k+1) - Cx(k)] \\ P(k+1) &= [I - K(k+1)C_T]P(k) \end{aligned} \tag{1.35}$$

After each time and measurement update pair, the process is repeated with the previous a posteriori estimates used to project or predict the new a priori estimates. This recursive nature is one of the very appealing features of the Kalman filter - it makes practical implementations much more feasible than (for example) an implementation of a Wiener filter [18] which is designed to operate on all of the data directly for each estimate. The Kalman filter instead, recursively conditions the current estimate on all of the past measurements.

An alternative form of the Kalman filter by algebraically manipulating the previous is:

$$\begin{aligned} P(k)^{-1} &= P(k-1)^{-1} + C^T R^{-1} C \\ K(k) &= P(k)C^T R^{-1} \end{aligned} \tag{1.36}$$

Note that the updated covariance can be computed without first finding the gain. Also, the expression for the Kalman gain now involves P(k); therefore if we need K(k), this must be computed after the P(k) computation. Thus the order of computation in the recursive algorithm is reversed from that presented previously:

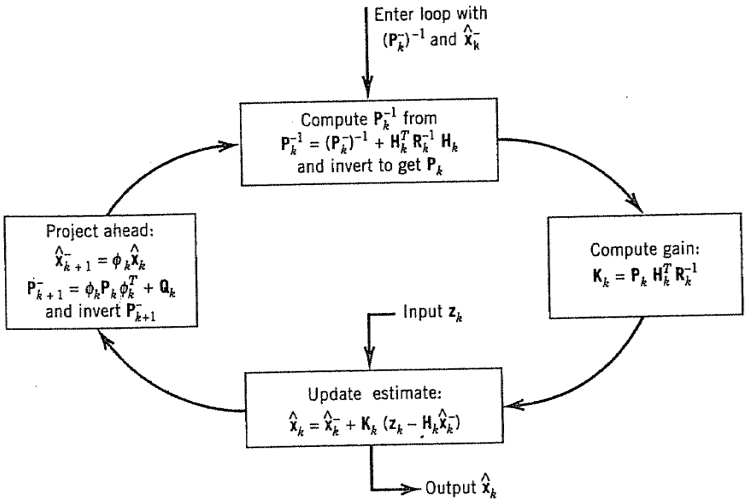

Figure 1.1 Alternative Kalman filter recursive loop [18].

1.4 Dynamic systems

To describe the dynamics of a structural system under the excitation of any applied force, you must have a mathematical model of the system that allows to describe the relationship between forcing and displacements, velocities and accelerations. The typical approach to correlate the response *x(t)* of a system to the forcing *f(t)* is to solve the differential equation of motion with appropriate initial conditions. Not all problems, however, can easily be solved by simple integration. It is then convenient to seek the solution by means of the definition of the functions of frequency response. This section presents the basics of Structural Dynamics. A mathematical representation of mechanical systems based on the use of state variables is obtained.

1.4.1 Equation of motion

The conventional representation of a linear time invariant dynamic system with N-degree of freedom is based on the equation of motion:

$$M\ddot{v}(t) + C\dot{v}(t) + Kv(t) = f(t) \tag{1.37}$$

where $v(t)$, $\dot{v}(t)$, $\ddot{v}(t)$ are, respectively, the vector of the displacements, velocities and accelerations corresponding to the various degrees of freedom; K, C, M are, respectively, the matrices of stiffness, damping and of the masses, each having size NxN. Finally, $f\ (t)$ is the vector of external forces applied, of dimension N.

Natural frequencies, damping ratios and mode shapes are recovered from the homogeneous equation:

$$M\ddot{v}(t) + C\dot{v}(t) + Kv(t) = 0 \tag{1.38}$$

whose solution is of the form $v = \varphi e^{\lambda t}$. Substituting this form into the first equation we can obtain the eigenvalue problem related to the K, C, M:

$$(M\lambda^2 + C\lambda + K)\varphi = 0 \tag{1.39}$$

Resolving this equation N, complex eigenvalues and eigenvectors are obtained. The eigenvalues are generally presented in the form [19]:

$$\lambda_j = -\omega_j\zeta_j + i\omega\sqrt{1-\zeta_j^2} \tag{1.40}$$

where ω_j is the undamped frequency and ζ_j is the relative damping ratio. In the case of underdamped systems, in which civil structures belong, the eigenvalues are obtained in conjugate couples:

$$\lambda_{2j-1}, \lambda_{2j} = -\omega_j\zeta_j \pm i\omega_j\sqrt{1-\zeta_j^2} \tag{1.41}$$

The corresponding couples of conjugate complex eigenvectors are of the form:

$$\Psi_j = \begin{bmatrix} \varphi_j \\ \lambda_j\varphi_j \end{bmatrix} \tag{1.42}$$

Since such modal parameters are determined from the structure's properties (mass, stiffness and damping), they can be used to describe the dynamic system's behavior.

1.4.2 Response to an impulse input

For the estimation of the solution of a stable linear system, the response $v(t)$ to an impulse excitation can be obtained from the *unit impulse response function* (IRF). If we define with *f(t)* the input force and with *y(t)* the response, the IRF can be defined as [20]:

$$h(t) = y(t) \text{ when } f(t) = \delta(t) \tag{1.43}$$

where t is the time measured from the instant of applying the function δ. For an arbitrary input the response of the system can be given by the convolution integral:

$$y(t) = \int_{-\infty}^{\infty} h(t) f(t-\tau) \cdot d\tau \tag{1.44}$$

which indicates that the response *y(t)* is given by a weighted sum of the input *f(t)* on the entire time history.

A system is said to be with constant parameters, if the IRF is independent from the particular instant in which the impulse is applied. The system is said to be stable if for every input excitation that is limited, gives a limited response:

$$y(t) = \int_{-\infty}^{\infty} |h(t)| \cdot d\tau < \infty \tag{1.45}$$

1.4.3 Frequency response function

It is of particular importance the representation in the frequency domain. The frequency response function (FRF) is obtained by taking the Fourier transformation of the IRF:

$$H(\omega) = \int_{0}^{\infty} h(t) \cdot e^{-j2\pi\omega\tau} d\tau \tag{1.46}$$

where

$$h(t) = 0 \quad \text{for } \tau < 0$$

If we define with *f(t)* the input force and with *y(t)* the response, from the definition of $H(\omega)$ and $h(t) = y(t)$ it is possible to attain, for every couple of excitation-response, the ratio between the Fourier transform of the response *Y(ω)* and the force *F(ω)*:

$$H(\omega) = \frac{Y(\omega)}{F(\omega)} \tag{1.47}$$

To decrease the measurement errors some estimators of the FRF are used. The product between the response at time t and at time $t+\tau$ is given by:

$$y(t)y(t+\tau) = \int_{0}^{\infty}\int_{0}^{\infty} h(\xi)h(\eta)x(t-\xi)x(t+\tau-\eta)d\xi d\eta \tag{1.48}$$

The right side of the equation (1.48) is the autocorrelation function defined in section 2.5.

Similarly, the product between the response $y(t)$ and the 'input evaluated at $t+\tau$:

$$y(t)f(t+\tau) = \int_0^\infty h(\xi)x(t)x(t+\tau-\xi)d\xi \tag{1.49}$$

that is the cross correlation function $R_{xy}(\tau)$. Applying the Fourier transform of the previous two expressions, and recalling the definitions of the function of spectral density, it is possible to obtain alternative expressions for the frequency response function. So it is easy to obtain [20]:

$$H_1(\omega) = \frac{S_{fx}(\omega)}{S_{ff}(\omega)} \tag{1.50}$$

that minimizes the effects of noise on the output. Alternatively, you can use the estimator $H_2(\omega)$, defined as:

$$H_2(\omega) = \frac{S_{xx}(\omega)}{S_{xf}(\omega)} \tag{1.51}$$

that instead reduces the effects of noise at the input. In the absence of measurement errors would verify the identity:

$$H_1(\omega) = H_2(\omega) = H(\omega)$$

Finally, to verify the reliability of the measurement carried out and control the congruence between the estimators, one can use the coherence function $\gamma^2(\omega)$, defined by the following expression:

$$\gamma^2(\omega) = \frac{\left|S_{fx}(\omega)\right|^2}{S_{ff}(\omega)S_{xx}(\omega)} \tag{1.52}$$

which indicates how the response is consistent with the excitation.

If $\gamma^2(\omega) < 0{,}75$, experimental data tend to be unreliable, in the sense that the signal/noise ratio is low. Even the presence of excitations not measured or the nonlinear behavior of the system are causes which may give rise to low values of coherence.

Regarding the FRF, more precisely, we define the function *Receptance* $\alpha(\omega)$ as the ratio between the transform of the displacement $y(t)$ of a point of the system and the Fourier transform of the forcing $y(t)$ applied [20]:

$$\alpha(\omega) = \frac{Y(\omega)}{F(\omega)} \tag{1.53}$$

Similarly, we define as *Mobility* the ratio between the Fourier transform of the velocity $\dot{y}$ of a point of the system and the transform of forcing *f.* Finally, the *Inertance* function $A(\omega)$ is defined as the ratio between the transformed acceleration $\ddot{y}$ of a point and the Fourier transform of the force *f(t)*:

$$A(\omega) = \frac{\ddot{Y}(\omega)}{F(\omega)} \tag{1.54}$$

The *Receptance* can be written as:

$$\alpha(\omega) = \frac{1}{(-\omega^2 \cdot M + i\omega \cdot C + K)}. \tag{1.55}$$

Using the Modal matrix φ whose columns are the eigenvectors, after some mathematical manipulations based on the mode shapes we obtain:

$$\alpha_{jk}(\omega) = \sum_{r=1}^{N} \frac{\phi_{rj}\phi_{rk}}{(\omega_r^2 - \omega^2 + 2i\zeta_r\omega_r\omega)} \tag{1.56}$$

At the same time, the *Inertance* can be extracted [20]:

$$A_{jk}(\omega) = -\sum_{r=1}^{N} \frac{\omega^2 \cdot \phi_{rj}\phi_{rk}}{(\omega_r^2 - \omega^2 + 2i\zeta_r\omega_r\omega)} \tag{1.57}$$

So the FRF in displacement terms is the sum of 2N elements, as the equation of motion in state form has 2N components. Having 2N complex conjugate eigenvectors, equation (1.57) becomes [20]:

$$\alpha_{jk}(\omega) = \sum_{r=1}^{N} \left[\frac{\Psi_{jr}\Psi_{kr}}{(i\omega - \lambda_r)} - \frac{\Psi_{jr}^*\Psi_{kr}^*}{(i\omega - \lambda_r^*)} \right] \tag{1.58}$$

The Frequency Response Function has an important role in the frequency domain system identification techniques, while the Impulse Response Function is important for the time domain system identification techniques.

1.4.4 State space formulation

In the previous paragraph the equation of motion was presented with the mathematical model that governs the dynamics of a mechanical system with N degrees of freedom (frequencies, modal damping and mode shapes).

By defining a state vector $x(t) = \begin{bmatrix} v(t) \\ \dot{v}(t) \end{bmatrix}$, the second-order differential equation of motion can be reformulated in the form of a first-order matrix differential equation [19]:

$$\dot{x}(t) = Ax(t) + Bu(t) \tag{1.59}$$

where $A \in \Re^{nxn}$ $(n = 2N)$ and $B \in \Re^{nxr}$ are defined as:

$$A = \begin{bmatrix} 0 & I \\ -M^{-1}K & -M^{-1}C \end{bmatrix} \qquad B = \begin{bmatrix} 0 \\ M^{-1} \end{bmatrix} \qquad u(t) = \begin{bmatrix} 0 \\ f(t) \end{bmatrix} \tag{1.60}$$

The system is formed by 2N differential equations of the first order. The corresponding equations of free motion are written by placing equal to zero, at every instant, the vector of external forces u(t), from which it follows:

$$\dot{x}(t) = Ax(t) \tag{1.61}$$

Considering a harmonic solution of the type $x(t) = \psi e^{\lambda t}$, the eigenvalue problem related to A is obtained:

$$\psi B = \lambda \psi \tag{1.62}$$

where ψ is a complex vector of 2N dimension, while λ is a complex parameter.

When recording the experimental response of a structure, measurements are performed in correspondence of some degrees of freedom. If it is assumed that the measurements y(t) are acquired through a number of sensors equal to one, between transducers accelerations, velocities and displacements, the equation of motion can be associated with the equation of observability:

$$y(t) = C_a \ddot{v}(t) + C_v \dot{v}(t) + C_d v(t) \tag{1.63}$$

In the above formula matrices C_a C_v and C_d are used to select the degrees of freedom recorded during acquisition. Such matrices have all components equal to zero except the elements at the *i-th* degree of freedom in which is placed the measuring instrument. In general, acceleration measurements are recorded for system identification purposes, although, recent technology developments allow to directly measure displacements (GPS sensors, see Chapter 5).

Whereas the motion equation and the equation of observability, the representation of the mechanical system in a second order form is therefore obtained:

$$\begin{aligned} M\ddot{v}(t) + C\dot{v}(t) + Kv(t) &= f(t) \\ y(t) = C_a\ddot{v}(t) + C_v\dot{v}(t) + C_d v(t) & \end{aligned} \tag{1.64}$$

Introducing the following equations:

$$\begin{aligned} C &= [C_d - C_a M^{-1}K \quad C_v - C_a M^{-1}C] \\ D &= C_a M^{-1} \qquad u(t) = \begin{bmatrix} 0 \\ f(t) \end{bmatrix} \end{aligned} \tag{1.65}$$

the measurement equation can be written as follows:

$$y(t) = Cx(t) + Du(t) \tag{1.66}$$

The matrices C and D are matrices of coefficients of dimensions, respectively, *lx2N* and *lxN*. Considering the equation of motion in form of state and observability, we finally obtain the representation of state of a mechanical system with N degrees of freedom in the form:

$$\begin{aligned} \dot{x}(t) &= Ax(t) + Bu(t) \\ y(t) &= Cx(t) + Du(t) \end{aligned} \tag{1.67}$$

1.4.5 Discrete state-space model

During the experimental acquisition, the physical quantities such as displacement, velocity and acceleration are available in discrete time, as data sequences. Is therefore necessary to reformulate the model from continuous to discrete representation. Defining t_0 as the generic instant, the solution at time t is given by the following *Lagrange formula*:

$$x(t) = x_L(t) + x_F(t) \tag{1.68}$$

where

$$x_L(t) = e^{A(t-t_0)}x(t_0) \tag{1.69}$$

is the component due to free vibration, while:

$$x_F(t) = \int_{t_0}^{t} e^{A(t-\tau)}Bu(t)d\tau \tag{1.70}$$

corresponds to the forced motion. Placing $t_0 = k\Delta t$ and $t = (k+1)\Delta t$ it's possible to obtain the discrete representation:

$$\begin{aligned} x_{k+1} &= A_d x_k + B_d u_k \\ y_k &= C x_k + D u_k \end{aligned} \tag{1.71}$$

The matrices A_d and B_d represent the corresponding discrete time equivalent of A and B, respectively, and they are obtained from their continuous-time counterparts:

$$\begin{aligned} A_d &= e^{A\Delta t} \\ B_d &= \int_0^{\Delta t} e^{A\tau} d\tau B = [A - I]A^{-1}B \end{aligned} \tag{1.72}$$

Equations (1.71) are referred to as a discrete-time state space model of dynamic systems.

The main task of system identification is to obtain a quadruple [A, B, C, D] that provide the mapping between given sequences of forces $u(k)$ *and measurements* $y(k)$.

With regard to the characteristic value, A_d can be written in terms of the eigenvalues and eigenvectors of A such as:

$$A = \Psi e^{\Lambda_c \Delta t} \Psi^{-1} \tag{1.73}$$

and the eigenvalues of A_d, denoted by λ_{di}, are related to their continuous counterparts by $\lambda_{di} = e^{\lambda_{ci}\Delta t}$.

Once the *[A, B, C, D]* are obtained (different methods, see Chapter 2 and Chapter 3), the eigenvalues of A and the corresponding damping ratios can be evaluated by:

$$f_j = \frac{\left|ln(\bar{\lambda}_j)\right|}{2\pi\Delta t}, \qquad \xi_j = -\frac{Re(ln(\bar{\lambda}_j))}{\left|ln(\bar{\lambda}_j)\right|} \tag{1.74}$$

2

SYSTEM IDENTIFICATION

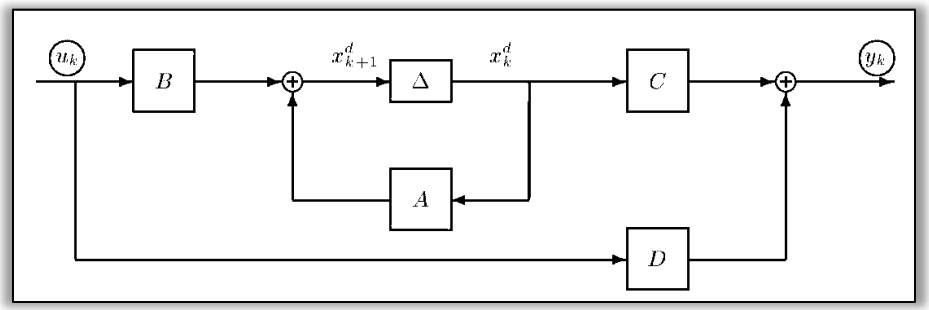

This chapter follows the basic dynamics introduction (estimate structural vibration responses of the system subject to any type of excitation) discussed in the previous chapter, and deals with system identification (identify dynamic properties of a system from measurements of its response) with the discrete time realization. Using the de-convolution process, the Markov parameters are obtained. Furthermore, the disposition of Markov Parameters in Hankel matrices and the use of singular value decomposition makes possible to obtain a realization of C_d and B_d. Finally, the discrete time system matrix A_d is obtained. The last step is the extraction of eigenvalues and eigenvectors of A_d.

2.1 Introduction

The main reason of interest in the experimental modal analysis is related to the consideration that the dynamic behavior of a structure is a kind of "fingerprint" in the sense that it depends only on its intrinsic characteristics (mass, stiffness, damping, constraints, etc.) and not on the extent or the type of load applied: therefore, if there are not internal modifications to the system (as, for example, of structural damage), the behavior of the structure remains unchanged, otherwise, you will notice a change in the natural frequencies and vibration modes. Furthermore, the structural identification is itself a non-destructive technique, and as such can be applied both to new structures, for example in the testing phase, and to existing structures.

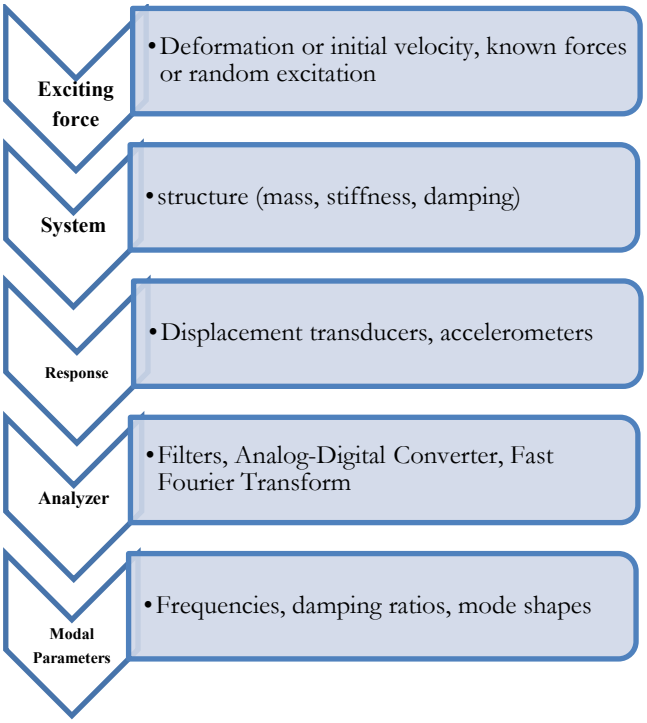

Figure 2.1 System identification Flowchart

Generally the problem is simplified, identifying the groups of characteristic parameters of the system; for example, the hypothesis of linear behavior (but also stationarity and observability) of the structure and its schematization according to a system having a finite number of degrees of freedom, that leads to the equation of motion. Therefore, the

experimental tests for the determination of the modal parameters are based on the possibility to describe the dynamic behavior of the structure either by means of a set of differential equations in the time domain, or by a set of algebraic equations in the frequency domain. The techniques of dynamic identification can, therefore, be grouped in frequency domain and time domain techniques. If measurements of input and output are available, the process is called *deterministic system identification*. On the other hand, if only the response is measurable and the excitation is ambient vibration, the SI is named *stochastic system identification*.

2.2 Controllability and observability

A state x_1 is reachable if there is a way to take the system from the origin to x_1 in finite time, given the input locations. A state x_1 is controllable if there is a way to take the system x_1 to the origin in finite time given the input locations. In our applications the system matrices are non-singular and reachability and controllability are equivalent. So if we apply this definition to the first of equations (1.71) the result is as follows [21]:

$$\begin{aligned} x(1) &= A_d x(0) + B_d u(0) \\ x(2) &= A_d x(1) + B_d u(1) = A_d\big(A_d x(0) + B_d u(0)\big) + B_d u(1) \\ &= A_d^2 x(0) + A_d B_d u(0) + B_d u(1) \end{aligned} \tag{2.1}$$

$$x(k) = A_d^k x(0) + \sum_{j=0}^{k-1} A_d^{k-j-1} B_d u(j) \qquad k \geq 0 \tag{2.2}$$

If we bring the first term of equation (2.2) at the left side, we obtain:

$$x(k) - A_d^k x(0) = C_k U_k \tag{2.3}$$

where C_k and U_k are defined as:

$$C_k = [B_d \quad A_d B_d \quad \cdots \quad A_d^{k-1} B_d] \qquad U_k = \begin{Bmatrix} u(k-1) \\ u(k-2) \\ \cdots \\ u(0) \end{Bmatrix} \tag{2.4}$$

The matrix C_k represented in equation (2.4) is called the controllability matrix. In considering the state-space model (equation (1.71)), it can be controllable if and only if C_k has rank n, the order of the system (full

column rank). To decide how many terms we do need for attaining a full rank, the Cayley-Hamilton theorem says that the largest power that is not a linear combination of previous powers is N-1 (where N=system order) so, to check controllability we only need to consider C_N; if the system is not controllable at $k = N$ it is not controllable.

Uncontrollable modes cannot be excited from the input locations and cannot, therefore be identified.

A system may be controllable but some modes may only be "marginally so" and thus may be difficult to identify. A practical question then is, how to locate excitation sources to minimize controllability difficulties in a certain bandwidth. The controllability Gramian [21] offers guidance. The minimum norm input sequence required to take the system from the origin to the state x in k steps is:

$$U_k = C_k^{-*} x(k) \tag{2.5}$$

It can be shown that:

$$|U_k|^2 = x(k)^T W_c^{-1} x(k) \tag{2.6}$$

where the controllability Gramian (that helps to find the input locations) [21] is:

$$W_c = C_k C_c^T \tag{2.7}$$

The state *x(0)* is observable if it can be obtained from observations of the inputs and the outputs. A state is constructible if one can identify it from the current and past values of the inputs and outputs. Observability implies constructability if the system matrix is not singular.

Similarly to the case of controllability, we can construct the observability matrix from the second of equations (1.71):

$$y(k) = C_d A_d^k x(0) + \sum_{j=0}^{k-1} C_d A_d^{k-j-1} B_d u(j) + D_d u(k) \tag{2.8}$$

If we bring the first term of equation (2.8) at the left side, we obtain [22]:

$$C_d A_d^k x(0) = y(k) - \sum_{j=0}^{k-1} C_d A_d^{k-j-1} B_d u(j) + D_d u(k) \tag{2.9}$$

States contained on the null space of the observability matrix are unobservable (i.e., if the system is given an initial condition in the unobservable space and no loads act, the measurements would remain identically zero).

As in the case of the controllability, Cayley-Hamilton ensures that the rank of this matrix will not increase after the power of the system matrix is N-1 so it is sufficient to stop at n = N to check the rank. The observability matrix is:

$$O_k = \begin{Bmatrix} C_d \\ C_d A_d \\ \vdots \\ C_d A_d^{N-1} \end{Bmatrix} \tag{2.10}$$

Since states that are not observable "cannot be seen" from the sensors, only observable states can be identified.

2.3 Identification of a DT model in state-space form

The principal steps to complete a system identification are:

- Use de-convolution to compute the DT Markov parameters,
- Organize the Markov parameters in Hankel Matrices and use Singular Value decomposition to obtain a realization.

The weighting-sequence model in equation (2.9) forms the so called Markov Parameters:

$$Y_l = C_d A_d^{l-1} B_d \quad l = k - j \tag{2.11}$$

So equation (2.9) can be rewritten as:

$$y(k) = C_d A_d^k x(0) + \sum_{l=0}^{k} Y_l u(k-l) \tag{2.12}$$

Markov parameters are invariant to state transformations. Since, they are the pulse responses of the system, they must be unique for a given system. This formulation is the basis for the Observer Kalman filter Identification (OKID) that was developed by [23]. Note that the input-output description in equation (2.12) is valid only under zero initial conditions (steady-state). It is not applicable if the transient effects are present in the system. If the system is asymptotically stable, then there are only a finite number of

steps in the weighting sequence model. However, for lightly damped systems, the number of terms in the weighting sequence model can be too large. Under these conditions, the state-space observer model is advantageous.

We can eliminate the initial condition from the input-output relation, provided that we start looking at the output sequence no earlier than step *p+1*, so:

$$y(k) = \sum_{l=0}^{p+1} Y_l u(k-l) \tag{2.13}$$

Equation (2.13) can be represented also in the following sequence [21]:

$$\begin{aligned} &[y_h \quad y_{h+1} \quad \cdots \quad y_z] \\ &= [Y_0 \quad Y_1 \quad \cdots \quad Y_{p+1}] \begin{bmatrix} u(h) & u(h-1) & \cdots & u(z) \\ u(h-1) & u(h) & \vdots & \vdots \\ \vdots & \vdots & \vdots & \vdots \\ u(h-(p+1)) & u(h-p) & \cdots & u(z-(p+1))) \end{bmatrix} \end{aligned} \tag{2.14}$$

or in short form:

$$y_{hz} = \Upsilon_{p+1} U_{hzp} \tag{2.15}$$

where U_{hzp} is known as the Toeplitz Block. The equation has a unique solution provided that U_{hzp} is full row rank.

If we add and subtract the term *Gy(k)* to first of equations (1.71), the following is obtained:

$$\begin{aligned} x(k+1) &= A_d x(k) + B_d u(k) + Gy(k) - Gy(k) \\ y(k) &= C_d x(k) + D_d u(k) \end{aligned} \tag{2.16}$$

Then, substituting the second expression on the first one:

$$\begin{aligned} x(k+1) &= A_d x(k) + B_d u(k) + Gy(k) - G(C_d x(k) + D_d u(k)) \\ x(k+1) &= (A_d - GC_d)x(k) + [B_d - GD_d)G] \begin{Bmatrix} u(k) \\ y(k) \end{Bmatrix} \end{aligned} \tag{2.17}$$

or

$$x(k+1) = \bar{A}x(k) + \bar{B}v(k)$$

Exactly the same form as the original expression except that the input now includes the true input and the output and the matrices are modified. The output equation has not changed.

Repeating the considerations performed from equation (2.11) to equation (2.15), the Observer Markov Parameters (OMP) $\overline{Y}_{p+1}$ are obtained by solving:

$$y_{hz} = \overline{Y}_{p+1} V_{hzp} \tag{2.18}$$

The Observer Markov Parameters depend on p but the Markov Parameters (which are unique) can be extracted from any OMP set that satisfies equation (2.18).

At this point, let's see the extraction of MP from OMP. Considering both solution equations (2.15) and (2.18) we obtain:

$$\begin{aligned} Y_j &= C_d A^{j-1} B_d \\ \bar{Y}_j &= C_d \bar{A}^{j-1} B \end{aligned} \tag{2.19}$$

For *j=1*:

$$\begin{aligned} Y_1 &= C_d B_d \\ \bar{Y}_1^{(1)} = C_d B_d - C_d G D_d \,, \;\; \bar{Y}_1^{(2)} &= C_d G \end{aligned} \tag{2.20}$$

So

$$\begin{aligned} Y_1 &= \bar{Y}_1^{(1)} + \bar{Y}_1^{(2)} Y_0 \\ \bar{Y}_1^{(1)} &= Y_1 - \bar{Y}_1^{(2)} Y_0 \end{aligned} \tag{2.21}$$

For *j=2* and *j=3*:

$$\begin{aligned} Y_2 &= \bar{Y}_2^{(1)} + \bar{Y}_1^{(2)} Y_1 + \bar{Y}_2^{(2)} Y_0 \\ Y_3 &= \bar{Y}_3^{(1)} + \bar{Y}_1^{(2)} Y_2 + \bar{Y}_2^{(2)} Y_1 + \bar{Y}_3^{(2)} Y_0 \end{aligned} \tag{2.22}$$

In general, we can state that the extraction of Markov Parameters is possible with the formulation:

$$Y_k = \bar{Y}_k^{(1)} + \sum_{j=1}^{k} \bar{Y}_j^{(2)} Y_{k-j} \tag{2.23}$$

2.4 The Eigensystem Realization Algorithm

Since from the previous section we extracted the Markov Parameters $[D, CA^iB]$, the matrices A, B, C, D separately represent the realization of the system. Such parameters can be achieved through the eigensystem realization algorithm [21].

Let us define the block Hankel matrix H_k as:

$$H_k = \begin{bmatrix} Y_{k+1} & Y_{k+2} & \cdots & Y_{k+\beta} \\ Y_{k+2} & Y_{k+2} & \cdots & Y_{k+\beta+1} \\ \vdots & \vdots & \vdots & \vdots \\ Y_{k+\alpha} & \cdots & \cdots & Y_{k+\beta+\alpha-1} \end{bmatrix} \tag{2.24}$$

where the number of α and β blocks is arbitrary.

We now recall that the observability block of order α is given by:

$$P_\alpha = \begin{bmatrix} C_d \\ C_d A_d \\ \vdots \\ C_d A_d^{\alpha-1} \end{bmatrix} \tag{2.25}$$

And the controllability block of order β is:

$$Q_\beta = \begin{bmatrix} B_d & A_d B_d & \cdots & A_d^{\beta-1} B_d \end{bmatrix} \tag{2.26}$$

It follows, therefore, that:

$$P_\alpha = \begin{bmatrix} C_d A_d^k B_d & C_d A_d^{k+1} B_d & \cdots \\ C_d A_d^{k+1} B_d & C_d A_d^{k+2} B_d & \cdots \\ \vdots & \vdots & \vdots \end{bmatrix} \tag{2.27}$$

or in other words the block Hankel matrix H_k is equal to the product of the observability block of order α times the system matrix to the power k times the controllability block of order β:

$$H_k = P_\alpha A_d^k Q_\beta = \begin{bmatrix} Y_{k+1} & Y_{k+2} & \cdots & Y_{k+\beta} \\ Y_{k+2} & Y_{k+2} & \cdots & Y_{k+\beta+1} \\ \vdots & \vdots & \vdots & \vdots \\ Y_{k+\alpha} & \cdots & \cdots & Y_{k+\beta+\alpha-1} \end{bmatrix} \tag{2.28}$$

From equation (2.28) we have:

$$H_0 = P_\alpha Q_\beta \tag{2.29}$$

If H is a matrix, then there exist two orthonormal matrices R and S so that (performing a Singular value Decomposition):

$$H_0 = R\Sigma \mathrm{S}^{\mathrm{T}} \tag{2.30}$$

where, Σ is a matrix with the same dimension as H_0, but diagonal.

Recalling from previous discussion that the rank of the observability and controllability blocks is not bigger than the order of the system and that the rank of a product is never larger than the smaller rank of the multipliers we conclude that the rank of H_0 is no larger than N - independently of the size of the blocks α and β - where N is the system order.

Examining the dimensions of $H_0 \epsilon\, R^{(\alpha m)x(\beta r)}$ and knowing that the rank of H_0 is not controlled by the number of blocks we select these block sizes such as:

$$\alpha \geq \frac{N}{m} \qquad \beta \geq \frac{N}{r} \tag{2.31}$$

We have, therefore:

$$\begin{gathered} H_0 = [R_S \quad R_n] \begin{bmatrix} \Sigma_S & 0 \\ 0 & 0 \end{bmatrix} [V_S \quad V_n]^T \\ H_0 = R_S \Sigma_S V^T \end{gathered} \tag{2.32}$$

We can express the non-zero singular values as a product of two diagonal matrices:

$$\Sigma_S = E_1 E_2$$

so

$$H_0 = (R_S E_1)(E_2 V^T) \tag{2.33}$$

and recalling equation (2.29), it is simply to set

$$P_\alpha = R_S E_1 \qquad Q_\beta = E_2 V_S^T \tag{2.34}$$

Recalling equation (2.25) we can say that the realization of the state to output matrix C_d is given, therefore, by the first m rows of the matrix $R_S E_1$. On the other hand from equation (2.26), it is possible to obtain a realization of the input state matrix B_d, therefore, by the first r columns of the matrix $E_2 V_S^T$.

We now face the question of how to compute the system matrix A_d. There are various ways to go about it; a commonly used one uses the block Hankel matrix H_1 as illustrated next.

$$H_1 = P_\alpha A_d Q_\beta = (R_S E_1) A_d (E_2 V^T) \tag{2.35}$$

Recognizing the orthogonality of the matrices R_S and S_S one gets

$$A_d = E_1^{-1} R_n^T H_1 S_n E_2^{-1} \tag{2.36}$$

And since D_d is the first Markov parameter we have obtained a DT realization. Now, taking in consideration the Zero Hold Assumption, A_d is converted in continuous form. Finally, using the *Jordan Form* $A_c = \Phi\Lambda\Phi^{-1}$, $X = \Phi Y$:

$$\begin{aligned} \dot{Y} &= \Lambda Y + \Phi^{-1} B_c U \\ y &= C_c \Phi Y + D_c U \end{aligned} \tag{2.37}$$

where $\Lambda = \mathrm{diag}(\lambda_1,\ \lambda_2 \ldots \lambda_1)$, from which $\lambda_j = -\omega\zeta \pm \omega\sqrt{1-\zeta^2}i$.

The identification approach where the Markov parameters are extracted from the Observer and the untangling using ERA is known in the literature as the ERA-OKID Algorithm.

2.5 Introduction to stochastic realization

There are instances where we can only measure output signals. If we know nothing about the input then we can't say anything about the system from the output but, if some assumptions on the input are reasonable then significant information can be extracted from the output signals. In absence of the input, it is impossible to calculate the frequency response function. However, by assuming that the input is stationary white noise, the system realization can be written as follows:

$$\begin{aligned} x(k+1) &= A_d x(k) + w(k) \\ y(k) &= Cx(k) + v(k) \end{aligned} \tag{2.38}$$

where w and v are process and measurement noises, assumed to be uncorrelated zero mean white noise of unknown covariance. The matrices A and C are system and observation matrices, respectively.

As already mentioned, it is assumed that the stochastic process is stationary, and the state is uncorrelated with both, process noise and output noise, so the following expressions are true:

$$E(x_k v_k^T) = 0 \qquad E(x_k w_k^T) = 0 \qquad E(x_{k+1} x_{k+1}^T) = \Sigma$$

or

$$E[(Ax_k + w_k)(Ax_k + w_k)^T] = \Sigma \tag{2.39}$$

The whiteness property and statistically independent property between the noises and the system's past measurements allow us to represent output covariance matrices in the form of Markov parameters.

Computing the multiplications inside the second equation of (2.39):

$$E(Ax_k w_k^T) + E(Ax_k x_k^T A^T) + E(w_k w_k^T) + E(w_k x_k^T A^T) = \Sigma \tag{2.40}$$

which simplifies into:

$$\Sigma = A\Sigma A^T + Q \tag{2.41}$$

where $Q = E(w_k w_k^T)$. We define the output covariance function matrix Λ_i for a time step *i:*

$$\Lambda_i = E(y_{k+1} y_k^T) \tag{2.42}$$

Substituting the output equation (2.38), one gets:

$$\Lambda_i = E[(Cx_{k+1} + v_{k+i})(Cx_k + v_k)^T]$$
$$\Lambda_i = E(Cx_{k+1} v_k) + E(Cx_{k+i} x_k^T C^T) + E(v_{k+i} v_k^T) + E(v_{k+i} x_k^T C^T) \tag{2.43}$$

Assuming that the noise is white, $E(v_{k+i}\, v_k^T) = 0$ and recalling that $E(x_k v_k^T) = 0$:

$$\Lambda_i = E(Cx_{k+i} x_k^T C^T) = CE(x_{k+i} x_k^T) C^T \tag{2.44}$$

From the state recurrence it is a simple matter to show that:

$$\mathrm{x}_{k+1} = A^i x_k + A^{i-1} w_k + A^{i-2} w_{k+1} + \cdots + w_{k+i-1} \tag{2.45}$$

Post-multiplying by x_k^T and taking the expectations:

$$E\left(x_{(k+i)} x_k^T\right) = A^i E(x_k x_k^T) = A^i \Sigma \tag{2.46}$$

Substituting in equation (2.44), the following expression is obtained:

$$\Lambda_i = CA^i \Sigma C^T \tag{2.47}$$

Recalling equation (2.43), it can be noticed that for $i = 0$ and for $R = E(v_k v_k^T)$ we have:

$$\Lambda_0 = C\Sigma C^T + R \tag{2.48}$$

and for $i \neq 0$:

$$\Lambda_i = CA^i\Sigma C^T \tag{2.49}$$

Defining $G = E\left(x_{k+1}y_k^T\right) = E[(Ax_k + w_k)(Cx_k + v_k)^T]$ and performing the multiplications:

$$G = E[Ax_k v_k^T + Ax_k x_k^T C^T + w_k v_k^t + w_k\, x_k^T C^T]$$

or

$$G = A\Sigma \mathrm{C}^{\mathrm{T}} \tag{2.50}$$

We know that equation (2.49) can be formulated as [21]:

$$\Lambda_i = CA^{i-1}\mathrm{A}\Sigma C^T \tag{2.51}$$

But $G = A\Sigma \mathrm{C}^{\mathrm{T}}$, so equation (2.49) can be rewritten as:

$$\Lambda_i = CA^{i-1}\mathrm{G} \tag{2.52}$$

We saw in section 2.4 that the Markov Parameters in the known input case are given by

$$Y_i = C_d A^{i-1} B \tag{2.53}$$

We conclude that the output covariance can be treated as Markov Parameters of a system having the matrices $[A,G,C]$. We can, therefore, estimate the output covariance and from there join our ERA algorithm at the point where the Hankel matrices are formed and proceed without any changes to obtain a realization for $[A\ G\ C]$. It is possible, at this point, to extract natural frequencies, mode shapes and damping ratios from the state matrix A.

3

STOCHASTIC SYSTEM IDENTIFICATION

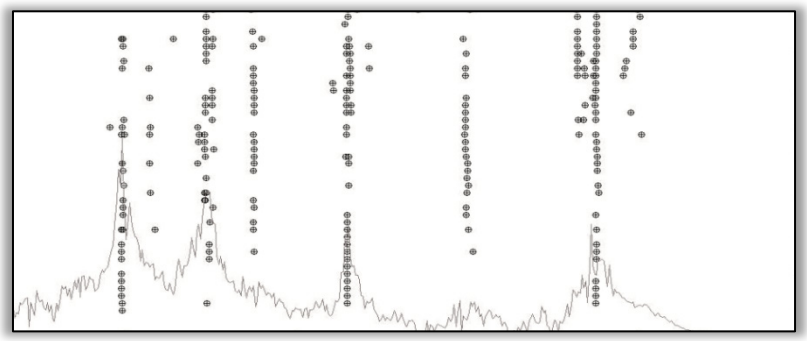

Following the introduction given in section 2.5, this chapter describes in detail system identification techniques in the case of stochastic input or output-only measurements. Since the techniques are divided into time and frequency domain system identification, both groups are presented. In particular, the Frequency Domain Decomposition, the Stochastic Subspace Identification and an Enhanced SSI will be described, in relation also to the applications that will be presented in Chapter 4. Three types of automatic system identification have been implemented for the dynamic SHM of bridges.

The primary assumption in the development of *stochastic system identification* techniques is to consider the input signal as a white noise. Under this consideration, the representation of the dynamic system parameters in the *frequency domain* is given by the Power Spectra Density, while for the *time-domain* case, covariance functions of the response and the realization of ARMA or state-space models are able to represent the system's properties.

3.1 Frequency Domain Decomposition

This technique is an extension of the classical approach in the frequency domain of PP (Peak Picking). It is a non-parametric method capable of taking into account the multiplicity of vibration modes at close frequencies. This is because, unlike the classical technique PP, it has been introduced a singular value decomposition (SVD) of the spectra matrix in order to separate the contribution of individual modes. Subsequently this technique has been extended to the Enhanced FDD [6].

An important property that relates the *function of autocorrelation in* equation (0.14) with the *Power Spectral Density* function is given by its Fourier transform: (0.12)

$$G_x(f) = 2\int_{-\infty}^{+\infty} R_x(\tau)e^{-i2\pi f\tau}d\tau = 4\int_{0}^{+\infty} R_x(\tau)\cos(2\pi f\tau)\,d\tau \tag{3.1}$$

where $G_x(f)$ is always positive. On the other hand if we take the Fourier transform of equation (0.48) we obtain the important relation:

$$G_y(f) = |H(f)|^2 G_x(f) \tag{3.2}$$

With similar steps to cross functions, you get another important relation:

$$G_{xy}(f) = H(f)G_x(f) \; = 2\int_{-\infty}^{+\infty} R_{xy}(\tau)\, e^{-i2\pi\omega\tau}d\tau \tag{3.3}$$

That is, the Fourier Transform of the cross-correlation functions $R_{xy}(\tau)$ is called cross-spectrum (CSD). As a result, the functions of cross-correlation will occupy the off-diagonal terms of the PSD matrix while the functions of autocorrelation terms are the diagonals of the former.

Consider a system with r inputs $x_i(t)\ i = 1,2,\dots,r$ and a measurement output $y(t)$; one may think that $y(t)$, is the sum of many $y_i(t)\ i = 1,2,\dots,r$:

$$y(t) = \sum_{i=1}^{r} y_i(t) \quad or \quad y_i(t) = y_1 \cup y_2 \dots \cup y_k \cup \dots \cup y_n \tag{3.4}$$

We know that $\mathrm{x_r(t)} \rightarrow \mathrm{h_r(\tau)} \rightarrow \mathrm{y_r(t)}$ and from equations (0.44) and (0.48) we obtain the Fourier transform:

$$G_y(f) = \sum_{i=1}^{r}\sum_{j=1}^{r} \overline{H_i}(f)H_j(f)G_{ij}(f) \tag{3.5}$$

where the symbol "-" indicates the complex conjugate. If we define an r-dimensional vector of inputs $x(t) = [x_1(t), x_2(t), \dots, x_r(t)]$, its r-dimensional frequency response function $H(f) = [H_1(f), H_2(f), \dots, H_r(f)]$, a cross-spectra vector of the output $y_i(t)$ with the input $x_i(t)$: $G_{xy}(f) = \left[G_{x_1y}(f), G_{x_2y}(f), \dots, G_{x_ry}(f)\right]$ and at last a matrix $r \times r$ for every input $x_i(t)$

$$G_{xx}(f) = \begin{pmatrix} G_{x_1x_1}(f) & G_{x_1x_2}(f) & \cdots & G_{x_1x_r}(f) \\ G_{x_2x_1}(f) & G_{x_2x_2}(f) & \cdots & G_{x_2x_r}(f) \\ \vdots & \vdots & & \vdots \\ \vdots & \vdots & & \vdots \\ G_{x_1x_r}(f) & G_{x_rx_2}(f) & \cdots & G_{x_1x_1}(f) \end{pmatrix} \tag{3.6}$$

then equation (3.4) becomes:

$$G_{yy}(f) = H(f)G_{xx}(f)H^H(f) \tag{3.7}$$

where $G_{xx}(f)$ is the matrix of spectral density of the inputs, $H(f)$ is the matrix of frequency response functions and $G_{yy}(f)$ is the spectral density matrix of the output:

$$G_{yy}(f) = \begin{pmatrix} G_{y1y1} & G_{y1y2} & \cdots & G_{y1ym} \\ G_{y2y1} & G_{y2y2} & \cdots & G_{y2ym} \\ \vdots & \vdots & & \vdots \\ G_{ymy1} & G_{ymy2} & \cdots & G_{ymym} \end{pmatrix} \tag{3.8}$$

At the basis of the FDD technique is the decomposition of the system response in a set of simple systems with single degree of freedom, one for each mode to identify. This decomposition takes place through the identification of a spectral bell around the peak considered, that corresponds to the *k-th* mode. Furthermore, a SVD of the spectral matrix is introduced in order to separate the contribution of each mode from

which is possible to distinguish the frequency peaks directly from the matrix of spectral densities. From an analytical point of view consists in obtaining vectors and singular values of the matrix of spectral density as follows:

$$G_{yy}(f) = USU^H \tag{3.9}$$

In matrix form:

$$S = \begin{pmatrix} S_1 & 0 & 0 & 0 \\ 0 & S_2 & 0 & 0 \\ 0 & 0 & \ddots & 0 \\ 0 & 0 & 0 & S_m \end{pmatrix} \qquad U = \begin{pmatrix} u_{11} & u_{12} & \cdots & u_{1m} \\ u_{21} & u_{22} & \cdots & u_{2m} \\ \vdots & \vdots & \vdots & \vdots \\ u_{m1} & u_{m2} & \cdots & u_{mm} \end{pmatrix} \tag{3.10}$$

where U is a matrix of orthonormal components of the singular vectors calculated as a function of ω from which it is possible to derive the singular vector plots; S is a diagonal matrix containing the singular values and U^H is the matrix of the right components of the vector. From a graphical point of view, the singular values are obtained through an envelope of the components of the orthonormal singular vectors. So the first singular value line contains almost all the modes identified, while the other lines can contain any left mode that are close to the previous ones (see Figure 3.1).

On the peak of the *k-th mode*, the corresponding singular value is a good estimate of the modal form $\hat{\varphi} = u_1$. The singular value represents the PSD function of the corresponding SDOF system given by:

$$G_{yy}(\omega) = \sum_{k=Sub(\omega)}^{n} \frac{d_k \varphi_k \varphi_k^T}{i\omega - \lambda_k} + \frac{\overline{d_k}\,\overline{\varphi_k}\,\overline{\varphi_k^T}}{i\omega - \overline{\lambda_k}} \tag{3.11}$$

The last expression is similar to equation (3.7) in the case where the input is white noise.

In the basic version of FDD, natural frequencies are mainly the peaks of the singular vector plots and damping ratios can roughly be estimated by the half-power bandwidth method. In the Enhanced version of the FDD, damping ratios and modes are estimated in a more accurate way.

The first step in the EFDD technique is to select the right spectral bell representing the SDOF system. This is realized by the use of the singular vector, (corresponding to the peak singular value) as a reference and comparing it in terms of MAC (Modal Assurance Criterion) [24] [25]:

$$MAC(\varphi_r, \varphi_i) = \frac{[\varphi_r^H \varphi_i]^2}{[\varphi_r^H \varphi_r] \cdot [\varphi_i^H \varphi_i]} \tag{3.12}$$

where φ_r is the reference singular vector and φ_i represent the singular vectors corresponding to the singular values in the neighborhood of the peak. One can fix a reference value of MAC and proceed with the comparison. If during the comparison with the *i-th* vector a MAC greater than the chosen level is obtained, this vector is selected and the corresponding singular value contributes to the definition of the spectral bell under the selected mode.

At this point the spectral area previously identified is transferred in the time domain with an Inverse Discrete Fourier Transform in order to obtain a SDOF system represented by a normalized autocorrelation function:

$$R(\tau) = \int s_1(\omega) e^{-i\omega\tau} d\tau \tag{3.13}$$

From this function, having a decreasing trend over time, the value of damping ratio can be extracted. The damping ratio is calculated by performing the logarithmic decrement:

$$\delta = \frac{2}{k} \ln \frac{r_0}{|r_k|} \tag{3.14}$$

where r_0 is the initial value of the autocorrelation function and r_k is the *k-th* step. The damping ratio is thus obtained by:

$$\xi = \frac{\delta}{\sqrt{\delta^2 + 4\pi^2}} \tag{3.15}$$

The frequency is determined by linear regression between measured intervals intersected with the time axes and extreme intervals. It is observed that the time interval between the intersection of the function with the time axis and a peak corresponds to a quarter of a period; consequently the frequency will be identified by taking into account two cycles in the plot of the autocorrelation.

3.2 Stochastic subspace Identification – PCA

A widely used technique of *stochastic system identification* is the Stochastic Subspace Identification [4] [7] [8] [9]. The basic idea in this method is to build a state-space model which estimates state vectors from output responses by decomposing them by LQ or SVD.

3.2.1 The general concept

If we suppose that an estimate of a sequence of state vectors of the state-space model is constructed from the observed input-output data (equation (0.67)), then for t = 0, 1, 2, … , N-1, where N is the number of data, we have

$$\begin{bmatrix} \bar{x}(t+1) \\ y(t) \end{bmatrix} = \begin{bmatrix} A & B \\ C & D \end{bmatrix} \begin{bmatrix} \bar{x}(t) \\ u(t) \end{bmatrix} + \begin{bmatrix} \eta(t) \\ v(t) \end{bmatrix} \tag{3.16}$$

Where $\bar{x} \in R^n$ is the estimate of state vector, $u \in R^m$ the input, $y \in R^p$ the output, and η, v are the residuals. It may be noticed that since all the variables are given, (3.16) is a regression model for system parameters $\Theta := \begin{bmatrix} A & B \\ C & D \end{bmatrix} \in R^{(n+p)(n+m)}$. This class of approaches are called the direct N4SID methods. This estimate uniquely exists if the rank condition

$$rank \begin{bmatrix} \bar{x}(0), \bar{x}(1), \dots, \bar{x}(N-1) \\ u(0), u(1), \dots, u(N-1) \end{bmatrix} \tag{3.17}$$

is satisfied. Moreover, the covariance matrices of the residual are given by:

$$\begin{bmatrix} Q & S \\ S^T & T \end{bmatrix} = \frac{1}{N} \sum_{t=0}^{N-1} \begin{bmatrix} \eta(t) \\ v(t) \end{bmatrix} [\eta^T(t), v^T(t)] \tag{3.18}$$

Thus, by solving a certain algebraic Riccati equation, we can derive a steady state Kalman filter of the form:

$$\begin{bmatrix} \hat{x}(t+1) \\ y(t) \end{bmatrix} = \begin{bmatrix} A & B \\ C & D \end{bmatrix} \begin{bmatrix} \hat{x}(t) \\ u(t) \end{bmatrix} + \begin{bmatrix} K \\ I_P \end{bmatrix} \hat{e}(t) \tag{3.19}$$

where K is the steady state Kalman gain, $\hat{x}$ is the estimate of state vector and $\hat{e}$ is the estimate of innovation process.

Computation of state vectors

As already mentioned above, the LQ decomposition is a basic technique in subspace identification methods. Suppose that we have an input-output data from an LTI system. Let the block Hankel matrices be defined by:

$$Y_{0|k-1} = \begin{bmatrix} y(0) & y(1) & \cdots & y(N-1) \\ y(1) & y(2) & \cdots & y(N) \\ \vdots & \vdots & \ddots & \vdots \\ y(k-1) & y(k) & \cdots & y(k+N-2) \end{bmatrix} \in R^{kp \cdot N} \tag{3.20}$$

$$Y_{k\,|2k-1} = \begin{bmatrix} y(k) & y(k+1) & \cdots & y(k+N-1) \\ y(k+1) & y(k+2) & \cdots & y(k+N) \\ \vdots & \vdots & \ddots & \vdots \\ y(2k-1) & y(2k) & \cdots & y(2k+N-2) \end{bmatrix} \in R^{km\cdot N}$$

Where k > n and N is sufficiently large. Let p and f denote the past and the future, respectively. Then we define the past as $\mathrm{U_p} := \mathrm{U_{0\,|\,k-1}}$ and $\mathrm{Y_p} := \mathrm{Y_{0\,|\,k-1}}$. Similarly we define the future data as $U_f := U_{k\,|\,2k-1}$ and $Y_f := Y_{k\,|\,2k-1}$.

Let the LQ decomposition be given by:

$$\begin{bmatrix} U_f \\ W_p \\ Y_f \end{bmatrix} = \begin{bmatrix} R_{11} & 0 & 0 \\ R_{21} & R_{22} & 0 \\ R_{31} & R_{32} & R_{33} \end{bmatrix} \begin{bmatrix} Q_1^T \\ Q_2^T \\ Q_3^T \end{bmatrix}$$

where $\mathrm{R_{11}} \in \mathrm{R^{km\ km}}$, $\mathrm{R_{22}} \in \mathrm{R^{k(m+p)\cdot k(m+p)}}$, and $\mathrm{R_{33}} \in \mathrm{R^{kp\ kp}}$ are upper triangular and $Q_i, i = 1,2,3$ are orthogonal matrices. The oblique projection of the future Y_f onto the join past $\mathrm{W_p} := \begin{bmatrix} \mathrm{U_p} \\ \mathrm{Y_p} \end{bmatrix}$ along the future U_f is given by

$$\xi := \hat{E}_{||U_f}\{Y_f|W_p\} = R_{32}R_{22}^{*}W_p$$

where $(.)^*$ denotes the pseudo-inverse. ξ can be factored as a product of the extended observability matrix $\mathcal{O}_k$ and the future state vector $\mathrm{X_f} := [\mathrm{x(k)}, \ldots, \mathrm{x(k+N-1)}] \in \mathrm{R^{n\,N}}$:

$$\xi = O_k X_f = R_{32}R_{22}^{*}W_p$$

Suppose that the SVD of ξ be given by $\xi = \mathrm{U}\sum\mathrm{V^T}$ with $\mathrm{rank}(\sum) = \mathrm{n}$. Thus we can take the extended observability matrix as

$$O_k = U\,\Sigma^{\frac{1}{2}} \tag{3.21}$$

It follows that the state vector is given by $X_f = O_k^{*}\xi = \Sigma^{1/2}V^T$. Alternatively, by using a so-called shift invariant property of the extended observability matrix of (3.21), we can respectively compute matrices A and C as

$$A = O_{k-1}^{*}O_k(p+1:pk, 1:n), \quad C = O_k(1:p, 1:n)$$

The approaches used in the stochastic identification are the classical method or subspace method. In the classical method, a transfer function model is first identified, and then a state space model is obtained by using some realization technique. In the subspace methods, we first construct the state estimates from given input-output data by using a simple procedure based on tools of numerical linear algebra, and a state space model is obtained by solving a least-square problem. An important point of the study of subspace methods is to understand the key point of how the Kalman filter state vectors and the extended observability matrix are obtained by using tools of linear algebra.

3.2.2 Stochastic LTI system and state estimation

In section 2.5 we defined a stochastic Linear Time Invariant system of the form (2.38):

$$\begin{aligned} x(k+1) &= Ax(k) + w(k) \\ y(k) &= Cx(k) + v(k) \end{aligned} \tag{3.22}$$

and covariance matrices in equations (2.39) -(2.41):

$$E\left\{\begin{bmatrix} w(t) \\ v(t) \end{bmatrix} [w^T(s), v^T(s)]\right\} = \begin{bmatrix} Q(t) & S(t) \\ S^T(t) & R(t) \end{bmatrix} \delta(k-s)$$

where $Q(t) \in R^{n\,n}$ is nonnegative definite, and $R(t) \in R^{p\,p}$ is positive definite for all $t = 0, 1, \dots,$ and δ(k- s) = 1 when k = s, otherwise $\delta(k-s) = 0$. In this way, the Markov parameters can be represented by equation (2.52):

$$\Lambda_i = CA^{i-1}\mathrm{G}$$

Explicitly, output covariance matrices can be treated as Markov Parameters of a system having the matrices [A,G,C]. Given the output observations of a dynamic system, the stochastic identification can be considered as the realization of a set [A,C, Λ_i,G].

The problem to solve in the state estimation is to find the minimum variance estimate $\hat{x}(t+m|t)$ of the state vector $x(t+m)$ based on the observations up to time t. This is equivalent to designing a filter that produces $\hat{x}(t+m|t)$ minimizing the performance index:

$$J = E\{\, ||x(t+m) - \hat{x}(t+m|t)||^2 \,\}$$

where $\hat{x}(t+m|t)$ is Ft-measurable. The optimal estimate is expressed in terms of the conditional expectation of $x(t+m)$ given $\mathcal{F}_t$ as:

$$\hat{x}(t+m|t) = E\{x(t+m)|\mathcal{F}_t\}$$

Let the estimation error be defined by $\hat{x}(t+m|t) := x(t+m) - \hat{x}(t+m|t)$ and the error covariance matrix be:

$$P(t+m|t) := E\{[x(t+m) - \hat{x}(t+m|t)][x(t+m) - \hat{x}(t+m|t)]^T\}$$

For Gaussian process, the conditional expectation $\hat{x}(t+m|t)$ is a linear function of observations y(0), y(1), ..., y(t), so that the optimal estimate coincides with the linear minimum variance estimate of $x(t+m)$ given observations up to time t. More precisely, we define a linear space generated by the observations as:

$$\mathcal{Y}_t = \left\{ c + \sum_{i=0}^{t} A_i y(i) \mid c \in R^n;\ A_i \in R^{n \cdot p} \right\} \tag{3.23}$$

The space $\mathcal{Y}_t$ is called the data space at time t. The minimum variance estimate $\hat{x}(t+m|t)$ is given by the orthogonal projection of $x(t+m)$ onto $\mathcal{Y}_t$:

$$\hat{x}(t+m|t) = \hat{E}\{x(t+m)|\mathcal{Y}_t\}$$

Let us introduce now a Kalman filter gain matrix derived by the following equations:

$$\begin{gathered} \hat{x}(t+1) = A(t)\hat{x}(t) + K(t)[y(t) - C(t)\hat{x}(t)] \\ \hat{x}(t|t) = \hat{x}(t) + K_f(t)[y(t) - C(t)\hat{x}(t)] \end{gathered} \tag{3.24}$$

where the innovation process is $e(t) = y(t) - C(t)\hat{x}(t)$ and the Kalman gains are $K(t) = [A(t)P(t)C^T(t) + S(t)][C(t)P(t)C^T(t) + R(t)]^{-1}$ and $K_f = P(t)C^T[C(t)P(t)C^T(t) + R(t)]^{-1}$. The error covariance matrix is derived from:

$$\begin{gathered} P(t+1) = A(t)P(t)A^T(t) - K(t)[C(t)P(t)C^T(t) + R(t)]K^T(t) + Q(t) \\ P(t|t) = P(t) - P(t)C^T(t)[C(t)P(t)C^T(t) + R(t)]^{-1}C(t)P(t) \end{gathered}$$

We see that the Kalman filter is a dynamic system that recursively produces the estimates $\hat{x}(t+1)$ and $\hat{x}(t|t)$ by updating the old estimates based on the received output data *y(t)*. The Kalman filter is, therefore, an algorithm suitable for the on-line state estimation. It follows from the definition of the innovation process *e*, that the Kalman filter equation is also written as

$$\begin{aligned} \hat{x}(t+1) &= A(t)\,\hat{x}(t) + K(t)\,e(t) \\ y(t) &= C(t)\,\hat{x}(t) + e(t) \end{aligned} \tag{3.25}$$

The two models (3.22) and (3.25) are equivalent state space representations that simulate the same output process *y*. The innovation model is less redundant in the noise model, and is used in stochastic realization, or the state space system realization.

For a stochastic LTI system (3.22), it follows from (3.24) that the Kalman filter is expressed as:

$$\hat{x}(t+1) = A\,\hat{x}(t) + K(t)[y(t) - C\hat{x}(t)] \tag{3.26}$$

where $\hat{x}(t) \coloneqq \hat{x}(t|t-1)$. The Kalman filter is given by:

$$K(t) = [AP(t)C^T + S][CP(t)C^T + R)]^{-1}$$

The error covariance matrix (Riccati equation) becomes:

$$P(t+1) = AP(t)A^T - K(t)[CP(t)C^T + R]K^T(t) + Q$$

where $P(t) \coloneqq P(t|t-1)$. Suppose that a solution P(t) of the Riccati equation converges to a constant matrix as $t \to \infty$. Put $P(t) = P(t+1) = P$ in Riccati equation to get an algebraic Riccati equation (ARE).

$$P = APA^T - (APC^T + S)(CPC^T + R)^{-1}(APC^T + S)^T + Q$$

In this case K(t) converges to a stationary Kalman gain, $K = [APC^T + S][CPC^T + R)]^{-1}$. Hence, the filter equation (3.26) becomes

$$\hat{x}(t+1) = [A - KC]\hat{x}(t) + K\,y(t) \tag{3.27}$$

This Kalman filter model plays a crucial role in the implementation of system identification using only output information because the Kalman state vector $\hat{x}(k)$ at the *k-th* time step can be represented in terms of the initial state vector $\hat{x}(0)$ and the past output observations *y(t)* for $t < k$ as follows

$$\hat{x}(t) = (A - KC)^t\,\hat{x}(0) + \sum_{i=0}^{k-1} (A - KC)^i\,K\,y(t-i-1) \tag{3.28}$$

For convenience of representation, it is assumed that the estimate of the Kalman state vector $\hat{x}(t)$ at the *t-th* time step is influenced by the infinite number of its past output vectors (i.e. y(t) for $-\infty < t < k-1$). Under

this assumption, from Equation (3.28), the Kalman state vector $\hat{x}(t)$ can be represented in a matrix form as

$$\hat{x}(t) = \Psi_k y_k^- \tag{3.29}$$

where

$$\Psi_k = [K, (A-KC)K, (A-KC)^2K, \dots] \in R^{n(p\cdot\infty)}, \quad y_k^- = \begin{bmatrix} y(t-1) \\ y(t-2) \\ y(t-3) \\ \cdots \end{bmatrix} \in R^{m\cdot\infty}$$

The Kalman state vector $\hat{x}(t)$ at the *t-th* time step is the minimum variance estimate of the state vector *x(t)* at the *t-th* time step. Such minimum variance properties make it easy to represent the relationships between $\hat{x}(t)$ and $x(t)$ in vector spaces (see equation (3.23).

In fact, the output vector $y(t+k)$ at the $(t+k)-th$ time step for $k \geq 0$ can be represented by:

$$y(t+k) = CA^k x(t) + \sum_{s=1}^{k} CA^{s-1} w(t+k-s) + v(t+k)) \tag{3.30}$$

Thus, orthogonally projecting the vector $y(t+k)$ on the space $\mathfrak{Y}_t$ leads to:

$$y(t+k)/\mathfrak{Y}_t = CA^k \hat{x}(t)$$

The last equality comes from the fact that the current and future process and measurement noises are uncorrelated with the past output. This allows us to estimate the Kalman state vectors using only output observations.

3.2.3 Data matrices of stochastic systems

With regard to equation (3.25), the output vectors $y(t)$ for $t \geq k$, which can be predicted using $\hat{x}(t)$, can be represented as:

$$\begin{bmatrix} y(k) \\ y(k+1) \\ \vdots \\ y(2k-1) \end{bmatrix} = \begin{bmatrix} C \\ CA \\ \vdots \\ CA^{k-1} \end{bmatrix} \hat{x}(k) + \begin{bmatrix} I & & & \\ CK & \ddots & & \\ \vdots & \ddots & I & \\ CA^{k-2}K & \cdots & CK & I \end{bmatrix} \begin{bmatrix} e(k) \\ e(k+1) \\ \vdots \\ e(2k-1) \end{bmatrix}$$

where

$$y_k^+ = \begin{bmatrix} y(k) \\ y(k+1) \\ \vdots \\ y(2k-1) \end{bmatrix} \in R^{kp}, \quad e_k^+ = \begin{bmatrix} e(k) \\ e(k+1) \\ \vdots \\ e(2k-1) \end{bmatrix} \in R^{km}, \quad O_k = \begin{bmatrix} C \\ CA \\ \vdots \\ CA^{k-1} \end{bmatrix}$$

and the Toeplitz matrix:

$$\psi_k = \begin{bmatrix} I & & & \\ CK & \ddots & & \\ \vdots & \ddots & I & \\ CA^{k-2}K & \cdots & CK & I \end{bmatrix} \in R^{kp \cdot km}$$

So we have

$$y_k^+ = O_k \hat{x}(k) + \psi_k \, e_k^+ \tag{3.31}$$

Putting equation (3.29) into (3.31) we have:

$$y_k^+ = O_k \hat{x}(k) + \psi_k \, e_k^+ \tag{3.32}$$

In this equation, as the output residual vector $e_k^+(k)$ at the $k-th$ time step is uncorrelated with the past output vector $y(t)$ for $t < k$, the vector y_k^- of the past output vectors is totally independent of the vector e_k^+ of the future residual vectors;

Similarly for the determination of the Kalman state vector sequence, *future output data matrix* can be formulated in terms of the Kalman state vector sequence $\widehat{\mathrm{X}}_{0|\mathrm{k}-1}$, as well as the output residual vectors as follows:

$$Y_{k|2k-1}^+ = O_k \Psi_k Y_{0|k-1}^- \; + \psi_k \, e_{k|2k-1}^+ \tag{3.33}$$

with obvious meaning of the symbols from (3.31). Now the problem is solved when we have estimated the principal directions, Ψ_{k}, of $\mathrm{Y}_{\mathrm{k}|2\mathrm{k}-1}^-$ that maximize the covariance between the past and future outputs. Some well-known methods for determining the principal direction are the principal component analysis and canonical correlation analysis (see section 3.3.1).

We usually consider rectangular data matrices with a large number N of columns. Thus if we apply the LQ decomposition to rectangular matrices, then we get block lower triangular matrices with zero block at the upper-right corner. In the numerical implementation, the estimate of $\widehat{\mathrm{X}}_{0|\mathrm{k}-1}$ can be obtained through a LQ decomposition of the output data matrix, denoted by Y^{-+}, which can be decomposed into $\mathrm{Y}_{0|\mathrm{k}-1}^-$ and $\mathrm{Y}_{\mathrm{k}|2\mathrm{k}-1}^+$as follows:

$$Y^{-+} = \begin{bmatrix} Y_{0|k-1}^- \\ Y_{k|2k-1}^+ \end{bmatrix} = \begin{bmatrix} L_{11} & 0 \\ L_{21} & L_{22} \end{bmatrix} \begin{bmatrix} Q_1^T \\ Q_2^T \end{bmatrix} \tag{3.34}$$

where L is a lower triangular matrix and Q is the orthogonal matrix.

This allows us to represent $Y^{-}_{0|k-1}$ and $Y^{+}_{k|2k-1}$ as follows

$$Y^{-}_{0|k-1} = L_{11}\, Q_1^T, \quad Y^{+}_{k|2k-1} = L_{21}Q_1^T + L_{22}Q_2^T \tag{3.35}$$

So the matrices of Hankel (equation (3.50)) and Toeplitz (equation (3.51)) become:

$$H = L_{21}L_{11}^T$$

$$T_- = L_{11}L_{11}^T, \quad T_+ = L_{21}L_{21}^T + L_{22}L_{22}^T$$

3.2.4 Realization algorithm for the SSI

The covariance matrices T_- and T_+ can be decomposed in :

$$T_- = LL^T, \quad T_+ = MM^T$$

By computing the SVD of the normalized covariance matrix we obtain:

$$L^{-1}HM^{-T} = U\Sigma V^T \cong \tilde{U}\tilde{\Sigma}\tilde{V}^T$$

where $\tilde{\Sigma}$ is obtained by deleting sufficiently small singular values of Σ, so the dimension of the state vector becomes $\tilde{n} = \dim\tilde{\Sigma}$. The next step is to compute observability and controllability matrices by:

$$O_k = L\tilde{U}\tilde{\Sigma}^{1/2}, \quad \psi_k = \tilde{\Sigma}^{1/2}\tilde{V}^T M^T$$

Now it is possible to extract the estimate of A, C, $\bar{C}$ by:

$$A = O^*_{k-1}\bar{O}_k\,, \quad C = O_k\,(1:p,:), \quad \bar{C} = \psi_k(:,1:p)$$

where $\bar{O}_k = O_k(p+1:kp,:)$. Then the covariance matrix of y_s is given by $\Lambda_s(0) \coloneqq O_k\,(1:\mathrm{p}, 1:\mathrm{p})$. So the Kalman gain is given by:

$$K = (\bar{C}^T - A\bar{\Sigma}C^T)(\Lambda_s(0) - C\tilde{\Sigma}C^T)^{-1}$$

so that the innovation model becomes:

$$x_s(t+1) = Ax_s(t) + K(t)\,e(t)$$

$$y_s(t) = Cx_s(t) + e(t)$$

Another method for determining the state matrices is by computing first the state vectors from the principal direction matrices (equation (3.18)):

$$\bar{x}(i) = V^T T_-^{-T/2} y(i)\ .$$

If we define matrices with *N-1* columns:

$$\hat{X}_{k+1} = \bar{X}_k(:,2:N), \quad \hat{X}_k = \bar{X}_k(:,1:N-1), \quad \hat{Y}_{(k|k)} = Y_{(k|k)}(:,1:N-1)\,,$$

we can compute the matrices $A\,, C$ by applying a least square method:

$$\begin{bmatrix} \hat{X}_{k+1} \\ \hat{Y}_{(k|k)} \end{bmatrix} = \begin{bmatrix} A \\ C \end{bmatrix} \hat{X}_k + \begin{bmatrix} \rho_w \\ \rho_v \end{bmatrix}$$

where $\rho_w \; and \; \rho_v$ are residuals. Then, we compute the covariance of residuals:

$$\begin{bmatrix} Q & S \\ S^T & R \end{bmatrix} = \frac{1}{N-1} \begin{bmatrix} \rho_w \rho_w^T & \rho_w \rho_v^T \\ \rho_v \rho_w^T & \rho_v \rho_v^T \end{bmatrix}$$

Now it's easy to solve the Riccati equation:

$$P = APA^T - \; (APC^T + S)(CPC^T + R)^{-1}(APC^T + S)^T + Q$$

and we have the Kalman gain:

$$K(t) = [APC^T + S][CPC^T + R)]^{-1}$$

Finally the innovation model (3.25) can be computed.

3.3 SSI via CCA and Enhanced CCA

In the previous section we have seen that in the SSI technique, the state vector has been estimated from the Kalman filter with a sort of updating process. In fact, the state vector has been estimated from the combination of the past output vectors in different time steps. If we try to analyze the mutual dependence between two sets of output vectors we can estimate the state vector that is related to them. This concept belongs to the well-known techniques of multivariate analysis used for dimension reduction problems. Multivariate analysis deals with observations on more than one variable where there is some inherent independence between the variables. One of the principal classes of this kind is the Canonical Correlation Analysis (CCA).

In this section the introduction to the CCA technique [7] and its further development to the Enhanced CCA [13] will be presented.

After obtaining the weighting matrices from these techniques, one can use them to compute the procedures seen in the previous section (SSI).

3.3.1 Canonical Correlation Analysis

The CCA is a technique of multivariate statistical analysis that correlates two sets of variables by finding a new coordinate system in the space of each set. CCA combines dependent variables to find pairs of new variables which have the highest correlation. However, the canonical variables (CV), even when highly correlated, do not necessarily explain a large portion of the variance of the original tables. This makes the interpretation of the CV sometimes difficult, but CC is nonetheless an important theoretical tool because most multivariate techniques can be interpreted as a specific case of CC. [7] gives a clear description of the CCA.

Let x and y be two vectors (e.g. past and future output vector) defined by:

$$x = \begin{bmatrix} x_1 \\ x_2 \\ \vdots \\ x_k \end{bmatrix} \in \mathbb{R}^k, \qquad y = \begin{bmatrix} y_1 \\ y_2 \\ \vdots \\ y_l \end{bmatrix} \in \mathbb{R}^l \tag{3.36}$$

we define linear spaces defined by x and y: $\mathbb{X} = span\{x_1, \dots, x_k\}$, $\mathbb{Y} = span\{y_1, \dots, y_l\}$. First we find the vectors $w_1 \in \mathbb{X}$ and $z_1 \in \mathbb{Y}$ with the maximum mutual correlation, and define (w_1, z_1) as the first coordinates in the new system. Then we find $w_2 \in \mathbb{X}$ and $z_2 \in \mathbb{Y}$ such that their correlation is maximum under the assumption that they are uncorrelated with the first coordinates (w_1, z_1). This process is repeated until two new coordinate systems are determined.

Let the covariance matrices of two vectors x and y be given by:

$$\Sigma = \mathrm{E}\left\{ \begin{bmatrix} x \\ y \end{bmatrix} \quad [x^T \quad y^T] \right\} = \begin{bmatrix} \Sigma_{xx} & \Sigma_{xy} \\ \Sigma_{yx} & \Sigma_{yy} \end{bmatrix} \tag{3.37}$$

where it is assumed for simplicity that $\Sigma_{xx} > 0$ and $\Sigma_{yy} > 0$. We also assume that $k \leq l$. We define two scalars variables:

$$w_1 = a^T x = \sum_{i=1}^{k} \alpha_i x_i\,, \quad z = b^T y = \sum_{j=1}^{l} \beta_j y_j \tag{3.38}$$

by using two vectors $a \in \mathbb{R}^k$ and $b \in \mathbb{R}^l$, respectively. We shall find the vectors a and b that maximaze the correlation between w_1 and z_1, which is expressed as:

$$\rho = \frac{cov\{a^T x, b^T y\}}{\sqrt{cov\{a^T x\}}\sqrt{cov\{b^T y\}}} = \frac{a^T \Sigma_{xy} b}{\sqrt{(a^T \Sigma_{xx} a)(b^T \Sigma_{yy} b)}} \tag{3.39}$$

Note that if a pair (a, b) maximazes ρ, than the pair $(c_1 a, c_2 b)$ also maximizes ρ for non-zero scalars c_1, c_2. Thus, we impose the conditions $a^T \Sigma_{xx} a = 1$ and $b^T \Sigma_{yy} b = 1$. The problem of maximizing ρ under the aforementioned conditions, is solved by means of the Lagrange function :

$$\mathcal{L} = a^T \Sigma_{xy} b + \frac{1}{2}\lambda_1 (1 - a^T \Sigma_{xx} a) + \frac{1}{2}\lambda_2 (1 - b^T \Sigma_{yy} b) \tag{3.40}$$

Then, differentiating the Lagrange function and setting equal to zero:

$$\frac{\partial \mathcal{L}}{\partial a} = \Sigma_{xy} b - \lambda_1 \Sigma_{xx} a = 0, \quad \frac{\partial \mathcal{L}}{\partial b} = \Sigma_{yx} a - \lambda_2 \Sigma_{yy} b = 0 \tag{3.41}$$

Pre-multiplying the first equation of (3.41) by a^T and the second by b^T, letting $\lambda_1 = \lambda_2 = \rho$ and since $\Sigma_{yy} > 0$ it follows that:

$$(\Sigma_{xy} \Sigma_{yy}^{-1} \Sigma_{yx} - \rho^2 \Sigma_{xx}) a = 0, \quad a \neq 0 \tag{3.42}$$

Since the only condition that a has a non-trivial solution is that

$$\det(\Sigma_{xy} \Sigma_{yy}^{-1} \Sigma_{yx} - \rho^2 \Sigma_{xx}) = 0 \tag{3.43}$$

If $\Sigma_{xx} = \Sigma_{xx}^{-1/2} \Sigma_{xx}^{T/2}$ and $\Sigma_{yy} = \Sigma_{yy}^{-1/2} \Sigma_{yy}^{T/2}$, and if we define $\Theta = \Sigma_{xx}^{-1/2} \Sigma_{xy} \Sigma_{xx}^{T/2}$then:

$$\det(\Theta \Theta^T - \rho^2 I_k) = 0 \tag{3.44}$$

where ρ^2 is eigenvalue of $\Theta\Theta^T$. Let $a_1, a_2 \ldots, a_k$ be the corresponding eigenvectors obtained from (3.43). Then, we define the matrix $L = [a_1, a_2 \ldots, a_k] \in \mathbb{R}^{kxk}$. Repeating the operations from (3.43) to (3.44) in order to eliminate a, we can define the matrix $M = [b_1, b_2 \ldots, b_k] \in \mathbb{R}^{lxl}$. L and M are the square root inverses of the covariance matrices Σ_{xx} and Σ_{yy}, respectively.

Let $w = L^{Tx}$ and $z = M^T y$. Then $E(ww^T) = I_k$ and $E(zz^T) = I_l$ and $E(wz^T) = diag(\rho_1, \rho_2, \ldots, \rho_k) = D$. The elements of canonical vectors w and

z are white noises with zero mean and unit variance, and they are arranged in descending order of mutual correlations. Thus, both whitening and correlating two vectors can perform by the CCA.

If we suppose that the covariance matrices of x and y are given by (3.37), then the canonical correlations are computed by the SVD:

$$\Theta = \Sigma_{xx}^{-1/2}\Sigma_{xy}\Sigma_{yy}^{-T/2} = UDV^T \tag{3.45}$$

Also, the canonical vectors are given by:

$$w = \mathrm{L}^{\mathrm{T}}x = U^T\Sigma_{xx}^{-1/2}x, \quad z = M^Ty = V^T\Sigma_{yy}^{-1/2}y \tag{3.46}$$

Once the state vectors have been estimated with the CCA, we can construct the realization problem similarly as in section 3.2. If we suppose that the mean of the output vector y is zero, then the covariance matrix is given by:

$$\Lambda(l) = E\{y(t+l)y^T(t)\}, \quad l = 0, \pm 1, \dots \tag{3.47}$$

Given the covariance matrices of a stationary process y, the stochastic realization problem is to find a Markov model of the form of equation (2.38), where the covariance matrices of the white noises w and v are:

$$\Sigma = \mathrm{E}\left\{\begin{bmatrix} w(t) \\ v(t) \end{bmatrix} \begin{bmatrix} w^T(s) & v^T(s) \end{bmatrix}\right\} = \begin{bmatrix} \mathrm{Q} & \mathrm{S} \\ \mathrm{S}^{\mathrm{t}} & \mathrm{R} \end{bmatrix}\delta_{ts} \tag{3.48}$$

Let t be the present time. We can define the future and past vectors:

$$f(t) = \begin{bmatrix} y(t) \\ y(t+1) \\ \vdots \end{bmatrix}, \qquad p(t) = \begin{bmatrix} y(t-1) \\ y(t-2) \\ \vdots \end{bmatrix} \tag{3.49}$$

Then, the cross-covariance matrix of the future and past is given by:

$$H = E[f(t)p^T(t)] = \begin{bmatrix} \Lambda(1) & \Lambda(2) & \Lambda(3) & \cdots \\ \Lambda(2) & \Lambda(3) & \Lambda(4) & \cdots \\ \Lambda(3) & \Lambda(4) & \Lambda(5) & \cdots \\ \vdots & \vdots & \vdots & \ddots \end{bmatrix} \tag{3.50}$$

And the covariance matrices of the future and past are respectively given by:

$$T_+ = E[f(t)f^T(t)] = \begin{bmatrix} \Lambda(0) & \Lambda^T(1) & \Lambda^T(2) & \cdots \\ \Lambda(1) & \Lambda(0) & \Lambda^T(1) & \cdots \\ \Lambda(2) & \Lambda(1) & \Lambda(0) & \cdots \\ \vdots & \vdots & \vdots & \ddots \end{bmatrix} \tag{3.51}$$

and

$$T_- = E[p(t)p^T(t)] = \begin{bmatrix} \Lambda(0) & \Lambda(1) & \Lambda(2) & \cdots \\ \Lambda^T(1) & \Lambda(0) & \Lambda(1) & \cdots \\ \Lambda^T(2) & \Lambda^T(1) & \Lambda(0) & \cdots \\ \vdots & \vdots & \vdots & \ddots \end{bmatrix} \tag{3.52}$$

H is a block Hankel Matrix and $T(\pm)$ are block Toeplitz matrices. Hence, from (3.45) and (3.46), and noting that $\Sigma_{xx}^{-1/2}\Sigma_{xy}\Sigma_{yy}^{-T/2} = T_+^{-1/2}HT_-^{-T/2}$, the estimate of the state vector can be represented as:

$$\bar{x}(i) = V^T T_-^{-T/2} y(i) \tag{3.53}$$

Afterwards, these vectors are used to calculate the Kalman state estimates.

3.3.2 Enhanced CCA

Thus, Hong [13] in 2010 has developed an Enhanced CCA technique in order to deal with non-white noise in the measurements. In the ECCA, individual future output vectors are separately normalized, so the Hankel matrices $\bar{T}_+ \; and \; T_-$ are

$$\bar{T}_+ = \begin{bmatrix} \Lambda(0) & & & \\ & \Lambda(0) & & \\ & & \Lambda(0) & \\ & & & \ddots \end{bmatrix} \tag{3.54}$$

The estimation of the state vector can be determined by defining the singular value decomposition as:

$$\bar{T}_+^{-1/2} H T_-^{-T/2} = UDV^T \tag{3.55}$$

and the estimate of the state vector is determined similarly as in equation (3.53).

Then, these vectors are used to calculate the Kalman state estimates. Once a sufficient number of Kalman state estimates are obtained, a least-squares problem may be set to determine the system matrices:

$$\begin{matrix}\widehat{\mathrm{X}}_{\{i+1|i+j\}} \\ \mathrm{Y}_{\{i|i+j-1\}}\end{matrix} = \begin{bmatrix}\mathrm{A} \\ \mathrm{C}\end{bmatrix} \widehat{\mathrm{X}}_{\{i|i+j-1\}} + \widehat{\mathrm{E}}$$

In this expression, A and C are the unknown system matrices that will be solved using this equation, $\widehat{\mathrm{E}}$ is the residual of the least squares solution which is associated with the process and measurement noises, and the remaining matrices are defined:

$$\widehat{\mathrm{X}}_{\{i|i+j-1\}} = [\hat{\mathrm{x}}(i) \;\; \hat{\mathrm{x}}(i+1) \;\; \cdots \;\; \hat{\mathrm{x}}(i+j-1)]$$
$$\widehat{\mathrm{X}}_{\{i+1|i+j\}} = [\hat{\mathrm{x}}(i+1) \;\; \hat{\mathrm{x}}(i+2) \;\; \cdots \;\; \hat{\mathrm{x}}(i+j)]$$
$$\mathrm{Y}_{\{i|i+j-1\}} = [\mathrm{y}(i) \;\; \mathrm{y}(i+1) \;\; \cdots \;\; \mathrm{y}(i+j-1)]$$

Now it is possible to determine the frequencies, modal damping ratios and mode shapes of the structure using order system matrices.

3.4 Automatic OMA implemented for SHM

Variations in the behavior of the system can be associated with the decay of mechanical properties [26]. The principal idea of structural health monitoring systems is that changes in their modal parameters are related to structural change and damage, so they can be used to understand the changings happening to the structure, since they are correlated to stiffness, damping and mass properties of a certain structure.

In particular, natural frequencies are able to provide valuable knowledge about the structural condition. The monitoring of modal parameters by repeated system identification has become nowadays an effective way to get accurate information by vibration Structural Health Monitoring (SHM). Hence, the comfort of using OMA as a means of SHM, is due to the fact that automated system identification algorithms can be implemented in order to get automatic and accurate modal parameter identification.

In this study three different kinds of automated procedures in the frequency and time domain have been implemented and developed using the modal techniques presented previously in the Chapter, i.e. the FDD, SSI and the ECCA. These techniques are shown in the following paragraphs.

3.4.1 Automated FDD

The FDD technique was previously described in this chapter. Its application in the SHM problem is straightforward when the pick peaking technique is used in an automated procedure as in [27] [28]. In order to improve the accuracy, it is suggested to use other comparison parameters, besides the peak searching. A largely used parameter is the Modal Assurance Criterion (MAC) that distinguishes clearly two similar modes.

Relying on the literature, for the case of frequency domain, the method presented here was further developed in order to avoid the need of a reference previous estimation of the modal parameters of a structure. The procedure can be described with the following steps:

- → The first step is based on the comparison of a large number of datasets (say 30-50 recorded signals). MAC calculation is performed between the first singular vectors (SV) corresponding to the first singular values of the first dataset and all the other SV of the other datasets. Then this operation is repeated for each dataset (i.e. MAC calculation between the selected recording and all the others). This operation is completed frequency line by frequency line, obtaining a Frequency vs. MAC function for every comparison. After performing n sequence evaluations, a final average Frequency vs. MAC function is plotted.
- → Hence, at a certain frequency line the corresponding MAC value is accepted for further analysis if it is greater than a certain value (0.8 in all case studies analyzed in this thesis). Moreover, MAC values accepted must appear sequentially for at least 10 times, otherwise they cannot define the so called 'modal domain'. By repeating this procedure for the whole investigated frequency range, all the modal domains are identified. (Figure 3.1)
- → After defining the possible range of interest, every dataset is analyzed locally aiming to find the structural modes within the modal domain. Consequently, identification of maximum peaks are performed in the frequency lines corresponding to the previously defined range.
- → The computation of another MAC calculation between singular vectors of the peak and a predefined range of frequency lines around the peak is carried out.
- → If the number of points is greater than a user-defined value and if such points are distributed in both sides of the peak, than it is considered as a structural mode and is stored in another array.
- → If the algorithm finds more structural modes than the predefined, a second control is performed by comparing their mode shapes with a

reference set (Only one or two modes out of ten automatically identified required this control for the applications presented here).

→ If no peak in the modal domain complies the controls, it is assumed to be a noise peak and the corresponding frequency lines are removed from the search domain.

→ The procedure is repeated for all the modal domain ranges, until the predefined number of modes has been identified.

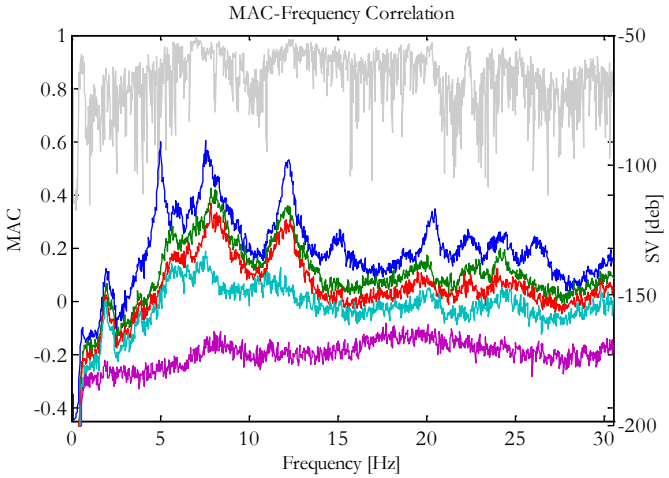

Figure 3.1 Example of MAC – Frequency plot on the People's New Bridge.

The procedure has been applied to two cases in Chapter 4 for the dynamic monitoring of two bridges, showing a good performance. As a matter of fact, all the automatic identification results were compared with the repeated manual identification through a commercial software, which showed high correlation.

3.4.2 Automated SSI

Time domain Automated Identification procedures using parametric methods have been recently developed [29]. The principal result of a Stochastic Subspace method is the identification of modal parameters via the stabilization diagram. Actually, for the developed automated technique, this is the crucial element of the procedure. The automated technique uses the well-known data-driven SSI which needs a model order number to be defined by the user.

The procedure relies on the previous estimate of the modal parameters of an averaged reference identification. For this 'reference' identification, a list of the natural frequencies mode shapes and a range defining the modal domain is considered. The only user-defined parameters needed to

implement the automatic procedure are the minimum model's order n and the MAC rejection level. The repeated SSI technique over all the monitoring records with definite values of n and MAC marks the automated process. After each modal analysis a stabilization diagram, which provides the selection of structural modes is computed. For the selection of these modes a procedure has been implemented that, among all the modes identified as stable, extracts structural ones through a triple control: frequency range, the model's order and MAC level.

The algorithm selects only those modes contained within a neighborhood of estimated frequency, defined by the range previously set and subsequently further restricts the research area properly going to exclude any mode corresponding to a model order, lower and greater than a certain value. Among all modes estimated until this step, the program proceeds to extract the one whose MAC is higher than a control value. Eventually, the modal parameters and the date of acquisition are saved in a matrix which is used to plot the standard date vs. time diagram.

This technique has been tested with all the applications and has been used for the two cases of SHM systems in Chapter 4.

3.4.3 Automated Clustering via ECCA

In order to develop this automated technique the initial ideas have been taken not only from the previous method, but they are also based on modal analysis in the time domain, using the advanced SSI technique called ECCA. Essentially, the main element which detects the stable modes in this case is the damping vs. frequency plot.

Parametric analyses

The consistency of the results is an important issue in the ambient vibration identification problems. Unfortunately, the real model's order which better fit the recorded data is unknown. Some of the parameters which can influence the identification results are the number, i, of the block rows of the output data matrix and the model's order, n. So, by combining these parameters in infinite ways, we can get different results, but as we know, only the stable modes can be considered as structural modes [30].

The presented approach for automatic estimation of modal parameters is composed by the following steps: (a) run analysis with different values, i,

and the model's order, n; (b) apply rules in order to clean the noise modes; (c) apply a cluster analysis; (d) plot frequency vs. damping results of stable modes; (d) determine mean values of structural modes and their 95% confidence intervals.

Modes are identified from each analysis conducted by using a different pair of (i, n). Among the identified modes from all the possible pairs (i, n), modes that can be considered as noise ones are eliminated first, then, the remaining modes are grouped with respect to their frequencies and mode shape vectors. Noise modes can be detected by considering the fact that:

- the estimation of structural modes is not affected by the specific selection of i and n;
- mode shapes corresponding to structural modes are likely to be similar in different analysis;
- and probably large damping values belong to noise frequencies.

A single mode should be identified within a single cluster at least 30 times using different combinations of n and i.

Cleaning procedure

In order to lead to a more evident mode selection, before applying the clustering rules, a cleaning procedure has been developed. First of all, after extracting all the poles from all analyses, modes whose damping ratio is negative or larger than 15% are eliminated. In SSI techniques spurious modes are eliminated by means of stabilization diagrams, where stable modes for different model's order are emphasized. Stability property of the poles is an indicator of structural modes assuming that noise poles do not appear with varying order of the model. In our case, similar noise eliminating rules used in a stabilization diagram are applied; however, these include not only variations of model's order, but also the number of block rows. Considering only modes remaining from the previous step, the identified modes are compared: modes are grouped on the basis of analogous frequency, damping and mode shape values, and after that, modes having frequencies that differ from each other by more than 1% are eliminated. In particular, the procedure begins from the definition of similarity rules applied on every loop of different n and i. The algorithm distinguishes only stable modes which are stored in the following matrix:

$$\begin{bmatrix} f_1 & \xi_1 & \cdots & \Phi_1 \\ f_2 & \xi_2 & \cdots & \Phi_2 \\ \vdots & \vdots & \vdots & \vdots \\ f_l & \xi_l & \cdots & \Phi_l \end{bmatrix}$$

where f_l, ξ_l and Φ_l are the frequency, damping and mode shape vector of the $l-th$ identified mode. Among all the poles identified with the previous analyses, only M of them are considered to be physical modes. The matrix containing stable modes has been constructed by choosing poles extracted from all the analyses with the following rules:

$$stable\ mode\ if \begin{cases} \Delta f_{n,n-1} \leq \Delta f_{lim} \\ \Delta \xi_{n,n-1} \leq \Delta \xi_{lim} \\ MAC_{n,n-1} \leq MAC_{lim} \end{cases}$$

$$\Delta f_{n,n-1} = \frac{|\Delta f_n - \Delta f_{n-1}|}{\Delta f_{n-1}} \quad \Delta \xi_{n,n-1} = \frac{|\Delta \xi_n - \Delta \xi_{n-1}|}{\Delta \xi_{n-1}} \quad MAC_{n,n-1} = MAC(\Phi_n, \Phi_{n-1})$$

where Δf_{lim}, $\Delta \xi_{lim}$ and MAC_{lim} are small tolerances defined according to the application, while $\mathrm{MAC_{n,n-1}}$ is the modal assurance criterion between Φ_n and $\Phi_{\mathrm{n-1}}$. The *n-th* mode is said to be stable when it is similar, in terms of frequency, damping ratio and mode shape to a minimum number of other modes.

Clustering procedure

To remove further noise modes, at this point, mode shapes, that show irregular behavior in relation to the group, are eliminated by operating with the following cluster analysis containing only those poles that correspond to the same mode. The aim of cluster analysis is to group all modes, cleared from the previous step, into separate sets belonging to the same structural mode. At the end, each cluster will contain only the stable frequency, damping and mode shape of the particular mode. The separation procedure is obtained by the use of a mutual distance between all clusters as follows:

$$d(j,l) = \left|f_j - f_l\right| + 1 - MAC(\Phi_j, \Phi_l)$$

where f_j and f_l are frequencies of modes j and l and Φ_j, Φ_l the corresponding mode shapes.

At the first step, a random mode is compared with all the data containing the stable modes, and the $n * i$ distances are computed for this comparison. The first cluster is created from the candidates that fulfill the limit

$d(j,l) \leq d_{\lim}$, where $d_{\lim}$ is a user-defined maximum allowed value that depends on the mean and standard deviation of the previous step. The first cluster is removed from the matrix and, the procedure is repeated for the second cluster and so on, until all different modes are grouped. At this point, two clusters that are close together are collected in a single cluster, and the mutual distance between all clusters is recomputed. As a last step, the average of the elements of all clusters is calculated and the clusters that contain less than the average value are eliminated. The procedure stops at the stage in which a certain number of clusters will be created. Each cluster can be plotted in terms of histograms, containing the number of elements of each data-set and in terms of frequency vs. damping. Clusters containing a minimum number (defined by the mean and standard deviation values) are selected for the candidate modes, otherwise they are rejected.

Confidence intervals

The merged cluster available can now be described by means of statistical parameters. Each modal parameter is characterized by a mean value $(\hat{f}, \hat{\xi})$, standard deviation σ and its 95% confidence intervals can be calculated as:

$$f_i = \left[\hat{f} - \frac{\left(1-\frac{0.5}{2}\right)\sigma_f}{\sqrt{N}} \ , \quad \hat{f} + \frac{\left(1-\frac{0.5}{2}\right)\sigma_f}{\sqrt{N}}\right]$$

$$\xi_i = \left[\hat{\xi} - \frac{\left(1-\frac{0.5}{2}\right)\sigma_\xi}{\sqrt{N}} \ , \quad \hat{\xi} + \frac{\left(1-\frac{0.5}{2}\right)\sigma_\xi}{\sqrt{N}}\right]$$

where N is the number of elements in a cluster, σ_f and σ_ξ are standard deviations of frequency and damping.

Automatically repeated procedure

The clustering algorithm is finally repeated in a third loop for all the data records from the monitoring period. For each cycle, the damping vs. frequency plot is formulated and accurate modal parameters are estimated. These parameters, together with the mode shapes, are stored in a matrix formed by as many lines as the data records. Finally, the accurate results are presented on frequency/damping vs. time diagrams.

This procedure neither relies on the prior estimate reference identification nor implies user tuned parameters for different applications. The parameters to be defined are: model's order range, blocks number range, distance limit between clusters, frequency limit, damping limit and MAC limit value. Once these parameters have been decided and calibrated, it

has been proved to work properly for different kinds of structures without any change.

This technique has been successfully applied to many case studies presented in Chapter 4, and compared with the other automatic techniques developed.

4

APPLICATIONS: SYSTEM ID. ON BRIDGES

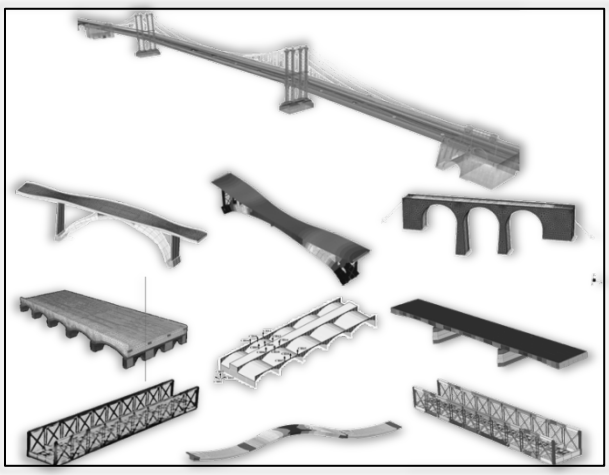

This chapter describes the structural identification through vibrational tests and monitoring on ten bridge structures. It deals with the modal analysis through different stochastic system identification for different kinds of structures such as suspension bridges, slender concrete arch bridges, masonry arch bridges, concrete beam bridges, railway steel bridges and highway steel box bridges. Advanced Cluster analysis, automatic algorithms for modal parameter identification and Regressive models will be applied for accurate data processing. Then, a summary of the results carried out is reported in order to differentiate the behavior of the group of structures.

4.1 Introduction

In the context of a large project developed between the University of Padua and the Regional Road Authority of Veneto, in the North-East of Italy, a great number of bridges were subject to structural investigation in order to examine their safety evaluation. The project initiated with the visual inspection and cataloguing of a total of 500 bridges (150 of which evaluated and analyzed by the author) of various structural kinds from masonry to reinforced and steel bridges. The additional step was to extend the investigation up to 80 bridges by using destructive and non-destructive tests in order to increase the material characterization of all kinds of structures available in the database. After that, a simplified procedure to evaluate the structural behavior of the entire fixed network has been developed by the team of University of Padua. During this step, parameterization of the safety levels and indexing of the structures not satisfying the National Code levels was carried out. This phase also stimulated the individuality of the first bridges to execute deeper structural identification and to simulate the response through numerical models. In particular, most of the structures presented in this work are crucial infrastructures, part of the database previously analyzed.

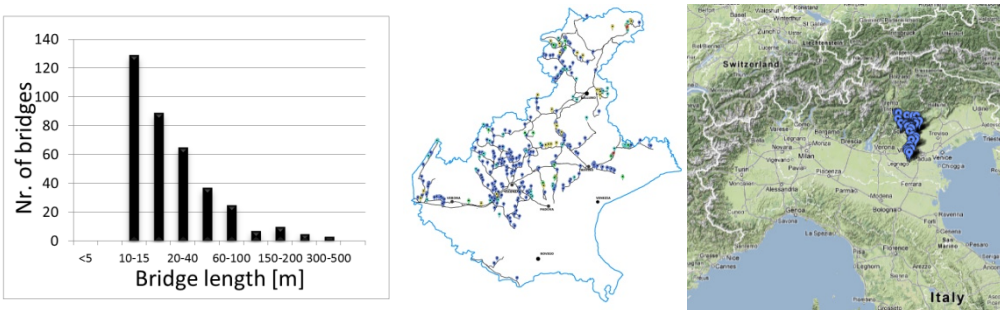

Figure 4.1 Example of a portion of the analyzed network of bridges

Dynamic identification techniques give a fundamental contribution in the calibration and updating of numerical results, because even the most refined FE model can hardly catch the real mechanical behavior of such structures, due to uncertainties in the material properties, the structural arrangement and the construction technology. The procedure that has been used during this study can be listed as follows:

→ Investigation, damage survey and material characterization of the structure.

→ Vibrational tests for dynamic characterization.

→ Numerical Modeling and calibration (trial-error methods).

→ Structural verification.

→ Installation of monitoring systems on critical bridges to control the behavior of the structure.

→ On-line automatic system identification of the bridge modal parameters

In the following paragraphs the application of the theoretical methods described in previous chapters will be presented. The first aim of this study is to present the behavior of different kinds of infrastructures under dynamic identification tests, emphasizing the particular response problems of suspension bridges, concrete arch bridges, masonry arch bridges, concrete beam bridges, reticular steel bridges and steel box bridges. In addition, the structural identification will be applied in cases of demolition process, validation of a seismic retrofit intervention, damage assessment and long term monitoring. The second aim is to compare the performance of the well-known Modal Analysis techniques SSI and FDD with the newly developed ECCA technique. It will be clearly seen how the new technique extracts additional modal information from the structures, especially when accompanied by advanced cluster analysis. Advanced Cluster analysis, automatic algorithms for modal parameter identification and Regressive models will be applied for accurate data processing. Finally, summary remarks will conclude the overall framework of the applications.

4.2 Concrete Arch bridges

4.2.1 St. Giustina Bridge

4.2.1.1 Description of the structure and measurement campaigns

The bridge of St. Giustina is a 68,0m single arch span, two-lane reinforced concrete valley overpass. It is located in the Region of Trento (Italy) in front of the St. Giustina Dam. The main characteristics and general layout are shown in Figure 4.3.

The bridge is supported by two tapered arches (open spandrel arcs) linked together by several r.c. beams. The height of the arch's section is 2,50m at the basis and 1,80m at the crown. Along the length of the arch there are 16 vertical concrete columns that connect the arches with the slab forming a rigid frame. All the columns are connected together with cross struts; the outer and higher columns are also transversally braced by X-shaped steel struts. The deck of the bridge is 9,00m wide for two traffic lanes and two

pedestrian walkways and consists of a cast in place r.c. slab supported by 6 longitudinal girders and 17 transversal beams. The bridge is fixed to the foundations at the basis of the arches and left free to move on the abutments.

Foundations at the beginning have been modeled as fixed in the Finite Element Model but as shown below, some sensitivity analysis has been developed changing the rotational stiffness of the foundations. The St. Giustina Bridge contains inside the concrete structure, the frame of the old steel bridge of St. Giustina erected in 1888 (Figure 4.3) The old steel bridge was incorporated inside the new bridge in a reinforcement intervention in 1960. From the different models developed, it has been demonstrated that, the presence of the steel structure inside the concrete has no influence in the dynamic analysis, due to huge geometrical difference of their cross sections.

Before the bridge was subjected to ambient vibration testing, several other destructive and non-destructive tests such as pullout, ultrasonic pulse wave, rebound hammer, traction tests on steel bars and core sampling (compression tests on concrete) techniques were executed in order to characterize the mechanical features of materials on-site and in the laboratory.

The acquisition campaigns were carried out in January 2010. During the three-day tests, generally low temperatures were detected and for this reason increasing values in the natural frequencies were expected because of the formation of ice inside the concrete and inside the road pavement. In order to obtain a good spatial resolution, the survey resulted in eight different setups (Figure 4.2, similar to [31]). Piezoelectric accelerometers with vertical axes were used to measure the bridge's response. Three accelerometers were placed as a reference in the middle of the bridges and eight others were simultaneously moved to cover the entire area of the bridge.

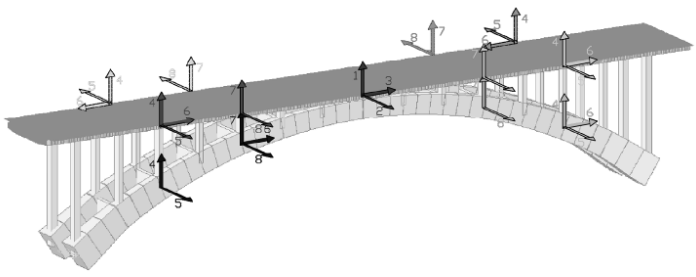

Figure 4.2 Sensor locations and directions for the St. Guistina bridge tests.

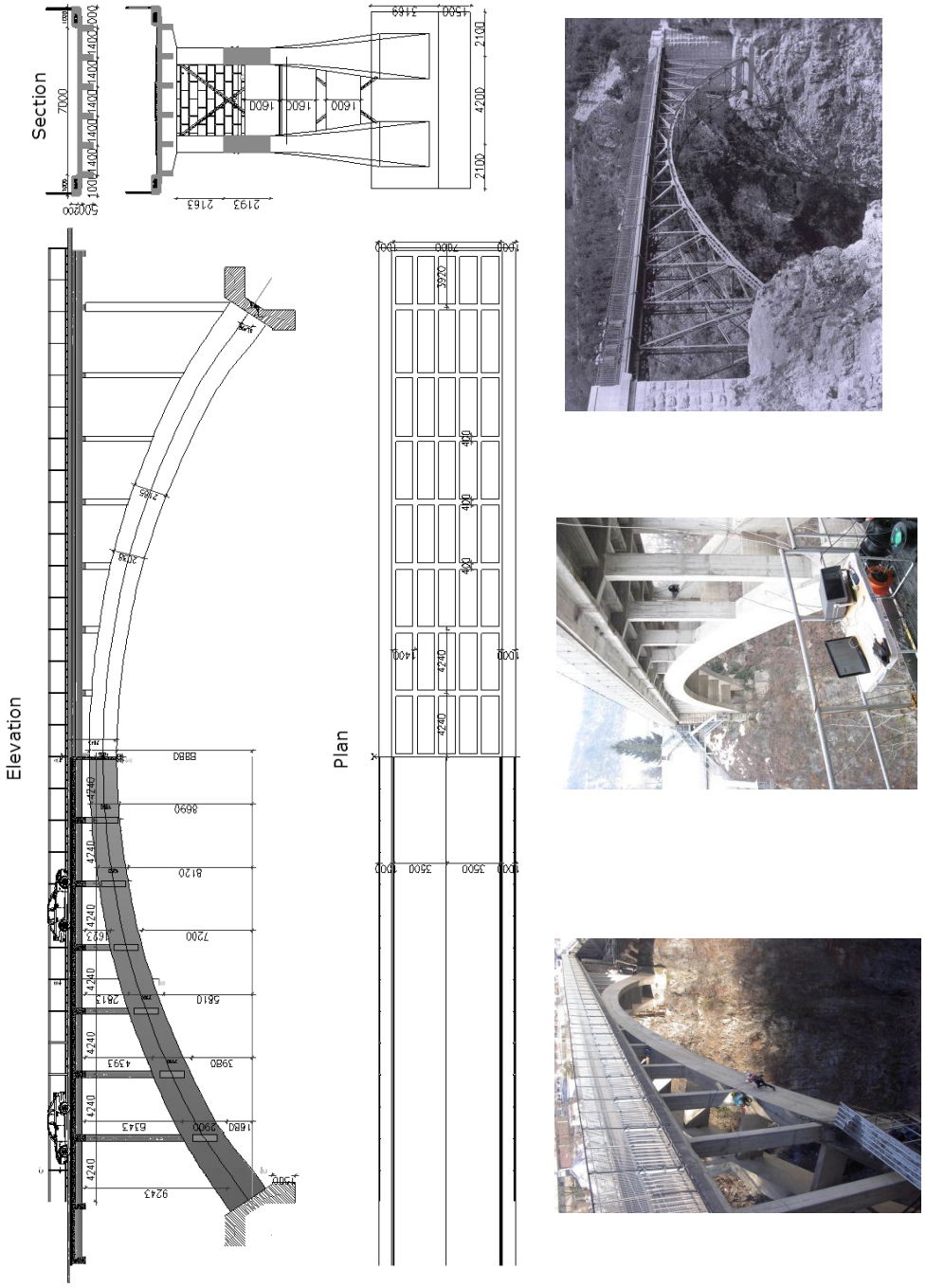

Figure 4.3 St. Giustina bridge: plan, elevation, cross-sections and photos.

The correct positioning of the accelerometers, placed along the concrete arch, was made possible thanks to the intervention of two climbers (Figure 4.3). The ambient accelerations time series were recorded for nearly 11 minutes with sampling frequency of 100 Hz (interval of 0,01s). For the spectral analysis a number of 2048 frequency lines was considered sufficient for the correct definition of the signal and overlapping windows of 66.67%.

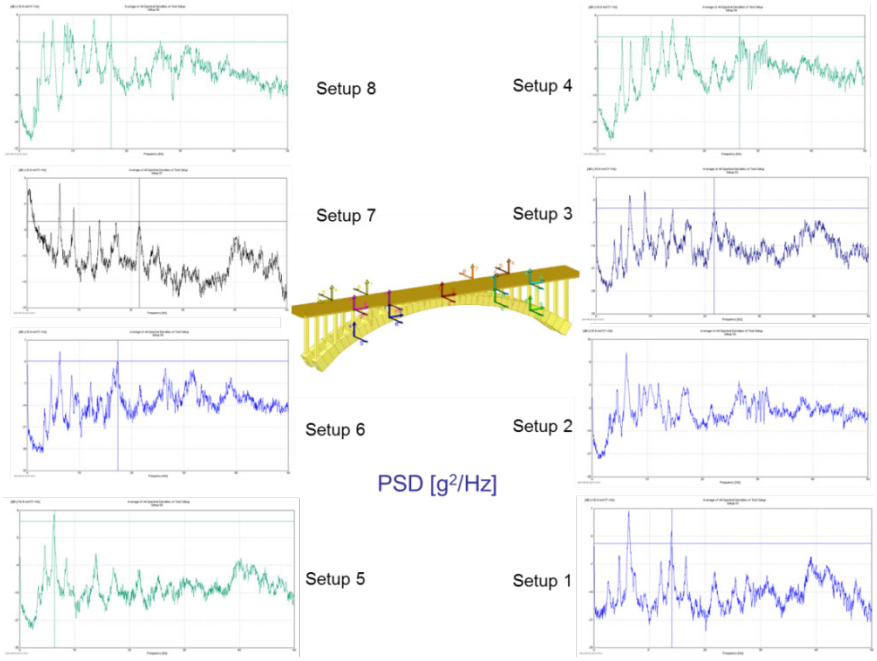

Figure 4.4 Average PSD for each setup configuration resulted from the tests.

4.2.1.2 Identification of the modal parameters

The extraction of modal parameters from ambient vibration data was carried out by using the Frequency Domain Decomposition (FDD) developed by Brincker et al. [6]. As expected, the principal natural frequencies were identified between 0 and 15 Hz. In Figure 4.5 the singular values and the modes identification are shown. There can be clearly distinguished structural modes in frequencies 3.36, 4.56, 6.20, 8.47, 8.96, 9.52, 10.91, 12.04, 13.94, 16.50 and 17.21 Hz. Figure 4.6 shows that the first mode is a transversal mode, the second mode is a vertical mode and the third one is a torsional mode.

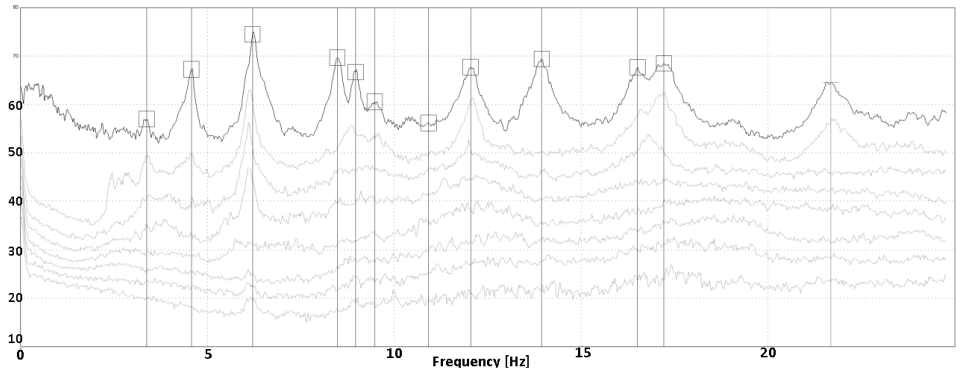

Figure 4.5 Singular values and identification of natural frequencies (FDD).

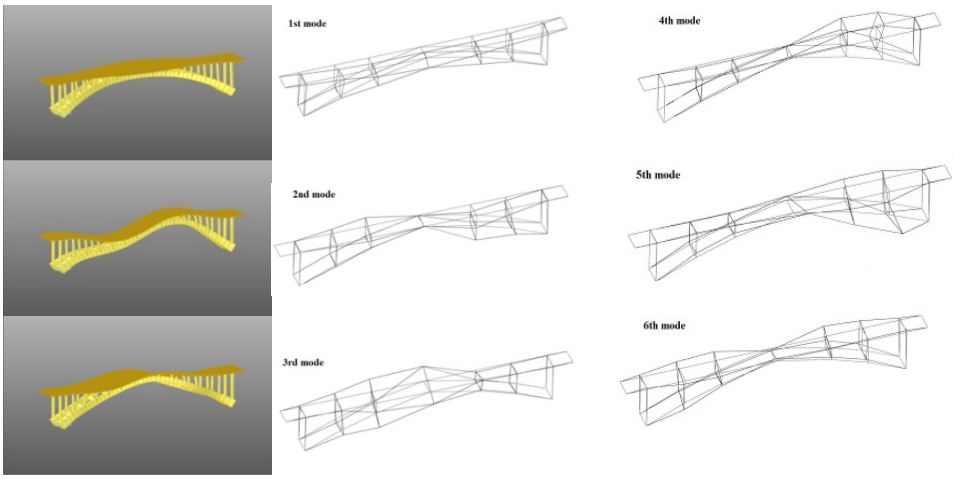

Figure 4.6 FEM and Experimental mode shapes of St. Giustina Bridge.

4.2.1.3 Comparison between experimental and FE models

Two different F.E models with two different software (Straus7 [32], and Midas [33]) have been created. All the materials, used in the model, were determined by laboratory tests of ten core samples taken from the S.Giustina Bridge. Arches, columns, and girders have been modeled with beam elements, while the deck slab is modeled with 4-node shell elements. From the comparison between experimental and analytical models almost all structural modes correspond with each other. The correlation of modal parameters can be analyzed both in terms of identified and calculated natural frequencies (Table 4.1) and by corresponding mode shapes using correlation coefficients or MAC (modal analysis criteria) values [25].

Table 4.1 Correlation between numerical and experim. modal behavior.

Mode	FDD f (Hz)	Model 1 (Straus7)			Model 2 (Midas/Gen)	
		f(Hz)	Δ (%)	MAC	f(Hz)	Δ (%)
1	3.369	3.402	1.039	0.967	3.312	-1.692
2	4.565	4.952	8.478	0.843	5.057	10.778
3	6.201	5.636	-9.111	0.645	6.068	-2.145
4	8.472	8.332	-1.653	-	8.852	4.485
5	8.96	9.187	2.533	-	-	-
6	10.91	10.520	-3.575	-	10.324	-5.371
7	12.04	12.540	4.153	0.610	-	-
8	13.94	13.630	-2.224	-	-	-
9	16.5	14.800	-10.303	0.287	-	-
10	17.21	17.050	-0.930	0.347	17.931	4.189
11	21.68	20.550	-5.212	0.521	-	-

From the obtained results (modal model and updated FE model), it can be observed that the theoretical model describes accurately the mode shapes extracted from the FDD with an average error of 4.6%. Furthermore the OMA allowed to identify three eigen-modes not predicted from the FE model. This can be traced back to one of the most important parameters that has influenced the results, i.e. the temperature. In fact, during the acquisition campaigns the temperature oscillated between -2°C and -7°C.

4.2.1.4 Sensitivity analyses

A sensitivity study (Figure 4.7) was performed on the St. Giustina Model Bridge, varying the stiffness of the elastic springs simulating the boundary conditions at arch bases and the Young's modulus of elasticity of reinforced concrete elements.

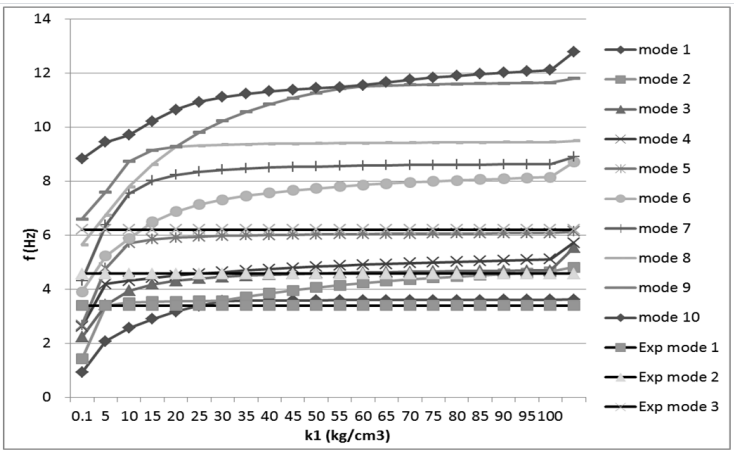

Figure 4.7 Sensitivity analysis: spring stiffness at the foundation of the arch.

The parametric results show, with adequate approximation, that the dynamic characteristics vs. the soil elasticity do not change after a certain value, so it is correct to model the constrains as fixed.

Another parametric study has been conducted on the elastic modulus of the concrete present on the structure.

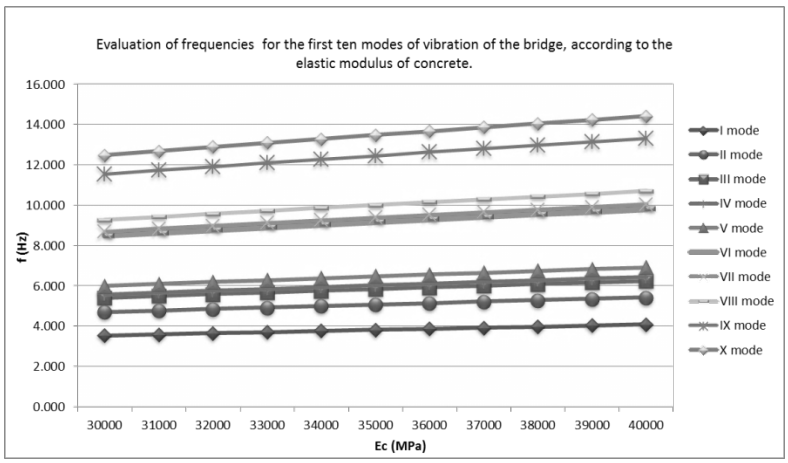

Figure 4.8 Sensitivity analysis on the elastic modulus.

As we know, temperatures lower than 0°C influence in a considerable way on the dynamic behavior as they determine a more rigid structure. This is due to the passage of water, present in the cortical layers of concrete, from liquid to solid state thus causing a consequent volume increase and eventually an increase in stiffness (connected to E) and frequency values. The same thing may have happened on the St. Giustina under low temperatures causing difficult transversal and longitudinal movement of the deck and pavement determined by the elastic modulus change (Figure 4.8).

4.2.2 Rovere Bridge

4.2.2.1 Dynamic tests on Gerber type arch structure

The Roverè bridge is a 76,0m single arched span, two-lane reinforced concrete valley overpass. It is located in the north of the city of Verona (Italy) and was constructed in the sixties. The main characteristics and general layout are shown in Figure 4.9. The bearing structure is realized by four r.c. tapered arches that do not support in a complete manner the deck (as in the case of usual arc structures), but provide support to the central

part of the roadway, whereas a second part of the deck is built with the traditional Gerber technique. The height of the section of the arch is 0,75m at the base and 1,40m near the key position. Near the basis of the arches there are supporting walls rising up and connecting with the deck to hold the first span of the bridge deck and the second part obtained by a saddle in a cantilever area, creating almost 7 expansion joints in total. The roadway has a difference in level of 6,0m from the entrance and the exit section, namely a 7,9% slope. Differently from the previous structure, this one presents a high level of degradation of concrete and steel materials.

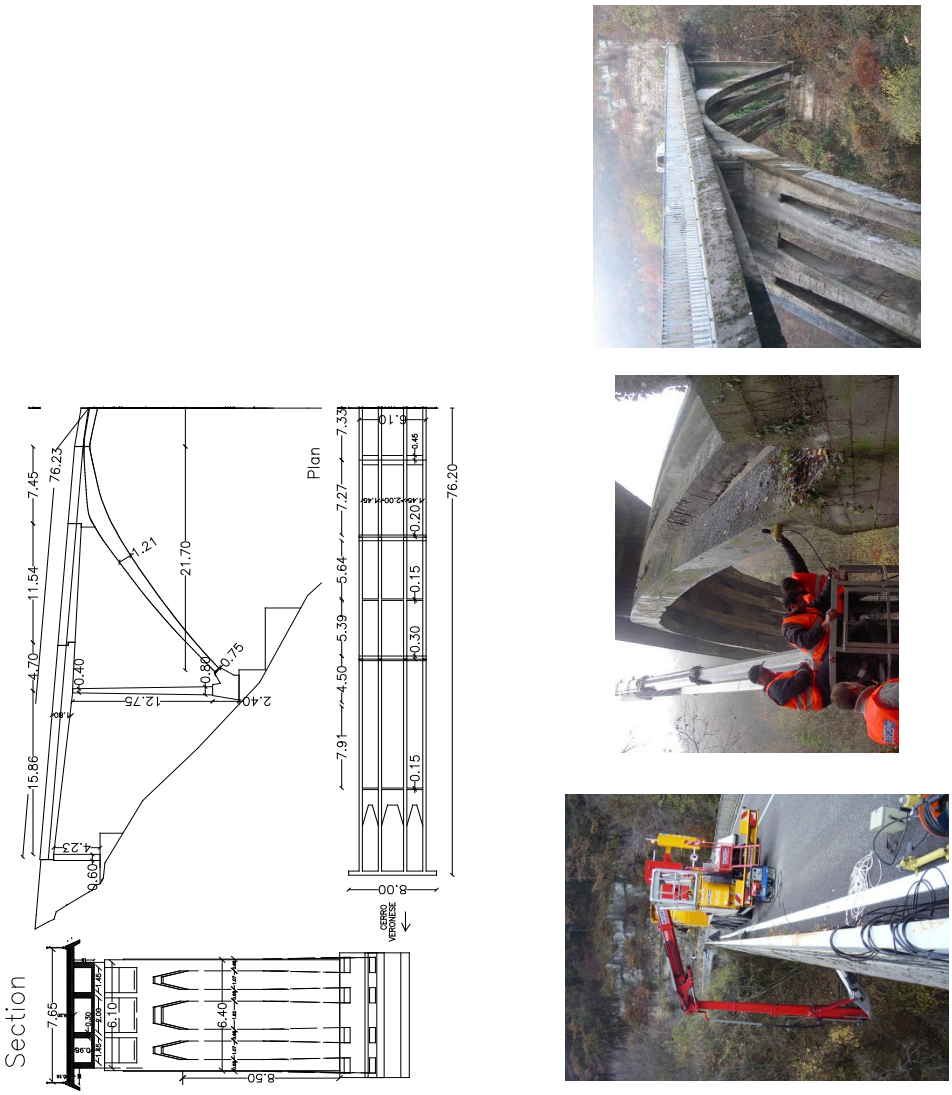

Figure 4.9 Roverè bridge: plan, elevation, cross-sections and photos.

Especially the lower extrados of the arches has no concrete cover and the corroded bars are clearly visible. Measurement campaigns took place in November 2009 and lasted three days. The configuration of acceleration sensors (Figure 4.10) and the data acquisition system were very similar to the case of the St. Giustina Bridge, due to their similarity. In this case the installation of the sensors onto the arches was made possible by the use of a by-bridge truck.

The ambient accelerations time series were recorded for nearly 11 minutes with sampling frequency of 100 Hz.

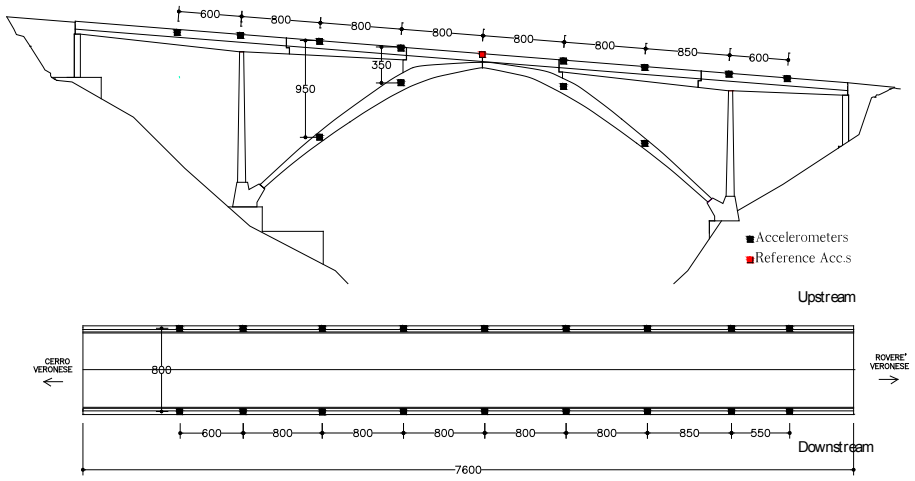

Figure 4.10 Sensor location for the Rovere bridge tests.

4.2.2.2 Modal identification

The extraction of modal parameters from ambient vibration data was carried out in the same way as the previous application (FDD and Peak Picking). It can be clearly seen that the two graphs (Figure 4.4 and Figure 4.11) present similar features and the first six modes are in both cases included in the range of 3 -10 Hz. Figure 4.12 shows that the first mode is a transversal + torsional mode, the second mode is a vertical mode and the third one is a vertical of side spans mode. As it will also be noticed in the mode shapes, the two arch structures, studied until now, have a very akin behavior and demonstrate immediately the slenderness of the arches, having a first vertical mode shape that mainly involves the concrete arches. Because of being slender structures, the two arch bridges were simply identified (structural modes), thus revealing similar sharp peaks in the

PSD representation. As it will be discovered during other applications, this doesn't happen with rigid concrete bridges or generally in masonry bridges.

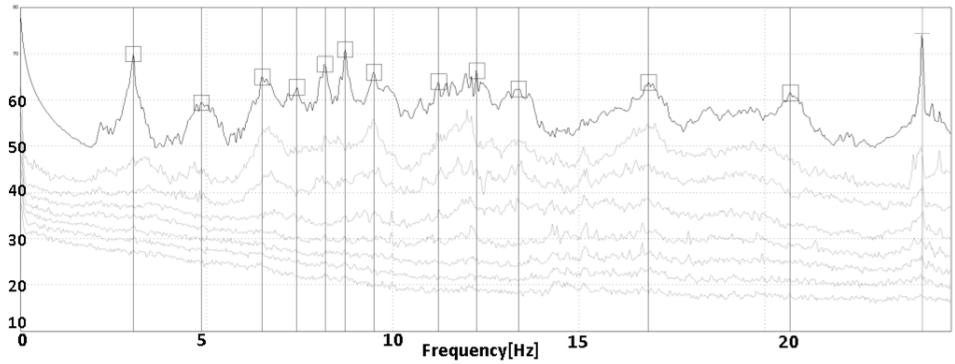

Figure 4.11 Frequency Domain Decomposition Method for the identification of natural frequencies of Rovere Bridge.

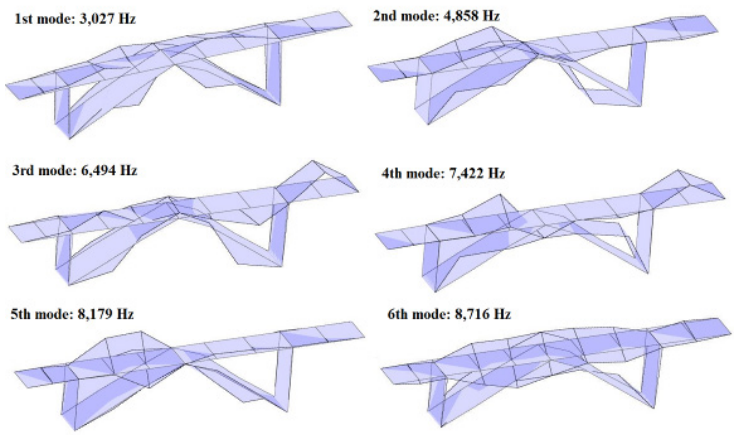

Figure 4.12 FEM and Experimental mode shapes of St. Giustina Bridge.

4.2.2.3 Comparison between experimental and FE model

The second bridge has been modeled using beam elements for arches and girders; plate elements for deck slab; wall elements (implemented in Midas/Gen [33]) for vertical walls. The Gerber cantilever bearings have been modeled with elastic springs for transversal and longitudinal displacements, and rigid links for vertical displacements. A good match was found between F.E. model and experimental data shown by the low percentage of difference (Table 4.2), in terms of natural frequencies. In some cases the modal analysis extracted mode shapes that was not feasible to find with the FE model, thus making this a sign of a model which needs to be studied in more detail.

Table 4.2 Correlation between numerical and experim. modal behavior.

Mode	FDD f (Hz)	Model (Midas/Gen)		
		f (Hz)	Δ (%)	MAC
1	3.027	3.007	0.665	0.92
2	4.858	4.683	3.737	0.94
3	6.494	-	-	-
4	7.422	7.320	1.393	0.81
5	8.179	8.025	1.919	0.85
6	8.716	-	-	-
7	9.497	9.384	1.204	-
8	11.23	-	-	-
9	12.26	-	-	-
10	13.38	13.333	0.353	-
11	16.87	-	-	-

4.2.3 Dynamic tests during the demolition of Tronto Bridge

4.2.3.1 The demolition process

In a project developed in San Benedetto del Tronto, central-east region of Italy, an arch bridge was subject to demolition due to life-cycle damage, after a new steel bridge was constructed. The old bridge was composed of five reinforced concrete arch spans, supported by masonry piers and abutments. Every span is composed by two parallel arches (15.5m) connected together with a reinforced concrete slab, casted between the two spandrel walls. The structure was bearing a two-lane roadway, one lane per direction, plus two sidewalks with a cross section of 12.30 m. The average thickness of the arch is 0,60 m. The maximum height of the piers is 6.5 m and their section is rectangular with dimensions 2.5 x 12.50 m.

The demolition process began on the 14th of November 2011, and the first step was to remove the pavement and the roadbed as shown in the photos in Figure 4.14.

The four principal sequences of the demolition process were:

- Removal of the roadbed and emptying of the infill material
- Demolition of the first three arches
- Demolition of the first three piers
- Demolition of the two remained arches and their piers

Figure 4.13 Prospect, longitudinal and cross section of the Tronto bridge.

Figure 4.14 Sequential demolition process of the Tronto bridge.

4.2.3.2 Measurement campaigns

During November - December 2011 several acquisition campaigns were carried out. The first measurements were performed in the first phases of the demolition process, i.e. in November 2011, when the roadbed and partial infill material was removed from the bridge.

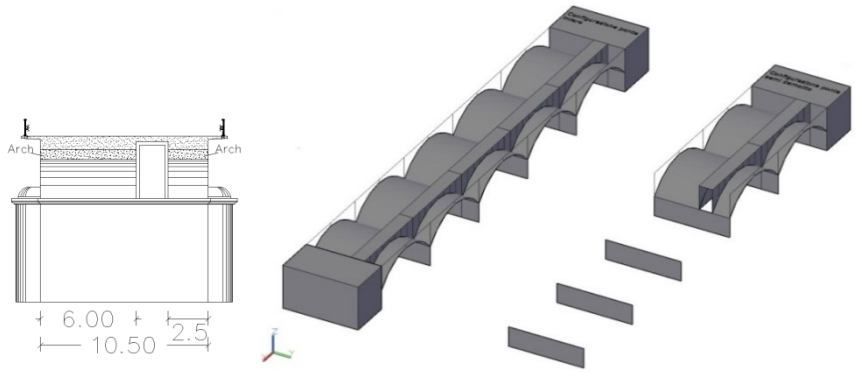

Figure 4.15 Cross section of the bridge. Two principal demolition configurations: a) five spans with some infill material, b) two spans without infill material.

The side on which the tests were performed, is the part which was demolished at the end, in hypotheses to repeat the measures after the demolition of three spans. In this description, only the local configuration will be considered in order to evaluate the differences encountered before and after the demolition of the 3/5ths part of the bridge. In the first case, the measurements were recorded with 16 velocity sensors for nearly 4 minutes with a sampling frequency of 200 Hz.

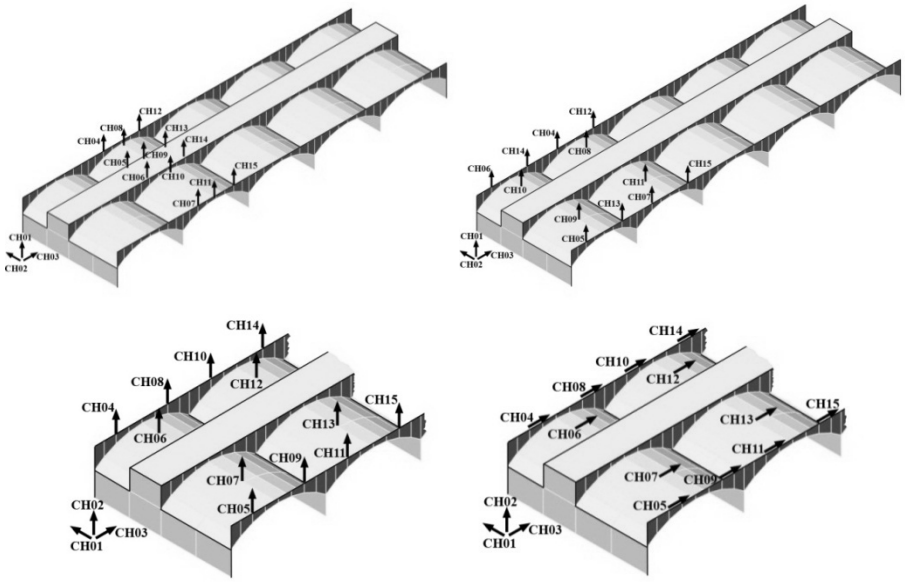

Figure 4.16 Velocity sensor configurations for the local measurements: entire bridge and the two spans remaining after demolition.

In the second case, three of the five spans were demolished, and only two spans on the Abruzzo side remained. Tests were performed in overlapping, but not simultaneously, with velocity and acceleration sensors (Figure 4.16).

4.2.3.3 Modal Analysis before and after the partial demolition

As previously mentioned, measurements have been taken before and after the demolition of three spans. In fact, the different results will be presented in this paragraph in terms of analysis conducted before and after the partial demolition. Modal analysis was carried out by using standard methods as Frequency Domain Decomposition (FDD) and the data-driven Stochastic Subspace Identification (SSI) technique. From the very beginning it was seen that noisy data were recorded and the structure was not sufficiently excited in order to capture its dynamic characteristics, so it was difficult to get clear results [34].

Velocity measurements were taken before and after the partial demolition, so it was straightforward to compare the results. In Figure 4.17 the Power Spectral Densities of the velocity measurements, before and after the demolition, are shown. The plots present similar features, but more importantly present a shift in the natural frequency values. In particular the first peak present in the first graph has a shift of nearly 1 Hz in relation to the second graph, resulting in an increase from 3.97 to 5.20 Hz, respectively before and after the partial demolition. Although, the SSI and FDD methods weren't capable of identifying many natural frequencies (noisy results), they revealed that the structure, after the partial demolition, seems to be more rigid than the entire structure (Table 4.3 and Table 4.4). These surprising results will be reviewed and exalted in the next paragraphs, but also validated with a theoretical model that represents the demolition process.

Figure 4.18 shows the FDD graphs before and after the demolition process for the case of velocity data recorded. Although already in the first plot the selection of the modes was not simple, when we consider the second plot, regarding the tests after the demolition, it is impossible to identify more than two modal modes.

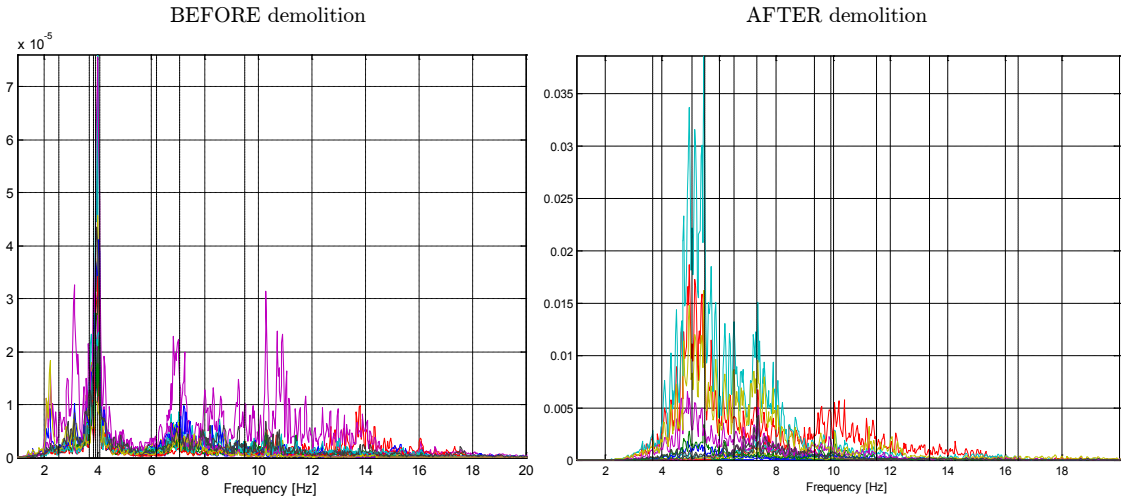

Figure 4.17 PSD of the velocities before and after the partial demolition.

Table 4.3 Differences between
Modal Analysis **before** the demolition (velocity data).

Mode	*FDD*		*SSI*	
	f [Hz]	*Damp[%]*	*f [Hz]*	*Damp[%]*
1	3.959	1.58	3.90	8.8
2	5.024	0.96	5.003	6.2
3	5.949	0.55	5.95	4.6
4	6.930	0.37	6.956	7.2

Table 4.4 Differences between
Modal Analysis **after** the demolition (velocity data).

Mode	*FDD*		*SSI*	
	f [Hz]	*Damp[%]*	*f [Hz]*	*Damp[%]*
1	5.206	0.116	5.24	8.2
2	-	-	6.14	9.2
3	7.335	0.815	7.345	6.4
4	-	-	9.46	4.2

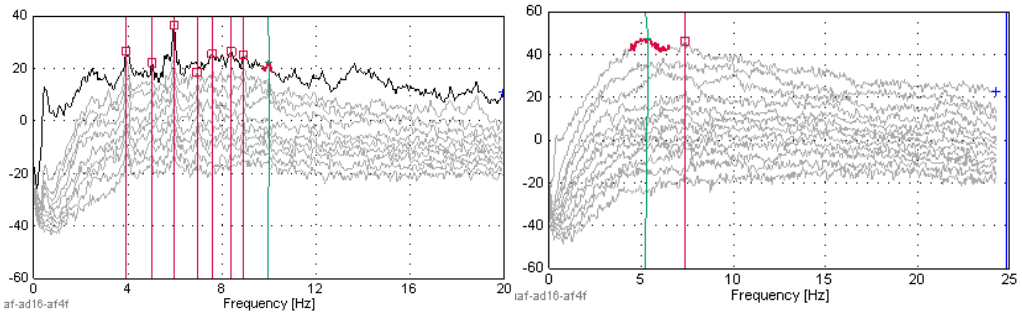

Figure 4.18 The FDD method with velocity data before and after the partial demolition.

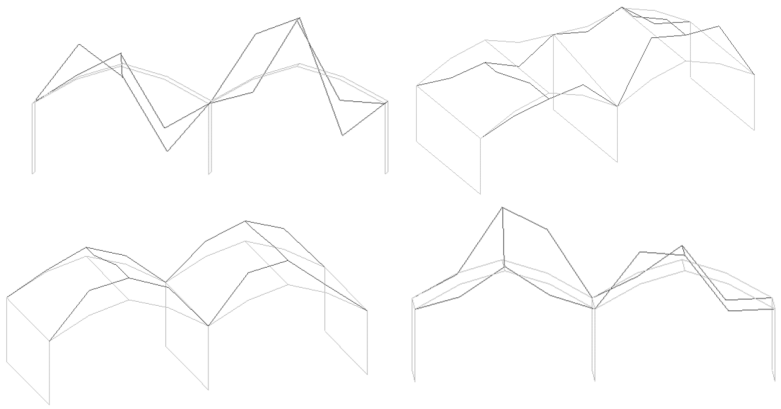

Figure 4.19 Four mode shapes of the two spans subject to analysis.

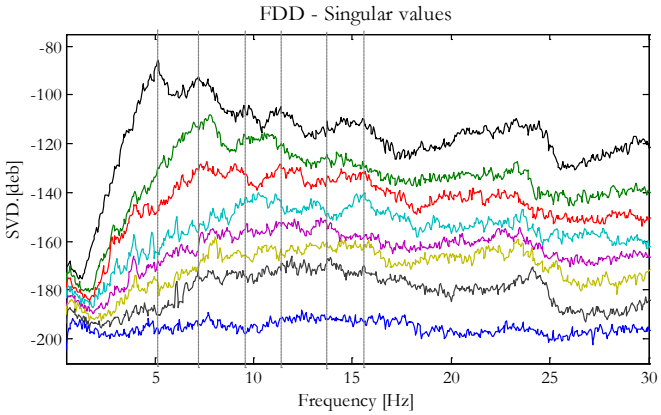

Mode	FDD	
	f [Hz]	Damp [%]
1	5.21	0.17
2	-	-
3	7.91	0.86
4	9.45	1.35
5	11.7	1.33
6	13.2	1.58

Figure 4.20 The FDD developed with accelerations after the partial demolition.

Both FDD (also implemented in Matlab®) and SSI techniques revealed few results; so it is difficult to certainly select the right modal parameters of the analyzed structure. For this reason, another study and some cluster analyses will be developed to get the best results from this interesting demolition process.

In the case of the acceleration measurements, the analysis is clearer and it was possible to identify more modal parameters than the case with velocity data after the demolition, although the first two principal frequencies coincide. Here, again, we have the confirmation that the natural vibration frequency values have increased after the partial demolition of three spans.

4.2.3.4 Modal Analysis via the ECCA

During the previous analysis with the standard modal methods we encountered some difficulties in finding the principal modal parameters of

the studied structure. In this paragraph some of the results obtained from the analysis with the ECCA method [13] (see section 3.3) will be shown. In this case, it was possible to identify more dynamic parameters and validate the previous results.

Theoretically, the order of a system's model is supposed to be determined by the singular value distribution in the SVD of the observability matrix O_i. In order to determine the order with the ECCA technique, the singular value distribution has been plotted in Figure 4.21.

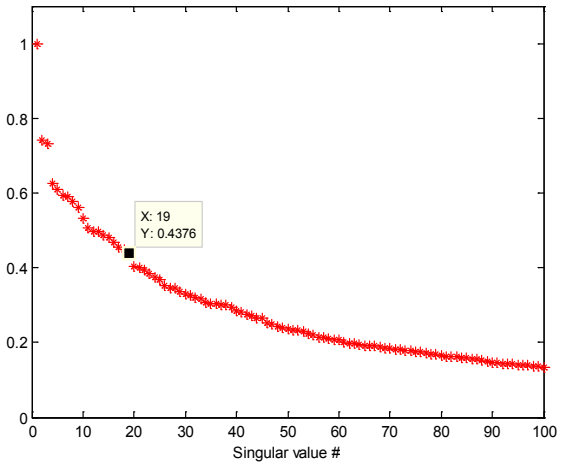

Figure 4.21 Normalized singular value distributions for the ECCA.

According to the gap present in the singular value plot, a model order of 19 can be chosen and then we can continue with the estimation of the modal parameters. The first values extracted: 5.202Hz, 7.468Hz, 9,73Hz and 11.43Hz helped immediately to concentrate the research around these values, for the "after demolition" case. Although the stabilization diagram subsequent to the SSI-ECCA technique gave more information about the modal parameters, it was difficult to clearly distinguish the structural modes. So a 60% overlap was applied to all the data, and in this way different parametric analysis were carried out resulting in the identification of higher modes, previously invisible. In order to capture every vibration frequency, different low pass filters were applied to the data, in relation to the frequency needed. In Figure 4.22 and Figure 4.23, it is obvious how the frequency values related to the model order number show a stable trend, especially for the first modes.

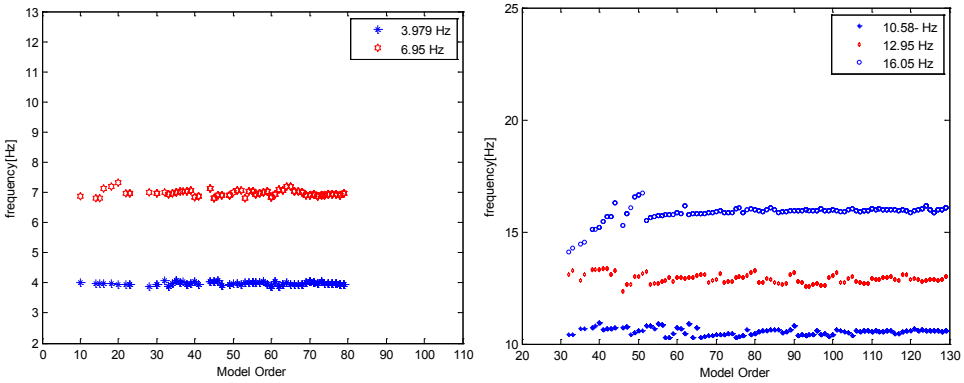

Figure 4.22 Natural frequencies relatively to the system model order (before demolition).

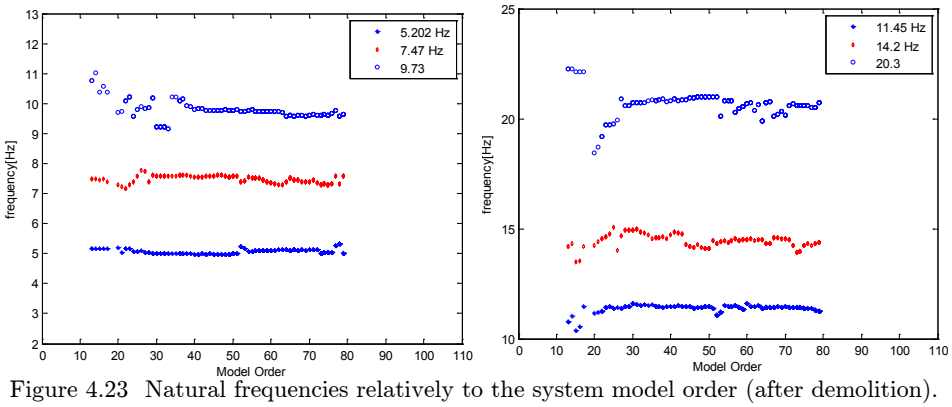

Figure 4.23 Natural frequencies relatively to the system model order (after demolition).

To examine the variations of the damping ratio estimates with the model's order, three modes have been considered: one around 5.2 Hz; the other around 7.47 Hz; and the third around 9.73 Hz. The damping ratios of these three modes are extracted from the models with different orders (such models are realized via the ECCA method) and displayed in Figure 4.24.

In the frequency range of 3-30, a total of 11 structural modes were identified with the ECCA (far more than the standard techniques). Four of them (first vertical-longitudinal, second hybrid vertical-torsional antisymmetric, third vertical and fourth torsional mode) are presented in Figure 4.19. The results reveal ones again that every vibrating mode, after the partial demolition, has a shift towards higher values.

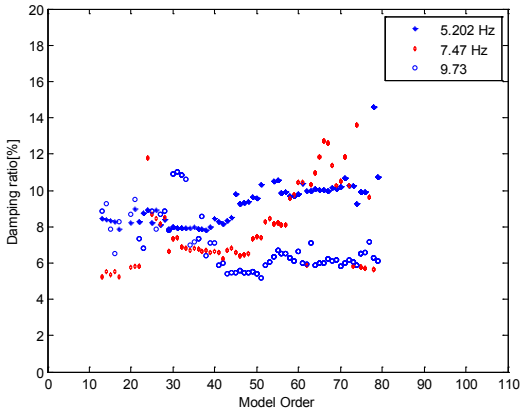

Figure 4.24 Damping values in relation to the model's order (after demolition).

4.2.3.5 Cluster Analyses

In order to take into account all the variations of estimated structural modes that can arise from different choices of the model's order, a cluster analysis (see Section 3.4.3) has been applied to the data of the "after demolition" case.

For a proper identification, a single mode should be identified within a single cluster at least 30 times, using different combinations of *n* and *i*. In this study, considering values of the model's order n ranging from 40 to 160 with increments of 5, and by considering the value of i number of blocks ranging from 40 to 120 with increments of 4, a total of 480 analyses have been conducted (Figure 4.25).

Results

The acceleration responses of the Tronto Bridge were subject to Band-pass filtering and de-trend processing before applying the identification algorithm. The results of clustering steps are presented in Figure 4.25 - Figure 4.27, where modal properties are plotted in terms of the frequency and damping ratio. Figure 4.25 shows all modes that have been identified by the total parametric analysis and the ones remaining after eliminating modes with damping larger than 15%.

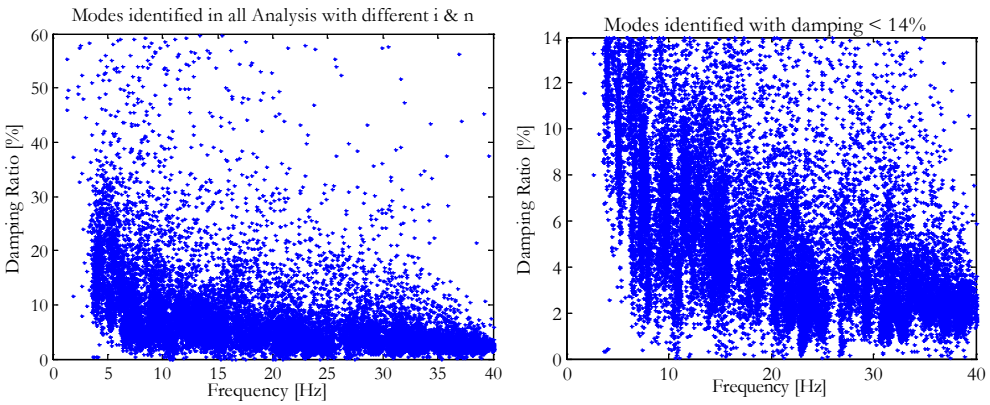

Figure 4.25 Modes identified from all analysis and modes with damping ≤ 15%.

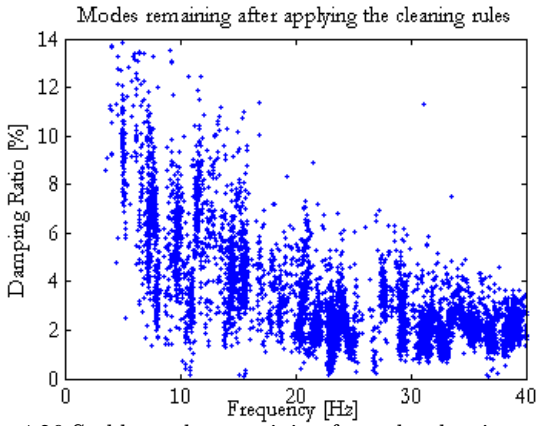

Figure 4.26 Stable modes remaining from the cleaning procedure

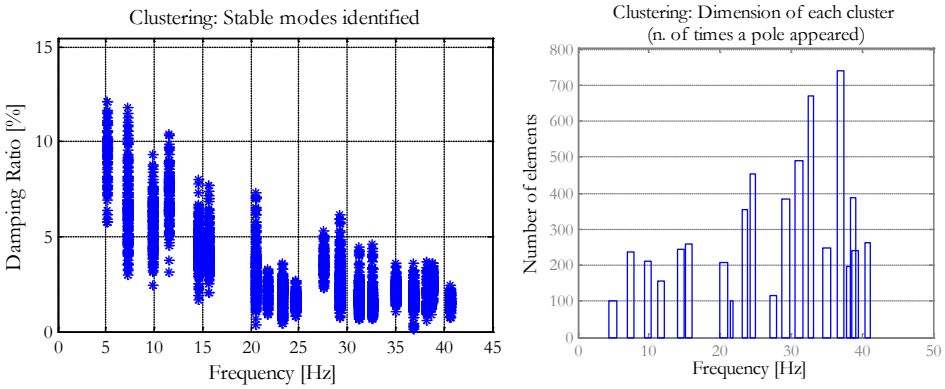

Figure 4.27 Cluster analysis: Modes remaining after applying the clustering rules and number of elements in each cluster.

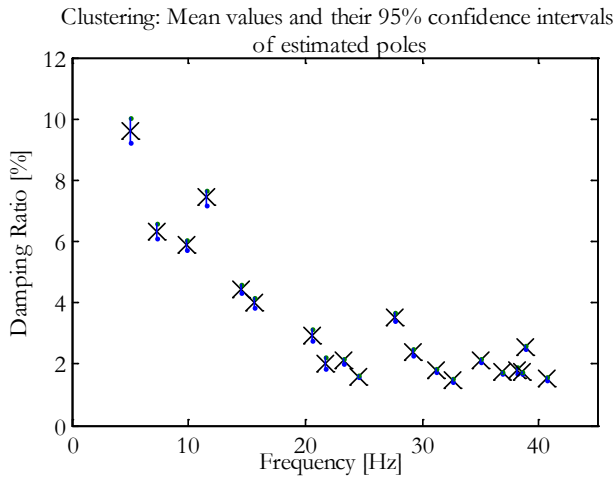

Figure 4.28 Mean Values and their 95% confidence intervals of stable modes.

Figure 4.28 represents the final results of the cluster analysis and a total of 20 groups can be observed, which indicates that a total of 20 structural modes are identified from the cluster analysis. Mean values and confidence intervals estimated modal parameters with very small uncertainties. In such analysis, even close modes seem to be well distinguished whereas noise modes are efficiently eliminated. Comparing Figure 4.26 and Figure 4.28, most of the noisy modes are eliminated by inspecting the consistency between modes estimated using different pairs of n and i.

With regard to modal parameters estimations, the natural frequencies and damping ratios can be calculated from the individual groups in relationship to their statistical properties (e.g. mean, standard deviation). Table 4.5 presents the mean and standard deviation values of 12 natural frequencies identified in this study from the cluster analysis. It is noteworthy to mention that the distribution of the frequencies is quite small, showing a good clustering process. Furthermore, in the last column of the table, the number of times a mode has appeared (in the 480 analyses) is also shown.

To summarize it, the ECCA has shown a good performance in identifying the modal parameters, especially when other standard techniques do not give a precise view of the structural modes. The ECCA method performs better than the others in discriminating structural modes from the noise ones. In addition, the use of the complementary clustering analysis for the parameter selection and discrimination between structural and noise modes helped to precisely choose the proper modes. This set of parameters is used in the subsequent study of the updated FE model of the Tronto Bridge, which will help to understand the structural behavior of the demolished bridge.

Table 4.5 The identified frequencies [Hz] from the cluster analysis for the experimental problem.

Mode	Freq. mean [Hz]	Freq. Std	Num of times found
1	5.2049	0.0280	98
2	7.4666	0.0441	230
3	9.7291	0.0489	210
4	11.4604	0.0563	155
5	14.2099	0.0887	232
6	15.5820	0.0563	255
7	20.3015	0.0936	205
8	21.5218	0.1206	94
9	23.1927	0.0671	345
10	24.6084	0.0942	452
11	27.6969	0.1311	112
12	29.4251	0.1249	392

As we know, not all modes observed in one segment of the data can be equally detected in all other segments since, depending on the excitation, different modal responses may be amplified at different times. Herein another statistical analysis is used to overcome this issue, refining the ECCA results. In fact, for the velocity data recording case, another statistical analysis was carried out in order to understand the distribution of the frequencies in the recorded signals.

The time history set was divided into 15 non-overlapping segments, each of 2460 points long, and separate state models were analyzed for these segments. The modal identification process for both cases (before and after demolition) was repeated in each segment. In this way, frequency values of the structural modes and their distribution were found. The order of the state-space models were determined based on the singular values carried out from the ECCA method. The optimum model order for the time histories of the set after the demolition appeared to be between 22 and 28, while in the case of the series before the demolition of the bridge, the optimum value was chosen between 26 and 34. If we represent the results in histogram graphs (Figure 4.29 and Figure 4.30) it is easy to observe their distribution in the two studied cases of "before and after demolition".

For almost every mode analyzed, it was possible to capture the corresponding frequency value in each segment of the time series. Eventually, the graphs display once again and clearly the frequency shift present in the structure, before and after the partial demolition.

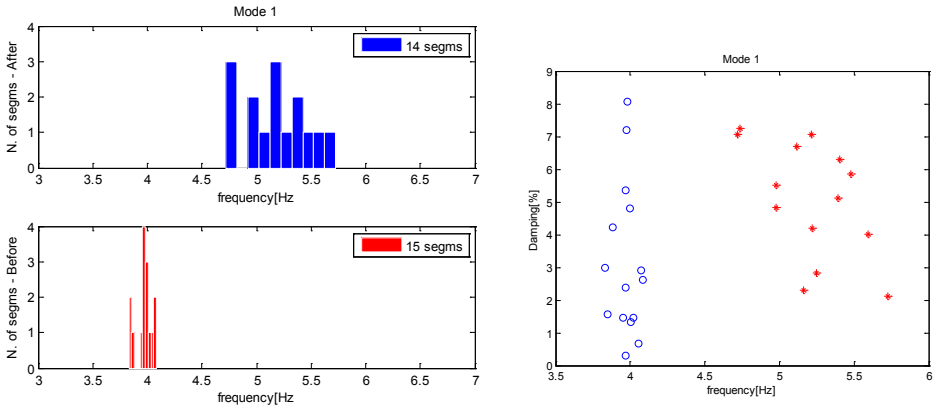

Figure 4.29 Appearance of the first mode among the time segments, before and after the demolition. Representation of the damping ratio for both cases.

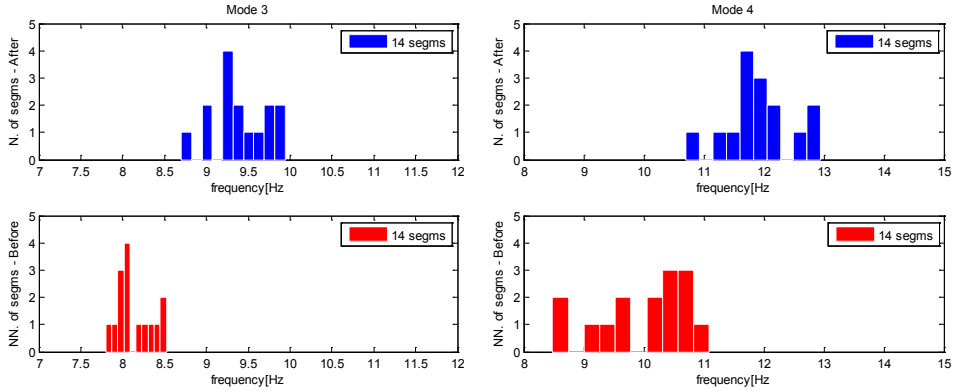

Figure 4.30 Appearance of the other modes among the time segments, before and after the demolition.

4.2.3.6 Validation of the demolition process with FEM Analysis

Generally, modal identification of bridges and other civil structures is required for the validation of finite element models used to predict static and dynamic structural behavior, either at the pre-functional stage or in case of structural damage or monitoring. The correlation of modal parameters can be analyzed both in terms of identified and calculated natural frequencies, and by the corresponding mode shapes using correlation coefficients or MAC (modal analysis criteria) values. In our case, this general use was more or less converted, i.e., the FE model was not only updated from the experimental results, but also served as a means of demolition scenario validation.

A tridimensional FE model of the Tronto Bridge has been developed in the STRAND7 [32] environment. Geometric and materials characterization has

been performed according to the surveys carried out in situ and in lab, even though several sensitivity analyses have been developed in order to calibrate the model. The concrete arches have been modeled with four node plate elements anchored at the masonry abutments and piers (plate elements). A high elastic modulus was assigned to the arches due to the fact that they are composed by concrete; while a low value has been assigned to the piers and abutments because they are made with external masonry walls filled with gravel material. In order to create the same situation existing during the tests, only the standing spandrel walls and part of the infill material were modeled, without the roadbed or slab. In fact, during the first tests before the demolition of the three spans, it was estimated that only one third of the infill material was present. Since it has poor mechanical characteristics, the infill material has been modeled as non-structural mass and has been placed on top of the piers between the arches. Three-degree-of-freedom elastic springs are placed at the bottom of the piers and at the abutments to reproduce soil-structure deformability.

After defining the base model and updating it according to the experimental data, a second model group has been generated. This model wants to reproduce what was left in site after the demolition of three spans of the bridge; from the previous model only the first two spans were present and a small portion of the infill material was extracted. In summary, we have two groups of models representing the bridge before and after the partial demolition, in accordance with the measurement configurations.

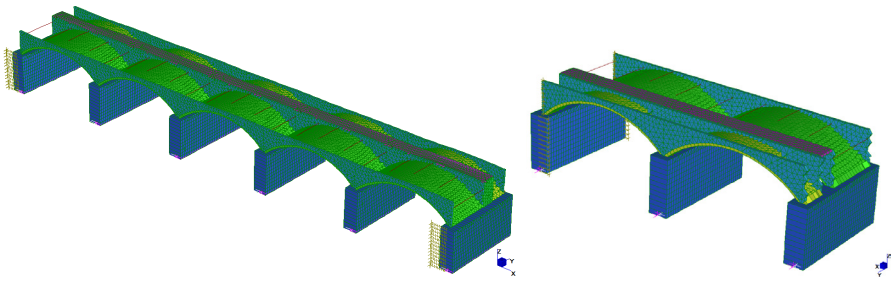

Figure 4.31 3D Finite Element Calibrated Model of the Tronto bridge: before and after partial demolition.

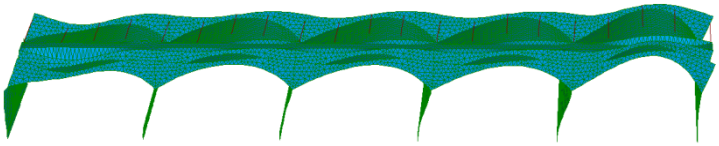

continues

Figure 4.32 First principal modes (3.989Hz and 6.011Hz) calculated by means of the calibrated FE model before the demolition of three spans.

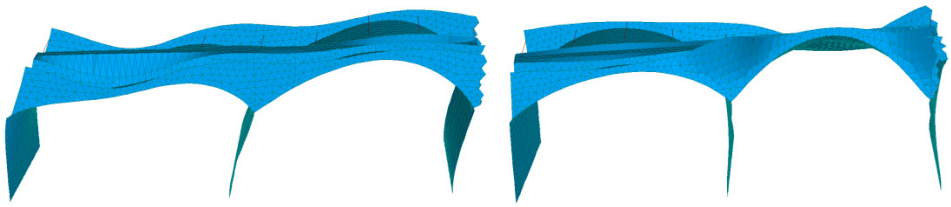

Figure 4.33 First principal modes (5.226 Hz and 7.264 Hz) of the calibrated FE model after the demolition of three spans.

Table 4.6 Comparison between experimental and theoretical models **before** and **after** the demolition .

Mode	*Experimental*		*MAC*	*FEM*	
	Before	*After*	*Exp.*	*Before*	*After*
1	3.959	5.204	0.46	3.989	5.226
2	5.949	7.466	0.56	6.011	7.264
3	6.950	9.729	0.60	6.413	8.245
4	10.58	11.460	-	10.02	10.25
5	12.95	14.209	-	12.50	13.42

Figure 4.32, Figure 4.33 and Table 4.6 show the results of what was carried out from the model updating and demolition scenario. In Figure 4.33 it can easily be noticed that the first mode shapes and natural frequencies of the entire structure are clearly similar to the results that were captured during the dynamic tests, before the demolition of the three spans. In fact, on both cases the first mode is a longitudinal arch bending one while the second is a vertical - torsional mode.

A better view of what happened in both cases of the experimental and analytical model, before and after the demolition, is shown in Table 4.6, where one can notice that the overall frequency values in both cases have augmented. We can now state that what was observed in the field from the experimental tests is also confirmed by the FE models. This result, at the beginning unexpected, is probably due to the order change of the mode shapes, to the different boundary conditions and small change of material present before and after the demolition.

An interesting topic in this study was the evaluation of the MAC value between the Modal model before and after the demolition. Poor correlation existing between the two cases show that mode shapes are different before and after the partial demolition, probably because the structure has changed. The structural change has been displayed although the change in frequency and mode shape switch. To validate the aforementioned result some other bridges were taken into consideration. Two other dynamically investigated arch bridges [35] were submitted to the demolition process through FE analysis (as they were not scheduled for real demolition). Surprisingly, they revealed the same result like the previous studied case: the natural frequency values always increase after the destruction of some of the spans of the bridges.

4.3 Masonry Arch bridges

4.3.1 Evaluation of the seismic intervention on Gresal Bridge

4.3.1.1 Measurements of the retrofitted bridge

The Gresal bridge is located in the North-East of Italy, in the Belluno province; it was built in the early XIX century and is currently used as a vehicular bridge, representing for the regional road network an important overcrossing of the Gresal river. The structure is a three span stone masonry arch bridge, with a total length of 67,40 m: the three spans are almost equal, the single arch clear length is about 15m; their shape is almost semicircular with a radius of 7.39m, slightly increasing at the springers. The average thickness at the crown is 0,50m. The maximum height of the two piers is 12,75m and their section is rectangular.

The roadway is 6.09m wide, and laterally the spandrel stone walls emerge beyond the deck level forming two 45cm thick parapets. The structural investigation has consisted in three core samples taken in the stone arch and a geometrical survey. These investigations have allowed to determine the thickness of the brick stone, as well as the layering of the material between the pavement and the masonry vault; and furthermore to characterize the mechanical property of the infill material. The infill has good mechanical characteristics and is made by loose material, stones and pebbles.

A retrofit intervention has been carried out, and a new r.c. slab has been built under the pavement. It was anchored to the piers with high strength vertical ties and restrained at the abutments in order to create a new

resistance arrangement withstanding inertial forces. The dynamic behavior has been initially assessed with numerical models comparing the response of the bridge before and after the repair, and has subsequently been tested by the Output-Only technique to detect the variation of the modal response induced by the strengthening intervention.

The effectiveness of the strengthening technique has been tested with appropriate nonlinear analytical models, comparing the seismic capacity of the bridge before and after the repair intervention. The capacity of the bridge has been increased (the ultimate displacement in the inelastic field) by the retrofit both in the longitudinal and transverse direction; the latter was the most vulnerable in the existing bridge, mostly due to the slenderness of the high piers.

Figure 4.34 Panoramic view and piers of the Gresal Bridge.

During February 2011 an acquisition campaign was carried out and piezoelectric accelerometers with vertical axes were used to measure the bridge's response. The sensor configuration (Figure 4.36) was mainly concentrated on the arches due to the facts that they were the key elements of the structure. Three acquisitions have been registered, one for every arch (Figure 4.36).

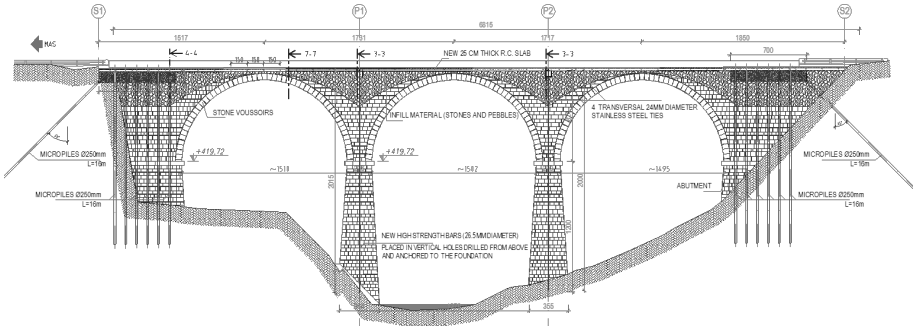

Figure 4.35 Longitudinal section with new structural elements (rc slab, micropiles and vertical ties)

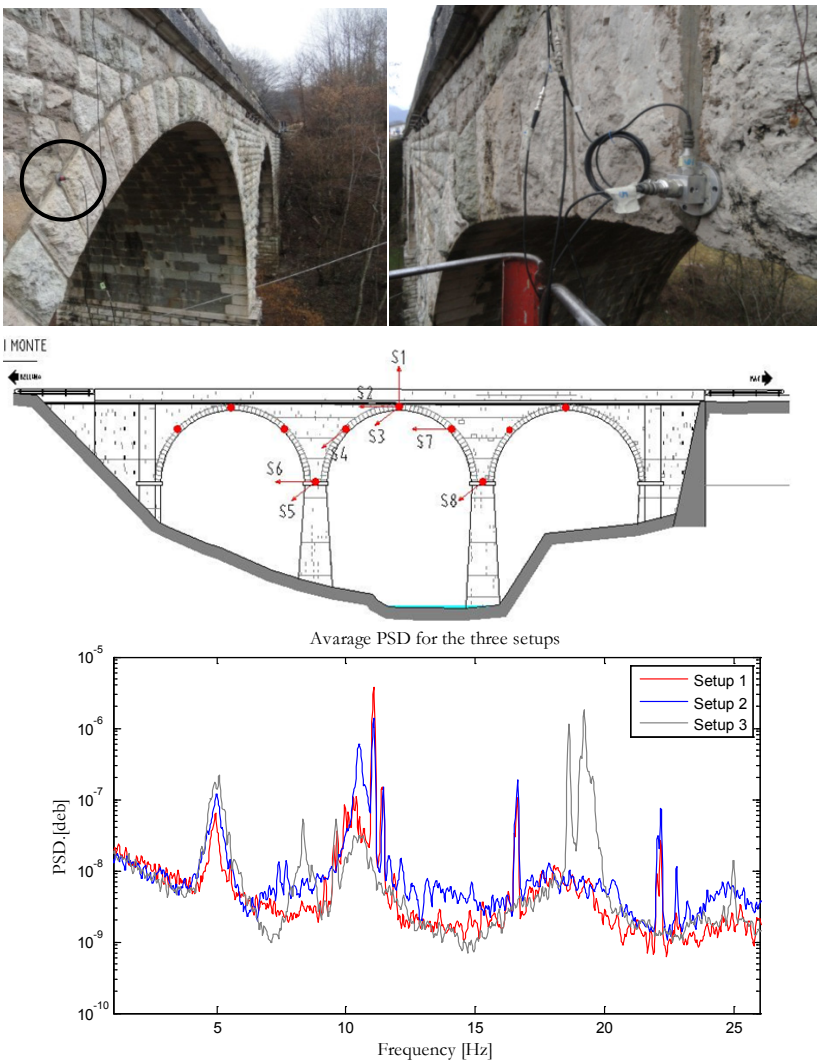

Figure 4.36 Sensor location on the arches for the Gresal bridge tests and PSD for the three setups.

4.3.1.2 Identification of the modal parameters

The extraction of modal parameters from ambient vibration data has been carried out by using the Frequency Domain Decomposition (FDD), the reference-based stochastic subspace identification [4] and the Operational poly-reference least squares complex frequency domain identification [36].

The analyses included frequencies corresponding to the first 10 eigenmodes. In Figure 4.37 the first modes identified are shown and it can be seen that the first six modes are included in the range 4-20 Hz.

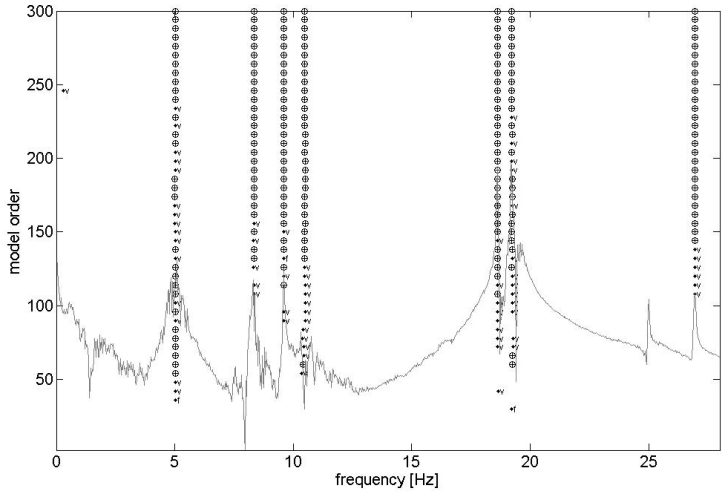

Figure 4.37 The stabilization diagram in the ref-SSI method.

Table 4.7 Comparison between more Modal Techniques

Mode	*Identification Method*				
	FDD	*SSI*		*pLSCF*	
	f [Hz]	*f [Hz]*	*ξ[%]*	*f [Hz]*	*ξ[%]*
1	4,932	4,962	*3,512*	4,991	1.621
2	8,350	7,762	*6,518*	-	-
3	9,619	-	-	9,675	0.625
4	10,500	10,118	*1,624*	10,590	0.087
5	11,080	10,825	*4,084*	-	-
6	11,430	14,788	*1,141*	12,849	0.721
7	16,650	17,675	*2,328*	-	-
8	18,600	18,977	*4,137*	-	-
9	19,240	-	-	19,045	0.510
10	19,530	21,438	*5,025*	-	-

For each method, in Table 4.7, natural frequencies identified and damping (where assessed) are shown. The frequencies not reported in the table refer to the unstable modes highlighted during the analysis of experimental data.

4.3.1.3 Model Updating and comparison with the retrofitted case

During the study of the bridge over the Gresal river, for the finite element model implemented, using the program Straus7, brick elements were used to model piers, abutments, spandrel walls and the infill. In particular, we have used two models: one for modeling the final bridge with its seismic retrofitting, and another to model the bridge before the intervention. Regarding the modeling of the intervention (Figure 4.38), the micropiles and Dywidag bars were modeled with beam elements positioned at the

abutments and at the piers; the same method was also used to model the integrative r.c. slab.

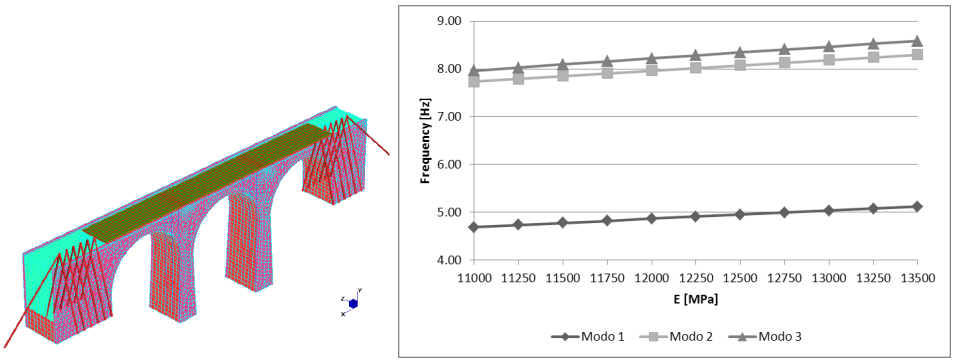

Figure 4.38 FE model used and the sensitivity analysis conducted.

As part of the calibration of the FE model with the experimentally measured data, a study has been made on two levels of sensitivity: one for the infill material modulus and another for the stone material constituting the bridge. Being in the presence of very massive stone blocks composing the arches, the values of elastic modulus can reach abnormal values in reference to usual masonry structures. The test results showed that the increase of elastic modulus induces a linear increase in the natural frequencies for all the modes being considered (Figure 4.38).

After calibrating, the model was put in comparison with the Modal model in terms of natural frequency and mode shape values (MAC).

Table 4.8 Correlation between numerical and experim. modal behavior

Mode	*FDD*	*Model [Straus7]*		
	f [Hz]	*f [Hz]*	*Δ [%]*	*MAC*
1	4,932	4,924	*0,17*	0,977
2	8,350	7,923	*5,39*	0,820
3	9,619	8,202	*17,28*	0,809
4	10,500	10,993	*-4,48*	0,825
5	11,080	11,193	*-1,01*	0,960
6	11,430	12,731	*-10,22*	0,291
7	16,650	15,992	*4,12*	0,906
8	18,600	16,416	*13,31*	0,671
9	19,240	17,174	*12,03*	-
10	19,530	18,878	*3,45*	-

From the results reported in Table 4.8, it was obtained a high correlation between the experimental frequencies and those derived from the numerical model, for the first five modes. One can observe a close similarity from the comparison between the same mode shapes, presented in Figure 4.39, as well. In particular, from both experimental and numerical evaluations, the first

vibration mode is of a bending type in the transverse direction, the second is a bending type in the longitudinal direction, while the third is torsional.

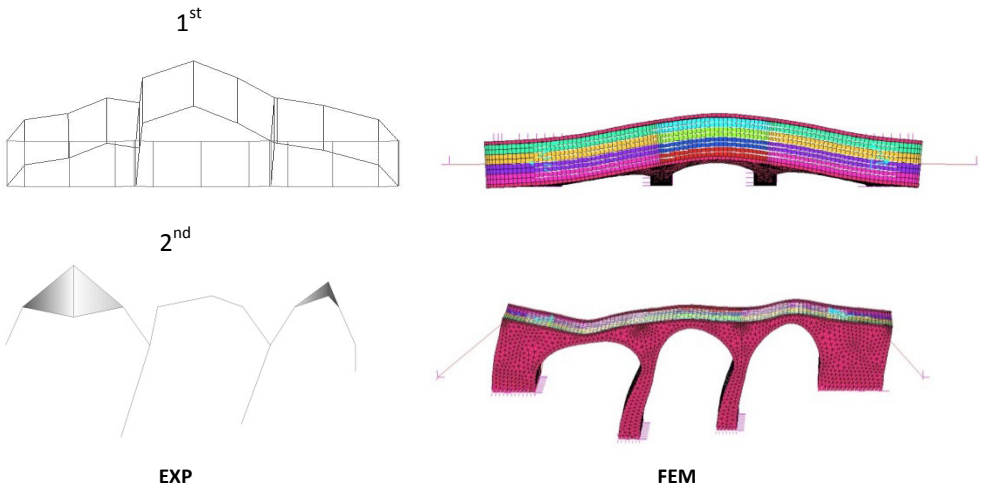

Figure 4.39 Comparison between experimental and analytical for the first and second mode shape.

The comparison, between the pre-intervention and post intervention frequencies, is shown in Figure 4.40.

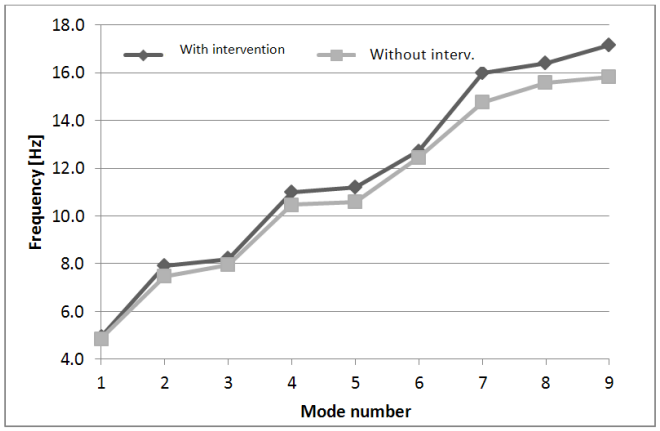

Figure 4.40 Natural frequencies comparison of the bridge before and after the intervention

By comparing the results of the two dynamic models, it was observed how the intervention slightly improved the seismic response of the bridge. We came to the conclusion that the retrofit increases the elastic stiffness (consequently the natural frequencies) less than expected, but enhances considerably the ultimate capacity of the structure in non-linear field.

4.3.2 Liberty Bridge: a very squat structure.

4.3.2.1 Description of the structure and measurement campaigns

The Liberty Bridge (constructed in 1930) is located along Regional Road 11, between the towns of Mestre and Venice in Italy. It is a bridge of strategic importance, being the only road bridge that connects the city of Venice to the mainland. The structure can be schematized as a succession of vaults combined with piers, abutments and terrain embankments. Between each square there are seven series of masonry vaults. Each series consists of five vaults, resulting in a total of 227 arches. The overall length of the infrastructure between Venice and the mainland is 3623.58 meters. The width of the bridge is 20 meters, comprises a parapet of 0.50 m, a sidewalk of 3 m, a road width of 15.75 m and a runway of 3 m reserved for cyclists. The height of the piers is 2 meters. Their thickness is 1.50 m, and the pier-abutment is 13.74 m thick. Each vault has a span of 10.63 m, the arch rise is 1.31 m and the thickness is 0.65 at the crown.

Figure 4.41 Panoramic views of Liberty Bridge in Venice.

As it can be easily noticed from Figure 4.43, the bridge has a squat and stiff structure. From the beginning, high values of natural frequencies were expected and this was proved by the experimental investigations. The main concern in the case of Liberty Bridge was the effect of the marine environment on the structure. In fact, during its age and before the dynamic tests, several material characterization campaigns has been carried out on the structure.

On June and July 2010 two vibrational acquisition campaigns (Figure 4.42) took place. The first measurements were done over the bridge, but during the second campaign, the sensors were installed under the vaults by means of small boats.

Although two series of measurements were taken, both of them carried noisy data and poor results could be reached. One of the main reasons was the low flexibility of the structure and the disposability to reveal its behavior, at least with the available instrumentation.

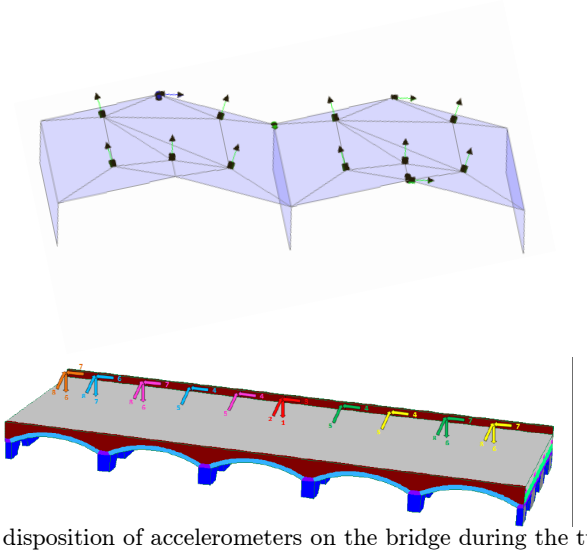

Figure 4.42 The disposition of accelerometers on the bridge during the two campaigns.

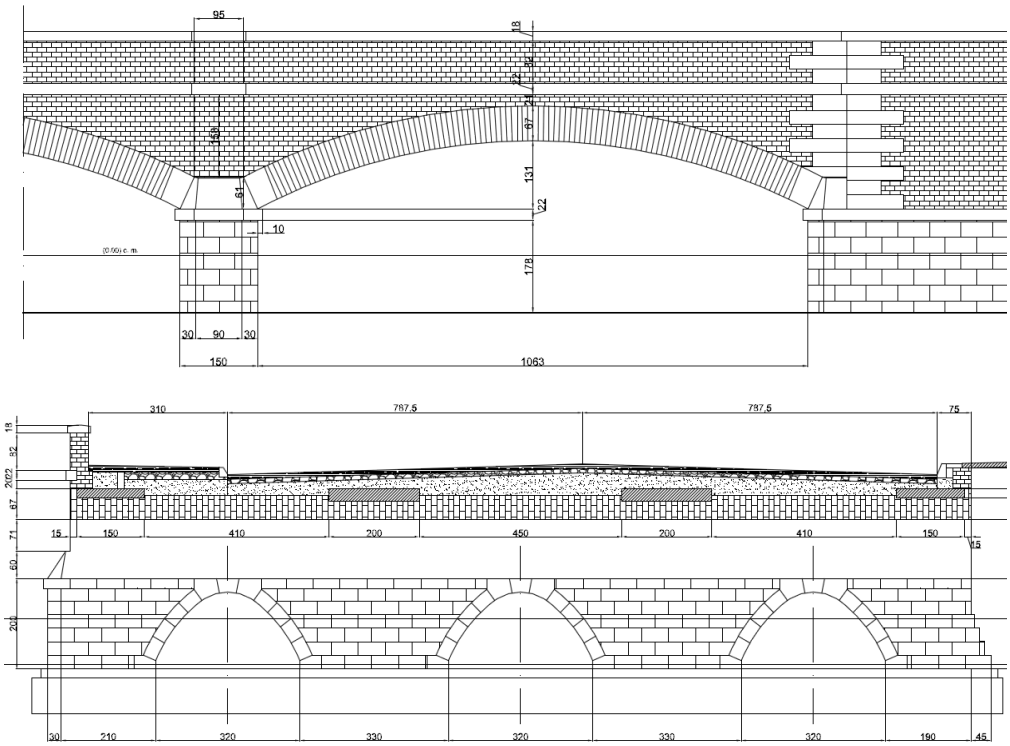

Figure 4.43 Longitudinal view of one of the vaults and the pear of Liberty Bridge.

Figure 4.44 Sensor installation on the structure.

4.3.2.2 Modal analysis

As the first step, the Frequency Domain Identification was used to analyze the measured data. For the singular values, for each dataset, difficulties in extracting the exact structural modes were revealed since the graph didn't present clear peaks as in the previous cases.

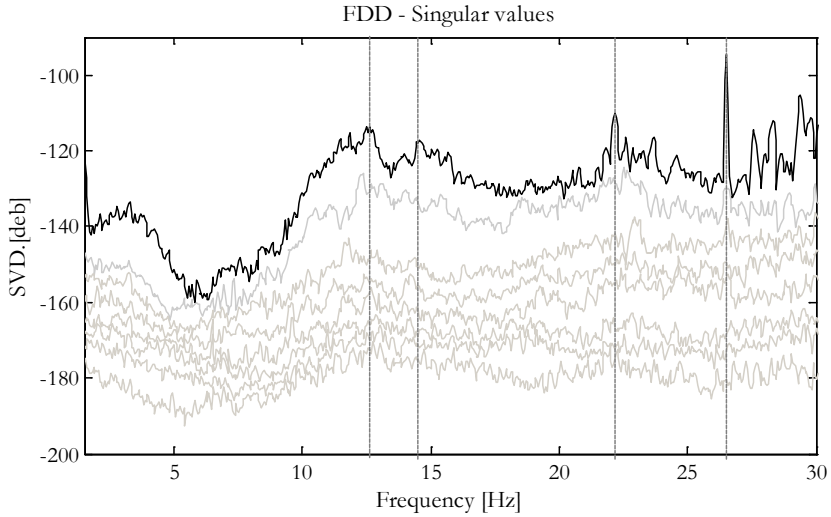

Figure 4.45 Example of Power Spectral Density graph for one of the setups.

The first natural frequency is at the value of 12.24 Hz. Two other clear peaks show up at 22.1 Hz and at 26.6 Hz as observed from Figure 4.45. These values are quite high for bridges in general, since the first modes

that were seen during all the applications presented in this work, had values that go from 2 to 6 Hz.
To integrate the results that were given by the preliminary analysis and the FDD, another method was used, in the time domain. This is the SSI Enhanced Correlation Covariance Analysis. In order to evaluate as much structural modes as possible, different model's orders has been chosen and a high value of block numbers have been selected. From the stabilization diagram (Figure 4.46), one can notice that the stable modes correspond to some of the values that were extracted by the previous analysis, but other structural modes were also discovered. In fact, the second mode of 12.8 Hz and the third of 14.50 Hz were not possible to identify from the FDD technique. In Figure 4.47 one can notice that the first mode shape is an asynchronous vertical deflection of the vaults, whereas the second mode is a longitudinal and vertical mode shape.

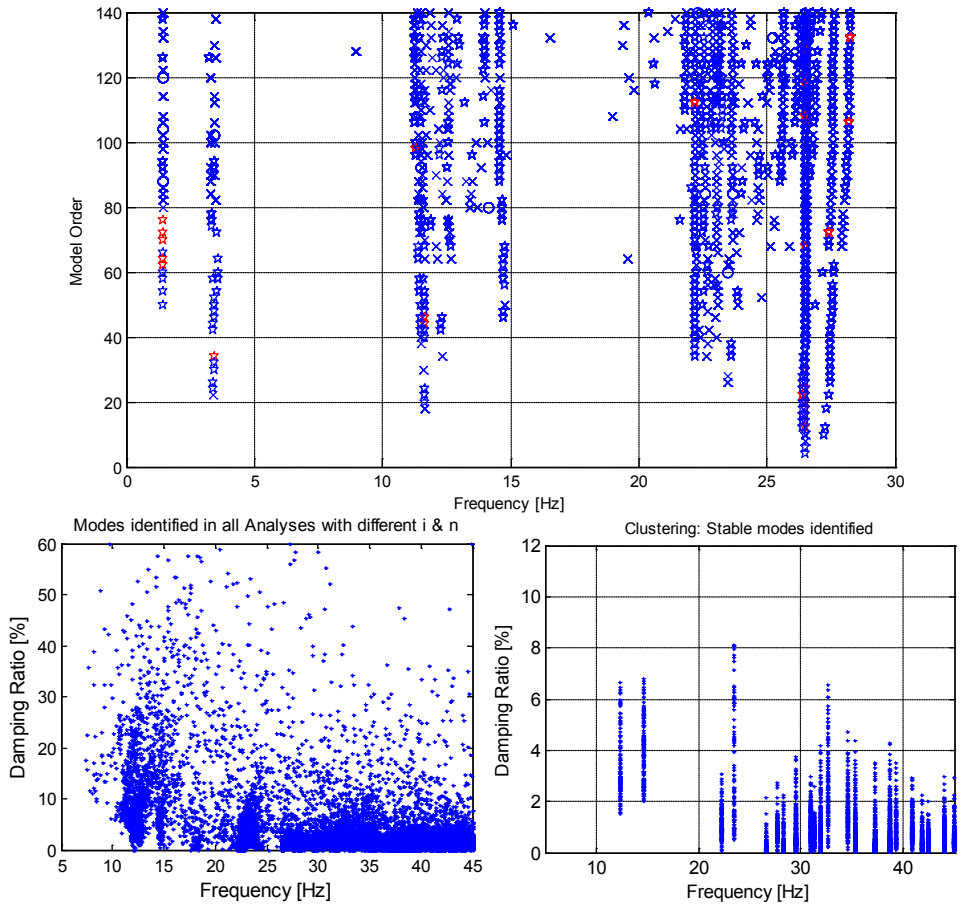

Figure 4.46 Stabilization diagram obtained from the ECCA method and results of cluster analysis.

More accurate results were needed for this case study. So a valuable solution in cases of squat structures is the use of cluster analysis (SSI analyses, with different block number and model's order, clustered) able to estimate all structural modes more precisely. In Figure 4.46 the results of the cluster analysis applied to the Liberty Bridge data are represented. It can be observed that the accuracy is quite good, especially for the higher well amplified modes.

4.3.2.3 Comparison between experimental and FE model.

After identifying the first natural frequencies with the aforementioned methods, we are now ready to compare them with the FE model developed.
The elements used in the model are *brick* elements, since it was not considered possible and convenient to schematize the complex structure with single or two-dimensional elements. Five arches of the bridge were modeled, at the ends of which have been placed symmetry constraints to represent the presence of abutments and the continuity of the long bridge. It can be observed that the theoretical model describes accurately the mode shapes extracted from the experimental analysis. But the Finite Element Model showed several mode shapes that were not possible to find with the OMA.

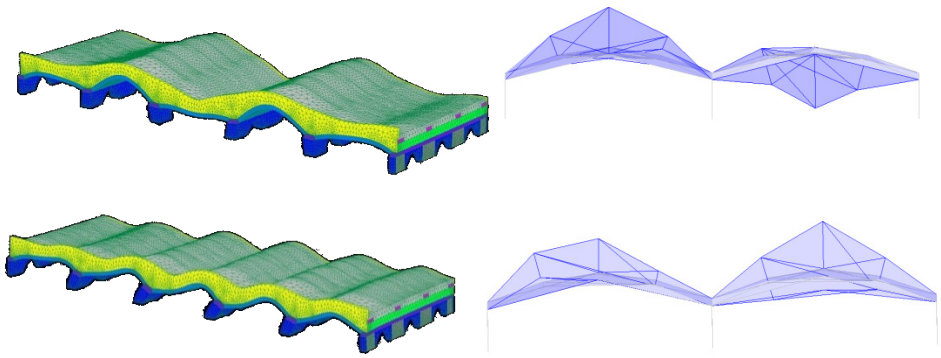

Figure 4.47 Comparison between experimental and analytical first and second mode shape.

4.4 Reticular and box girder steel bridges

4.4.1 Fosso Bridge

4.4.1.1 In-site measurement on the railway bridge

The analyzed bridge is located in Saint Stino of Livenza along the railway line that connects Venice with Trieste in Italy. Its steel reticular truss structure is built in 1922, with the overall length of 33.6m and the width of 4.5m. Being subject to the phenomena of fatigue due to train loads, the bridge has been replaced with a new one. Besides the dynamic tests, some elements of the bridge were subject to fatigue tests in the laboratories of the University of Padua, in order to determine their lifetime. In absence of the original projects, detailed geometric survey has been done. The structure is very complex because each section is obtained by overlapping steel plates of varying thickness from 10 to 12 mm (riveted together). There are some differences due to metal plates added over the years to cover the machine gun holes (2nd World War) that have weakened the structure. The bridge has a substantial symmetry along the longitudinal and transverse direction with ten repetitive modules of 3.36m.

Figure 4.48 Views of the bridge during measurement operations and from below.

Measurements took place on the bridge in June 2011. Four different configurations (Figure 4.49) of sensors were installed in order to get the vibrations of the reticular trusses in both lower and higher parts. The number of gaining points used, is conditioned by the spatial resolution needed to characterize appropriately the shape of the most relevant modes of vibration (according to preliminary finite element model). The ambient accelerations time series were recorded for nearly 11 minutes with sampling frequency of 100 Hz (interval of 0,01s). For the spectral analysis a number of 2048 frequency lines was considered sufficient for the correct definition of the signal and overlapping windows of 66.67%.

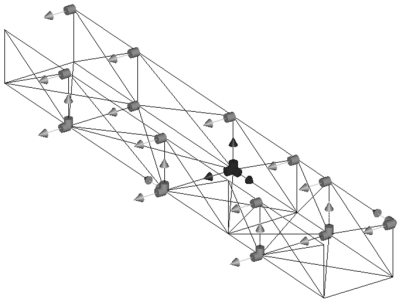

Figure 4.49 All setups with all connected channels.

4.4.1.2 Dynamic identification results

During the registration of the signal from the bridge, two cases of signals were distinguished: with train and without train passing. This is crucial for the modal analysis, since the presence of a convoy changes radically the masses of the structure and the dynamic response is different from what should be. Furthermore during a train route, the signal is highly amplified (Figure 4.50) causing distortion and other problems.

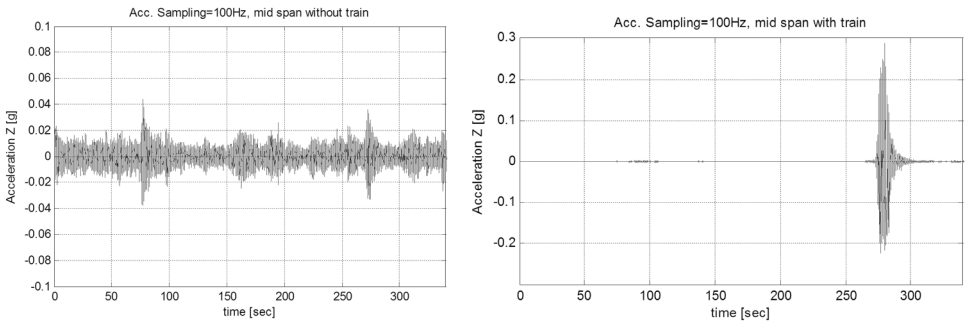

Figure 4.50 Acceleration signal without and with train presence.

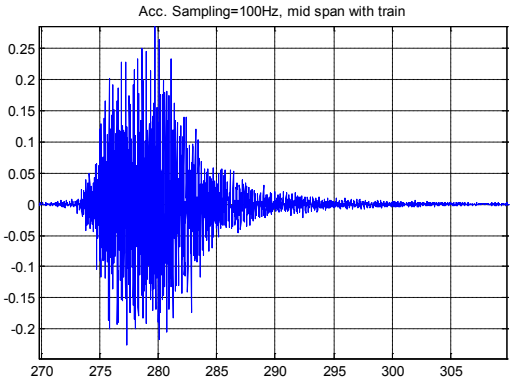

Figure 4.51 Zoomed view with train presence.

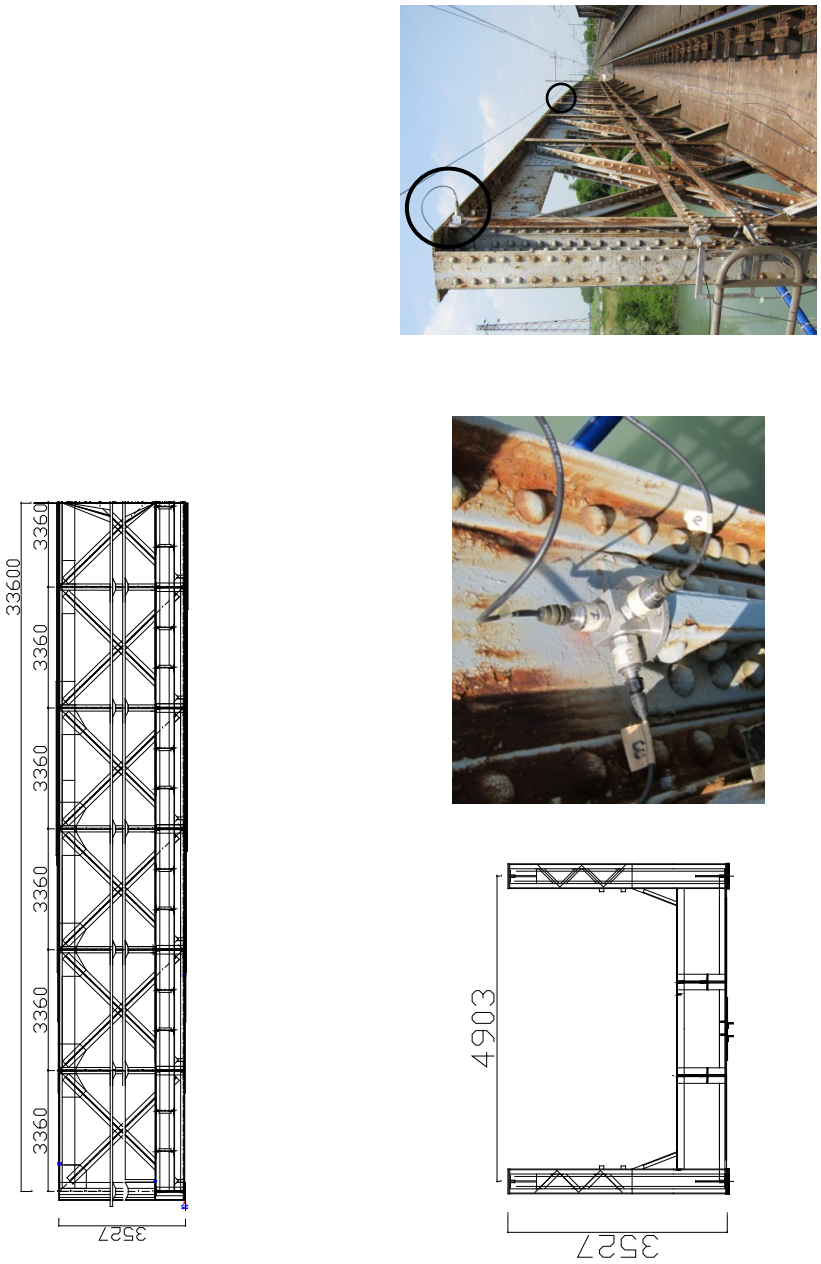

Figure 4.52 Prospect, cross section and instrumentation installation.

One can notice from Figure 4.50 and Figure 4.51 that there is an amplification of the signal during the train passage, and it is noteworthy to mention the free decay after the convoy has left the structure. The structure managed

to dissipate the vibrations in 15-20 seconds showing a nearly perfect damping graph similar to theoretical results.

The FDD analysis implemented in Matlab® gave also a well-defined graph that is presented in Figure 4.53.

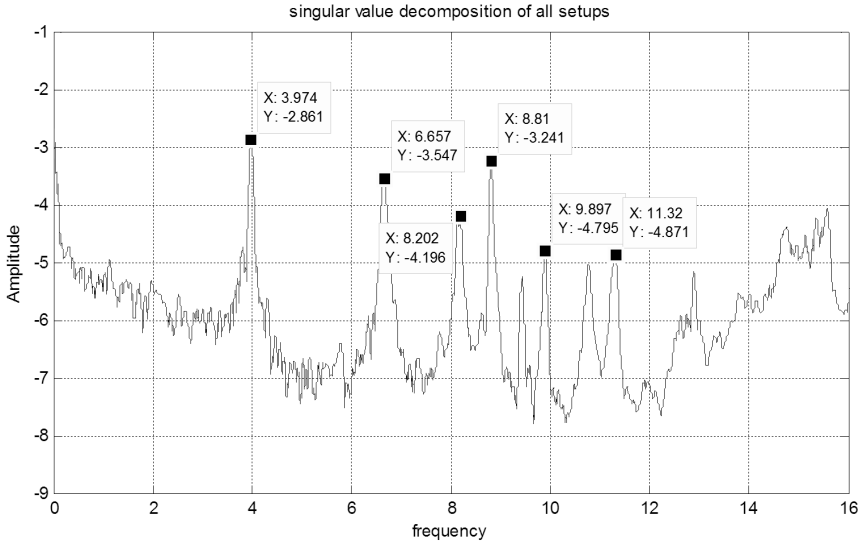

Figure 4.53 Average SVD for all signals.

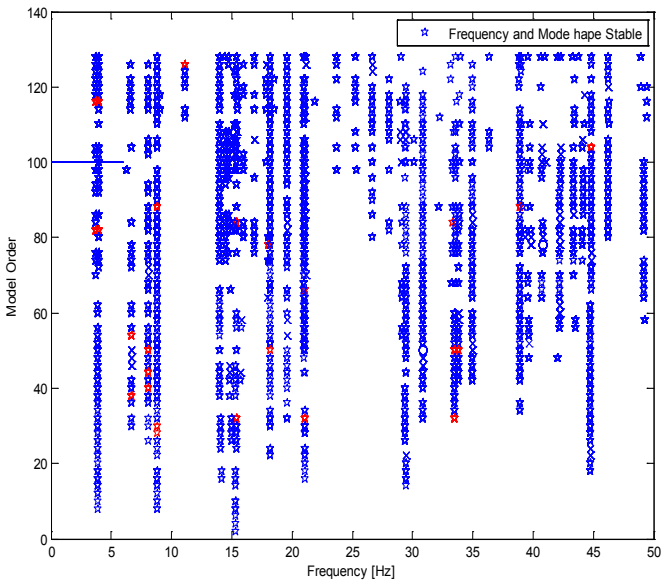

Figure 4.54 Stabilization diagram (ECCA) obtained from Fosso bridge.

Other techniques of modal analysis have been used to assess the dynamic behavior: data driven SSI, reference driven SSI and the ECCA. A total of

15 structural modes were found but only six of them are enlisted in Table 4.9.

Table 4.9 Comparison between more Modal Techniques

Mode	*FDD*	*SSI-data*	*SSI-ref*	*ECCA*
	f [Hz]	*f [Hz]*	*f [Hz]*	*f [Hz]*
1	3.974	3.935	3.960	3.979
2	6.657	6.648	6.661	3.884
3	8.202	8.356	8.061	8.210
4	8.813	8.914	8.766	8.820
5	9.424	-	-	9.452
6	9.897	9.885	10.063	9.892

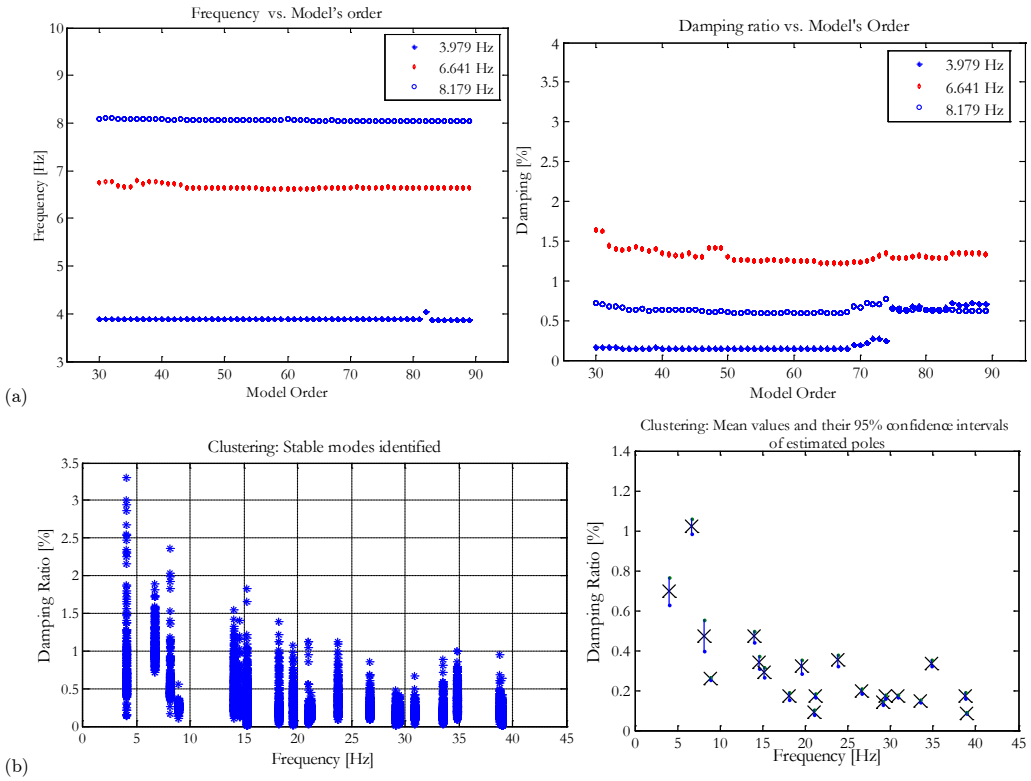

Figure 4.55 (a)Frequency and Damping ratio vs. model's order and (b) cluster analysis results.

At this point, the first three natural frequencies were separated from the whole results, and were analyzed in relation to the change of the model's order; and for the respective damping ratio values has been done the same thing as well. In both cases, it can be observed (Figure 4.55-a) that the values are impressively stable and in particular the damping values remain constant without having many shifts as usually seen for other structures. In Figure 4.55-b the results of a cluster analysis applied to the Fosso Bridge

response are represented. It can be observed how the accuracy is quite high especially for the damping ratio.

4.4.1.3 Sensitivity analysis on the FE model.

Because of the complexity of the sections, during the model construction, all the critical sections have been created through made-up *beam* sections. Different models with progressively higher levels of detail, going to outline bracing, parapets and the rails have been created. In order to increase the rigidity of the model the gusset plates have also been modeled as *shell* elements. Non-structural masses have been added in order to represent the large amount of rivets and bracing elements. During the analysis, it was observed that the values of the frequencies were grossly affected by the masses inserted; for this reason a precise calculation was done to consider all non-modeled masses. After this clustering analysis with the change in mass and elasticity module, a highly accurate FE model was attained (Figure 4.56) through 'trial-error' method calibration.

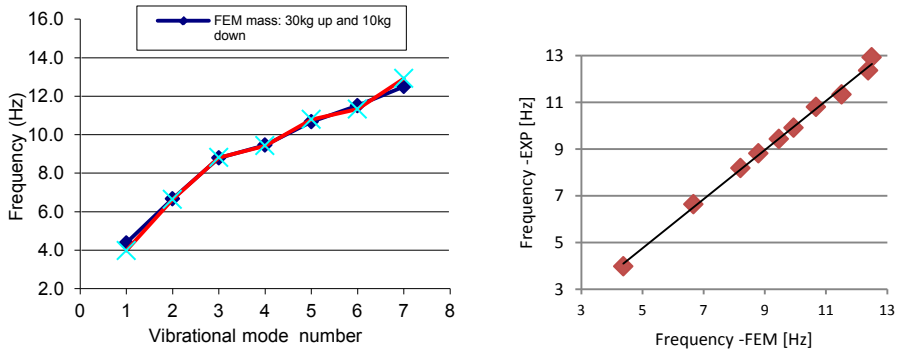

Figure 4.56 Frequency comparison between Exp. and FE data.

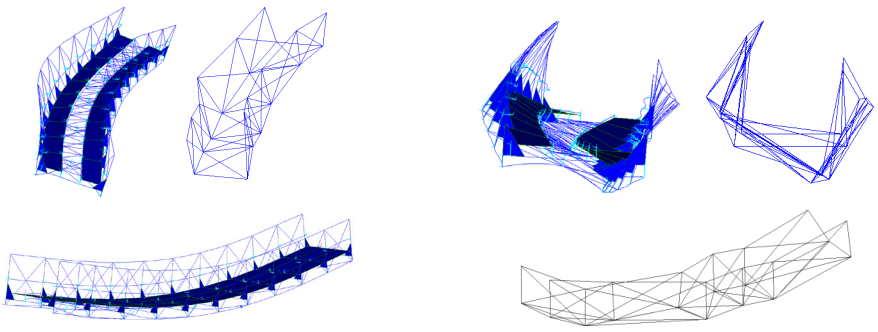

Figure 4.57 1st , 2nd and 3rd mode shape: FE and Exp. model.

In Figure 4.56 one can observe the perfect correlation that exists between the analytical and the experimental model. In fact, the disposition of the values in the graph is akin to a linear dependence, moreover disposed at 45°. It is useless to say that the MAC values in this case are very close to unity (0.9614, 0.9643, 0.9645, 0.8368 for the first 4 mode shapes). Therefore, having satisfied this condition for the main modes of vibration, the model can be assumed as well calibrated and can be used as an analytical tool (fatigue tests).

4.4.2 Musile Bridge

4.4.2.1 Dynamic tests on the reticular bridge

The Musile reticular steel bridge is very similar to the previous structure, but with 3 spans of over 50m each overpassing the Musile river. The bridge is composed by double separate reticular structures equipped with diagonal rods and vertical supports that connect the two lower and upper currents, all resting on masonry pears and abutments. The measurement campaigns have been carried out in September 2012, before the bridge (constructed in 1920) has been disposed of and replaced in October 2012 for its uncertain durability. It was interesting to analyze the second of this kind of bridges, that revealed similar behaviors. The steel structure, as it will be seen, enhances the modal characteristics in the sense that the peak modal analysis are well marked, and this results in an easier identification of structural peaks.

Figure 4.58 View of Musile bridge and sensor installation on it.

Some of the preliminary results are summarized in the following figures. The first responses of train passages are presented in Figure 4.59, where 12 sensors recorded a signal of 1300 seconds long. Performing an average RMS

over every 100 samples (1 sec), the continuous RMS was constructed. It shows the courses of two trains in the studied deck (high peaks) and other trains on the opposite direction deck. Then the signals were subdivided in five segments and their RMS is showed in the same figure, displaying high values for the fourth segment due to high speed train passage. It is noteworthy to mention the influence of the load excitation to identified frequencies presented in Figure 4.63. Although only a small amount of data is available, it seems that frequency values are lower when the level of excitation is higher.

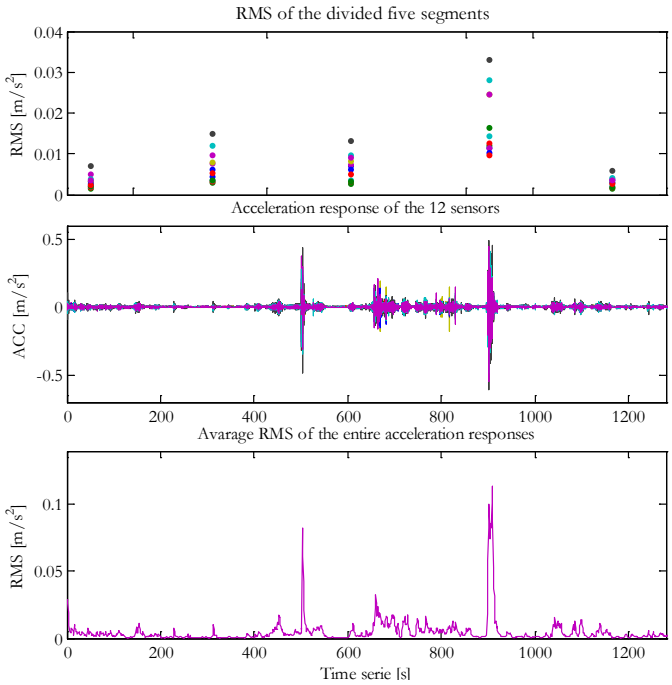

Figure 4.59 Average RMS for the five segments, long time series and their RMS.

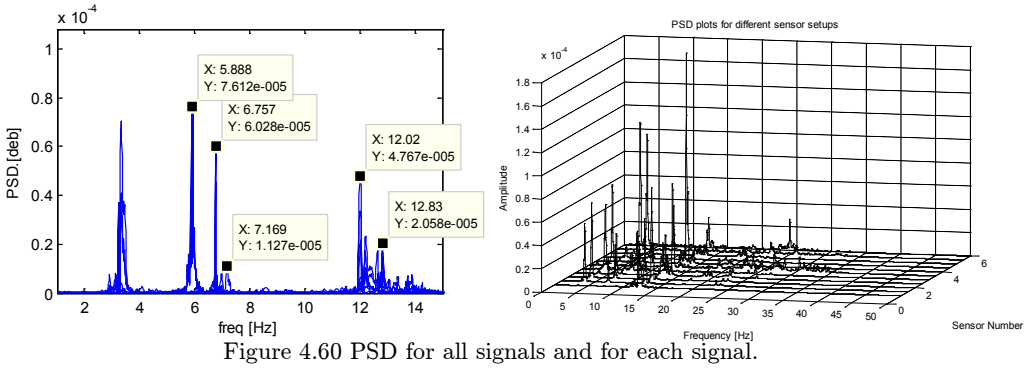

Figure 4.60 PSD for all signals and for each signal.

4.4.2.2 System identification and model calibration

The acquisition campaign is quite similar to the Fosso Bridge, but here a new acquisition data board was applied in order to reduce the number of setups. Two setups with thirteen accelerometers each made possible to acquire sufficient data on the studied span. As it can be seen on Figure 4.60, the simple PSD of each signal reveals quite accurate results, even though other standard modal analysis were performed.

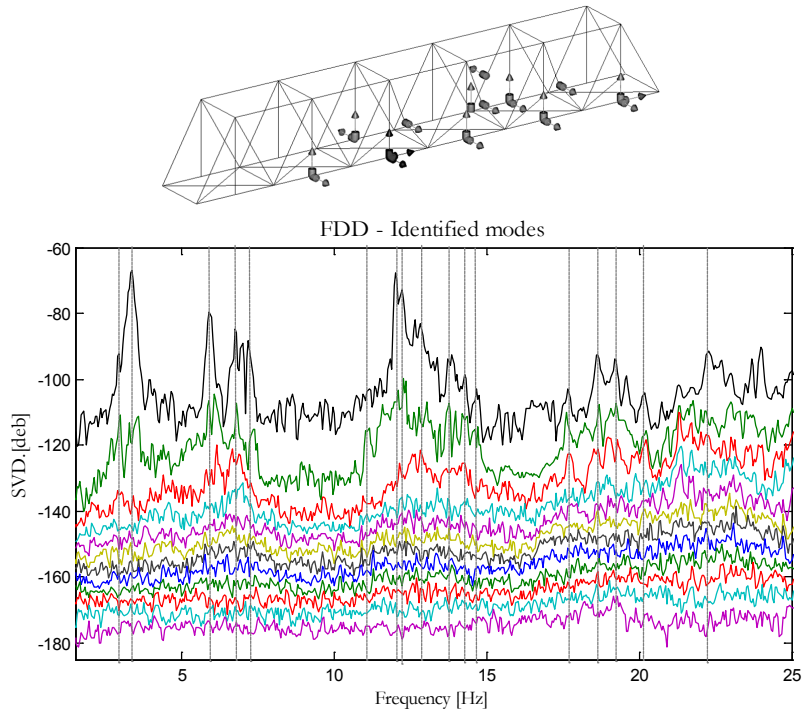

Figure 4.61 Sensor deployment and identified modes with the FDD technique.

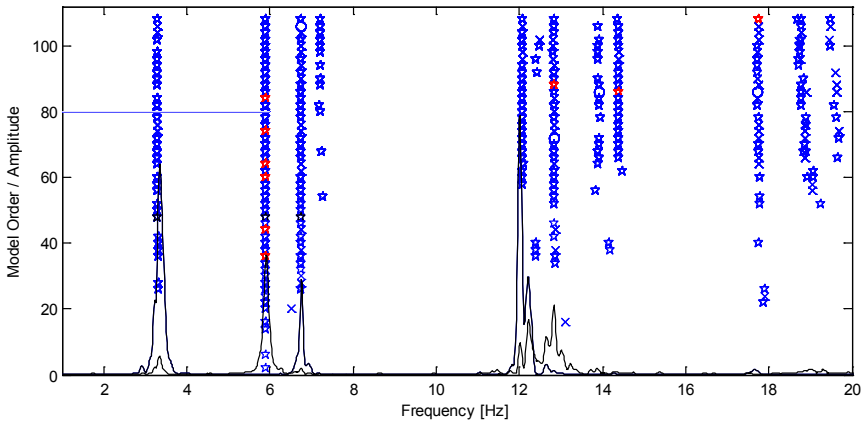

Figure 4.62 PSD peaks and stabilization diagram with SSI for the Musile Bridge.

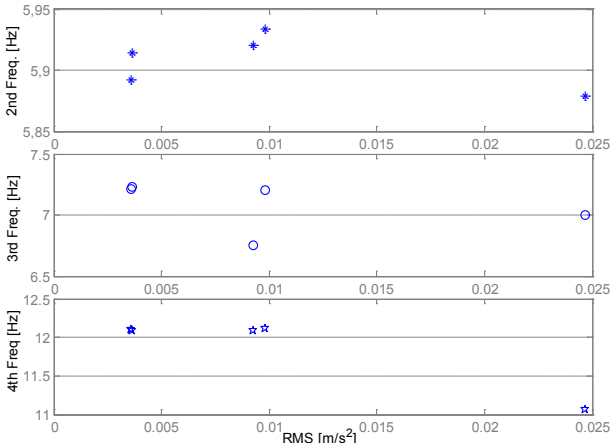

Figure 4.63 Frequency vs. excitation level through the five data series.

EFDD (Figure 4.61) and SSI (Figure 4.62) analysis have been executed for the Musile Bridge, revealing accurate results in structural mode identification. Over 20 modes were estimated ranging from 2-25Hz

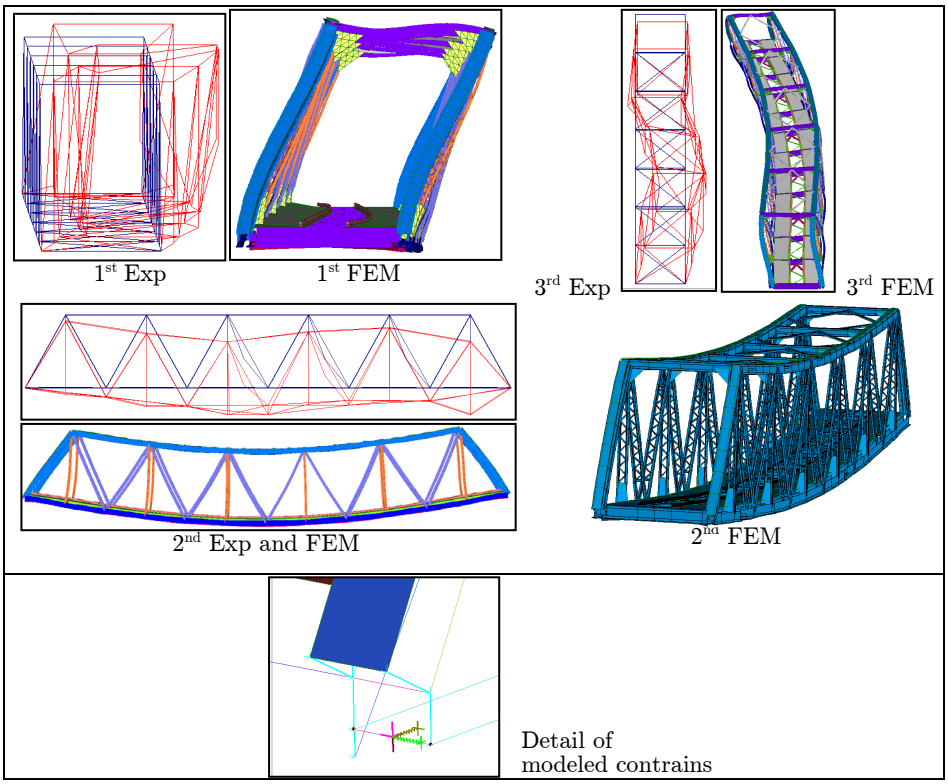

Figure 4.64 1st, 2nd and 3rd mode shape: FE and Exp. model.

During the FE model updating procedure, three phases were included: (a) elastic modulus variation, (b) non-structural masses estimation and (c) constrains modification. Especially

for the last requirement a detailed analysis was carried out: ideal fixed constrains were not suitable, so adequate translational stiffness were associated to the free supports in the longitudinal direction and rotational stiffness around Z axis; instead, to the hinges, only rotational stiffness around Z axis have been associated. The constraints listed above were also connected to the structure by a rigid beam.

The final result is a high correlation between FE model and experimental model as presented in Figure 4.64 and in Table 4.10.

Table 4.10 Comparison between FEM and Modal model

FEM modes	FEM. Freq.	Exp. modes	Exp. Freq.	MAC.
1	2,498	**1**	2,872	0,84
3	5,86	**4**	5,872	0,80
4	6,439	**5**	6,785	0,85
5	8,794	**6**	7,239	0,82
6	10,03	**7**	11,02	0,82
7	10,15	**8**	11,81	0,73
8	10,21	**9**	11,94	0,75

4.4.3 Mincio Bridge: fatigue deterioration

4.4.3.1 Operational Modal Analysis with four techniques.

The Bridge on Mincio River is situated in Peschiera del Garda on the A4 Milan-Venice highway. The three-span bridge consists of two steel box continuous girders, side by side disposed, resting on concrete abutments and piers. The lateral spans are 41m long and the central one is 70m long (152m total length). The overall width is 15.55m. The cross-section of the bridge has constant height, equal to approximately 3.30 m, and is constituted by a monocellular trapezoidal box having the lower flange of a width of 5m and the upper flange of 7m plus the wings of 2.5m each. The orthotropic plate (Fe 510 steel) permits to put the pavement directly on it, without any concrete slab. The plates constituting the thin walls of the cross section are stiffened longitudinally by "V" shape bracing, welded continuously to the plates. The principal reason of analyzing this structure was the deterioration of member welds due to fatigue. In fact, under the passage of the highway traffic, the ribs reinforcing the upper orthotropic deck have begun to detach. The first step was to install a strain monitoring system that was able to observe the micro-deformation taking place due to fatigue. After that, a dynamic identification was performed in order to update the model expected to reproduce the damage verified. A challenging step is that of using the strain-gage data to obtain dynamic results and compare them with the standard identification by

accelerometers. This argument will be studied in more detail in the next paragraphs.

Figure 4.65 Views of the Mincio steel box girder bridge.

During its lifetime, the considered structure has been monitored and studied with almost all kinds of measurement techniques (Figure 4.66). Only 10 years after the construction it has been subject to a novel monitoring technique at the time, i.e. fiber optic (FBG) for strain measurement. Warning results were collected. The structure begun to deteriorate and soon cracks appeared on the ribs due to fatigue. Dynamic test campaigns with accelerometers were performed in December 2011; FE models were calibrated in order to assess the damage due to fatigue. Afterwards, a welding intervention took place during January-March 2012. In order to control the behavior of this latter intervention a strain monitoring system was installed in April 2012. During this long term monitoring, not only strain and stress analysis were executed, but also the global dynamic behavior of the bridge was monitored. The results of the dynamic tests and monitoring campaigns with strain data are detailed in the next paragraphs. After the low efficiency of the local welding campaign executed previously, a major retrofitting intervention will be applied in a near future in order to bring the structure in a safe condition.

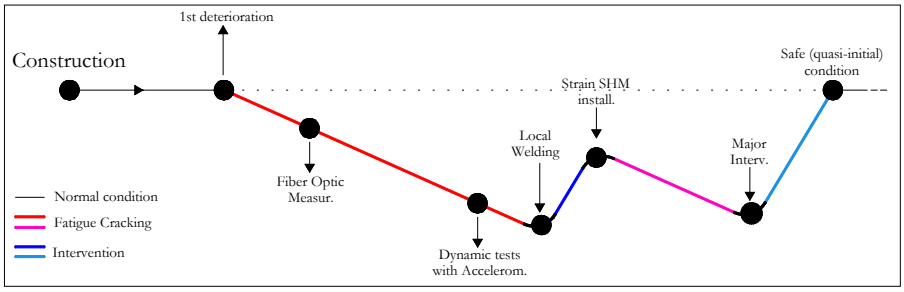

Figure 4.66 Lifecycle structural condition of Mincio Bridge.

Operational Modal Analysis has been performed on December 2011 with piezoelectric acceleration sensors disposed with only three setups inside the box girder. The symmetry of the structure allowed to reduce as much as possible the measurement points. The cross section of the modal model has been schematized with a triangular section, based on the location of the sensors. They are positioned laterally in the upper transverse, while centrally at the base of the caisson.

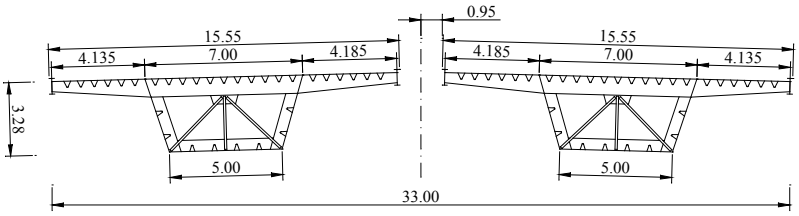

Figure 4.67 Cross-section of the steel box girder decks.

Besides the FDD, the SSI and the Polyreference Least Square Complex Frequency identification (PLSCF), the newly developed method of the ECCA (Figure 4.69), has been used in order to validate it with this kind of structures. Before conducting a parametric analysis on the number of the model order and blocks number, with which the matrix will be divided for the past and future analysis, the ECCA method was applied related to a specific model order. In determining the order of the system with the ECCA technique, the singular value distribution is plotted in Figure 4.69. According to the gap present in the singular value plot, a model order of 16 (from the SVD during the SSI method an order of 14 was determined) can be chosen and continue the valuation of the modal parameters.

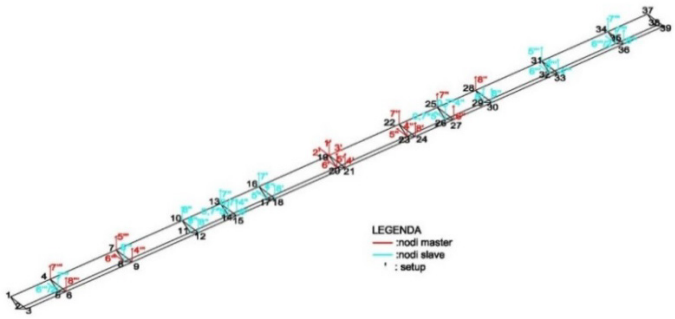

Figure 4.68 Scheme of the sensor distribution on the bridge.

The stabilization diagram permits to identify the modes whose properties do not change significantly when varying the model order. Modes classified as “stable” are considered as structural modes. As expected for steel bridges, the definition of structural modes in this particular case is clearly

given by the stabilization diagram with the ECCA (Figure 4.70). Observing Table 4.11, where a detailed comparison between the techniques used is presented, one can notice that the Enhanced CCA can identify two hidden structural modes that the other methods did not discover. This is also confirmed by the stabilization diagram below.

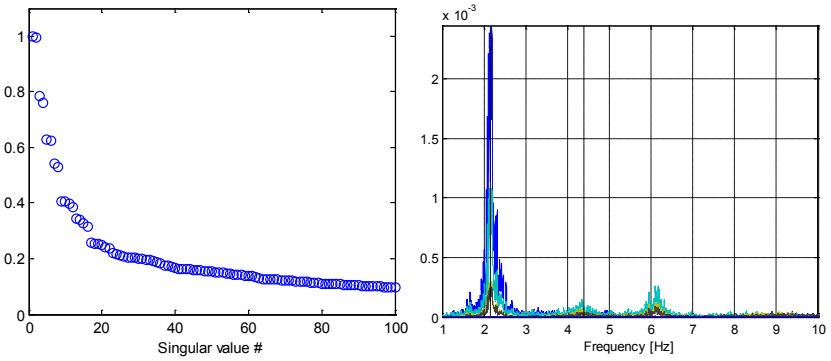

Figure 4.69 Normalized singular values and linear PSD on the Mincio bridge.

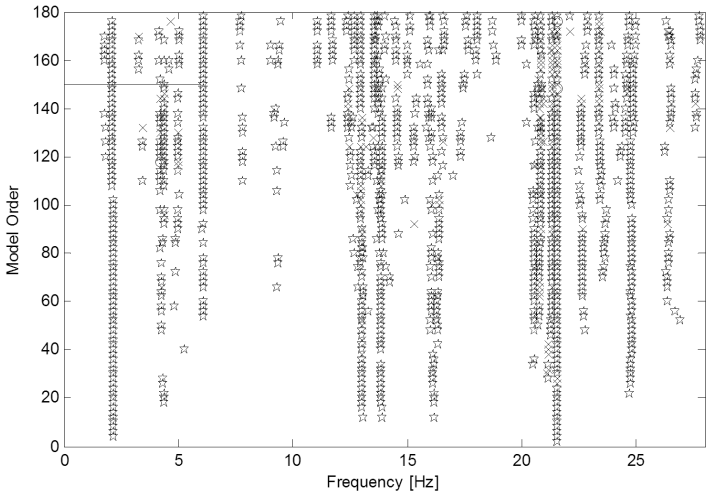

Figure 4.70 Structural modes identified with the ECCA method.

Table 4.11 Comparison between four modal techniques.

Mode	*FDD*	*SSI*	*PLSCF*	*ECCA*
	f [Hz]	*f [Hz]*	*f [Hz]*	*f [Hz]*
1	2,164	2,168	2,167	2.162
2	4,339	4,492	4,247	4.240
3	5,525	-	-	5.009
4	6,585	6,365	6,356	6.171
5	9,496	9,578	9,489	9.489
6	-	-	-	12.630
7	13,08	13,041	13,067	13.040
8	-	-	-	13.480
9	13,73	13,782	13,803	13.910

As mentioned above in this paragraph, a detailed FE model was intended to calibrate in order to use it as a damage assessment scenario. A large amount of b*eam* and *plate* elements were used to model the structure, and the calibrated result by 'error and trial' method is shown in Figure 4.72.

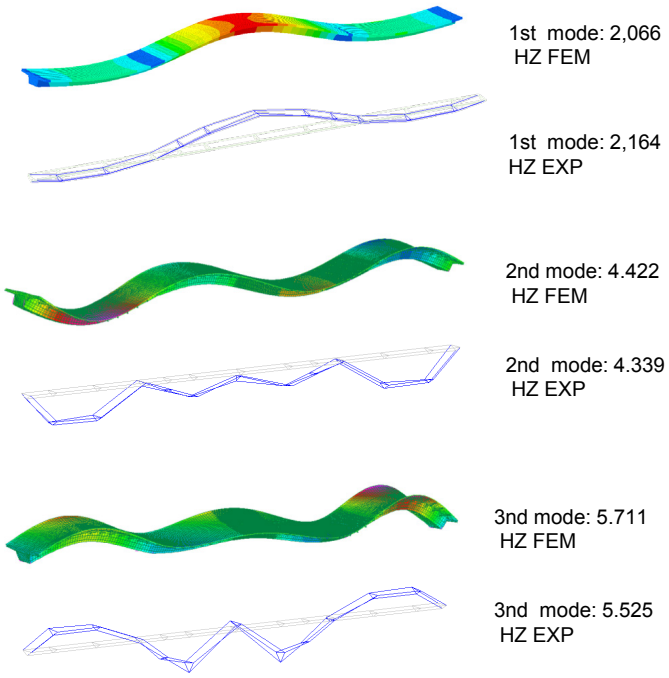

Figure 4.71 Mode shape comparison between updated FEM and OM model.

4.4.3.2 Experimental Modal Analysis

As we all know, the difference between the OMA and the Experimental modal analysis [37] [38] [39] [40] is that in the first case we record measurements of only the response of the structure due to ambient excitation, whereas in the second case there is an external known excitation that we apply to the structure and measure both input and output data. Being economically more convenient, OMA is nowadays used at almost every modal application, but in some cases where the structures are flexible and susceptible to even light excitations, the EMA can also be used. In fact, in the Mincio Bridge a heavy Impact Hammer has been used to hit the steel structure in order to measure its excitation together with the acceleration sensors installed. Figure 4.72 refers to the results collected after the impact on the main plate at the basis of the steel box.

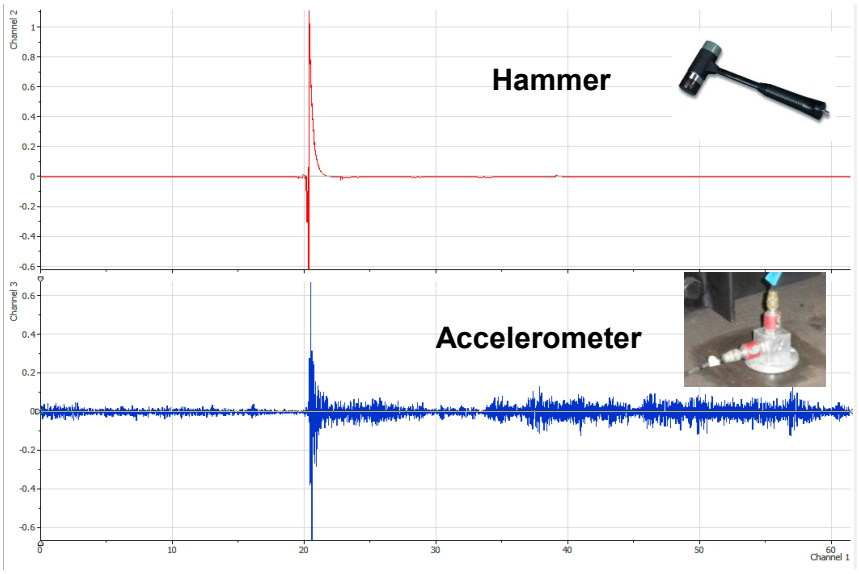

Figure 4.72 Recorded signals for the Impact Hammer and one accelerometer.

The acceleration applied by the Hammer overpasses 1 m/s^2 and the registered acceleration by the sensors goes until 0.5 m/s^2. Theory tells us that with these two signals the Frequency Response Function can be constructed in order to get the dynamic behavior of the system. The FRF is represented in Figure 4.73, where the first two natural frequencies can be identified. The excitation on the structure was an impulse that lasted for a very short time, so the measured time series are very short. This is the reason why we don't see a clear FRF graph where all the peaks can easily be identified. However it has once again been shown that different modal techniques can provide the real dynamic performance of the system under unknown or known external excitation with good accuracy.

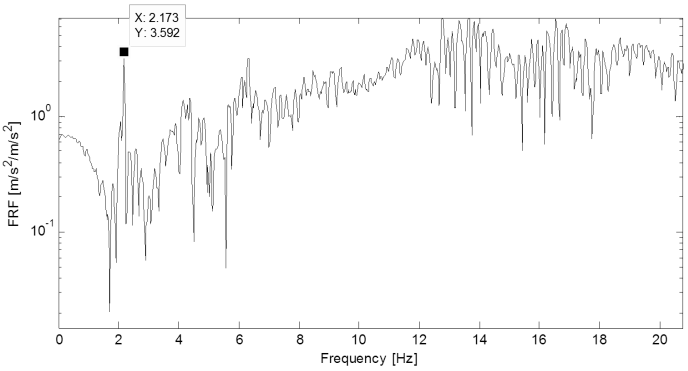

Figure 4.73 FRF for the Mincio bridge under hammer impact.

4.4.3.3 Modal Analysis with strain gauge sensors

The next challenging step in this study is to use the strain data [41] [42], sampled at high frequencies, to extract the dynamic behavior of the structure. Let's suppose the data are equivalent of acceleration or velocity and perform the usual modal analysis to identify the principal vibrational modes. On the bridge a large number of strain gauges (56) has been installed, so choosing the proper ones it is possible to get real pseudo-vibrations from the monitoring system. The disposition of the sensors has been decided in order to observe the structural behavior of the bridge in its critical points. For simplicity, it was chosen to place the sensors only in the East girder, in five sections (A, B, C, D, E). In particular sections B and D corresponds to the position of the piers whereas section C is disposed in correspondence to the middle point of the main central span. For each section were placed a number of sensors from a minimum of nine to a maximum of thirteen strain gauges, arranged both inside and outside of the steel box of the deck, in the longitudinal and transversal directions. Multicore cables of 0.5 mm^2 section connecting the strain gauges with the system have been chosen in such a way that, for longer cables (about 90 m) the measured strain to the strain gauges was not appreciably affected from the resistance growth of the electrical system (this increase is still limited to maximum about 5Ω, measured in the laboratory). A preliminary study has been performed looking only at sensors number 6 which are disposed on the lower flange of the caisson, at five locations along the bridge (Figure 4.74). The data resulting from each sensor was normalized relatively to the maximum value of strain detected by each sensor. As we know, strain measurements are characterized not only by low frequency signal features but also by high frequency samples. Thus, each channel has been subjected to a Bessel High-pass Filter of 1 Hz, for eliminating the oscillations of the signal. At the end a de-trend and phase correction has been applied in order to resemble the signal (Figure 4.75).

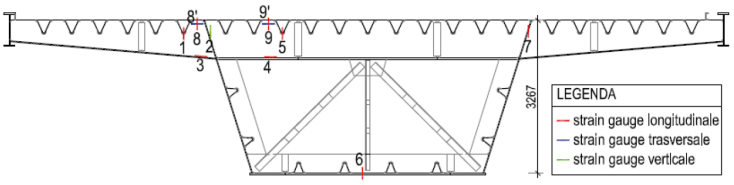

continues

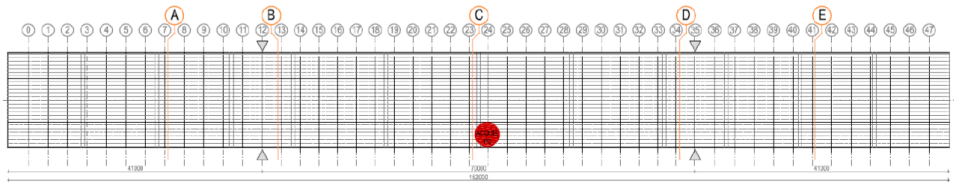

Figure 4.74 Strain gauges disposition on the cross section and along the bridge.

The SVD represented in Figure 4.76, displays the identified modes resulted from strain measurements and its correspondent with acceleration data. One can notice that frequencies able to identify with the strain gauges are 2.14Hz, 4.25Hz 5.52Hz, 6.04Hz, 6.58 Hz, 9.50Hz, 13.08Hz, ecc., very similar to results obtained with accelerations. A more detailed comparison can be made with the following stabilization diagram (Figure 4.77). It is noted that comparing diagrams: Figure 4.70 and Figure 4.77 are very similar and structural modes correspond in the two cases. So we can say that modes 2.12Hz, 4.25Hz, 4.85Hz, 6.07Hz, 8.86Hz, 11.63Hz, 13.43Hz, 15.89 Hz, 17.04Hz, 20.7Hz and 21.91Hz were successfully identified through the analysis of strains.

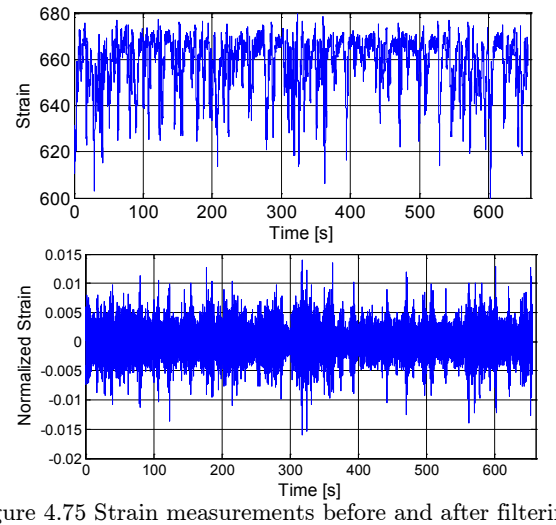

Figure 4.75 Strain measurements before and after filtering.

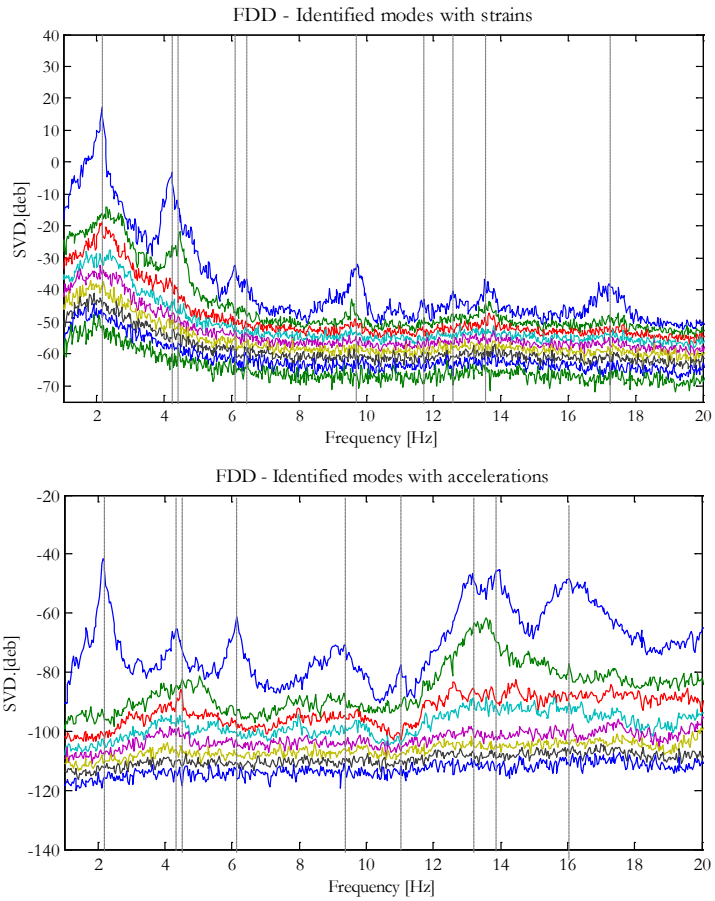

Figure 4.76 FDD results from strain and acceleration measurements.

In the second case of strains, other signs of non-structural modes are present, but through a cluster analysis, only structural modes can be highlighted. Ten principal structural modes were identified and compared with the conventional analysis of acceleration data. Since a high correlation is found, these types of cheap sensors can probably be applied in order to estimate the global dynamic behavior of such bridges, together with the local strain monitoring. In fact, such analysis has led to the development of an algorithm that automatically calculates the main vibration frequencies, via strain measurements, through the FDD method. This automated FDD procedure is described in Section 3.4, where the associated singular vectors at each frequency are estimated. The extraction of the modal parameters for monitoring purposes, is assessed by automated peak-picking procedure and evaluation of the mode shapes at every peak frequency. After the comparison of every frequency line, through MAC value, with the peak

frequency, the monitoring development of each mode is generated (Figure 4.78).

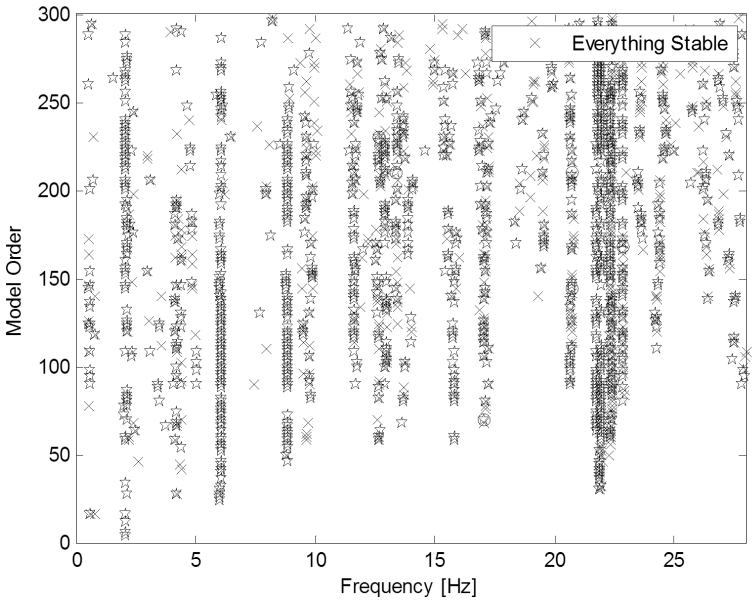

Figure 4.77 Stabilization diagram from strain measurements on the bridge.

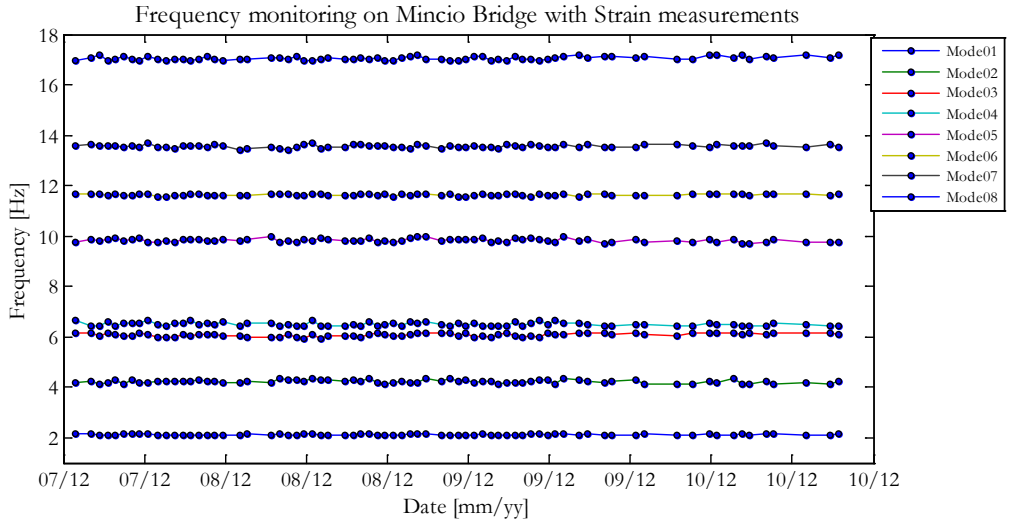

Figure 4.78 Frequency monitoring through Automated FDD Strain measurements.

As can be seen from the SHM with this cheap technique, powerful results are obtained. In this case the global behavior of the structure is quite stable and shows slight fluctuations due to temperature.

A detailed development of the first natural frequencies extracted by Automated FDD and manually by Artemis software is displayed in Figure

4.79. The automated procedure seems to be very effective as it clearly follows the manual identification technique.

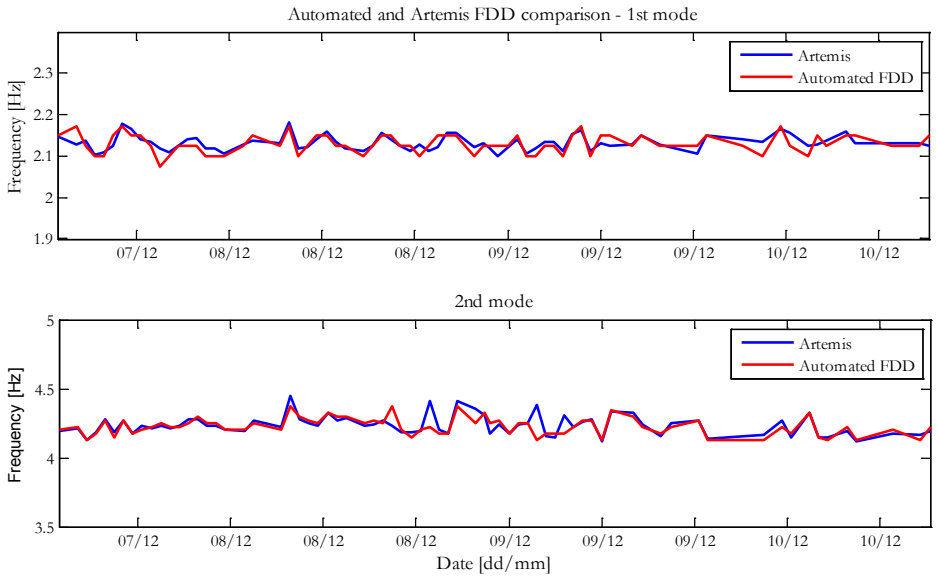

Figure 4.79 Comparison between modes extracted by Automated FDD and manually by Artemis software.

4.5 Concrete beam bridges

4.5.1 Monitoring the highly damaged "People's New Bridge"

4.5.1.1 Structural identification of the damaged structure

The bridge is located in the city center of Verona and is characterized by three spans having a total length of over 90m. The structure holds a four-lane roadway, two for each direction of travel, plus two sidewalks for a total width of 14.32 m (see Figure 4.80). The static schema consists of seven main girders and eleven cross beams in the transverse direction with stiffening function. The 7 girders and the thin slab (18 cm), due to bad maintenance since constructed in 1946, revealed severe damage in the middle of the spans due to water percolation. Girders' and cross beams' concrete (Figure 4.81) is highly deteriorated, moldy and carbonated. Before deciding to retrofit it, the Municipality required to evaluate the life of the bridge. It was subject to investigations, like an ambient modal test to detect the principal modal parameters and in each structural element lots of destructive and non-destructive tests were executed.

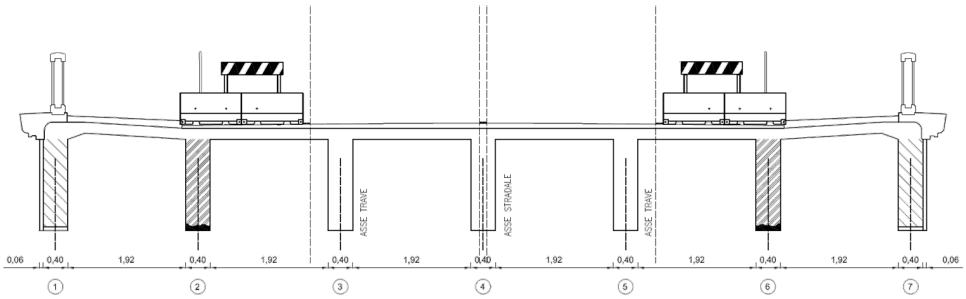

Figure 4.80 Section of the People's New bridge and the main beams damaged.

The vibration acquisition campaigns were carried out in two days, on May 10 and 11, 2011. The flow of vehicles over the bridge was normally allowed [26] in a single direction of travel, in a two-lane carriageway. The owner has required the sensors not to be placed on the stone or marble elements, so the accelerometers has been placed on the roadway where the thickness of the pavement was very small (in spite of that very good results were obtained). Eleven setup measurements were installed with 8 DOFs each (total 88 DOFs) allowing a high resolution areal coverage (Figure 4.82). It can be seen that the two plots in Figure 4.83 (FDD and SSI method) present very similar features and comparable natural frequency values. For both methods, identified modes and damping ratios are listed in Table 4.12.

Figure 4.81 View of the People's New Bridge and the damaged elements.

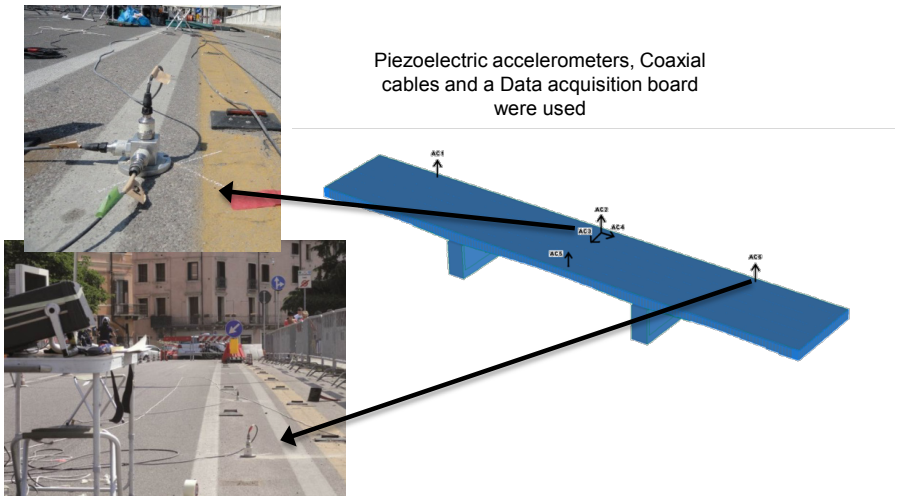

Figure 4.82 Monitoring sensor installation after the eleven configurations.

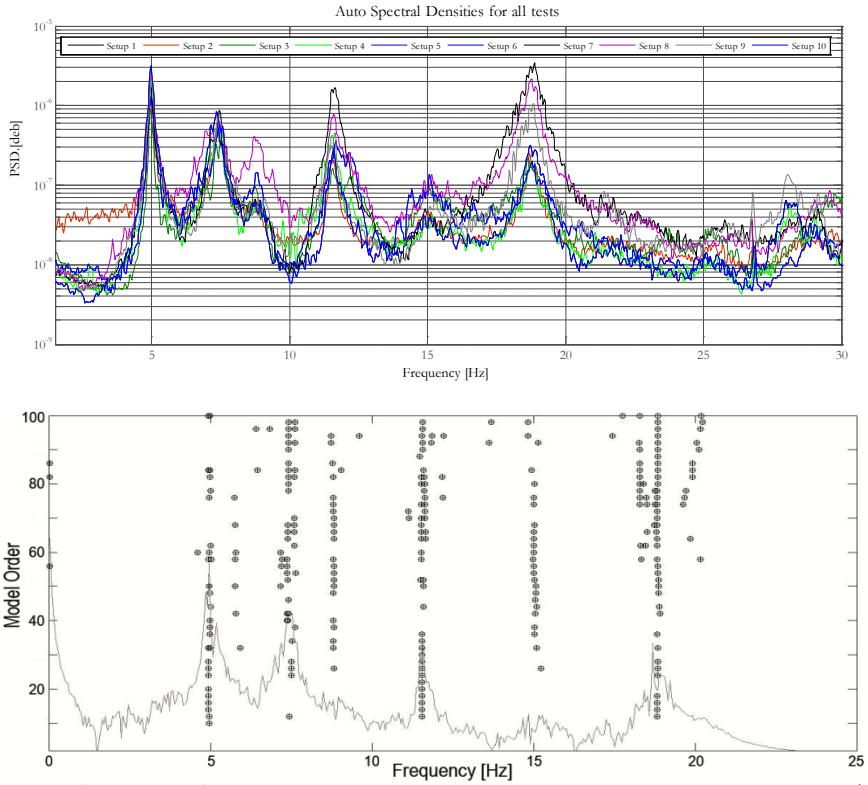

Figure 4.83 Average of Auto Spectral Densities for all tests and stabilization diagram (SSI).

Table 4.12 Comparison between modal techniques and FEM.

Mode	*FDD*	*SSI*	*FEM*
	f [Hz]	*f [Hz]*	*f [Hz]*
1	4.980	4.985	4.958
2	6.250	-	5.654
3	6.738	6.702	5.895
4	7.422	7.337	6.605
5	8.691	8.691	7.510
6	8.960	-	7.510
7	-	10.466	10.89
8	11.600	12.308	12.91
9	15.060	14.384	13.87

4.5.1.2 Sensitivity analysis and FEM calibration

A preliminary analysis revealed that the 3D F.E. model initially was underestimating the real deformations and the actual stiffness of the bridge. Therefore the influence of a possible change in the system constraint modeling was evaluated by a sensitivity analysis on the elements and the restraints. Originally, all translational and rotational DOF were free except vertical translation at the supports. This configuration has been changed, and the percentage error between FEM and experimental frequencies, depending on the type of constraints, have been plotted (Figure 4.84).

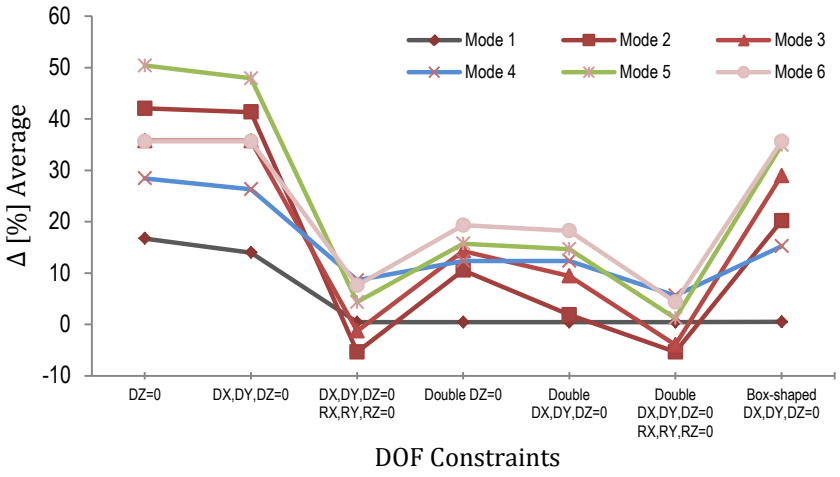

Figure 4.84 Sensitivity analysis: % error between FE and Experimental frequencies, depending on the type of DOF Constraint.

The comparison in terms of frequencies between results of different DOF shows how the real behavior of the constraints is much more similar to a rigid joint (due to deterioration and not scheduled maintenance since 1946), although the project tables provide a simple support.

Consequently, the FE model has been updated by fixing horizontal translations at the connections, since translating possibilities no longer exists, letting the rotations free. Figure 4.85 shows that the first mode is a vertical bending mode of the mid-span, second and third modes are bending modes of the lateral spans, while 4th, 5th and 6th are all torsional modes. It can easily be observed that these modes have the same form in both numerical and experimental results.

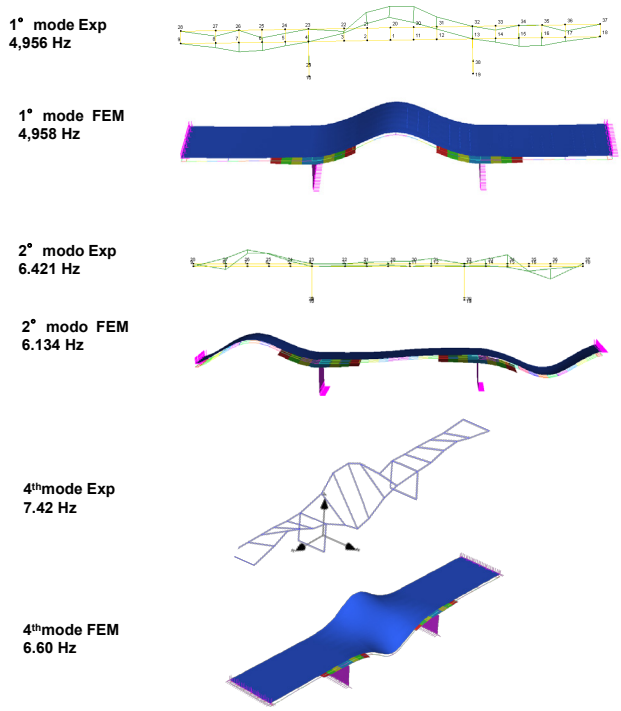

Figure 4.85 . Comparison between FEM and experimental identified mode shapes.

In order to study in more details the structural response of the most deteriorated elements some validations have been conducted under the Italian Codes (NTC 2008). In order to simulate the behavior of the degradation, it has been considered a reduced section of concrete. This vulnerability analysis revealed the deficiency of the elements and suggested the installation of a permanent monitoring system.

4.5.1.3 Structural Health Monitoring

A monitoring system has been installed in order to evaluate the general behavior of the structure for further damage detection and the local displacement at the damaged elements. Guided by the need to monitor only some essential parameters, a few sensors were installed (Figure 4.86).

The hardware include:

- PC all in one, 24", CPU atom 1.6 GHz, 160 Gb hard disk;
- 2 accelerometer modules NI 9234, 4 channels 24bit each, 51.2KS/s;
- master real-time embedded NI 9792, CPU 533MHz, 2GB disc, 256MB ram, VXWorks OS;
- 1 module NI 9215, 4 channels, 16bit, 100KS/s;

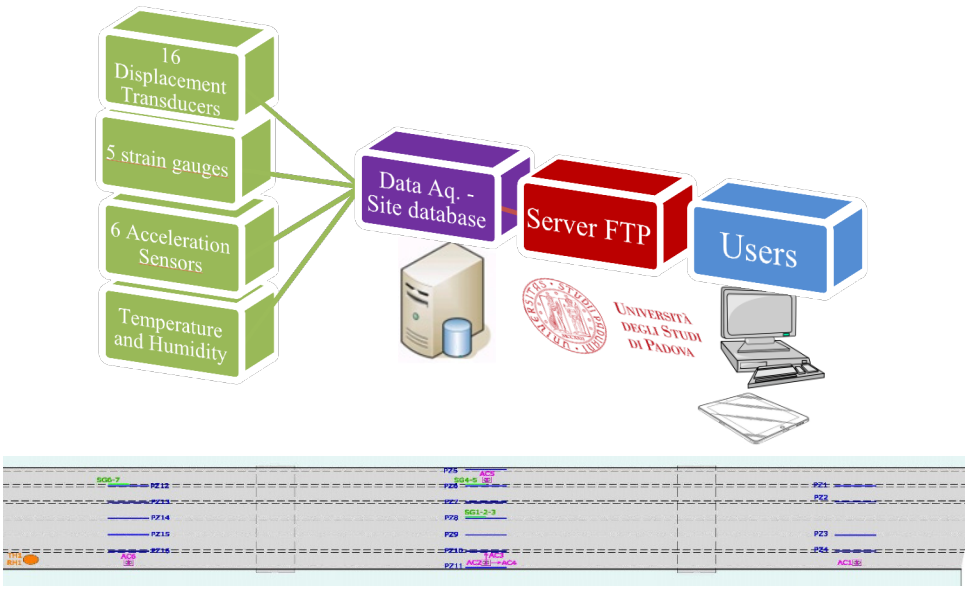

Figure 4.86 . SHM schematic representation.

Three automated modal identification algorithms has been implemented in order to continuously estimate the modal parameters during monitoring [43] [44]. During these eight months of data gathering the behavior of the structure stood stable from both dynamic and static point of view. In fact, the Modal Parameters did not show worrisome jumps due to possible further damage (Figure 4.87), but followed the trend of environmental parameters. In particular, during May – June 2012, several seismic events occurred at nearly 100km from the structure (Emilia Earthquakes). Some of these events were captured by the system, showing a slight change in the frequency values. During the first event, in reference to the PGA, the amplification factor of the accelerations on the bridge is about 11 (Figure 4.88). Another big seismic event was the one of the 3rd of June 2012, during which a modal analysis was performed. An increase in the frequency values between the two seismic events was found. Right after these events the structural modes became stable. No structural change due to ongoing damage was detected so far (Figure 4.87), as it will also be confirmed by the

regression models. In Figure 4.87 and Figure 4.89, the development of the identified modes by automated Cluster ECCA, SSI and FDD is presented.

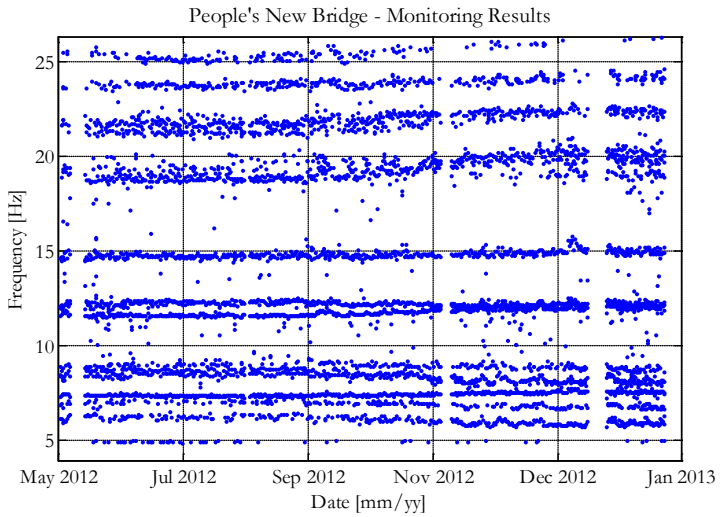

Figure 4.87 Natural Frequencies observed during the monitoring period.

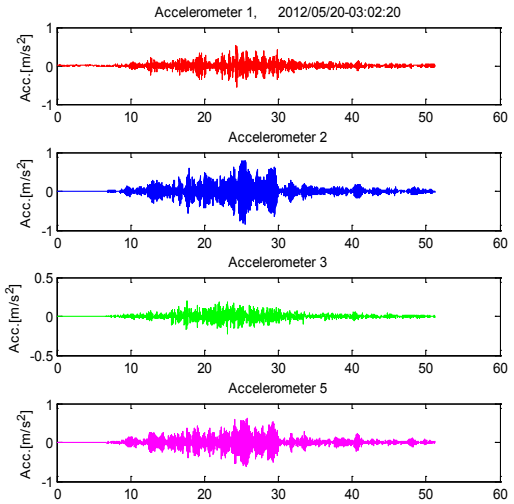

Figure 4.88 . Accelerations during the May 20th 2012 event on the bridge.

Besides the automated procedure, a repeated manual modal identification was performed by a commercial software for the purpose of comparing the obtained results. They ended up to be quite similar for all the techniques, revealing slight differences (Figure 4.89) in some modes, although equally being effected by temperature. The three automated procedures have been successfully validated for the response of this structure, and have also been used in the other case studies.

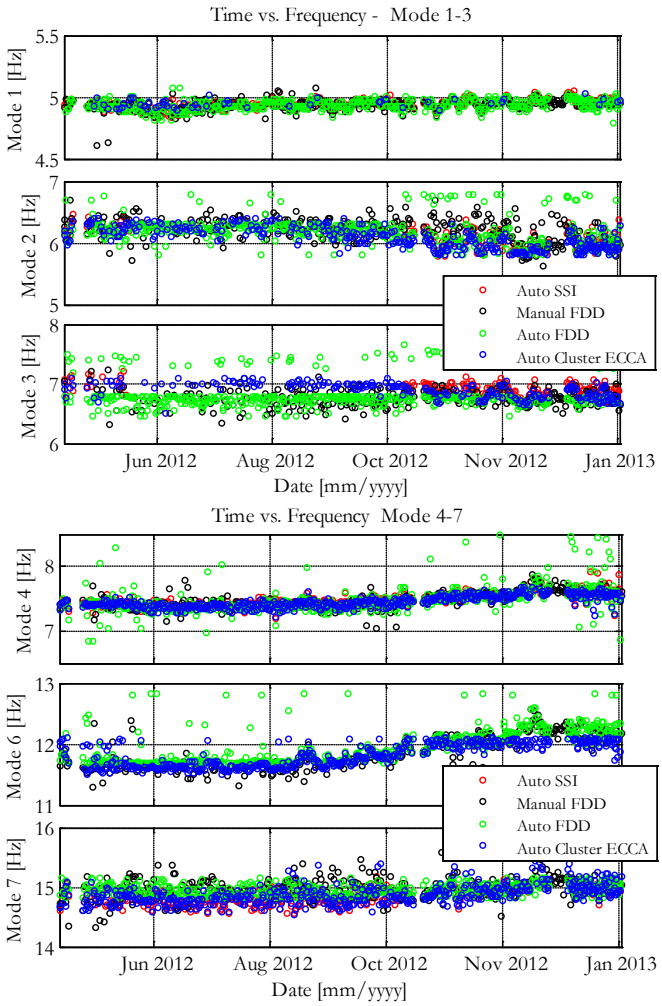

Figure 4.89 Comparison between the four methods implemented: Modes 1-7.

4.5.1.4 Loading effects on modal parameters

An important factor with relevant influence on the natural frequencies is the amplitude of bridge vibration, which is related to traffic intensity. The root mean square (RMS) of accelerations is showed in Figure 4.90 during one week of continuous recording. It is easily noticeable that during night hours limit traffic is present and vibrations on the bridge are lower than daily hours. The cycle is repeated every 24 hour and it is believed to affect the frequencies of the structure as characterized in Figure 4.91. In fact, the second and third modes are the modes that experience the highest daily effects. The influence of vibration amplitude are observed on the frequency plots, where there is a frequency increase, when the excitation level is low. With respect to this aspect, it should be stressed that a trend for a linear

relation between these two quantities exists and can be observed in Figure 4.91 (bottom).

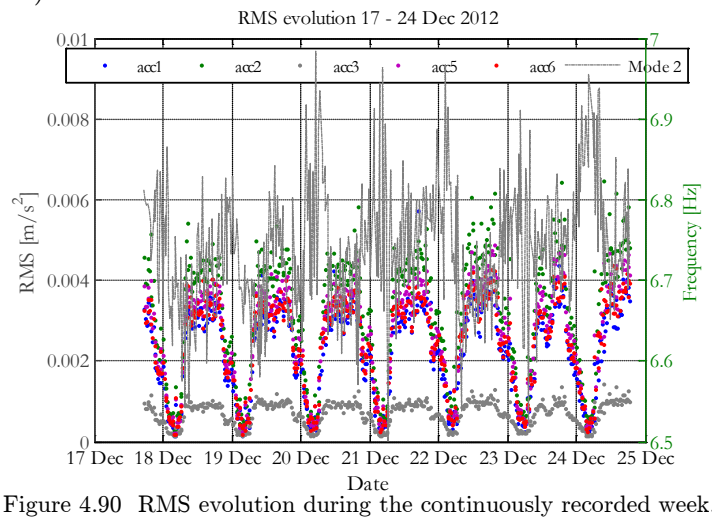

Figure 4.90 RMS evolution during the continuously recorded week.

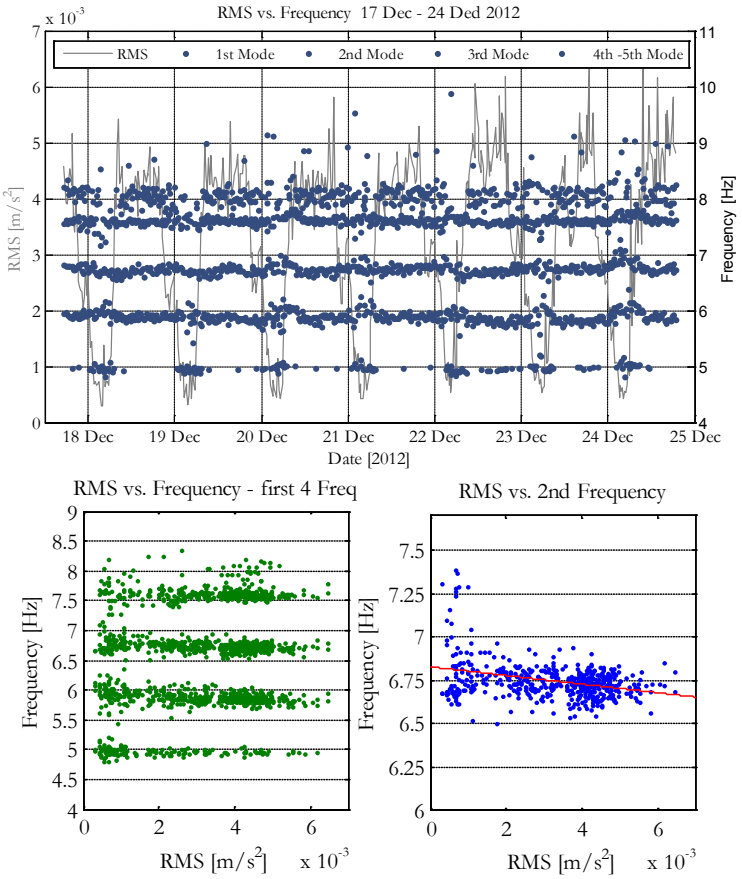

Figure 4.91 Natural frequency vs. RMS values during the continuously recorded week (top) time evolution, (bottom) RMS – Frequency relation.

4.5.1.5 Environmental Effects and Regression Models

In order to highlight the effects of changing environment on the natural frequency of the principal modes, frequency estimates were correlated to temperature during the monitored period (Figure 4.97). Generally, all modes show slight change with temperature and particularly in the fourth mode the linear dependency is highlighted by a linear correlation. Actually, the plot shows a decreasing trend of frequencies when temperature increases. However, some frequencies are less influenced by temperature, continuing a horizontal trend. This is due to the slight thermal and humidity swing verified during the year's monitored period as displayed in Figure 4.92.

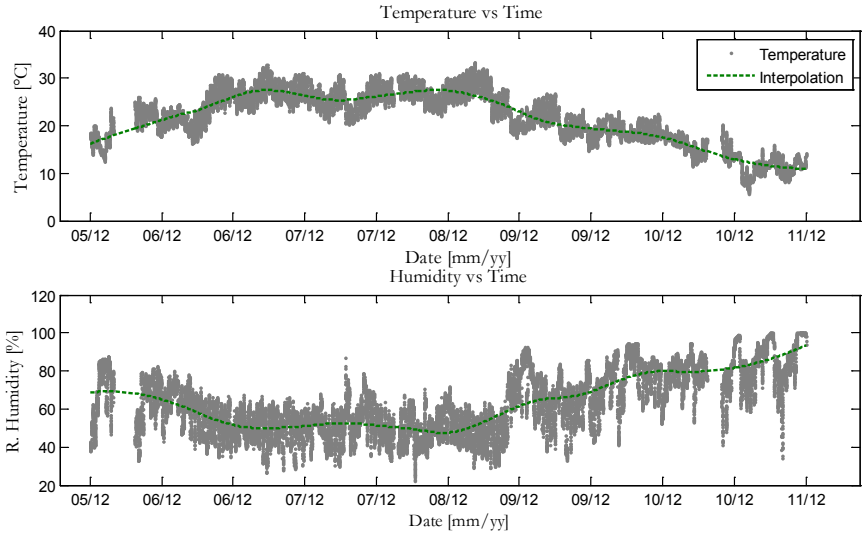

Figure 4.92 . Temperature and Relative Humidity over 1/2 year.

Besides the dynamic and the environmental monitoring, several displacement potentiometers were installed on the main girders of the bridge in order to detect any crack opening due to damage or overpassing traffic loads. These readings are related to environmental parameters, since it turns out to be depending on. As it is also evidenced by the finite element model, the movements expected from ordinary loads are of the order of millimeters for the entire length of the beam, while the portions of the beams monitored the order of movements is less than one millimeter. A regular trend of movements is observed, congruent with the environmental parameters (Figure 4.93, inversely proportional to temperature and directly proportional to humidity). Despite the many damages and corroded bars present, there are good reserves of resistance evidenced by the small natural frequency and displacement fluctuations.

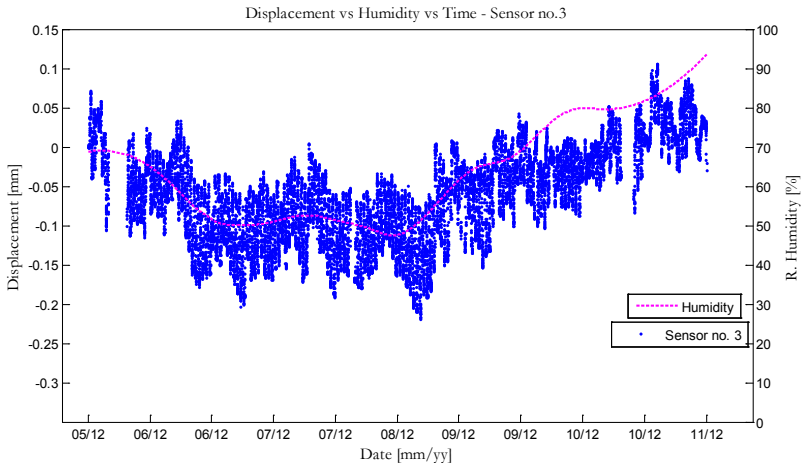

Figure 4.93 . Crack monitoring on one of the girders of People's New Bridge.

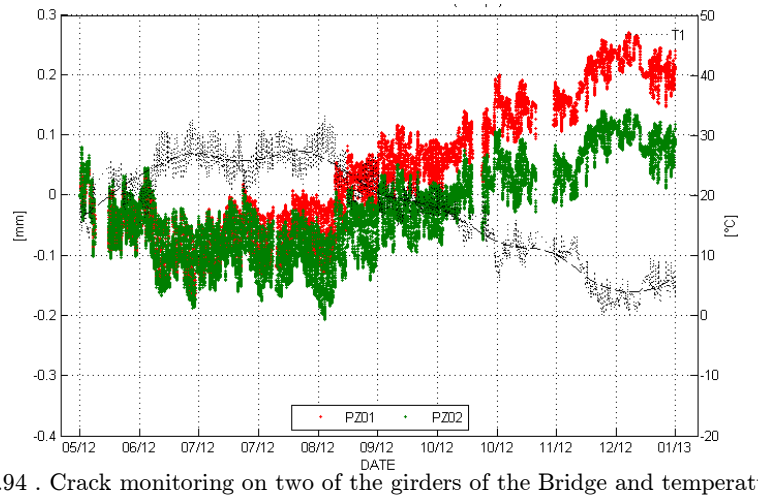

Figure 4.94 . Crack monitoring on two of the girders of the Bridge and temperature plot.

In Figure 4.94 the deflection on beams n. 2 and 3 have been compared. The plots relate the displacements between a well-conserved element (beam n. 3) and the adjacent damaged beam n.2. Although the entities are relatively small, it was observed that the damaged beam tends to deform more in relation to expansion due to the temperature.

Regression Models

With the introduction and extent of the procedures of dynamic tests on civil structures, we have noticed a strong dependence of the results obtained, in terms of frequency oscillation, from environmental factors, primarily temperature. Nevertheless, it is clear that the most influential and studied factor is temperature, since it can be correlated, especially in the context of an annual analysis to humidity, rain and ice. With particular reference to temperature, there is an increase of the frequencies in the cold periods, especially for structures whose

elasticity parameters are heavily dependent on temperature, such as steel. Concrete or masonry structures, instead, show a decrease of frequencies in wet periods, in particular in the presence of precipitations. This is due to absorption of water, which, by decreasing their rigidity, increases their mass.

It is therefore possible to evaluate the level of correlation of the natural frequencies of the structure with any environmental variable measured in site. In addition to temperature, one can even estimate the effects of vehicular traffic, in the case of road bridges. The more interesting side, on the most innovative applications, is related to the detection of damage. It is possible, in fact, once identified all environmental variables that determine the independent oscillatory behavior of the structure, to isolate possible effects due to events of irreversible damage, revealed by a permanent decrease of frequencies. The modal operational automated identification techniques allow to record changes in the oscillatory behavior in real time, and quickly detect the anomaly. The implications of the development of techniques of dynamic identification, of statistical modeling of the response of structures, and gathering and processing data in real time are important especially in the context of particularly sensitive structures.

The objective to be achieved in the present study is to verify whether the extensiveness of some environmental variables measured in situ influence the static or dynamic behavior of a structure. Therefore, it is very important to eliminate the influence of these factors, so that small changes due to damages can be detected. This is made possible by the use of regressive models able to determine the modal characteristics of the structure or static variables starting from a predefined input. Comparing the trend of the measured output variables and the variables estimated by the model, the model can be validated, confirming that the input variable chosen substantially, determines the response.

As described in [45], structural health monitoring is based on real-time monitoring of structural parameters, but what information is important and which data should be processed and stored for damage detection is a crucial point.

The task of damage analysis can be subdivided in four steps (partly applied to People's New Bridge):

- Geometrical and structural survey, damage survey, mechanical materials characterization, dynamic tests and numerical model analysis, static and dynamic analysis.
- SHM of the structure with a limited number of sensors (as in this case). Data storage and periodically data processing for damage detection. Global modal parameters should be related to environmental and traffic effects.

- When a damage alarm is triggered, an intensive dynamic survey with more sensors and measuring points should be performed. This phase aims to detect and locate the possible damage after eliminating the environmental effects.
- Nondestructive tests and local inspections should be carried out in order to locally assess the damage. Other advanced techniques as sonic or tomographic analysis can be used to define in detail the damage.

In the framework of a dynamic monitoring project, a regression model for each frequency has to be built. These should be constructed using data collected during at least an entire year, so that the influence of environmental factors in the natural frequencies is well characterized by considering a large range of variation, with data from summer and winter periods.

The models that will be used later, for the simulation of the behavior of monitored structures, may be placed in the framework of linear time invariant systems.

$$y(t) = \sum_{k=1}^{\infty} g(k)u(t-k) + v(t) \tag{4.1}$$

where $y(t)$ is the output, k is the time step, g is the impulse response function, u is the measured variable, v is the disturbance (measurement noise and unknown input). While, the shift operator $qu(t) = u(t+1)$.

Equation (4.1) can be written as:

$$y(t) = G(q)u(t) + H(q)\, e(t) \tag{4.2}$$

where G is the transferring operator and constitutes a sequence of random variables with zero mean. Let us introduce now the concepts of simulation and prediction. The first is given by a time series of input u^*, in deriving an estimate y^* by the simple relationship:

$$y^*(t) = G(q)u^*(t) + H(q)\, e^*(t) \tag{4.3}$$

where e is a white noise. The prediction, instead, introduces the number of time steps, at which one wants to make the prediction. It takes the following form:

$$\hat{y}(t|t-1) = H^{-1}(q)G(q)u(t) + [1 - H^{-1}(q)]\, y(t) \tag{4.4}$$

The models used in here are called AutoRegressive output with eXogeneus inputs (ARX) and assume the following expression:

$$y(t) + a_1 y(t-1) + \cdots + a_{n_a} y(t-n_a) = b_1 u(t-n_k) + \cdots + b_{n_b} y(t-n_k-n_b+1) + e(t) \qquad (4.5)$$

where n_a and n_b are called orders of the model, a_i and b_i are coefficients for the autoregressive and exogeneous part and n_k is the delay. We can now introduce the following vectors:

$$\theta = [a_1, \dots, a_{n_a}, b_1, \dots, b_{n_b}]^T$$
$$A(q) = 1 + a_1 q^{-1} + \cdots + a_{n_a} q^{-n_a}$$
$$B(q) = 1 + b_1 q^{-1} + \cdots + b_{n_b} q^{-n_b}$$

Comparing equations (4.4) and (4.5), we obtain:

$$G(q,\theta) = \frac{B(q)}{A(q)} \ , \qquad H(q,\theta) = \frac{1}{A(q)}$$

The choice of the delay depends on the type of that process that is meant to simulate. In the case where the inertia of the system is small, i.e., the response takes place with a limited time lag, it is assumed that $n_k = 0$.

Before applying this method to the crack openings (Figure 4.94) of the People's New Bridge, we will now consider which is the variable input more influential on the response of the structure, including temperature and humidity. This is done by considering the correlation coefficient between two signals *x* and *y*:

$$r = \frac{cov(x,y)}{\sigma_x \sigma_y}$$

The value of the correlation coefficient ranges between -1 and +1: the closer to unity, the more the two variables are related. The correlations are:

	T-H	**y-T**	**y-H**
r	-0,8038	-0,9409	0,776

Note how all the variables are related. The temperature, it is therefore chosen, as a representative variable, since it presents a higher correlation coefficient. This choice can be checked a posteriori, after having implemented the SISO autoregressive model based on the only thermal input.

Similarly to [45], the variables were first normalized so as to avoid any offset, as follows:

$$Y = \frac{y - \bar{y}}{\sigma_y}$$

A linear regression model of ARX type is used, described by Equation (4.5). The choice of the orders n_a, n_b, n_k, was carried out by opting for the most closer model to the measures carried out, in addition the delay was set to

0, since the inertia of the process is moderate. The parameters used to evaluate the adequateness of the model are the loss function, the final prediction error (FPE) and the coefficient of determination, respectively:

$$V = \frac{1}{N}\sum_{k=1}^{N} {e_k}^2 \ , \quad FPE = V\frac{1+d/N}{1-d/N}, \quad r^2 = \left[\frac{cov(x,y)}{\sigma_x \sigma_y}\right]^2$$

where N is the number of measurements, d the number of estimated parameters and k the time step. The parameters of the model, equal to $n_a + n_b$, were calculated using a least-squares procedure, minimizing the *residue*:

$$\hat{e}_k = y_k - \hat{y}_k$$

where y_k is the measured output and $\hat{y}_k$ is the output predicted by the model at the same time step. The residue was then reported on a time chart, together with the relative *confidence interval*, calculated as follows:

$$\left[y - t_{\alpha/2,\nu}\sigma \ , \ y + t_{\alpha/2,\nu}\sigma\right]$$

where $t_{\alpha/2,\nu}$ is the *t-student* distribution with ν degrees of freedom, for a probability of 0.025. When the sample is relatively large, this value tends to 1.96. The model parameters and confidence intervals were estimated for an initial period chosen arbitrarily, defined as the estimation period. It is therefore assessed the validation period, where the residues must not overwhelmingly come out the confidence interval. Thus, the detection of damage should be carried out by observing shifts that significantly go out of the confident intervals. Although at least one year of monitoring is needed, the following plots show the results on a limited time: the evaluation and the validation phases are separated by a vertical black line. It is first presented a table comparing the static and dynamic models.

Table 4.13 Static and dynamic regressive models results

	ARX Model				Static Regression Model			
Crack	***Orders***	***V***	***FPE***	***r²***	***Orders***	***V***	***FPE***	***r²***
1	190	0,00227	0,002275	0,9481	010	0,11519	0,115206	0,8808
2	190	0,00208	0,002078	0,9519	010	0,11961	0,119631	0,8918

The residue plot shows that the model estimates in a correct way the displacement, because the validation residues remain within the confidence interval. Moreover, as seen from the graph of the autocorrelation of the residuals, the latter can be treated essentially as a process of white-noise. Therefore it can come to the conclusion that the temperature is the independent variable that influences the crack opening of the bridge. In case one wants to make the detection of the damage through this kind of output, it would be sufficient to isolate only the thermal effect.

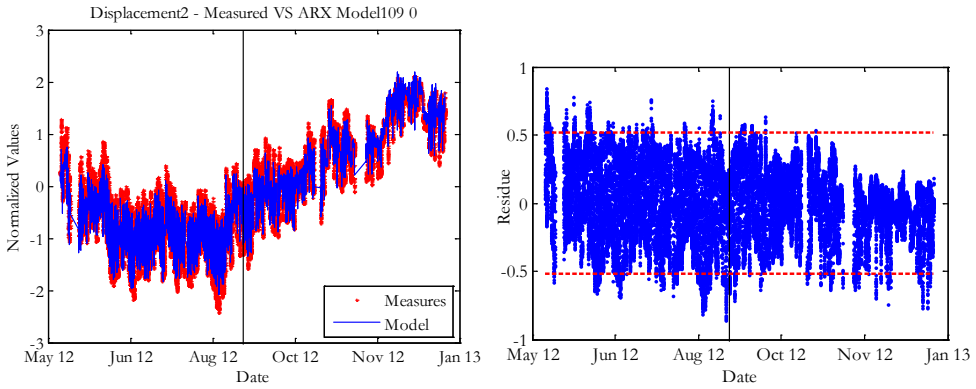

Figure 4.95 Measured and Estimated Output and their residue.

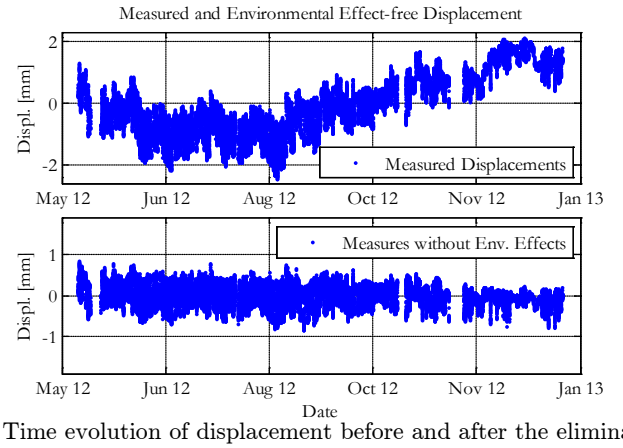

Figure 4.96 Time evolution of displacement before and after the elimination of the environmental effects (regression model).

Figure 4.96 shows the time evolution of the displacement on beam number two over a period of 8 months before and after the elimination of the environmental effects with the dynamic regression. It can be observed (also in Figure 4.97) that the variation of this value is reduced to a small range, which proves that the selected regression model takes into account the factors with greater influence on the output.

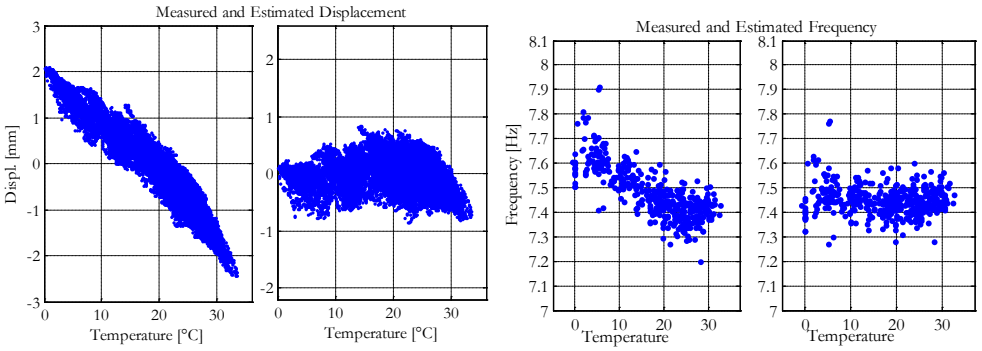

Figure 4.97 Temperature effects on the static and dynamic measurements.

A similar procedure of environment effects elimination was used for the dynamic data of the People's New Bridge. Although less effected by temperature (because data were available for less than a year), the natural frequencies showed some dependency, and a good regression model was estimated. Figure 4.98 shows the fitting model through the normalized frequency with the 95% confidence intervals and the autocorrelation of the simulated errors. In general, the model represents the frequency variation with a reasonable fitting. The model can be used for damage detection, and frequency shifts that significantly stay outside the confidence intervals are valuable candidates. At this point, few data are available, and for an accurate model, another year of monitoring is needed to proper calibrate the model.

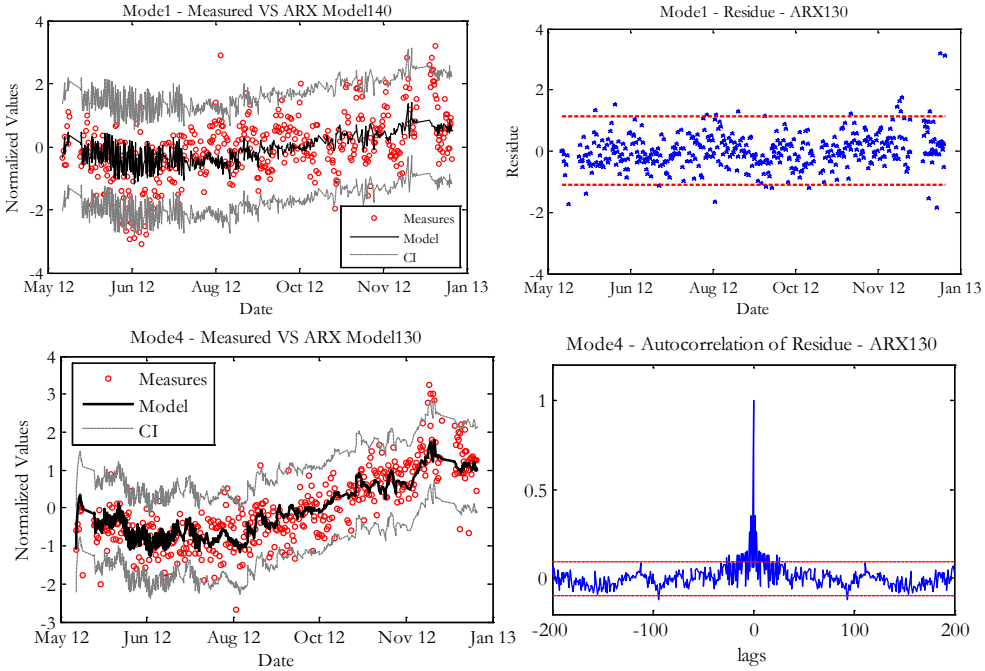

Figure 4.98 ARX Model of mode 1 and 4, CI, Residue and Autocorrelation.

The reduction of the range of variation of the natural frequencies after their correction by the regression model can be also be evidenced by the use of histograms. Figure 4.99 presents the histograms of the first and fourth natural frequency. After the application of the regression model, frequencies are concentrated in a narrower range, correcting the influence of temperature.

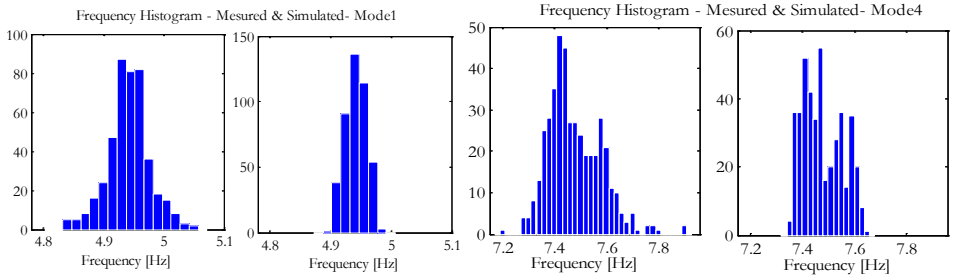

Figure 4.99 Histogram of the mode 1 and 4: distribution before and after the elimination of environmental effects.

4.6 Suspension bridges

4.6.1 Monitoring of the Manhattan Bridge

4.6.1.1 The suspension bridge

The Manhattan Bridge (Figure 4.100) was opened to traffic in 1909 and since then has become a major artery for both highway and rapid transit traffic crossing New York City's East River, between Brooklyn and Manhattan [46] [47].

continues

Figure 4.100 First photos during construction, opening and current conditions of the Manhattan Bridge.

The main river crossing is a suspension bridge with a main span of 448 meters (1470 feet) and two side spans of 221 meters (725 feet) each. The Manhattan approach is about 394 meters (1293 feet) long and the Brooklyn approach about 369 meters (1212 feet) (Figure 4.102), with a total length of 2,089 m (6855 feet). The main structural elements are: steel cables, steel boxed deck, masonry foundations, steel pylons and masonry anchorages. There are 4 cables with 27 strands each and diameter of 21 inches (largest at that time). The width of the deck is 36.6 m and the depth is 7.3 m, while the height of the pylons is 102.4 m.

The cross section is similar for both approaches and suspended spans (Figure 4.101). In the suspended spans, the bridge has four cables, each supporting a stiffening truss. At the approaches, the trusses are supported on unreinforced concrete filled stone masonry piers. There are seven simply supported truss spans in each approach. The bridge carries seven lanes of vehicular traffic on three separate roadways and four transit tracks. Two upper roadways, with two lanes each, are located at the level of upper truss chords between each pair of inner and outer truss. The three-lane lower roadway is located at the lower truss chord level between the two inner trusses.

After some years of operation, traffic on the bridge was considerably increasing and the suspended spans of the bridge started exhibiting

abnormal deterioration due to twist generated by eccentric loads when transit trains passed on one side of the bridge. A rehabilitation strategy (the $834M Manhattan Bridge Reconstruction Program that began in 1982) to address fatigue and corrosion damage was developed, including the installation of a truss stiffening system (to reduce twisting), implemented over the course of several years while maintaining most of the bridge traffic. The effect was achieved by creating "torque tubes" with new braces under the roadways and strengthening the truss diagonals. During the measurements presented herein, the difference in elevation between opposite cross section edges at mid-span under asymmetric train distribution reached about 0.5m, which is lower than what was estimated before the intervention.

Manhattan Bridge was the first suspension bridge to use flexible steel towers, unlike some other bridges such as the Williamsburg and the George Washington that used braced steel towers. The Manhattan bridge was the first modern steel suspension bridge to use a Warren type stiffening truss. It was the first modern steel suspension bridge to use two suspender ropes straddled over the main cables to attach to the floor beams. As many as 75,000 vehicles and 970 subway trains cross the bridge daily. The bridge towers were designed for up to 4 ft (1.22 m) total sway at the top, thus eliminating the need for the traditional rollers under the cable saddles. Each of the four cables was composed of nearly 10,000 wires bundled into the 37 strands.

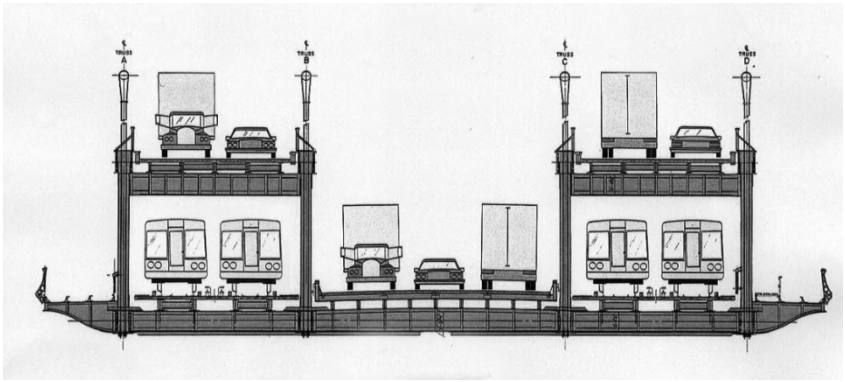

Figure 4.101 Cross section of the Manhattan Bridge.

4.6.1.2 Monitoring campaigns

During September-October 2008 a sophisticated monitoring system was installed on the Manhattan Bridge by the team of the Department of Civil Engineering and Engineering Mechanics of Columbia University - New

York. During this period, vibration and displacement measurements were monitored in several locations of the bridge. The main objectives for these tests were to identify the dynamic behavior of the structure in order that a computational model could be refined and verified for use in other dynamic (seismic) analyses.

The instrumentation consisted of a portable network of data-loggers, each with its accompanying triaxial force balance accelerometer. Since there are no interconnecting wires, each data-logger is triggered independently and has the time base synchronized accurately. Each data-logger has a highly accurate internal clock which was resynchronized every 30 minutes through a small GPS receiver. The sensitivity of the monitoring instrumentation was set to 2.5 volts/g. Therefore, this was adequate to detect the low frequencies of response of the structure even below 1 Hz. The sampling frequency was of 200 Hz and the recording length of nearly 1 hour. With this recording configuration four time windows were registered per day in hours where traffic and ambient excitation were very different.
The accelerometers were placed on the top of the outer truss next to the upper roadway and well secured between the chord member lacing. They were disposed in number and position in order to capture the global dynamic response of the structure (Figure 4.103 and Figure 4.105).

In addition to the accelerometer sensor array, GPS instruments were used to measure displacements, especially the very low frequency displacements such as the deflection produced by passing subway trains or the very low frequency motions caused by wind loading. Such pseudo dynamic motions have very little accompanying acceleration and are often undetected by accelerometers. In this application there were used one reference station antenna near the Brooklyn anchorage and four roving stations in order to cover the pre-planned positioning points such as the upper deck or the top of the towers.

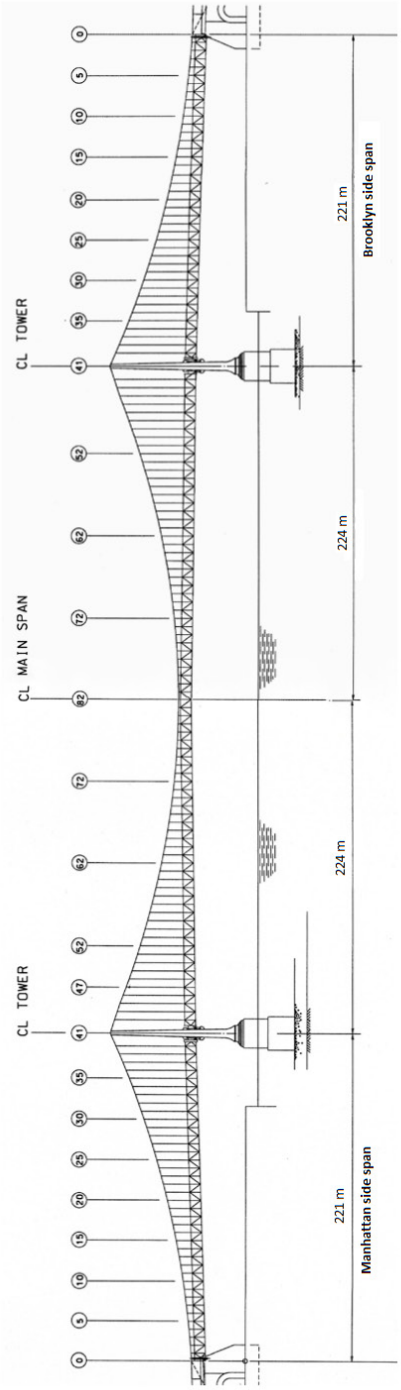

Figure 4.102 Longitudinal section of the Manhattan Bridge.

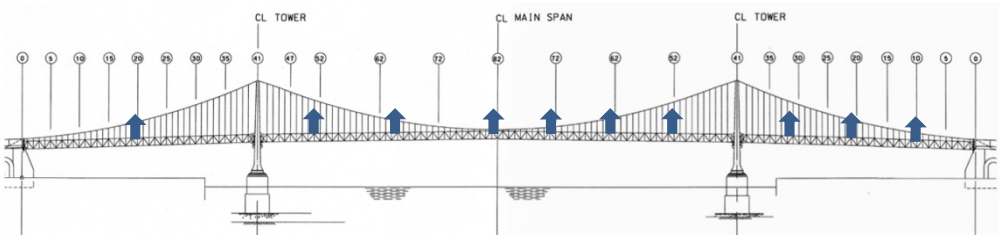

Figure 4.103 Example of global sensor configurations: vertical positioning.

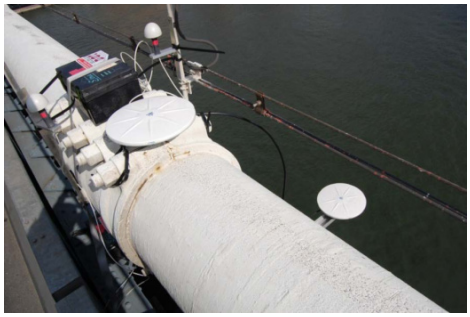

Figure 4.104 A typical GPS antenna and accelerometer installation.

In this way the different measurements between the fix position and the moving ones can measure accurately the relative motion. The GPS receivers had a lower sampling rate of 10 Hz, but still challenging in this new technology.

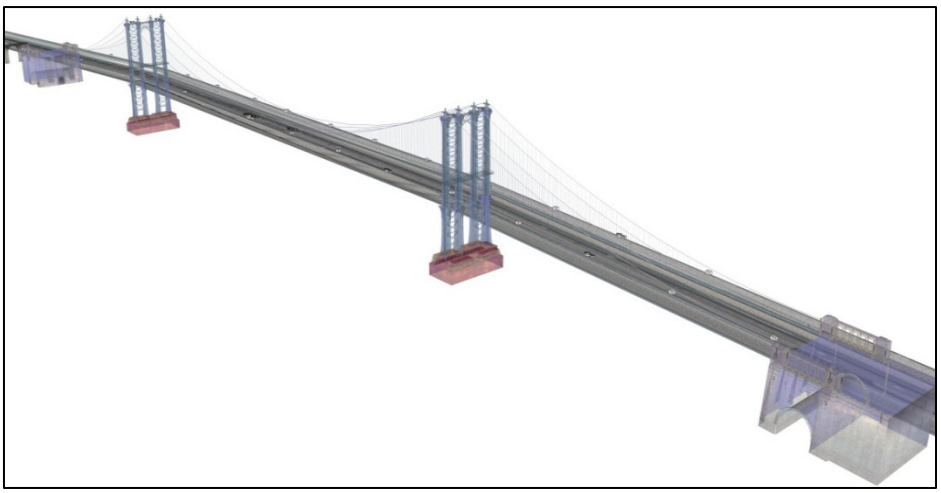

continues

Figure 4.105 Installation of the sensors on the deck and on the Manhattan Tower.

In Figure 4.105, and Table 4.14 it is seen how the different sensors are located on the structure. For over a month, there have been recorded more than a dozen configurations (where the sensor positions changed frequently), but here only the collocated sensors have been presented (for data fusion where both acceleration and displacement measurements are recorded). Table 0.14 includes also the 5 configurations used to initially extract the dynamic response of the bridge. In Table 4.14 the ACC indicates an accelerometer and MAB indicates a GPS station, whereas the other symbols refer to the possible position of the sensor on the structure. For example, if we consider the position PP6262NE, this means: the panel point number 62 (see Figure 4.102) on the deck on the northern side of the bridge and on the east half. If we consider TBN, this means that it is located on Brooklyn tower top, on northern side.

4.6.1.3 Dynamic results: Modal Analysis

During the dynamic tests [48] [49] [50] [51] on the Manhattan Bridge, windows of 60 minutes with 200 Hz of sampling frequency were recorded. In this way each measurement consisted of nearly 720 000 point samples and has a Nyquist frequency of 100 Hz. With regard to the amplitudes of the accelerations, the vertical responses are in general double the transverse response: the maximum amplitude in the vertical direction observed in channel 1 (mid-span) is 1.1066 m/s2 while the largest value in transverse direction is 0.7099 m/s2.
An example of the time series from one of the deployments on Manhattan Bridge is presented in Figure 4.106. The signals are accelerations in three directions recorded for 60 minutes. A Power Spectral Density graph is then obtainable by using the Welch's method (Figure 4.108). A very high frequency resolution (0.003 Hz) could be reached here because the number of samples was high.

The data recorded were selected in order to analyze the dynamic behavior of the structure as a whole. So 5 different configurations recorded at 3am were selected in order to have a uniform excitation on the structure free from the potential effect of the numerous subway trains which cross the bridge during the rush hour period.

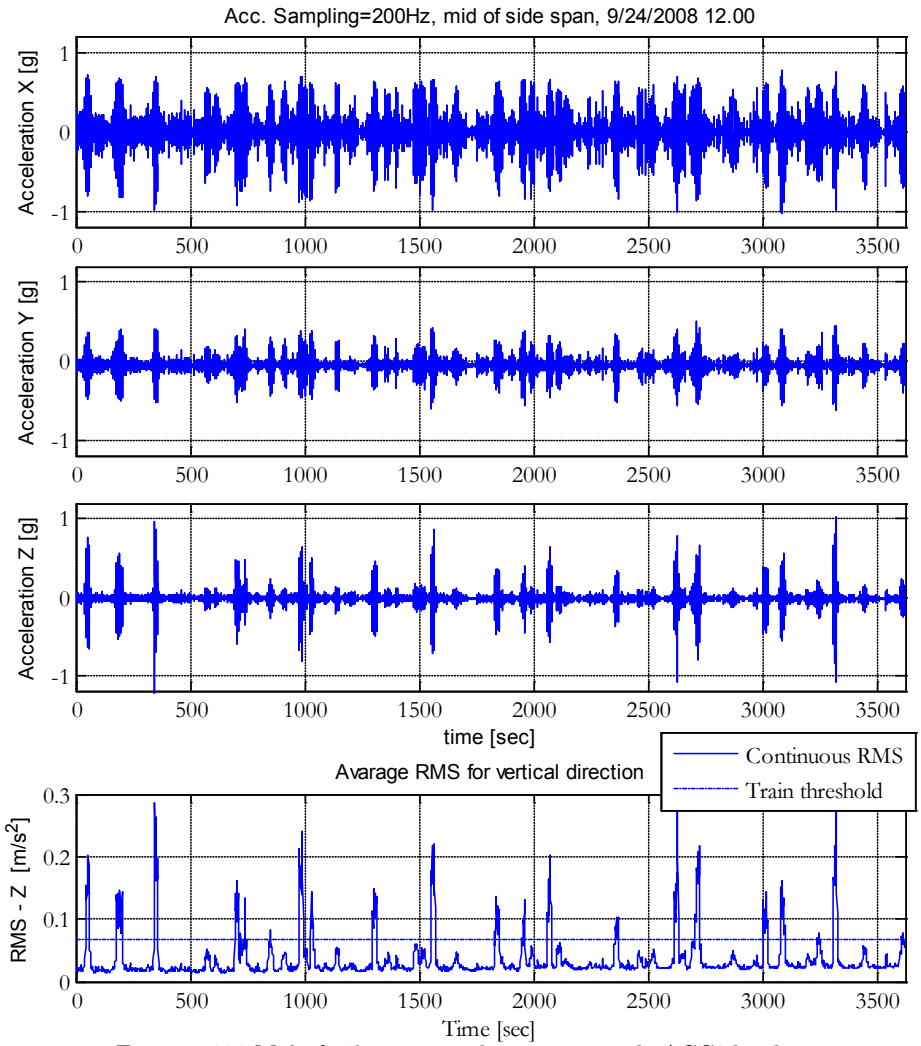

Figure 4.106 Mid of side span acceleration example ACC3:by day.

Table 4.14 The general view of the collocated (GPS and FBA) measured setups on the Manhattan Bridge.

Sensor Location	set-23	set-24	set-25	set-26	**set-27**	set-28	set-29	set-30	**10-gen**	10-feb	10-mar	**10-apr**	10-mag	10-giu	10-lug	**10-ago**	10-set	10-ott	**10-nov**	10-dic	ott-13	ott-14
PP0NE (reference)	MAB4	MAB4	MAB4	MAB4	**MAB4**	MAB4	MAB4	MAB4	**MAB4**	MAB4	MAB4	**MAB4**	MAB4	MAB4	MAB4	**MAB4**	MAB4	MAB4	**MAB4**	MAB4	MAB4	MAB4
PP10NE																**ACC7**						
PP21NE(1/2 side span)	MAB2 ACC3	MAB2 ACC3	MAB2 ACC3	MAB2 ACC3	**MAB2 ACC3**	MAB2 ACC3	MAB2 ACC3	MAB2 ACC3	**MAB2 ACC3**	MAB2 ACC3		**ACC3**				**ACC3**			**ACC2**			
PP30NE																**ACC10**						
PP40NE																						
PP42NE																						
PP52NE					**ACC4**							**ACC7**										
PP62NE					**ACCCACC2**				**ACC2**			**ACC2**				**ACC2**			**ACC2**			
PP72NE					**ACC8**																	
PP82N (mid span)	MAB5 ACC1	MAB5 ACC1	MAB5 ACC1	MAB5 ACC1	**MAB5 ACC1**	MAB5 ACC1	MAB5 ACC1	MAB5 ACC1	**MAB5 ACC1**	MAB5 ACC1	MAB5 ACC1	**MAB5 ACC1**	MAB5 ACC1	MAB5 ACC1	MAB5 ACC1	**MAB5 ACC1**	MAB5 ACC1	MAB5 ACC1	**MAB5 ACC1**	MAB5 ACC1	MAB5 ACC1	MAB5 ACC1
PP72NW												**ACC10**							**ACC6**			
PP62NW					**ACC9**				**ACC9**			**ACC9**										
PP52NW												**ACC4**										
PP42NW																						
PP20NW									**ACC4**													
PP20SW									**ACC8**													
PP62SW									**ACC5**													
PP82S (mid span)	MAB3 ACC7	MAB3 ACC7	MAB3 ACC7	MAB3 ACC7	**MAB3 ACC7**	MAB3 ACC7	MAB3 ACC7	MAB3	**MAB3**	MAB3	MAB3	**MAB3**	MAB3	MAB3								
PP72SE																						
PP62SE					**ACC5**											**ACC5**						
PP52SE																**ACC4**						
PP21SE (1/2 side span)															MAB3 ACC8	**MAB3 ACC8**	MAB3 ACC8	MAB3	**MAB3**	MAB3	MAB3	
PP10SE																						
TBN (tower)	MAB1 ACC10	MAB1 ACC10	MAB1 ACC10	MAB1 ACC10	**MAB1 ACC10**	MAB1 ACC10	MAB1 ACC10	MAB1 ACC10	**MAB1 ACC10**	MAB1 ACC10	MAB1	**MAB1**	MAB1	MAB1	MAB1	**MAB1**	MAB1	MAB1 ACC5	**MAB1 ACC5**	MAB1 ACC5	MAB1 ACC5	
TBS																			**ACC4**			
TMN (tower)											MAB2	**MAB2**	MAB2	MAB2					**ACC10**			
TMS																			**ACC7**			
PP14SE (Cable)																			**ACC6**			
PP62NW(Cable)																						

The average RMS value, in the case of the vertical direction was evaluated over the time interval of 1 second, leaving the RMS length the same as the original signal. As a result, in Figure 4.106 it can be noticed that every peak of the RMS corresponds to each train passage. The threshold estimated underlines a certain value of load excitation under which there are no train courses but only road traffic. In fact, this tool might be a precious means of traffic monitoring for the owner, so different patterns can be detected for a rush hour and by night (Figure 4.107 and Figure 4.111). An average of twenty trains courses per hour is observed during day times, whereas only four passages are witnessed at night hours.

The extraction of modal parameters from ambient vibration data was carried out by using standard methods as Frequency Domain Decomposition (FDD), and the data-driven Stochastic Subspace Identification (SSI) technique. After extracting the modal parameters with these methods, the newly developed Enhanced Canonical Correlation Analysis has been applied in order to validate it. The analysis included frequencies corresponding to the first Eigen-modes in a range of 0 - 1.5Hz.

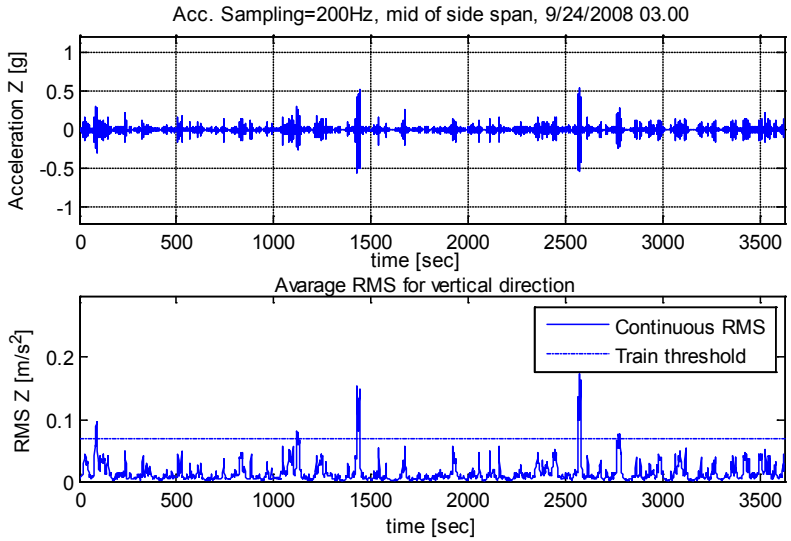

Figure 4.107 Mid of side span acceleration example and RMS: by night.

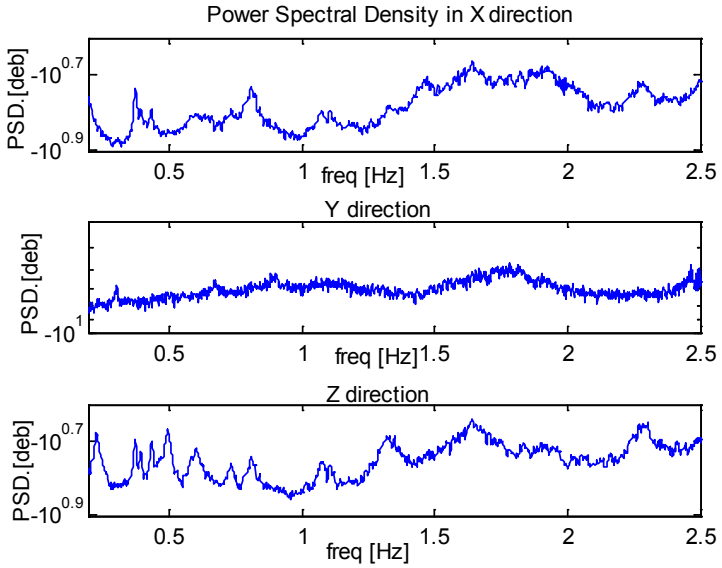

Figure 4.108 PSD of the mid of side span in ACC3 transversal and vertical direction.

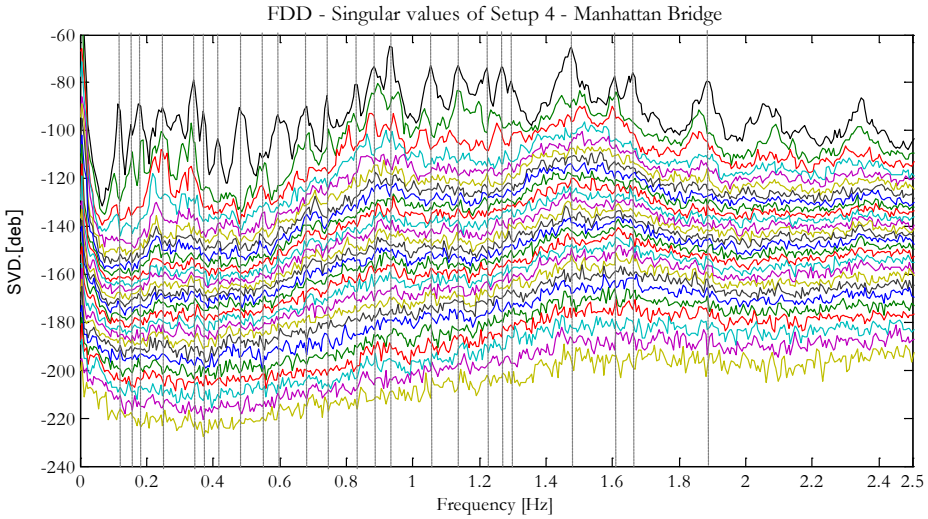

Figure 4.109 Identified modes with FDD for Setup test no.5 (27 channels).

Table 4.14 Identified mode shapes of the Manhattan Bridge

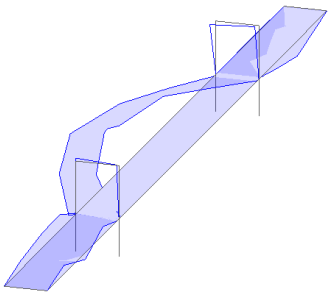	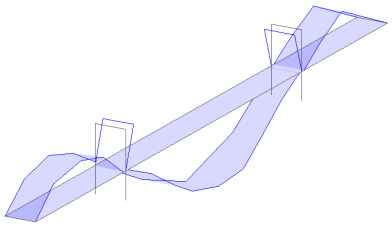
1st lateral - 0.1963 Hz	1st vertical - 0.2336 Hz
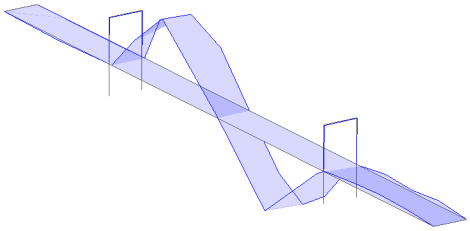	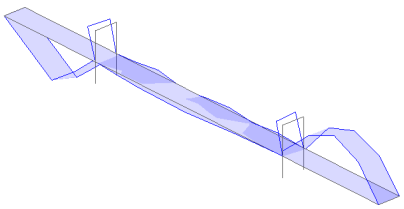
2nd vertical - 0.3076 Hz	3rd vertical - 0.3551 Hz
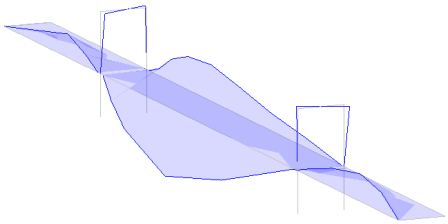	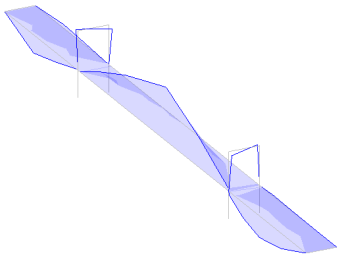
1st torsional - 0.3732 Hz	2nd torsional - 0.3923 Hz
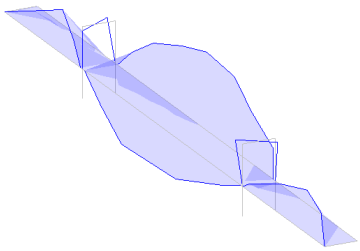	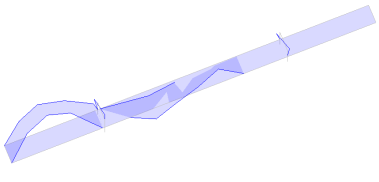
3rd torsional - 0.4343 Hz	4th vertical - 0.4759 Hz
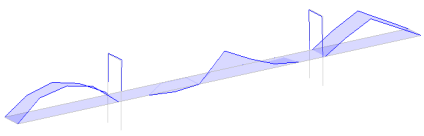	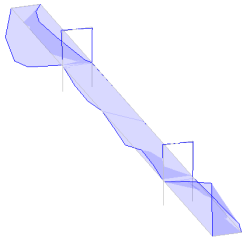
5th vertical - 0.5055 Hz	2nd lateral - 0.5772 Hz

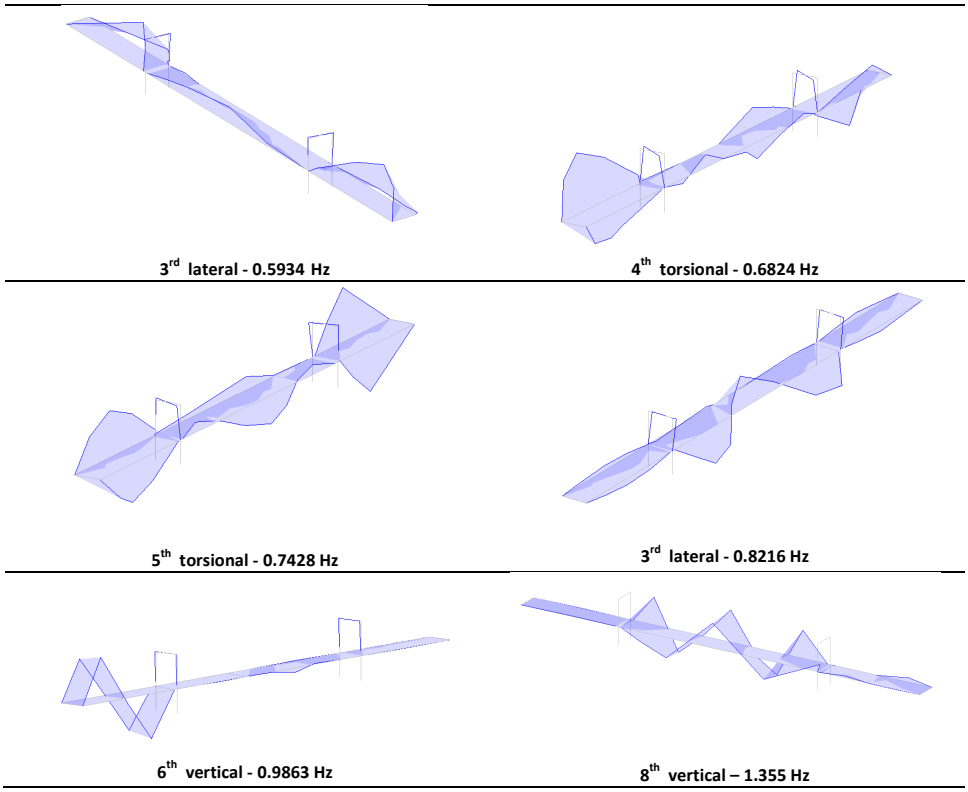

Table 4.15 Identified mode shape and damping ratios

Mode	*Frequency [Hz]*	*Damping Ratio [%]*
1	0.1963	1.182
2	0.2336	3.556
3	0.3076	2.011
4	0.3551	1.841
5	0.3732	0.7033
6	0.3923	0.5964
7	0.4343	0.5454
8	0.4759	0.704
9	0.5055	0.642
10	0.5772	0.6928
11	0.5934	0.7184
12	0.6824	0.5042
13	0.7428	0.7795
14	0.8216	1.815
15	0.8748	0.3848
16	0.9351	0.8416
17	0.9863	1.053
18	1.082	0.4682
19	1.102	0.3316
20	1.355	0.8564

On the acceleration signals extracted from one hour registration during a day-night cycle (i.e. at 3am, 8am, 12pm and 5pm), a parametric analysis has been done. This time, the purpose was to evaluate the differences in the frequency shift through the Welch PSD on the signals on 4 moments of

the day. As observed from Figure 4.110 and Table 4.17, there are slight differences between the four results, but generally the difference is under 2 %. This is due not only to the conservation of loads conditions on the bridge, but also to the minimal thermal gradients existing during the daily monitoring campaigns.

Table 4.16 Comparison of natural frequencies in a day-night cycle record.

Mode	*Freq.[Hz] 3am*	*Freq.[Hz] 8am*	*Freq.[Hz] 12pm*	*Freq.[Hz] 17pm*
1	0.2320	0.2210	0.2238	0.2238
2	0.3702	0.3715	0.3715	0.3702
3	0.3936	0.3923	0.3923	0.3923
4	0.4351	0.4351	0.4323	0.4337
5	0.4959	0.5069	0.4945	0.4959
6	0.5967	0.5981	0.6022	0.6008
7	0.7307	0.7431	0.7320	0.7307
8	0.8052	0.8163	0.8080	0.8094

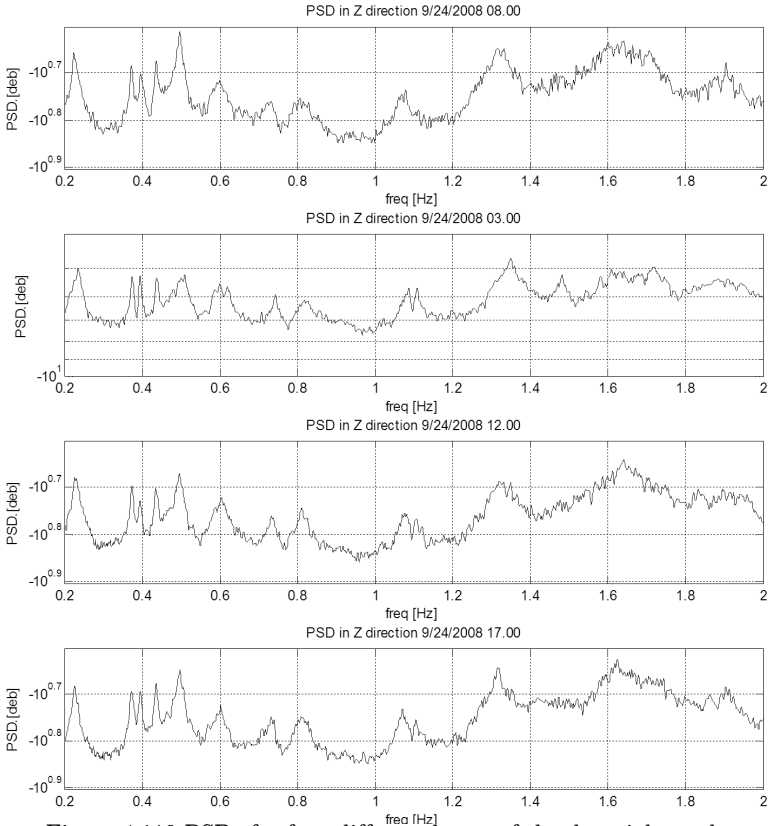

Figure 4.110 PSDs for four different hours of the day-night cycle.

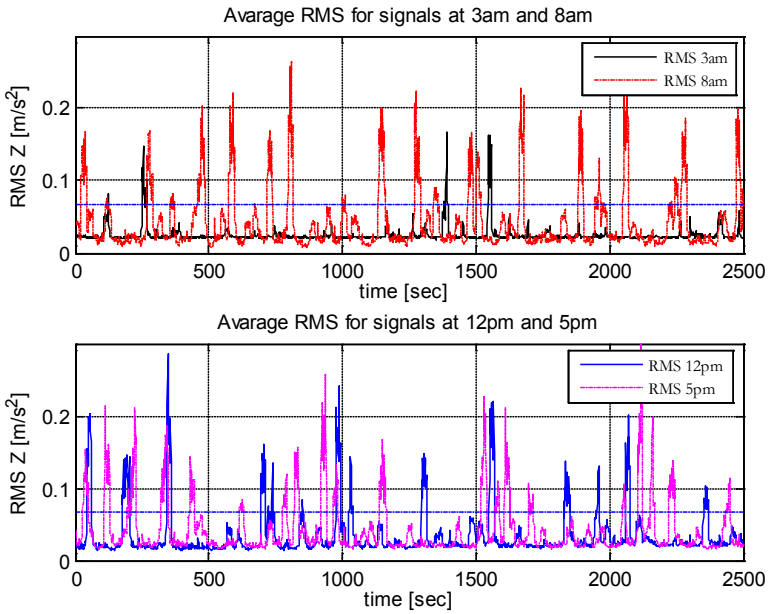

Figure 4.111 Average RMS of signals on four different hours of the day.

4.6.1.4 Cable vibration analysis

During the monitoring campaigns, besides the deck and the towers of the Manhattan Bridge, the cables were also instrumented with acceleration and displacement sensors. The principal locations investigated are at mid-span, above the deck sensor, at 1/4 of the main span and at 1/3 of the side span. The first of these locations was monitored with both triaxial accelerometer and a GPS displacement sensor, whereas the other two only with accelerometers.

The general trend of the data collected from the cables reveal a quite similar response with the deck motions. We see that peaks coincide especially in the vertical direction. In Figure 4.112 the PSD for the three directions of the accelerations in the mid-span deck and in the respective position on the cable is represented. As already mentioned, there is no difference in the vertical motion, since a vertical amplification would presumably be accompanied by stretching of the suspender ropes. On the other hand it is easy to observe that the transversal motion is amplified around 0.4 Hz and at 0.7 Hz (probably a cable mode only).

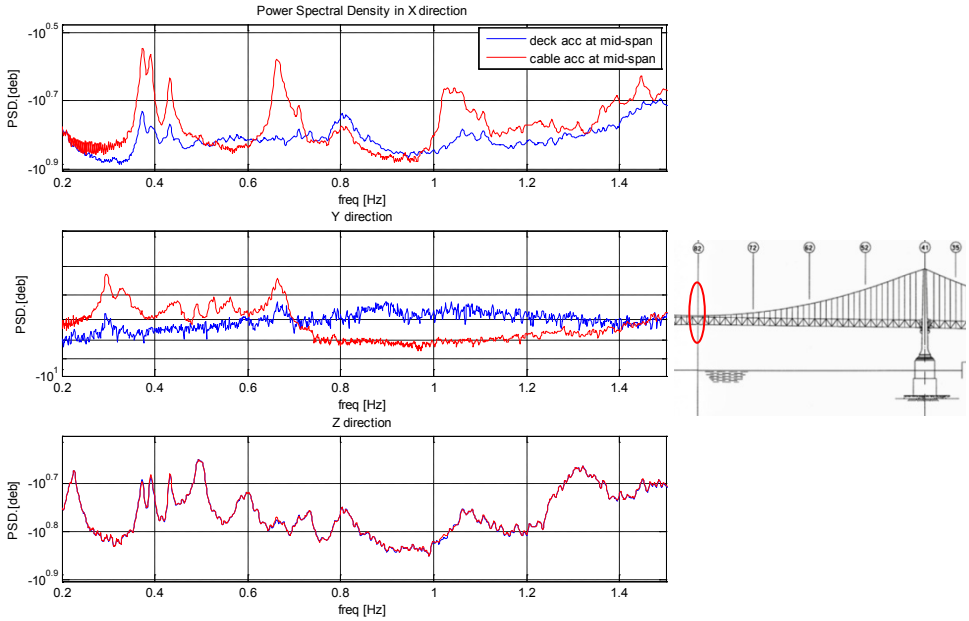

Figure 4.112 Comparison of PSD of the cable accelerations at the mid-span (above PP82N) and at the deck (PP822N).

In Figure 4.113, the PSD for the three directions in the mid-span cable and at 1/4 of the deck on the cable is presented. In this case the vertical distinct is more evident because of the difference in the sensor's distance from the deck and due to the flexibility of the cord at 1/4 span. Note that the motion at 0.659Hz is about half the motion at mid-span.

4.6.1.5 Modal parameter identification via the ECCA

During the previous analysis with the standard modal methods we saw some good results in finding the principal modal parameters. In this paragraph some of the results obtained from the analysis with the ECCA will be shown. It will be seen that, in this case, it was possible to identify more dynamic parameters, and at the same time confirm the previous results.

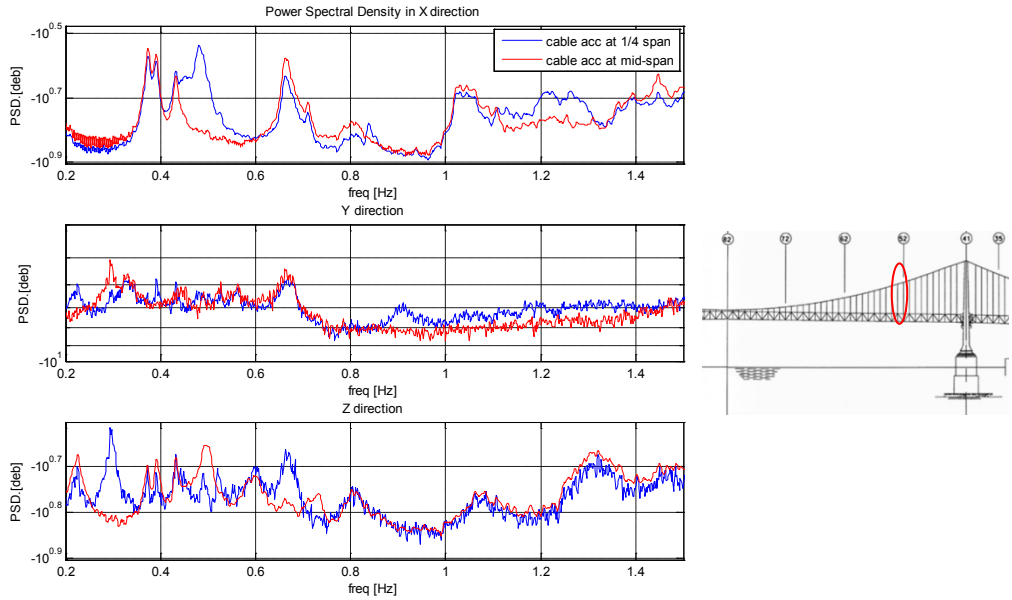

Figure 4.113 PSD of the cable accelerations at the mid-span (above PP82N) and at 1/4 of the span (PP62NW).

The stabilization diagram permits to identify the modes whose properties do not change significantly when varying the model order. Modes classified as "stable" are considered as structural modes. However, such modal parameter estimates, especially damping ratios, are influenced by the particular selection of the model order, as presented in Figure 4.115. Different filters were applied to all the data, and different parametric analysis were carried out resulting in the identification of higher modes, previously invisible. In order to capture every vibration frequency, various low pass filters were applied to the data, in relation to the frequency needed. On Figure 4.114 it can be noted how the frequency values related to the model order number show a stable trend, especially for the first modes. To examine the variations of the damping ratio estimates with the model's order, all the modes have been considered. It seems (Figure 4.115) that the proper model order of the model is for sure greater than 75.

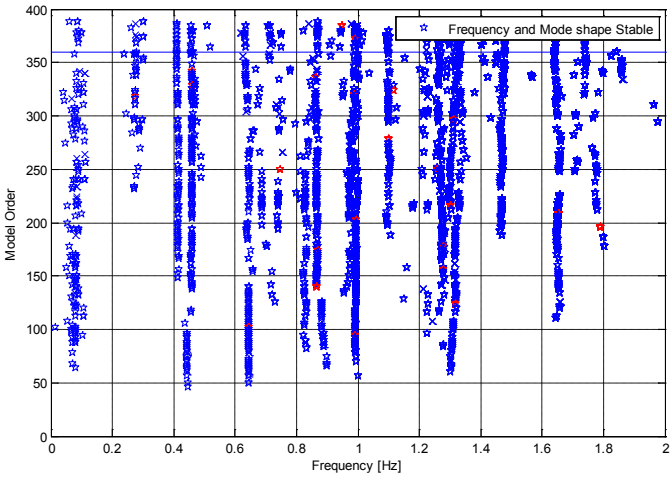

Figure 4.114 Stabilization Diagram for the ECCA, Manhattan Bridge.

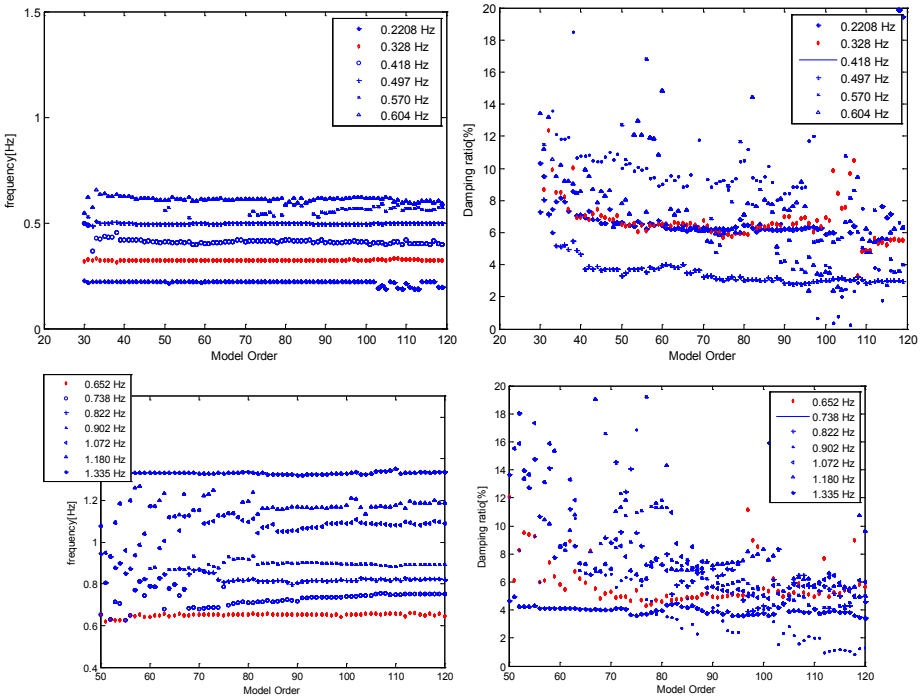

Figure 4.115 Natural frequencies relatively to the system model order and damping ratios.

The damping ratios of these modes are extracted from the models with different orders (such models are realized via the ECCA method) and displayed in Figure 4.115. In this figure, a small variations of the damping ratio estimates related to the model's order can be observed for all the modes. In the frequency range of 0-1.5, a total of 20 structural modes are identified.

4.6.1.6 Monitoring results

The monitoring campaigns lasted for more than one month and were prepared to cover the entire elements of the bridge. Besides the detailed modal analyses conducted on different configurations, a general review of the change of the modal parameters during the monitoring period was carried out. All day-night cycles (four times in 24h) registered were analyzed and for each day the principal natural frequencies and damping ratio were observed. The aim of this study was to extract any noteworthy change in the monitored structural system: for example, frequency shifts. This kind of analysis was computationally expensive because of the high resolution of the signal and the long time series recorded. In particular, every single registration (724000 points x 24 channels) was analyzed with the automated SSI and FDD method in order to get all the modal parameters.

Some of the principal structural modes (extracted with the SSI) are presented in Figure 4.116 in relation to the period of measurement. It can be noticed that apparently no important shifts are present in the data, showing only the slight fluctuations related to environmental factors and load conditions.

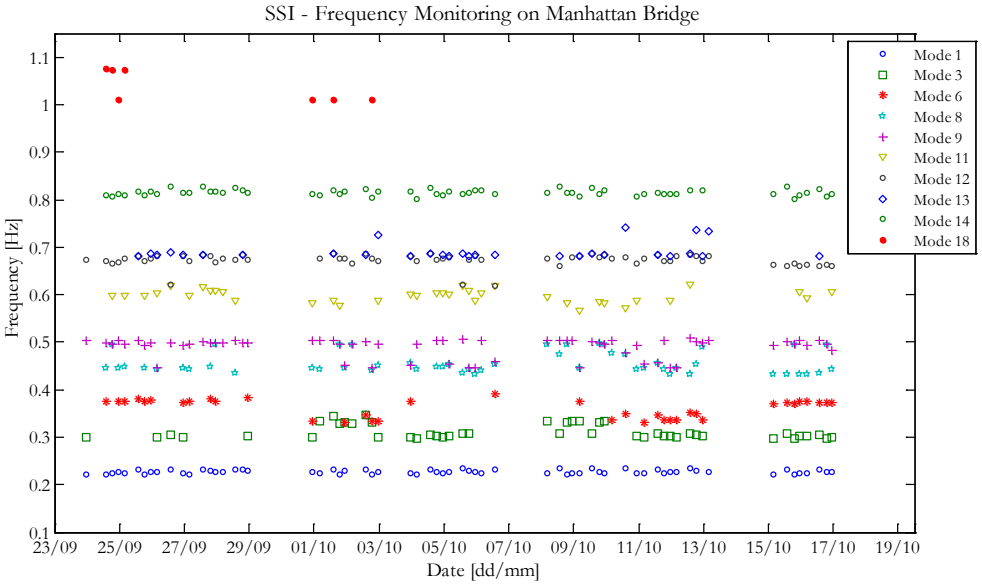

Figure 4.116 Frequency distribution for the monitoring period (SSI technique).

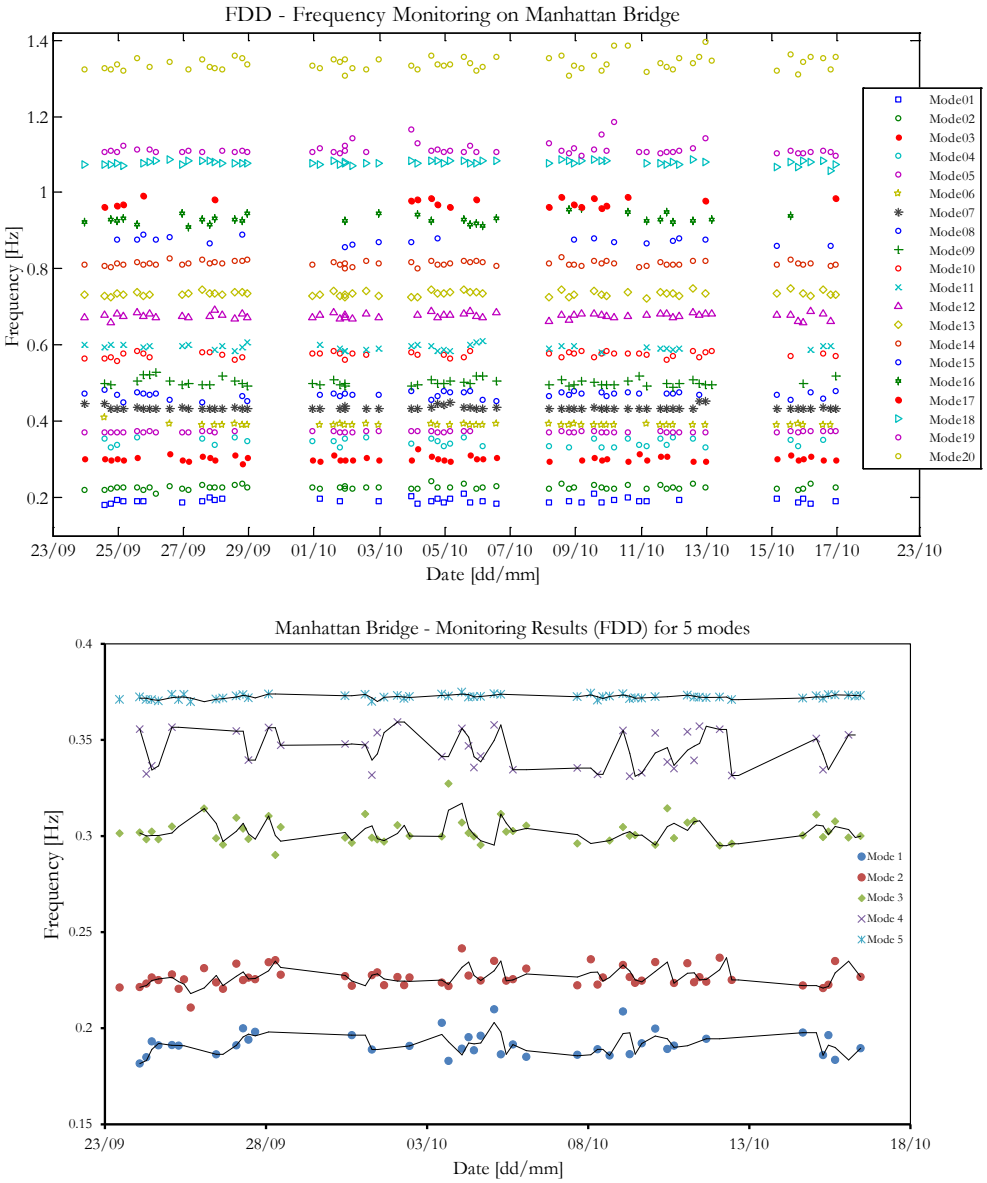

Figure 4.117 Frequency shifts for the 20 modes identified (FDD) and a close-up of the first 5 modes during the monitoring period.

In the FDD case, 20 of the natural frequencies were identified for all the monitoring period. As it can be observed from Figure 4.116, this values are quite stable and seem to conserve the structural behavior during the entire period. But, looking into a narrow window with only five of the frequencies, it is worthy to note that some shifts took place during the months of monitoring. Looking at the trend lines of modes represented in Figure 4.117(b) and the trend of temperature represented in Figure 4.118, one

can realize that they are closely correlated. Instead, damping ratios Figure 4.119 fluctuate a lot during the monitored period, but seem to stay under values of 4%.

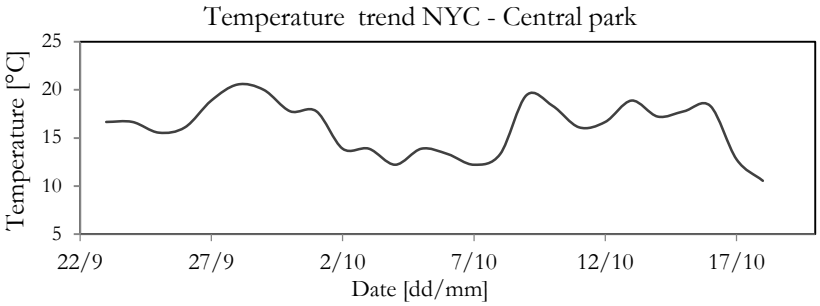

Figure 4.118 Temperature values during the monitoring period.

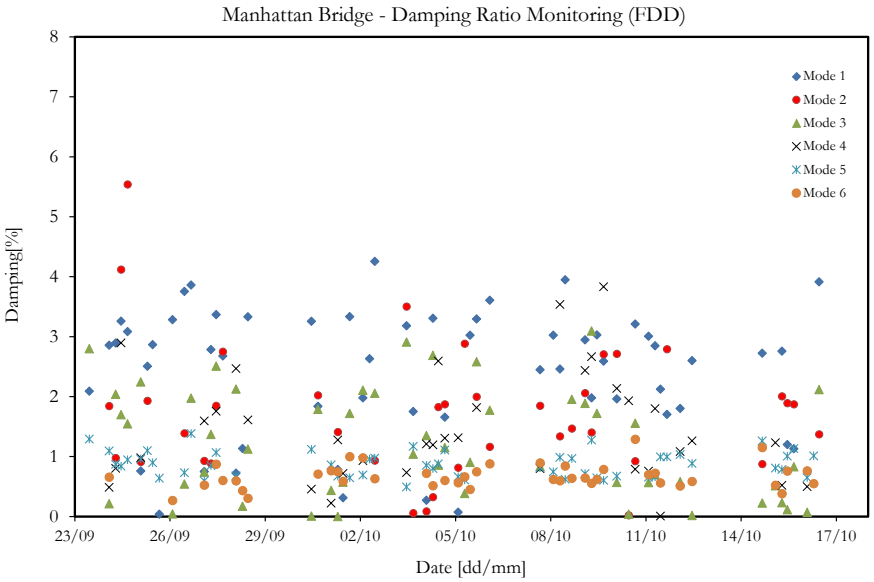

Figure 4.119 Damping ratios for the first 6 modes identified during the monitoring period.

4.7 Summary of the dynamic features and performance of OMA techniques

In this chapter, a wide picture of different applications has been presented. The main aim of this study was to understand the different behavior of several kinds of bridges and their affinity to modal analysis techniques. After looking into detail each analysis, it is now appropriate to compare their dynamic performance and their sensitivity to several system identification techniques. In fact, among others, so far we have seen the response of suspension bridges, slender concrete arch with upper deck bridges, masonry arch bridges, simply supported concrete bridges, reticular steel bridges and steel box girder bridges. Within these analysis, structural identification helped to investigate cases of demolition assessment, validation of a seismic retrofit, damage assessment, short and long term monitoring with acceleration and strain data and apparently model updating for each structure.

If we look at every group of bridges analyzed, we must certainly start with slender reinforced concrete (RC) arch bridges. We saw that this together with steel bridges were the most susceptible to ambient vibration. Indeed, it was clearly simple to distinguish structural modes using basic techniques as PSD or FDD analysis because very clear peaks were estimated. Both structures had similar features of natural frequencies and mode shapes; it was observed that in this kind of structures, the first mode is a transversal mode (that involves the central part of the arch) while the second mode is a clear vertical one. From this fact, it can obviously be stated that in order to extract the dynamic behavior (for seismic assessment) of these structures, it is important to monitor the arch vibrations installing sensors not only on the deck but also on the structural arch (operation not easily feasible). Once this is fulfilled, one can obtain clear results with simple data analysis.

Another case of concrete arch is the demolition of the Tronto bridge, where the system identification was a challenging process. Actually, during the demolition process, two measurement campaigns were performed and in both cases the FDD technique could barely find two modes. The PSD showed a flat plot due to noisy data, but most of all, due to low amplification of the principal modes. Being a squat structure, it is not willing to be identified, but an important contribution was given by the application of new OMA techniques which are capable of extracting the structural modes from noisy data. The standard SSI and FDD methods weren't capable of identifying the principal modes. After applying the ECCA, several modes were identified and only after performing a cluster

analysis, more than 20 structural modes were estimated. In both cases, before and after the demolition, the estimation of more modes confirmed the structural change taking place during the demolition process. The results revealed that every mode, after the partial demolition, tends to increase towards higher values.

Masonry arch bridges behave in different ways depending on the type of the structural components. In the case of high rise arches with high piers, it is easy to get dynamic estimations. In fact, standard system identification techniques perform very well in the cases when the sensors are positioned along the arches. Generally, in this kind of structures, the first mode is a transversal mode and the second one is longitudinal, due to the fact that the piers are very slender. An important role of system identification was also the seismic retrofitting assessment. By comparing the system identification before and after the intervention, it was possible to observe that the retrofit increased the seismic response of the bridge, revealing a higher stiffness shown by higher identified frequencies.

On the other hand, when we deal with squat masonry arch bridges, where the arch rise is very low, system identification, at least with conventional instruments, encounters a challenging aspect: the impossibility to get proper excitation of the principal structural modes. This was the case of Liberty Bridge, where the conventional techniques could hardly identify the first mode (12.24 Hz). Using the ECCA technique and clustering analysis, more vibrating modes were estimated, but only with a high model order and a stabilization diagram application. The rigidity of the structure and the squat piers contribute on the rigid deformation of the structure; the first modes involve only vertical deflections of the arches accompanied with slight longitudinal pier deflection. Although eventually some of the principal natural frequencies were identified, these kinds of stiff structures remain a challenging issue for operational modal analysis.

When we talk about steel structures and in particular for steel bridges, we know that they are very flexible and as a consequence easy to identify by ambient vibration methods. In the case of reticular steel bridges, due to symmetric geometry, few sensors can get pretty accurate results. In both reticular bridges analyzed, principal modes (first transversal and second vertical) were identified using both time and frequency domain techniques that showed excellent results. In fact, using the stabilization diagram, it appeared to be really simple to estimate the stable structural modes, and at the same time peaks of the PSD appeared to be very sharp. Experimental and theoretical models, in this case, were perfectly

correlated, so MAC values were close to unity. It is also noteworthy to mention that when we tried to plot damping ratios associated to the first modes in relation to the model's order, we could observe that damping is impressively stable without any jump, as usually seen in other structures. While ambient vibration is quite feasible for these systems, their disturbance by high speed heavy loads overpassing the bridge can cause high signal amplification and consequential distortion. The last consideration on reticular steel bridges is that their model calibration is very sensitive to mass participation, so models must be very detailed and the presence of the huge amount of rivets and rail connections must be taken into account.

Remaining in the field of steel bridges, when we talk about box girder structures, it reminds us of their massive orthotropic plates forming the caisson. The easiest way of carrying out dynamic tests on these structures is to deploy the instruments inside the caisson, attaching the sensors directly to the steel plates or bracing elements. Generally, all OMA techniques performed well in identifying structural modes, but FDD and ECCA could estimate more modes than standard SSI and PLSCF. The typical modes, are vertical bending mode shapes of the central span, then vertical modes of lateral spans and so on. Being in presence of a very flexible system, it was possible to perform an experimental modal analysis with the application of a heavy impact hammer that could excite vibrations over the gravity values. After constructing the FRF, a couple of modes (pretty close to the OMA) were identified even with this method, demonstrating the efficiency of both techniques. Since the system identification aim, in this case, was to update a FE model that could assess the deterioration under fatigue, together with the accelerometers, a strain monitoring system composed of 56 strain gauges was installed. Besides the fatigue monitoring, a challenging step was to obtain dynamic results from strain data. In fact, after applying filters and de-trending functions to the strain signals, conspicuous results were obtained. Ten principal structural modes were identified and compared with the conventional analysis of acceleration data. Since a high correlation was found, it was observed that for steel bridges these kind of cheap strain monitoring strategy can successfully be applied in order to estimate the global dynamic behavior of the system, together with the local dynamic strain monitoring. This was confirmed by the automated mode estimation developed in order to check the effectiveness of modal analysis by strain data. Thus, all principal modes were tracked during this several months of monitoring, showing a stable behavior.

Simply supported or continuous RC bridges are not as hard to identify as masonry bridges, but (for sure) harder than steel bridges. Actually, their dynamic behavior is an intermediate way between masonry and steel structures. When considering damaged RC bridges, their behavior is highly influenced by the level of damage present in the structural elements or in the constraints. So, only after considering these aspects, a model can be updated properly in order to catch the principal vertical bending modes of the central span and the side spans. After installing a permanent SHM system, the local and global behavior of the damaged structure was monitored under traffic load, environment effects and under seismic events as well. The implementation of automatic dynamic identification algorithms made it easy to control the modal parameters on time and to develop regression models that permitted the possible damage detection. During the survey, a stable performance was observed, highlighting only some frequency shifts during the seismic events.

Finally, suspension bridges are the most remarkable structures that cover this structural identification study. Suspension bridges have a considerably different dynamic behavior relatively to all the other classes previously described. The vibration levels, in such structures, can reach values of $1 m/s^2$ in operational conditions. Despite this, appropriate sensors must be used in order to pick out the low frequencies that characterize these systems, deploying wireless data loggers that overcome the problem of cable length (bridge spans of 0.5-0.9km). Deck, cables and towers must be monitored in order to extract the global behavior by means of high resolution data recording. Due to all these circumstances, it was possible to estimate over 20 structural modes within 0-1.5Hz on the Manhattan Bridge by using frequency and time domain techniques. The principal mode shapes involve the main truss in both transversal and vertical direction, followed by the vertical bending mode of lateral spans and with other vertical and torsional modes, too. In this case, at the beginning, the ECCA did not show a good performance but after applying appropriate filters and high model's order the same results of the FDD were obtained. Additional GPS sensors were collocated with the accelerometers, noticing large deflections (typical of suspension bridges) of all spans under transit train loads. This kind of deployment would not be applicable to the previous classes of bridges due to the fact that displacements taking place, are of one or two orders smaller than in suspension bridges. Eventually, the huge amount of monitoring data were subject to long term survey that revealed stable behavior, although some slight fluctuations related to environmental factors as wind and temperature were seen.

5

DISPLACEMENT AND ACCELERATION DATA FUSION

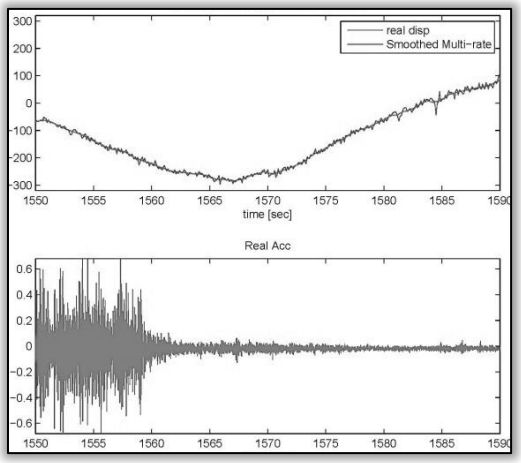

This chapter deals with the GPS displacement and FB acceleration data fusion. Combining together these kinds of measurements, a very accurate velocity and displacement estimate can be achieved through the implementation of the Kalman filter. Exploiting the smoothed results, a clear scene of the structural displacements taking place under the heavy traffic loads on the bridge is obtained. At the end of the Chapter, a future research topic is described.

During the last years of technology development, sensors for SHM (especially the wireless ones) are becoming very sophisticated for the particular use in civil infrastructures. Not only acceleration sensors but also displacement ones have become very accurate and provide high sampling frequencies compared to some years ago. The presence of both acceleration and displacement sensors, during measurement campaigns, provides a beneficial redundancy that can be utilized to better assess the structural behavior.

All over the world, there are already several advanced applications of SHM systems on bridges [52]. Trying to cover representative examples from different countries, the following applications can be mentioned: Tsing Ma Bridge in Hong Kong, Akashi Kaikyo Bridge in Japan, Seohae Bridge in Korea, Confederation Bridge in Canada, Commodore Barry Bridge in the United States and Oresund Bridge in Denmark.

In the context of this study, the Manhattan Bridge in the City of New York was subject to condition assessment via SHM system through FB accelerometers and GPS displacement sensors. During the monitoring process, several dynamic tests were carried out with different kinds of measurement sensors and different configurations. The main aim of the study is to give a structural assessment of the structure by evaluating its modal parameters from ambient output-only measurements, but also observing the displacement effects of transit trains over the bridge. The most interesting aspect is the fusion of the measured acceleration data with collocated displacement data, based on which accurate velocity and displacement data will be estimated with the Kalman filtering technique [47] [53] [54]. As the sampling frequencies of the various measurements are different, a multi-rate Kalman filter [12] is also used to process the data fusion. This technique, together with the dynamic analysis developed, will help to get consistent results which are used to update FE models representing the real behavior of the Manhattan Bridge.

5.1 Displacement results of Manhattan Bridge

At the same time of the acceleration observations, displacement motions with GPS sensors were also recorded. The GPS monitoring was able to capture the overall vertical deflection as well as the rotation of the deck (Figure 5.4) at mid-span due to passing subway trains. It is also interesting to observe the lateral displacement of the deck and the longitudinal deflection of the towers during these measurements.

As it can be perceived on Figure 5.1 there is relevant displacement in the vertical direction that overpasses 490mm during the MTA subway train passages. On the other hand, in transversal direction, lower motions take place, and in the longitudinal one there are nearly no significant displacements.

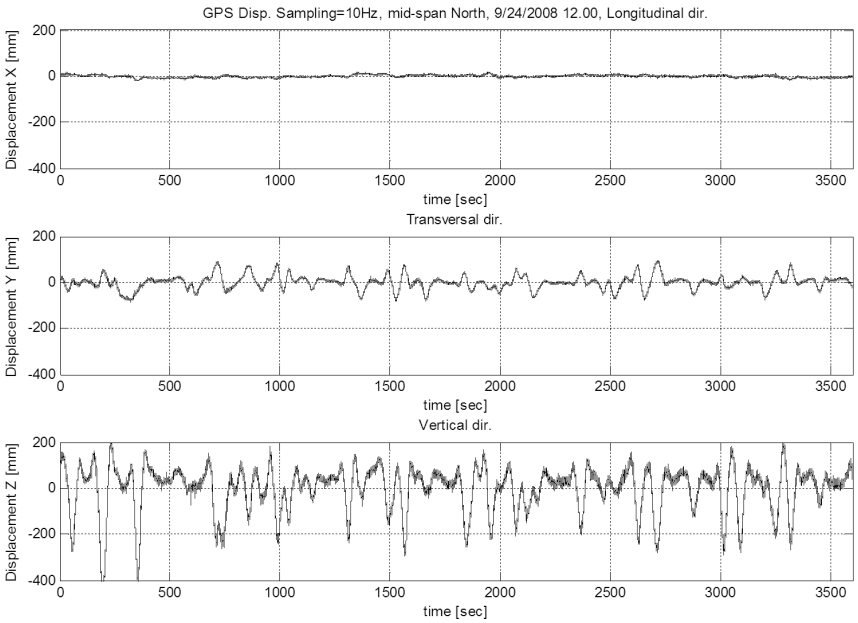

Figure 5.1 Sample mid-span (Manhattan-bound) GPS observation.

Figure 5.2 presents the vertical displacement of the central section of the main span resulting from the passage of a single train over the deck. The measured peak displacement at mid-span is 46.5 cm but it decreases moving towards the bridge piers. The train entrance can clearly be identified by the vertical deflections of the cross-sections of the side span because a positive vertical deformation of 15.3 cm can be detected when the train passes to the side span. Afterwards, the deflection begins to become negative until the peak of 46.5cm (when the train is in the middle span); then the deflection increases and returns positive after the train has passed.

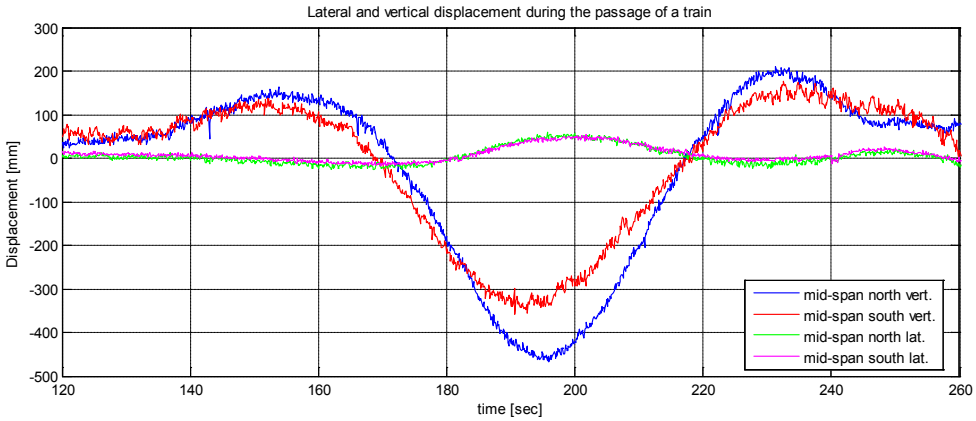

Figure 5.2 Displacements during the passage of a train.

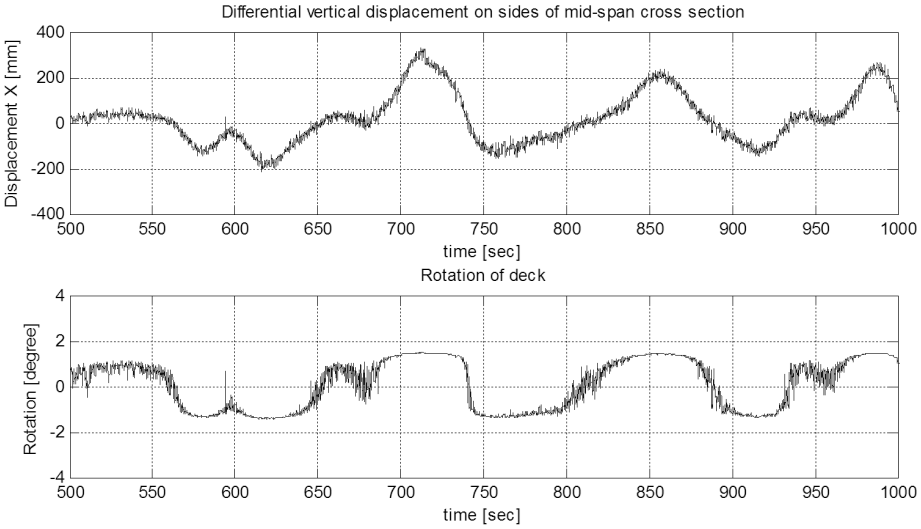

Figure 5.3 Differential deflection and rotation of the deck.

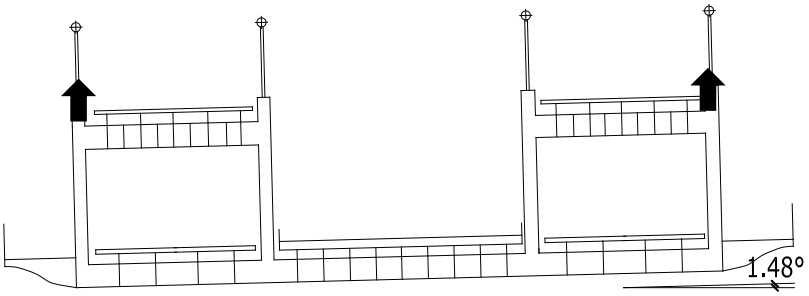

Figure 5.4 Maximum rotation of the cross section during a train route on the left tracks and sensor location.

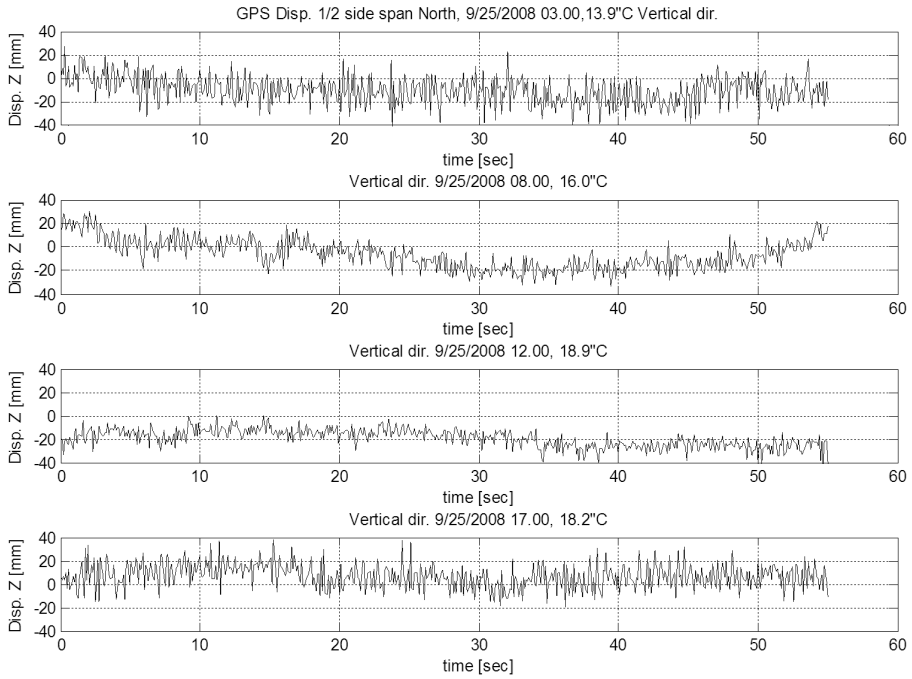

Figure 5.5 Displacement on 1/2-side span during four time-windows of a day-night period.

Although very hard to achieve, a window of displacements without train load deflections, was extracted from the original data during the cycle of a day-night recordings. During these windows, the temperature gradient is only 5 degrees Celsius, so the observations taken show that there is small influence of temperature in the structure's deflection. This was repeated during the 25 days of recordings resulting in the same behavior.

5.2 Data fusion via the Kalman filter implementation

The main aim of monitoring the structure was to assess the response of the bridge under a variety of factors such as heavy traffic and ambient vibrations, but also to reveal the possible combination of both methods of measurements, GPS and FBA. When it is possible to exploit the presence of collocated acceleration and displacement sensors, very accurate motion trend can be achieved.

With respect to the frequency of the structure, acceleration measurements are sensitive to vibrations of the bridge at its natural frequencies. Whereas,

the GPS capture slow deflections caused by the passage of traffic on the structure. The acceleration measurement has high-frequency resolution and high sampling frequency, in contrast with the low sampling of the displacement. The combination of these two kinds of measurements can improve the deformations observed, joining data samples at different frequencies. The use of the Kalman Filter algorithm made possible to estimate more accurate displacements and velocity, based on measured displacements and accelerations. Regarding acceleration and displacement measurements, the process can be modeled as:

$$\begin{aligned} \dot{x}(t) &= Ax(t) + Bu(t) + w, \\ y(t) &= Cx(t) + v \end{aligned} \tag{5.1}$$

Or in matrix form:

$$\begin{aligned} \begin{bmatrix} \dot{x} \\ \ddot{x} \end{bmatrix} &= \begin{bmatrix} 0 & 1 \\ 0 & 0 \end{bmatrix} \begin{bmatrix} x \\ \dot{x} \end{bmatrix} + \begin{bmatrix} 0 \\ 1 \end{bmatrix} \ddot{x}_m + \begin{bmatrix} 0 \\ 1 \end{bmatrix} v_a \\ y &= [1 \quad 0] \begin{bmatrix} x \\ \dot{x} \end{bmatrix} + v_d \end{aligned} \tag{5.2}$$

where $\ddot{x}_m$ and y are the measured acceleration and displacement, $\mathrm{v_a}$ and $\mathrm{v_d}$ are the associated noise measurement proportional to the noise covariance *(q and r)* with $w \sim (0, Q)$, $Q = \begin{bmatrix} 0 & 0 \\ 0 & q \end{bmatrix}$; $v \sim (0, R)$, $R = r$.

Considering the discretization of the state matrices at time steps T_a, the system becomes:

$$\begin{aligned} \begin{bmatrix} x_1(k+1) \\ x_2(k+1) \end{bmatrix} &= \begin{bmatrix} 1 & T_a \\ 0 & 1 \end{bmatrix} \begin{bmatrix} x_1(k) \\ x_2(k) \end{bmatrix} + \begin{bmatrix} T_a^2/2 \\ T_a \end{bmatrix} u(k) + \begin{bmatrix} T_a^2/2 \\ T_a \end{bmatrix} v_a(k) \\ y &= [1 \quad 0] \begin{bmatrix} x_1(k) \\ x_2(k) \end{bmatrix} + v_d(k) \end{aligned} \tag{5.3}$$

Written in short form:

$$\begin{aligned} x(k+1) &= A_T x(k) + B_T u(k) + w(k), \\ y(t) &= Cx(k) + v(k) \end{aligned} \tag{5.4}$$

The covariance matrices of the discrete system are

$$\begin{aligned} Q_d &= \int_0^{T_a} e^{A\tau} Q e^{A^T \tau} d\tau = \begin{bmatrix} qT_a^3/3 & qT_a^2/2 \\ qT_a^2/2 & qT_a \end{bmatrix} \\ R_d &= \frac{R}{T_a} \end{aligned} \tag{5.5}$$

These equations represent the formulation on which the Kalman Filter has been applied in order to estimate the displacement and velocity. The Kalman filter estimates a process by using a form of feedback control: the

filter estimates the process state at some time and then obtains feedback in the form of (noisy) measurements. As such, the equations for the Kalman filter fall into two groups: time update equations and measurement update equations [55].

The time update equations are responsible for projecting forward (in time) the current state and error covariance estimates to obtain the a priori estimates for the next time step. The measurement update equations are responsible for the feedback - i.e. for incorporating a new measurement into the a priori estimate to obtain an improved a posteriori estimate. The final estimation algorithm resembles that of a predictor-corrector algorithm for solving numerical problems.

Time Update:

$$\begin{aligned} x(k) &= Ax(k-1) + Bu(k) \\ P(k) &= AP(k-1)A^T + Q \end{aligned} \tag{5.6}$$

Measurement Update:

$$\begin{aligned} K(k) &= P(k)C^T[CP(k)C^T + R]^{-1} \\ x(k+1) &= x(k) + K(k)[y(k+1) - Cx(k)] \\ P(k+1) &= [I - K(k+1)C_T]P(k) \end{aligned} \tag{5.7}$$

where K is the Kalman gain. The process is repeated with the previous a posteriori estimates used to project or predict the new a priori estimates.

5.2.1 Multi-rate Kalman filter

When designing the overall fusion algorithm, we must take into consideration the multi-rate sensor collection, and design our algorithm appropriately. That is, we need to fuse inertial and GPS data, when we are sampling our inertial sensors at 200 Hz and receiving GPS data at 10 Hz. Here, the term “fusion” refers generally to the process of combining two sets of data to produce a better output. Sensor fusion can be accomplished with a filter, or it can be done by weighting each set of data based on a set of rules.

With a loosely coupled integration, the GPS measurements are preprocessed by a Kalman filter internal to the GPS receiver, which produces “GPS derived” geographic position and velocity as the receiver

outputs. That is, our Kalman filtered state vector is not directly dependent on the GPS receiver output. Instead, we use some sort of fusion algorithm to combine the output from the Kalman filtered inertial data and the GPS data.

If we assume that the displacement measurement sampling interval is T_d and the acceleration measurement sampling frequency is T_a, their ratio $T_d / T_a = M$ is an integer. Since no displacement is available between the times kT_d, this is equivalent to optimal filtering with arbitrary large displacement errors so $R_d^{-1} \to 0$ and hence $K \to 0$. Thus only the time update is performed:

$$\begin{aligned} x(k+1) &= A_d x(k) + B_d u(k) \\ P(k+1) &= A_d P(k) A_d^T + Q_d. \end{aligned} \tag{5.8}$$

When displacement measurements are available at time kT_d, both the time and measurement updates should be computed.

5.2.2 Smoothing

We will consider the recursive smoothing problem i.e., we wish to form the optimal estimate at some point back in the past, relative to the current measurement. In general, the recursive algorithms for smoothing are considerably more complicated than those for filtering and prediction. It works through a combination of the forward Kalman filtering and backward filtering over the entire sequence of available measurements.

The Kalman smoothing can be classified [18] in three categories:

- Fixed-interval smoothing. The time interval of measurements is fixed, and we seek optimal estimates at some interior points. Off-line problem.
- Fixed-point smoothing. In this case we seek an estimate at a single fixed point in time, and we think of the measurements continuing in indefinitely ahead of the point estimation.
- Fixed-lag smoothing. We imagine the measurement information proceeding on indefinitely with the running time variable t, and we

seek an optimal estimate of the process at a fixed length of time back in the past.

The smoothing algorithms investigated here are based on fixed-lag smoothing. Brown and Hwang [18] proposed a simple way to implement fixed-lag smoothing by using Rauch-Tung-Striebel (RTS) algorithm for fixed-interval smoothing in fixed-lag smoothing. We can first filter up to the current measurement and then sweeping back a fixed number of steps with the RTS algorithm. If the number of backward steps is small, this is a simple way and effective way of doing fixed-lag smoothing.

The recursive equations for the backward steps are

$$\hat{x}(k|N) = \hat{x}(k|k) + A_b(k)[\hat{x}(k+1|N) - \hat{x}(k+1|k)] \tag{5.9}$$

where $\hat{x}(k|N)$ is the smoothed estimate and A_b is the smoothing gain given by

$$A_b(k) = P(k|k)A_d^T P^{-1}(k+1|k). \tag{5.10}$$

5.2.3 GPS displacement and data fusion results

In the following figures, the estimated displacement taking place in one hour of measurement on the 24th of October 2008 at noon in different location of the bridge is reported. In Figure 5.6 the measurement for the mid-span north location is showed. The first panel represents the graphs of the actual displacement confronted with the estimated one by the Multi-rate Kalman Filter; whereas in the second section the smoothed version of the above signal is showed. Comparing the peaks of displacement and accelerations presented in the third panel, it can be observed that they perfectly match and point out that there are up to 20 passages of subway trains within one hour on the bridge.

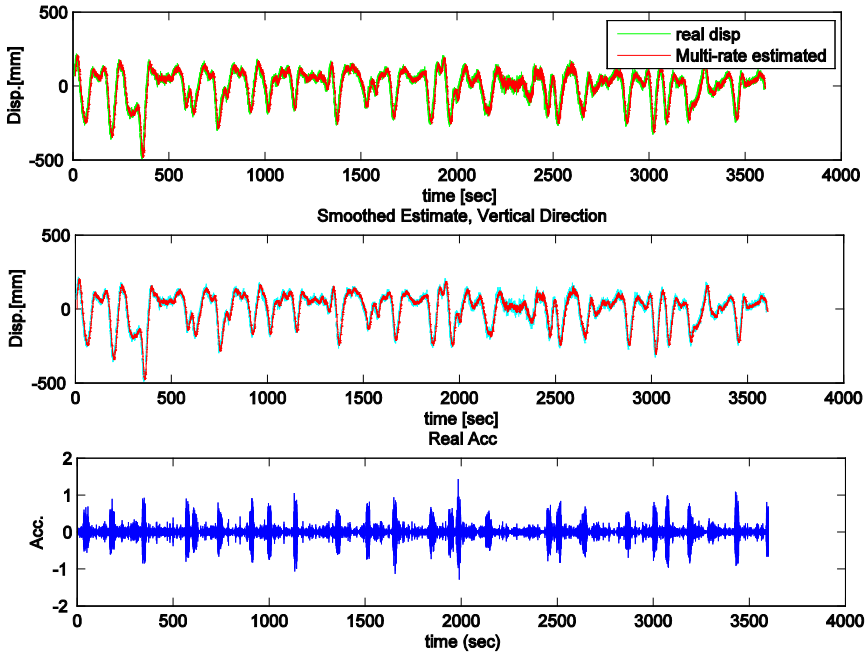

Figure 5.6 Multi-rate Kalman filtering results for the signal on North mid-span (vertical disp.).

Figure 5.6 and Figure 5.7 represent the whole displacement for the signal on North mid-span of the recording hour and a zoomed window of 40 seconds, respectively. It can be observed that the estimated smoothed displacement follows a more significant law of deflection, eliminating also the measurement noise present in the signal. The procedure not only reduces the GPS measurement noise, but it also gives the possibility to study the signal beyond its Nyquist frequency. As we know the Nyquist frequency is the bandwidth of a sampled signal, equal to half the sampling frequency, i.e. 5 Hz in our case. So it is impossible to get information beyond this frequency with our displacement measurements. Combining acceleration and displacement signals with the Multi-rate Kalman filtering, makes possible to detect frequencies higher than the low sampling rate. These results can also be observed in Figure 5.8 and Figure 5.9, where the deflection of the side span for an hour and a single train passage are depicted.

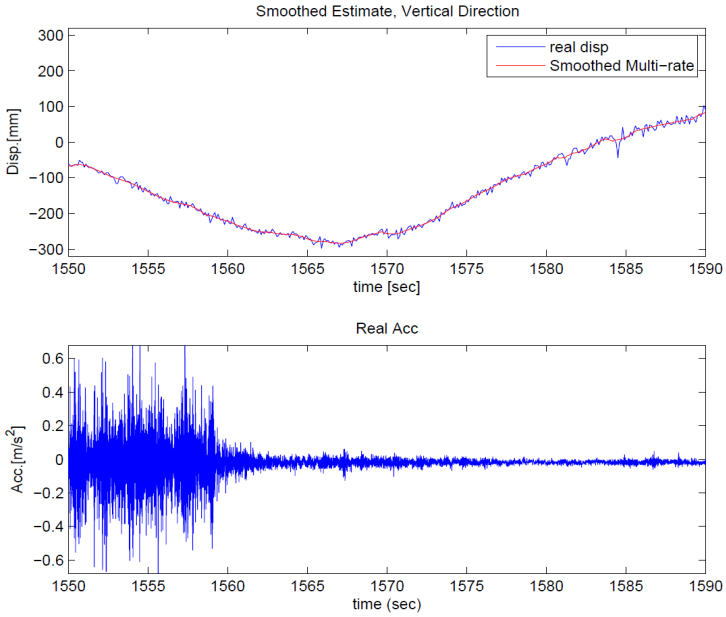

Figure 5.7 Smoothed Kalman filtering (displacement) on North mid-span and acceleration (40 sec Zoom).

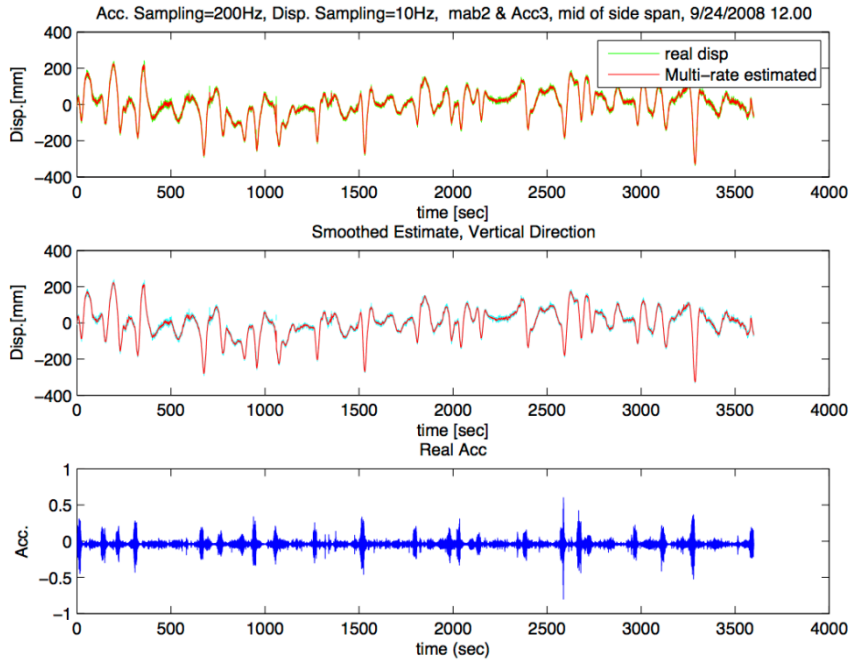

Figure 5.8 Multi-rate Kalman filtering results for the signal on South side-span (vertical disp.).

Other elements with interesting results can also be the towers. During monitoring, different disposition of GPS and acceleration sensors were used in order to detect the motion in all directions. It can be observed from Figure 5.11 that the towers are very flexible (designed on purpose). In fact, in the longitudinal direction when trains are overpassing the bridge some displacement of the order of 80mm can be noticed. Bearing in mind that the height of the tower is 100m we can say that it has 1 % out of plain deflection.

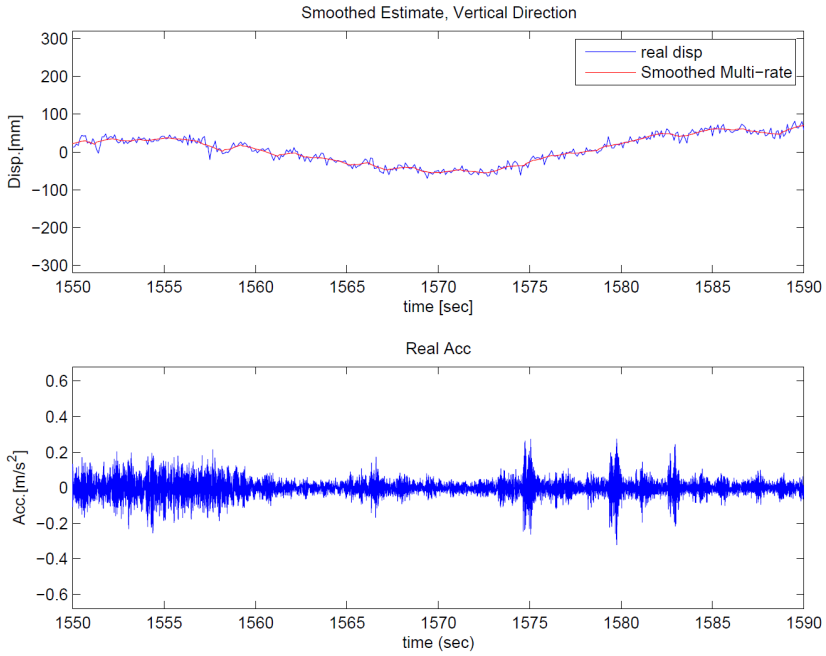

Figure 5.9 Smoothed Kalman filtering on South mid-span (40 sec Zoom).

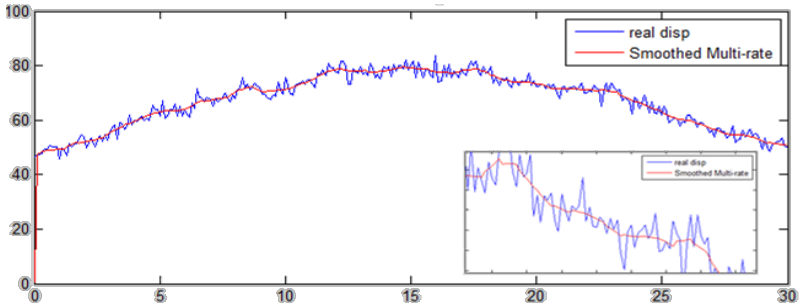

Figure 5.10 Multi-rate Kalman filtering on Brooklyn tower longitudinal deflection (30 sec Zoom).

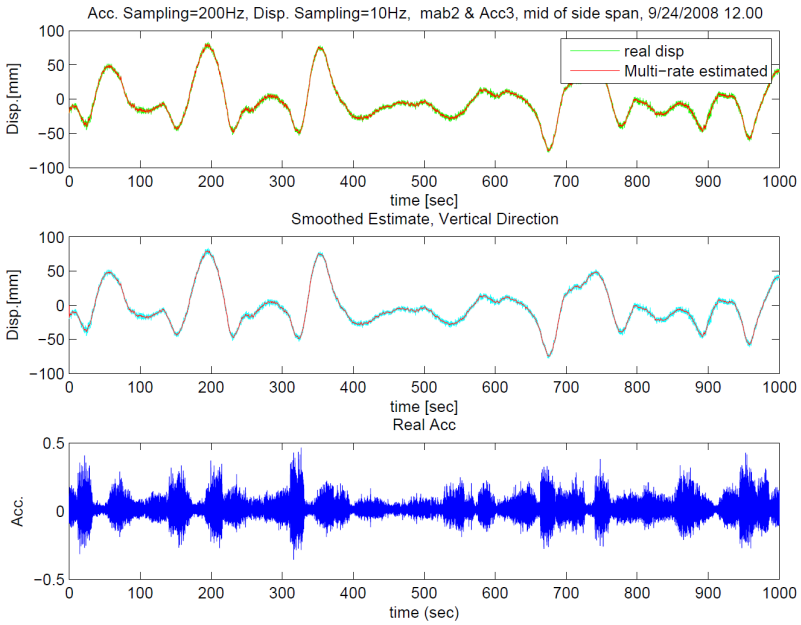

Figure 5.11 Multi-rate Kalman filtering on Brooklyn tower longitudinal deflection.

A Kalman filtering technique with multi-rate estimates has been applied to the Manhattan bridge data in order to accurately estimate the velocity and displacement from noise contaminated measures of the acceleration and displacement. The results show that this technique can estimate displacement precisely integrating the higher rates of accelerometers to the low sampling frequency of the GPS sensors. A maximum deflection of 49.0 cm has been observed on the deck during the passage of a transit train, applying to the structure not a negligible rotation transmitted in the form of torsional stresses on the deck.

It is also noticeable to comment the vertical displacement taking place in the middle of the central span during the monitoring period. In fact max min deflections taking place each day on the bridge are plotted in Figure 5.12 also related to temperature.

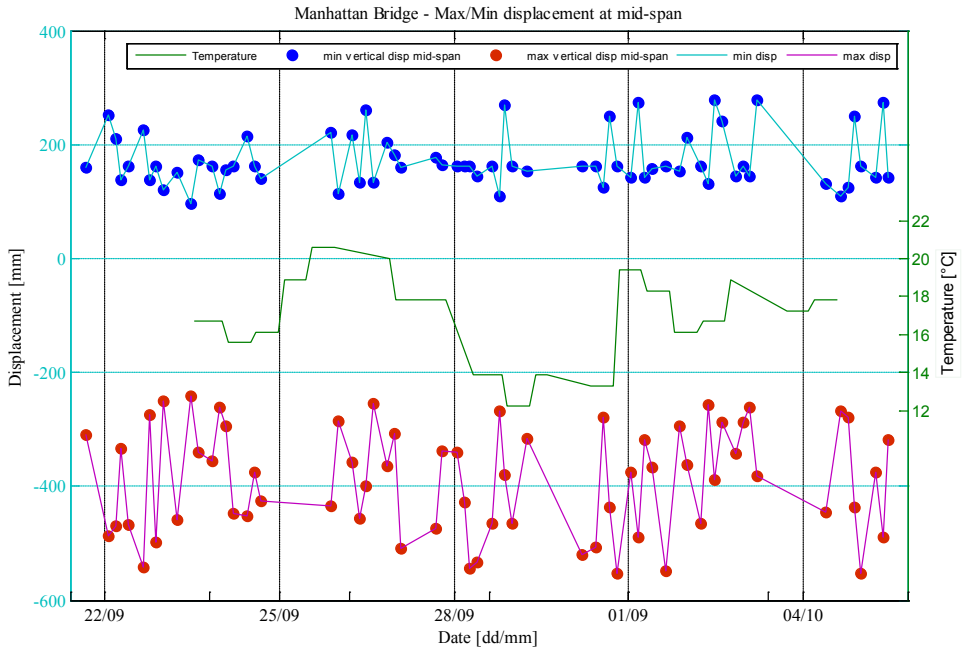

Figure 5.12 Maximum and minimum vertical displacement in the mid-span during the monitoring period.

5.3 Non-collocated sensor problem as a future research

As exposed in the previous section, in presence of multiple sensors, highly accurate results can be estimated for the response of a structure. Nowadays, sensors allow to obtain measurements with high sampling rate, but they still appear to be expensive. In case of limited sources, acceleration (or velocity) sensors cover almost all the structural nodes, while displacement GPS sensors are positioned in few nodes. This can be an unfavorable situation when a particular node of the structure must be measured, and there are only acceleration measures available. So the non-collocated problem, to be defined in this section is connected to the problem of estimating displacement features of a node where we actually have only acceleration measures. *Three possible solutions will be introduced here, reminding that this part of study is just at the beginning, but of a significant interest for the author.*

On the basis of the **first solution** stands the theoretical formulation of the modal contribution, in order to extract the behavior of the structure where we don□t have measurements, exploiting the available displacement data and the identified modal parameters. The basic idea will be presented in the following simple example.

A three-mass system [56] is used mainly for illustration purposes, and to make concepts easy to follow. Its simplicity allows for easy analysis, and for straightforward interpretation. The system is shown in Figure 5.13. In this figure $m_1, m_2,$ and m_3 represent system masses, k_1, k_2, k_3 are stiffness coefficients, while d_1, d_2, d_3 are damping coefficients.

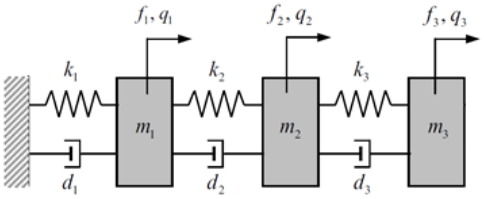

Figure 5.13 A simple 3-dof dynamic system.

Let n_d be the number of degrees of freedom of the system (linearly independent coordinates describing the finite-dimensional structure), let r be the number of outputs, and let s be the number of inputs. A flexible structure in nodal coordinates is represented by the following second-order matrix differential equation:

$$\begin{aligned} M\ddot{x} + C\dot{x} + Kx &= B_T u \\ y &= C_T x + D_T \dot{x} \end{aligned} \tag{5.11}$$

In this equation x is the $n_d x1$ nodal displacement vector; $\dot{x}$ is the nodal velocity vector; $\ddot{x}$ is the nodal acceleration vector; u is the s $x1$ input vector; y is the output vector, r $x1$; M is the mass matrix, n_d x n_d ; C is the damping matrix, n_d x n_d; and K is the stiffness matrix, n_d x n_d. The input matrix B_T is n_d x s, the output displacement matrix B_T is r x n_d, and the output velocity matrix D_T is r x n_d. For this system we selected masses $m_1 = m_2 = m_3 = 1$, stiffness $k_1 = k_2 = k_3 = 3$ and a damping matrix proportional to the stiffness matrix, $0.01K$.

There is a single input force at mass 3, and four outputs: displacement and velocity of mass 1 and velocity of masses 2 and 3.

The stiffness and damping matrices are:

$$K = \begin{bmatrix} k_1 + k_2 & -k_2 & 0 \\ -k_2 & k_2 + k_3 & -k_3 \\ 0 & -k_3 & k_3 \end{bmatrix}, \quad C = \begin{bmatrix} c_1 + c_2 & -c_2 & 0 \\ -c_2 & c_2 + c_3 & -c_3 \\ 0 & -c_3 & c_3 \end{bmatrix}$$

The natural frequency matrix and the modal matrix are:

$$\omega^2 = \begin{bmatrix} 3.1210 & 0 & 0 \\ 0 & 2.1598 & 0 \\ 0 & 0 & 0.7708 \end{bmatrix} \qquad \Phi = \begin{bmatrix} 0.5910 & 0.7370 & 0.3280 \\ -0.7370 & 0.3280 & 0.5910 \\ 0.3280 & -0.5910 & 0.7370 \end{bmatrix}$$

In order to obtain a state representation from the nodal model as in equation of motion we rewrite equation (5.11) as follows (assuming that the mass matrix is nonsingular):

$$\ddot{x} + M^{-1}C\dot{x} + M^{-1}Kx = M^{-1}B_T u$$
$$y = C_T x + D_T \ddot{x}$$

We define the state vector x as a combination of the structural displacements, x, and velocities, ẋ, i.e.,

$$\boldsymbol{x} = \begin{Bmatrix} x_1 \\ x_2 \end{Bmatrix} = \begin{Bmatrix} x \\ \dot{x} \end{Bmatrix}$$

And thus

$$\dot{\boldsymbol{x}} = A\boldsymbol{x}(t) + B\boldsymbol{u}(t) \quad \dot{x_1} = x_2$$
$$\dot{x}_2 = -M^{-1}Cx_2 - M^{-1}Kx_1 + M^{-1}B_T u$$
$$y = C_T x_1 + D_T x_2$$

Combining the above equations into one, we obtain the state equations, with the following state-space representation:

$$A = \begin{bmatrix} 0 & I \\ -M^{-1}K & -M^{-1}C \end{bmatrix}, \qquad B = \begin{bmatrix} 0 \\ M^{-1}B_T \end{bmatrix}, \quad C^* = [C_T \quad D_T]$$

$$\begin{bmatrix} 0 & 0 & 0 & 1 & 0 & 0 \\ 0 & 0 & 0 & 0 & 1 & 0 \\ 0 & 0 & 0 & 0 & 0 & 1 \\ -6 & 3 & 0 & -0.06 & 0.03 & 0 \\ 3 & -6 & 3 & 0.03 & -0.06 & 0.03 \\ 0 & 3 & -3 & 0 & 0.03 & -0.03 \end{bmatrix} \quad \begin{bmatrix} 0 \\ 0 \\ 0 \\ 0 \\ 0 \\ 1 \end{bmatrix} \quad \begin{bmatrix} 1 & 0 & 0 & 1 & 0 & 0 \\ 0 & 0 & 0 & 0 & 1 & 0 \\ 0 & 0 & 0 & 0 & 0 & 1 \end{bmatrix}$$

Thus we can determine the transform function. The magnitude and phase of the transfer function are plotted

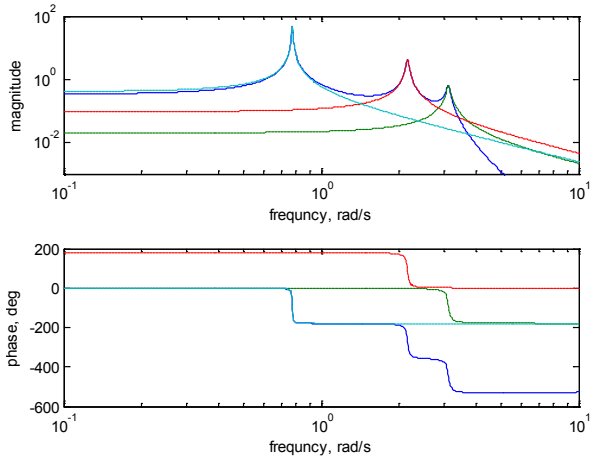

Figure 5.14 The displacement transfer functions of single modes: (a) Magnitudes show three resonance peaks; and (b) phases.

From dynamics theory [57] [58] [59] it is known that the modal participation factor is an important element to express displacement and acceleration by:

$$\boldsymbol{u} = q_1(t)\phi_1 + q_2(t)\phi_2 + \ \ldots + \ q_n(t)\phi_n \ = \sum_n q_n(t)\phi_n \tag{5.12}$$

where $u_n = q_n(t)\phi_n$ is the n-th modal displacement response component, referring to the modal contribution to the total displacement response; ϕ_n is the n-th natural vibration mode; q_n is the modal coordinate.

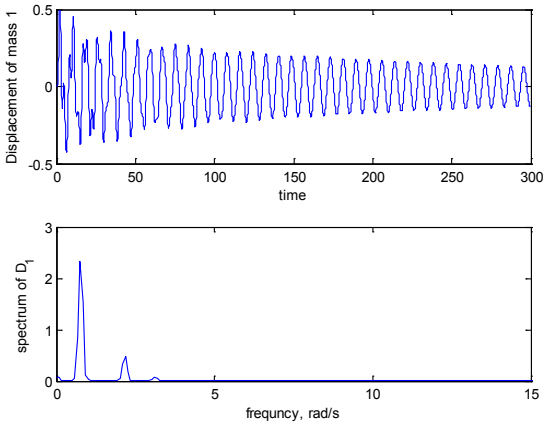

Figure 5.15 Impulse response of the simple system: (a) Time history of displacement measurement at mass 1; and (b) its spectrum.

In our case the previous expression would be:

Measurement equation:

$$\begin{bmatrix} x_1 \\ x_2 \\ x_3 \\ \dot{x_1} \\ \dot{x_2} \\ \dot{x_3} \end{bmatrix} = \begin{bmatrix} \phi_{11} & \phi_{12} & \phi_{13} & \phi_{14} & \phi_{15} & \phi_{16} \\ \phi_{21} & \phi_{22} & \phi_{23} & \phi_{24} & \phi_{25} & \phi_{26} \\ \phi_{31} & \phi_{32} & \phi_{33} & \phi_{34} & \phi_{35} & \phi_{36} \\ \phi_{41} & \phi_{42} & \phi_{43} & \phi_{44} & \phi_{45} & \phi_{46} \\ \phi_{51} & \phi_{52} & \phi_{53} & \phi_{54} & \phi_{55} & \phi_{56} \\ \phi_{61} & \phi_{62} & \phi_{63} & \phi_{64} & \phi_{65} & \phi_{66} \end{bmatrix} \begin{bmatrix} q_1 \\ q_2 \\ q_3 \\ \dot{q_1} \\ \dot{q_2} \\ \dot{q_3} \end{bmatrix}$$

or written in short form:

$$\boldsymbol{y}(t) = C\boldsymbol{x}(t)$$

This, as it is shown later, will be our measurement equation of the state space model. On the other hand we have the equation of motion [60]:

$$M\ddot{x}(t) + C\dot{x}(t) + Kx(t) = f(t)$$

A more convenient way of solving this is to define a state vector z(t) as

$$z(t) = \begin{Bmatrix} x(t) \\ \dot{x}(t) \end{Bmatrix}, \quad A = \begin{bmatrix} 0 & I \\ -M^{-1}K & -M^{-1}C \end{bmatrix}, \quad F(t) = \begin{Bmatrix} 0 \\ M^{-1}f(t) \end{Bmatrix}.$$

So the equation of motion can be written:

$$\dot{\boldsymbol{z}}(\boldsymbol{t}) = \boldsymbol{A}\boldsymbol{z}(\boldsymbol{t}) + \boldsymbol{F}(\boldsymbol{t})$$

The normal mode method [60] represents the response as a summation of normal mode coordinates, and the in state space form it can be written as

$$z(t) = \sum_{j=1}^{2n} \phi_j q_i(t) = \Phi Q$$

So, the previous equation becomes

$$\Phi \dot{Q}(t) = A\Phi Q(t) + F(t)$$

Pre-multiplying by Φ^{-1}

$$\dot{Q}(t) = \Phi^{-1} A\Phi Q(t) + \Phi^{-1} F(t)$$

that can be written in 2n uncoupled first-order linear differential equations, that is,

$$\dot{q_r}(t) = S_r q_r(t) + \sum_{j=1}^{n} \phi_j{}^T \mathrm{f}_j(t)$$

with $\mathrm{S_r} = -\omega_r \xi_r + \mathrm{i}\omega_r \sqrt{1-\xi^2}$, the eigenvalues of A and ϕ_j the eigenvectors.

State equation:

$$\begin{bmatrix} \dot{q}_1 \\ \dot{q}_2 \\ \dot{q}_3 \\ \ddot{q}_1 \\ \ddot{q}_2 \\ \ddot{q}_3 \end{bmatrix} = \begin{bmatrix} S_1 & & & & & \\ & S_2 & & & & \\ & & S_3 & & & \\ & & & S_1 & & \\ & & & & S_2 & \\ & & & & & S_3 \end{bmatrix} \begin{bmatrix} q_1 \\ q_2 \\ q_3 \\ \dot{q}_1 \\ \dot{q}_2 \\ \dot{q}_3 \end{bmatrix} + \begin{bmatrix} \phi_{11} & \phi_{12} & \phi_{13} & \phi_{14} & \phi_{15} & \phi_{16} \\ \phi_{21} & \phi_{22} & \phi_{23} & \phi_{24} & \phi_{25} & \phi_{26} \\ \phi_{31} & \phi_{32} & \phi_{33} & \phi_{34} & \phi_{35} & \phi_{36} \\ \phi_{41} & \phi_{42} & \phi_{43} & \phi_{44} & \phi_{45} & \phi_{46} \\ \phi_{51} & \phi_{52} & \phi_{53} & \phi_{54} & \phi_{55} & \phi_{56} \\ \phi_{61} & \phi_{62} & \phi_{63} & \phi_{64} & \phi_{65} & \phi_{66} \end{bmatrix}^T \begin{bmatrix} 0 \\ 0 \\ 0 \\ 0 \\ 0 \\ u_3 \end{bmatrix}$$

This formulation can be used in our case to construct the state equation of our state space model i.e.,

$$\dot{\boldsymbol{x}} = A\boldsymbol{x}(t) + B\boldsymbol{u}(t)$$

that, with the previous measurement equation, becomes our state space model:

$$\begin{aligned} \dot{\boldsymbol{x}} &= A\boldsymbol{x}(t) + B\boldsymbol{u}(t) \\ \boldsymbol{y}(t) &= C\boldsymbol{x}(t) \end{aligned} \tag{5.13}$$

The discrete time state-space model corresponds to:

$$x_T(k) = A_T \boldsymbol{x_T}(K-1) + B_T \boldsymbol{u_T}(k-1)$$

$$\boldsymbol{y_T}(k) = C_T \boldsymbol{x_T}(k)$$

The input vector u(t) here is a unit impulse force at mass nr. 3. This makes the state-space representation of the formulation on which a discrete-time Kalman filter can be applied to obtain estimates of the modal contributions and then acceleration information in any node of the structure.

The implementation herein presented was applied with a chosen sampling rate of 10 Hz for simplicity, in order to analyze its contribution afterwards with the displacement that has the same sampling frequency. A white noise process with 10% RMS noise-to-signal ratio is superimposed to both the exact displacement and velocities.

The following figures show the Kalman filtering results. In order, first it can be seen the modal contribution factors extracted from the analysis, than the

representation of the estimated displacements for the three dofs. Furthermore, the comparison graphs for the displacement of the first mass utilizing the normal Kalman filter and then the smoothed version are presented. The last figure shows the Kalman estimate error.

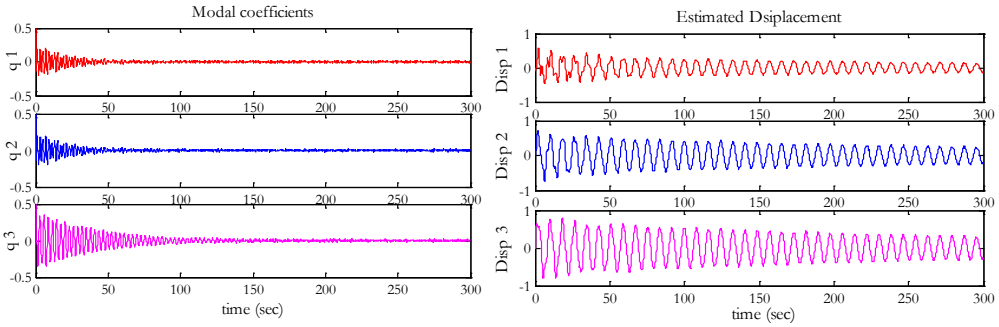

Figure 5.16 Estimated modal coefficients and displacement for the three modes.

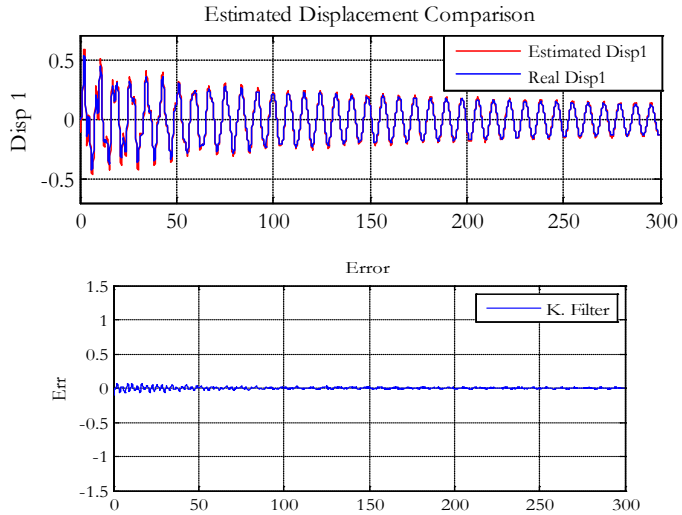

Figure 5.17 Comparison between estimated and real disp. at mass 1 and its error.

The **second possible solution** proposed here deals with the use of the system matrices. The main difficulty in estimating states for a dynamic system is to identify matrixes M, K, D that relate accelerations to velocities and displacement quantities, but revealed in some researches [61] [62]. Furthermore, if we determine the state matrices A and B in equation (5.13), for example extracted by any system identification technique seen in Chapter 3, the problem can easily be solved by applying a Kalman filter algorithm. For the stochastic case, where there is no B matrix but a K (not stiffness) matrix, during this study it was noticed that B and K were similar.

However, if the assumption of performing particular system identification techniques [61] [62] (to obtain M, M and K) is true or matrices A and B are identified, they can be used in the following discrete equations:

$$x(k+1) = A_T x(k) + B_T u(k) + w(k),$$
$$y(t) = Cx(k) + v(k)$$

where the Kalman filter can be applied to estimate displacements.

Let us consider again the 3-dof example where only velocities (real velocities with 10-20% RMS noise) are measured from the three masses. By applying the aforementioned procedure we can estimate the displacements on every mass.

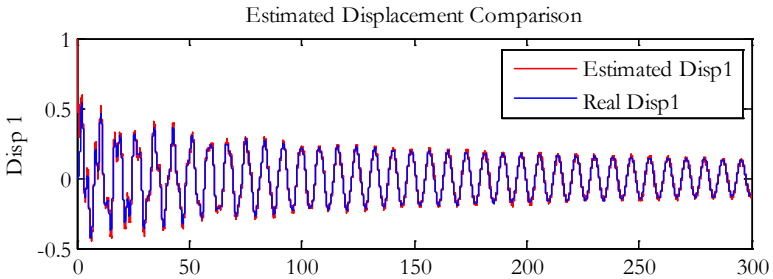

Figure 5.18 Comparison between estimated and real disp. at mass 1 (2nd solution).

The **third possible solution** proposed, similarly to the first one, is based on the knowledge of the modal properties of the structure but applied with the concepts of the transfer function.

Suppose that we want to determine the displacement at location $\mathbf{r}$, that the accelerations (or velocities) component $\ddot{\boldsymbol{u}}$ at locations $\boldsymbol{r}_m$ are measured, and that the response of the body can be approximated by a finite number of n modes. The equation (5.12), for the two cases can be written as:

$$\boldsymbol{u}(r,t) = \sum_n q_n(t)\phi_n(r) \qquad \ddot{\boldsymbol{u}}(r_m,t) = \sum_n q_n(t)\ddot{\phi}_n(r_m) \tag{5.14}$$

The second of the previous equations is a linear algebraic equation in the n unknowns q_n. If the $\ddot{\phi}_n$ were known, using n accelerometers (or velocities) would allow to solve for these unknowns. If we consider the transfer functions between the displacement at location $\mathbf{r}$, which is to be determined, and the n measured $\ddot{\boldsymbol{u}}$ at r_m locations we can reach a solution. Taking the Fourier Transforms of (5.14):

$$\boldsymbol{U}(r,w) = \sum_n Q_n(w)\phi_n(r) \qquad \ddot{\boldsymbol{U}}(r_m,w) = \sum_n Q_n(w)\ddot{\phi}_n(r_m) \tag{5.15}$$

where $Q_n(w)$ is the Fourier Transform of $q_n(t)$. Thus we have: $\frac{\boldsymbol{U}(r,w)}{\ddot{\boldsymbol{U}}(r_m,w)}$. Assuming that the modes of the structure are uncoupled, that is at each one of the resonant frequency w_j only the contribution of the mode j is significant, we have the transfer function ratio:

$$\frac{\boldsymbol{U}(r,w)}{\ddot{\boldsymbol{U}}(r_m,w)} = \frac{\phi_n(r)}{\ddot{\phi}_n(r_m)}$$

Therefore, with the mode shape functions $\phi_n(r)$ known and the n transfer functions measured, we can use the previous equation to calculate the coefficients $\ddot{\phi}_n(r_m)$.

In order to obtain the displacement u at a generic location $\mathbf{r}$ of a structure the sequent steps should be taken [63]:

a) Identification of n modes of vibration and their mode shapes $\phi_n(r)$
b) Have at least n velocity (similar to acceleration) sensors at locations $\boldsymbol{r}_m$.
c) Determine the n transfer function values $\frac{\boldsymbol{U}(r,w)}{\ddot{\boldsymbol{U}}(r_m,w)}$ after measuring the displacement $\boldsymbol{u}(r,t)$ in few locations.
d) Use the transfer function to calculate the coefficients $\ddot{\phi}_n(r_m)$.
e) Use the velocity signals under operational conditions to solve (5.14) for the $q_n(t)$'s. Substitute these values in (5.14) to get the desired displacement $\boldsymbol{u}(r_m,t)$.

This technique was applied to the three-dof example. Displacement was estimated in all nodes through measurements of velocity in all nodes and measurement of displacement in only one node. Thus, the transfer function between displacement in node one and all the other velocities in all nodes, made possible to calculate the coefficients $\ddot{\phi}_n(r_m)$. These coefficients were in turn used to solve equation (5.14) for $q_{1-3}(t)$'s. Finally, these were substituted in equation (5.14) to reconstruct the displacement signal.

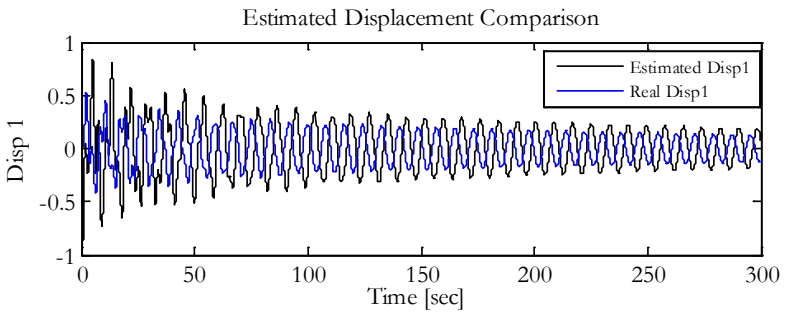

Figure 5.19 Comparison between estimated and real disp. at mass 1(3rd option).

As can be seen from the plots, there is a shift on the estimated displacement that will be object of further work in the future.

All the presented methods need to be better validated and eventually a future application on a real structure will be proposed.

5.4 Conclusions on Chapter 5

In this chapter, deflection monitoring of the Manhattan Bridge and its application to the data fusion theory with acceleration measurements was presented. In the first part of the chapter we saw the relevant displacement activity taking place on the main span of the suspension bridge. Besides the vertical deflections, the transversal direction on the steel truss and the longitudinal direction on the towers were also observed. Over 20 passages of transit trains with deflections that could reach 50cm in the vertical direction were noticed. Although in transversal direction the deformations were smaller, they caused a considerable torsional rotation of the deck transmitted in form of fatigue stresses on each structural element.

In the second part, exploiting the presence of both acceleration and displacement sensors, their data fusion has been carried out. By applying a multi-rate Kalman filter, displacement and acceleration data have been combined in order to improve the deformation results by eliminating noise. The resulting displacement and velocity data, besides being free of noise, give the possibility to study the signal beyond its Nyquist frequency limited by the low rate of displacement sampling. The results show that this technique can estimate displacement precisely integrating the higher rates of accelerations to the low sampling frequency of the GPS sensors.

Finally in the last part of the chapter, the non-collocated sensor problem is described as a start for future research. At the basis of the problem stands the fact that GPS sensors are expensive and their deployment is limited to a few position. So, in order to get displacement estimations on nodes where we have only acceleration measurements, three methods are proposed, described with a simple 3-dof example. The first method proposed, based on modal contribution factors and modal parameters, show a good correlation between the estimated and the real displacement. The second method, based on system identification and determination of state matrices, is a more robust procedure that is able to estimate all desired displacements. The third technique based on the transfer function of different signals did not perform as well as the previous. Once one of the methods has been consolidated to work properly, it will be applied on a simplified model (17-dof) of the Manhattan Bridge, where we have all nodes covered by acceleration measurement and only few points of displacement measured. So, the ultimate goal will be the assessment of deflections in locations where there are not such sensors.

6

CONCLUSIONS

This study discussed system identification and data fusion analysis in civil infrastructures. The research introduced the state-of-the-art of stochastic system identification methods – with time and frequency domain – along with their theoretical and experimental aspects.

Once familiarized with the random nature of vibrating signals, their relation to stochastic state-space models and to the Kalman filter for stochastic estimation has been introduced. Additionally, clear theoretical basics of dynamic systems were described, including not only FRF and IRF but also controllability and observability matrices that led to the system identification problem. For the purpose of theoretical interpretation and investigation of system identification techniques, the eigensystem realization procedure and its application to the stochastic case has been exposed firstly. The use of stochastic system identification to estimate the modal parameters of a structure excited by white noise has been exploited during the past 20 years to develop techniques such as FDD, data-SSI, cov-SSI and PLSCF which are explained in Chapter 3 and later applied in Chapter 4.

Although great theoretical development has been reached in the field of modal parameter identification, in this work, it was verified that still not a negligible performance difference exists when various modal techniques are used in real applications. In fact, during the dynamic tests on ten bridges, the research was focused on three main issues: a) to compare the dynamic behavior of different kinds of structures; b) to compare the sensitivity (or performance) of various modal techniques applied and c) to improve their performance with advanced statistical analysis. We have examined the response of suspension bridges, slender concrete arch with upper deck bridges, masonry arch bridges, simply supported concrete bridges, reticular steel bridges and steel box girder bridges. Within these analysis, structural identification helped to investigate cases of demolition assessment,

validation of a seismic retrofit, damage assessment, short and long term monitoring with acceleration, velocity and strain data and finally model calibration for each structure. Automated FDD and SSI techniques were developed in order to analyze in real time the global behavior of the monitored structures. Furthermore, the combined ECCA cluster analysis and automatic system identification for long term monitoring could get highly accurate modal parameter recognition. The three automatic procedures were finally validated with a manual repeated system identification, showing a high accuracy. This result was then used in the autoregressive models to validate/estimate the behavior of the structure and finally detect possible significant changes in the structural properties. The results allow to conclude that the environmental effects change the dynamic response of the structure. The ambient temperature, the relative humidity and the traffic excitation were correlated to the natural frequency and displacement. The Auto Regressive models estimated in order to evaluate the environmental effects could simulate the natural frequencies. Temperature has a significant effect on the dynamic response, but in a short term, excitation also plays an important role in frequency fluctuation due to day-night traffic cycle. The natural frequency observation seems to be a consistent method for damage detection, although no damage occurred during the measurement.

What was noticed by these extensive analyses can be summarized into these points:

- → Slender concrete arch bridges and steel bridges are highly susceptible to ambient vibration. All OMA techniques performed very well in identifying structural modes. Indeed, it was clearly simple to distinguish structural modes by using basic techniques, as PP and FDD, or advanced ones such as data-SSI or ECCA. Being such flexible structures, their first modal deformations are generally bending mode shapes, in vertical or transversal direction. Without the need of sophisticated tools as stabilization diagrams or cluster analyses, one can easily estimate accurately all the structural modes and subsequently calibrate FE models or develop automatic system identification for SHM. A remarkable property of such structures is the impressive stability of damping ratios estimation related to the model's order. In the case of steel bridges, even more features were explored by system identification with experimental impact tests, and most of all with strain data. Modal Analysis was applied to strain data, and the automated identification techniques developed, helped to demonstrate the effectiveness of this last discovery that can turn the SHM in a very cheap practice in steel bridges.
- → Squat concrete or masonry arch bridges are challenging structures from a system identification point of view. Standard

methods in the frequency domain are not suitable for modal parameter identification due to weakly exited modes. In one case, although the standard SSI could get some more modal information, only after applying the ECCA's stabilization diagram and after performing two cluster analysis, more than 12 structural modes were estimated. This detailed analysis could estimate the structural change taking place during the demolition process on that particular structure.

→ High rise masonry (or stone) arch bridges are more rigid than concrete arch bridges, but their dynamic behavior is more or less similar to them. Standard system identification techniques perform very well in these cases when the sensors are positioned along the arches, but high model orders are preferred to accurately estimate structural modes. Generally, in this kind of structures, the first mode is a transversal mode and the second one is a longitudinal mode.

→ Simply supported or continuous r.c. bridges are not as hard to identify as masonry bridges; their dynamic behavior is an intermediate way between masonry and steel structures. Both frequency and time domain techniques can be applied, but subspace methods are the preferred methods in estimating their typical principal vertical bending modes. Automated Modal Monitoring Algorithms developed, in the time and frequency domain, appeared to work very well in this kind of structure.

→ Suspension bridges have a considerably different dynamic behavior relative to all the other classes previously described. High levels of vibration, low natural frequencies and wind excitation are possible to be estimated only with high resolution data recordings. In general, principal mode shapes involve the main truss (and towers) in both transversal and vertical direction, followed by the vertical bending mode of lateral spans and with other vertical and torsional modes as well. In this case, PSD and SV line -peaks are quite sharp and clear, so they can be used to get accurate estimates, whereas SSI methods needed to be accompanied by filtering analysis and high model orders before obtaining accurate results. Eventually, the huge amount of monitoring data were subject to long term survey that revealed stable behavior; although, some slight fluctuations related to environmental factors, as wind and temperature, were seen.

When additional GPS sensors are collocated with the accelerometers, typical large deformations of suspension bridges can be observed. Besides the vertical deflections, transversal movements are also detected during the passage of heavy eccentric loads, and high longitudinal movements of the tower's top are observed with maximum load on mid-span.

The presence of both acceleration and displacement sensors during measurement campaigns provide a beneficial redundancy that can be utilized to better assess the structural behavior. By applying a multi-rate Kalman filter, displacement and acceleration data have been combined in order to improve the deformation results by eliminating noise. The resulting displacement and velocity data, apart from being free of noise, give the possibility to study the signal beyond its Nyquist frequency, limited by the low rate of displacement sampling. The efficiency of this technique was demonstrated through the application on the measurements of the Manhattan Bridge.

Future Research

Future research is certainly needed to further improve the treatments presented in this study. First of all, other sensitivity analyses must be done with the various modal identification techniques and possibly improve the automatic modal analysis procedures to use in more structures and in SHM.

Moreover, concerning the case of SHM with strain data, its validation with more available data and different system identification techniques must be completed. Then, modal analysis with strain measurements must be observed in a long term, looking at the stability of the structural response. The most effective sensor positioning must be evaluated with different deployments on steel bridges. Once this method is consolidated, it can be used to install low cost SHM systems for the characterization of both global and local behavior of structures, with the deployment of only one kind of sensor (strain gauge).

Regarding the 'non-collocated sensor problem', in order to find displacement estimations on nodes of the structure where we have only acceleration measurements, three possible methods have been proposed, shown with a simple 3-dof example. The first and second method proposed, based on modal contribution factors and modal parameters, show a good correlation between the estimated and the real displacement. Once one of the methods has been consolidated to work properly, it will be applied to a simplified model (17-dof) of the Manhattan Bridge, where all nodes are covered by acceleration measurement but only few points by displacement measurements. So, the ultimate goal will be the assessment of deflections in locations where there are no such sensors.

BIBLIOGRAPHY

[1] K.J. Astorm and T. Bohlin, "Numerical identification of linear dynamic systems for normal operating records," in *Proc. 2nd IFAC symp. Theory of self-adaptive systems*, Teddington, 1965.

[2] L. Hermans, P Guillaume, and H. Van der Auweraer, "A frequency domain maximum likelihood approach for the extraction of modal parameters from output-only data," , Leuven, Belgium, 1998.

[3] B.L. Ho and R.E. Kalman, "Effective construction of linear state-variable models from input/output data," , 1965.

[4] Bart Peeters and De Roeck, "Stochastic system identification for operational modal analysis: a review," *Journal of Dynamic Systems, Measurement, and Control*, no. 123, pp. 659–667, 2001.

[5] C.Y Shih, G.Y. Tsuei, R.J. Allemang, and D.L. Brown, "Complex mode indication function and its application to spatial domain parameter estimation," *Mechanical Systems and Signal Processing*, vol. 2, no. 4, pp. 367-377, 1988.

[6] Rune Brincker, Lingmi Zhang, and Palle Andersen, "Modal identification of output-only systems using frequency domain decomposition," *Institute of physics publishing, Smart materials and structures*, pp. 441–445, 2001.

[7] T Katayama, *Subspace Methods for System Identification*. London: Springer, 2005.

[8] P. Van Overschee and B De Moor, *Subspace Identification for Linear Systems: Theory - Implementation- Applications*.: Kluwer Academic Publishers, 1996.

[9] P Van Overschee and B. De Moor, "N4SID-Subspace algorithms for the stochastic identification problem," *Automatica*, vol. 30, no. 1, pp. 73-93, 1994.

[10] Greg Welch and Gary Bishop, *An Introduction to Kalman Filter*. North Carolina: ACM, Inc., 2001.

[11] B. Peeters, *System Identification and Damage Detection in Civil Engineering*. K. U. Leuven, Belgium: Ph.D. Thesis, 2000.

[12] Andrew Smyth and Meiliang Wu, "Multi-rate Kalman filtering for the data fusion of displacement and acceleration response measurements in dynamic system monitoring," *Mechanical Systems and Signal Processing, ScienceDirect, Elsevier*, pp. 21:706-723, 2006.

[13] A.L. Hong, "Weighting Matrices and Model Order Determination in Stochastic System Identification for Civil Infrastructure Systems," in *PhD thesis*, Columbia University, 2010.

[14] Peters S. Maybeck, *Stochastic models, estimation, and control, Vol 1*. New York: Academic Press, 1979.

[15] J.G. Reid, *Linear system fundamentals: continuous and discrete, classic and modern*. University of Michigan: McGraw-Hill, 1983.

[16] T Kailath, A. Sayed, and B. Hassibi, *Linear Estimation*.: Prentice Hall, 2000.

[17] Dan Simon, "Kalman Filtering," *Embedded Systems Programming*, pp. 72-79, JUNE 2001.

[18] G. Robert Browm and Y.C. patrick Hwang, *Introduction to Random Signals and Applied Kalman Filtering*. New York: John Wiley & Sons, 1997.

[19] D.J. Ewins, *Modal Testing: Theory, Practice and Application*. London: Research Studies Press, Ltd, 2001.

[20] N., et al Maia, *Theoretical and Experimental Modal Analysis*. UK: Research, 1997.

[21] J.N. Juang, *Applied System Identification*. Upper Saddle River: Prentice Hall PTR, 1994.

[22] J.N. Juang and M.Q. Phan, *Identification and control of mechanical systems*. USA: Cambridge University Press, 2001.

[23] M. Phan, L. G. Horta, J.-N. Juang, and R. W Longman, "Improvement of Observer/Kalman Filter Identification (OKID) by Residual Whitening," *Journal of Vibration and Acoustics*, vol. 117, pp. 232-239, 1995.

[24] Burns V. Lawrence, "MAC evaluations utilized in FEA analysis for mode identification," , Munich, 2004.

[25] R.J. Allemang, "The modal assurance criterion - twenty years of use and abuse," *Sound and Vibration*, vol. August, pp. 14-21, 2003.

[26] A. Morassi and S. Tonon, "Dynamic Testing for Structural Identification of a Bridge," *Journal of Bridge Engineering Φ ASCE*, pp. 573-585, November/December 2006.

[27] R. Brincker, P Andersen, and N.J. Jacobsen, "Automated Frequency Domain Decomposition for Operational Modal Analysis," in *24th International Modal Analysis Conference*, Florida, USA, 2007.

[28] C. Rainieri, G. Fabbrocino, and E. Cosenza, "An Automated procedure for modal parameter identification of structures under operational conditions," *Materials Forum*, vol. 33, pp. 62-78, 2009.

[29] E. Reynders and G. De Roeck, "Fully automated modal parameter estimation for SHM," in *4th International Conference on Experimental Vibration Analysis of Civil Engineering Structures*, Varenna, Italy, 2011.

[30] F Ubertini, C. Gentile, and A.L Materazzi, "On the automatic identification of modal parameters by subspace msthods," in *4th International Conference on Experimental Vibration Analysis of Civil Engineering Structures*, Varenna, Italy, 2011.

[31] Carmelo Gentile, "Modal and structural identification of a R.C. arch bridge," *Structural Engineering and Mechanics*, pp. Vol. 22, No. 1 (2006) 53-70, 2006.

[32] s.r.l. HSH computing. Strand7.

[33] s.r.l. Cspfea. Midas Gen.

[34] S. Benfratello and Fossetti, M. Di Paola, "Analisi dinamica di ponti ad arco in muratura soggetti a sisma e ad azioni mobili," Italy, 1999.

[35] K. Islami, G. Tecchio, and C. Modena, "Seismic intervention and dynamic testing of a bridge," *Applied Mechanics and Materials, Trans Tech Publications.*, vol. Vibration, Structural Engineering and Measurement , pp. 1159-1164, 2011.

[36] Bart Cauberghe, "Applied frequency-domain system identification in the field of

experimental and operational modal analysis," in *PhD thesis*, Vrije University Brussel, 2004.

[37] E. Caetano and A. Cunha, "Experimental and Numerical Assessment of the Dynamic Behaviour of a Stress-Ribbon Bridge," *Structural Concrete, Journal of FIB*, pp. Vol. 5, No. 1, pp. 29-38, 2004.

[38] A. Cunha, E Caetano, R. Calcada, and G. Peeters, B. De Roeck, "Dynamic measurements on bridges: design, rehabilitation and monitoring," *Istitution of Civil Engineering, Bridge Engineering*, pp. 135-148, 2004.

[39] A. Cunha and E. Caetano, "Experimental Modal Analysis of Civil Engineering Structures," *SOUND AND VIBRATION*, pp. 12-20, June 2006.

[40] A. Cunha and R. Calçada, "Ambient Vibration Test of a Steel Trussed Arch Bridge," in *18th Int. Modal Analysis Conference* , San Antoni TX, 2000.

[41] P., & Chikermane, S Banerji, "Structural Health Monitoring for Life Extension of Railway Bridges: Strategies and Outcomes," *Civil Structural Health Monitoring Workshop (CSHM-4)*, 2012.

[42] Leung T.P., Xue K. Z. Yam L.H, "Theoretical and experimental study of modal strain analysis.," *Journal of Sound and Vibration*, pp. 191(2), 251-260., 1996.

[43] Loris Vincenzi, *Identificazione dinamica delle caratteristiche modali delle proprieta' mecaniche di strutture mediante algoritmi di ottimizzazione*. Bologna, Italy, 2007.

[44] Universiteit Leuven, MACEC, A MATLAB Toolbox for Experimental and Operational Modal Analysis, 2011.

[45] Luis Ramos, *Damage identification on Masonry Structures based on Vibration Signatures.*: Universidade do Minho, 2007.

[46] G-N Fanjiang, R.B. Gajer , and Q. Ye, "Seismic Evaluation and Retrofit of the Manhattan Bridge," *Structures - ASCE* , 2004.

[47] Andrew Smyth and Rene B. Testa, "Motion Monitoring of the Manhattan Bridge," New York, 2009.

[48] Andrew W. Smyth, Jin-Song Pei, and Sami F. Masri, "System identication of the Vincent Thomas suspension bridge using earthquake records," *Earthquake Engineering and Structural Dynamics*, pp. 32:339–367, 2003.

[49] Mikhail G. Kogan, Kim, Won-Young, Yehuda Bock, and Andrew W. Smyth, "Load Response on a Large Suspension Bridge during the NYC Marathon Revealed by GPS and Accelerometers," *Seismological Research Letters*, pp. Volume 79, Number 1:, January/February 2008.

[50] Helmut Wenzel and Dieter Pichler, *Ambient Vibration Monitoring*. West Sussex, England: John Wiley & Sons, Ltd, 2005.

[51] A.L Hong and R. Betti, "Identification of the Baseline Modal Parameters of the Carquinez Suspension Bridge Using Ambient Vibration Data ," *SMIP08 Seminar on Utilization of Strong-Motion Data*, pp. 63-82, 2008.

[52] F. Magalhaes, Cunha A., and Caetano E., "Vibration based structural health monitoring of an arch bridge: From automated OMA to damage detection," *Mechanical Systems and Signal Processing*, vol. 28, pp. 212-228, 2012.

[53] Meiliang Wu and Andrew W. Smyth, "Application of the unscented Kalman filter for real-time nonlinear structural system identification," *Structural Control and Health Monitoring, Wiley Interscience*, pp. 14:971-990, 2006.

[54] Markus Kohler, "Using th Kalman Filter to track Human Interactive Motion Modelling and Initialization of Kalman Filter for Translational Motion," 2000.

[55] Jann N. Yang, Silian Lin, Hongwei Huang, and Li Zhou, "An adaptive extended Kalman filter for structural damage identification," *StructuralL Control and Health Monitoring, Wiley Interscience*, pp. 13: 849-867, 2006.

[56] Wodek K. Gawronski, *Advanced Structural Dynamics and Active Control ot Structures*. Panasada, CA, USA: Springer, 1998.

[57] N. M. M. Maia and Silva J. M. M., "Modal analysis identification techniques," *Phil. Trans. Royal Society Lond. A*, pp. 359, 29-40, 2001.

[58] M Wamsler, "The role of actual modal-contributions versus frequency to optimize the structure," *Engineering with Computers*, vol. 25, pp. 131-138, 2009.

[59] Ch. Liang, "Effects of Column Stiffness on the Modal Contribution to Displacement Response of Singe-column Bent Viaducts in the Transverse Direction," *Advanced Materials Research*, vol. 255-260, pp. 1711-1715, 2011.

[60] G.C. Hart and K. Wong, *Structural Dynamics for Structural Engineers*. Canada: John Wiley & Sons, 2000.

[61] H. De Angelis, H. Lus, R. Betti, and R.W. Longman, "Extracting physical parameters of mechanical models from identified state-space representation," *ASME Jopurnal Applied Mechanics* , vol. 69, pp. 617-625, 2002.

[62] M. Bruschetta, G. Picci, and A. Saccon, "A variational integrators approach to second order modeling and identification of linear mechanical systems," 2012.

[63] Attilio C., Santolini C., Hauf D.E., and Dubowsky S., "Displacements in a vibrating body by strain gauge measurements.," in *Proceedings of the 13th International Conference on Modal Analysis.*, 1995.

[64] M.L. Beconcini, G. Buratti, P. Croce, M. Mengozzi, and P. Orsini, "Dynamic characterization of a five spans historical masonry arch bridge," in *ARCH'07 – 5th International Conference on Arch Bridges*, 2005, pp. 399-407.

[65] C. P. Lamarche, P. Paultre, J. Proulx, and S. Mousseau, "Assessment of the frequency domain decomposition technique by forced-vibration tests of a full-scale structure," *Earthquake Engineering and Structural Dynamics*, pp. 37:487–494, 2007.

[66] Calmelo Gentile and Angelo Valsechi, "Analisi Modale sperimentale del ponte sul Pioverna a Cremona," 2007.

[67] Jimin He and Zhi-Fang Fu, *Modal Anlysis*. Oxford: Butterworth-Heinemann, 2001.

[68] B. Peeters, G. De Roeck, E. Caetano, and A. Cunha, "Dynamic Study of the Vasco da Gama Bridge," in *International Conference on Noise and Vibration Engineering*, Leuven, Belgium, 2002.

[69] B. Peeters and G. De Roeck, "One year monitoring of the Z24-Bridge: environmental effects versus damage events," *Earthquake Engineering and Structural Dynamics*, pp. 30, No 2, 149-171, 2001.

[70] Structural Vibration Solutions, ARTeMIS Extractor, 2008.

[71] F.A. Badawi, "A utilization of properties of the discrete-time Riccati equation in stochastic realization theory," *Journal of Optimization Theory and Applications*, vol. 49(2), pp. 91–206, 1986.

[72] L. Lennart, *System Identification:Theory For The User*. 1999: Prentice Hall PTR, New Jersey.